Syracuse University

SURFACE

5-14-2017

Combining Smart Material Platforms and New Computational Tools to Investigate Cell Motility Behavior and Control

Megan Brasch
Syracuse University

Follow this and additional works at: https://surface.syr.edu/etd

Part of the Engineering Commons

Recommended Citation

Brasch, Megan, "Combining Smart Material Platforms and New Computational Tools to Investigate Cell Motility Behavior and Control" (2017). *Dissertations - ALL*. 688.
https://surface.syr.edu/etd/688

This Dissertation is brought to you for free and open access by the SURFACE at SURFACE. It has been accepted for inclusion in Dissertations - ALL by an authorized administrator of SURFACE. For more information, please contact surface@syr.edu.

Abstract

Cell-extracellular matrix (ECM) interactions play a critical role in regulating important biological phenomena, including morphogenesis, tissue repair, and disease states. *In vivo,* cells are subjected to various mechanical, chemical, and electrical cues to collectively guide their functionality within a specific microenvironment. To better understand the mechanisms regulating cell adhesive, differentiation, and motility dynamics, researchers have developed *in vitro* platforms to synthetically mimic native tissue responses. While important information about cell-ECM interactions have been revealed using these systems, a knowledge gap currently exists regarding how cell responses in static environments relate to the dynamic cell-ECM interaction behaviors observed *in vivo*. Advances at the intersection of materials science, biophysics, and cell biology have recently enabled the production of dynamic ECM mimics where cells can be exposed to controlled mechanical, electrical or chemical cues to directly decouple cell-ECM related behaviors from cell-cell or cell-environmental factors. Utilization of these dynamic synthetic biomaterials will enable discovery of novel mechanisms fundamental in tissue development, homeostasis, repair, and disease.

In this dissertation, the primary goal was to evaluate how mechanical changes in the ECM regulate cell motility and polarization responses. This was accomplished through two major aims: 1) by developing a modular image processing tool that could be applied in complex synthetic *in vitro* microenvironments to asses cell motility dynamics, and 2) to utilize that tool to advance understanding of mechanobiology and mechanotransduction processes associated with development, wound healing, and disease progression. Therefore, the first portion of this thesis (**Chapters 2 and 3**) dealt with proof of concept for our newly developed automated cell tracking

system, termed ACT*IV*E (automated contour-based tracking for *in vitro* environments), while the second portion of this thesis (**Chapter 4-7**) addressed applying this system in multiple experimental designs to synthesize new knowledge regarding cell-ECM or cell-cell interactions.

In **Chapter 1**, we introduced why cell-ECM interactions are essential for *in vivo* processes and highlighted the current state of the literature. In **Chapter 2**, we demonstrated that ACT*IV*E could achieve greater than 95% segmentation accuracy at multiple cell densities, while improving two-body cell-cell interaction error by up to 43%. In **Chapter 3** we showed that ACT*IV*E could be applied to reveal subtle differences in fibroblast motility atop static wrinkled or static non-wrinkled surfaces at multiple cell densities. In **Chapters 4 and 5**, we characterized fibroblast motility and intracellular reorganization atop a dynamic shape memory polymer biomaterial, focusing on the role of the Rho-mediated pathway in the observed responses. We then utilized ACT*IV*E to identify differences in subpopulation dynamics of monoculture versus co-culture endothelial and smooth muscle cells (**Chapter 6**). In **Chapter 7**, we applied ACT*IV*E to investigate *E. coli* biofilm formation atop poly(dimethylsiloxane) surfaces with varying stiffness and line patterns. Finally, we presented a summary and future work in **Chapter 8**. Collectively, this work highlights the capabilities of the newly developed ACT*IV*E tracking system and demonstrates how to synthesize new information about mechanobiology and mechanotransduction processes using dynamic biomaterial platforms.

COMBINING SMART MATERIAL PLATFORMS AND NEW COMPUTATIONAL TOOLS TO INVESTIGATE CELL MOTILITY BEHAVIOR AND CONTROL

By

MEGAN E. BRASCH

B.S. Bioengineering, SUNY Binghamton University, 2011

DISSERTATION

Submitted in partial fulfillment of the requirements for the
degree of Doctor of Philosophy in Bioengineering

Syracuse University
May 2017

Copyright © Megan E. Brasch 2017

All Rights Reserved

Dad - *this one’s for you.*

In loving memory of my father, Robert Brasch, my second father, Bernie Agins, Grandma and Grandpa Dahlberg, Grandma and Grandpa Brasch, Grandma and Grandpa Chaffee, and Uncle Joe. You all inspired me to pursue my dreams.

Acknowledgements

First and foremost, I want to thank my advisor and mentor, Professor James H. Henderson for encouraging and supporting me over the past five and a half years to accomplish this lofty goal. Jay always pushed me to thrive, regardless of whether I was an undergraduate REU or the most senior PhD student in his research lab. I want to also acknowledge and thank Professors Lisa Manning and Christopher Turner for their amazing guidance and care throughout our many collaborative efforts. Thank you for introducing me to some of your amazing PhD students and for always being there for me when I needed an extra little push. To the rest of my dissertation committee, Professors Dacheng Ren, Zhen Ma, and Pranav Soman, thank you for your valuable input in molding my candidacy proposal into this impactful thesis.

I additionally want to thank all of the professors in the biomedical and chemical engineering, physics, and chemistry departments at SU and the professors from the cell and developmental biology department at Upstate Medical University who enabled me to accomplish all of the research presented in this dissertation. In particular, thank you Dr. Mather, Dr. Gilbert, Dr. Finkelstein, Dr. Sureshkumar, Dr. Hasenwinkel, Dr. Bond, Dr. Marchetti, and Dr. Hehnly-Chang for all of the extra feedback you provided along the way. A special thanks to Lynore de la Rosa, Karen Low, Dawn Long, Sabina Redington, Jason Markle, and Amy Forbes for the "behind the scenes" support you provided me with every day.

To all of the past and current members of the Henderson lab, thank you for helping me sort out all of the technical details (and providing great company in lab, regardless of the day or time). Specifically, thank you Dr. Ling-Fang Tseng for being my first mentor and an amazing colleague,

Dr. Richard Baker for sticking by me through long coding sessions, and Dr. Jing Wang for working with me to sort out all of the tedious details related to our time-lapse work. You three set an amazing precedent for what to strive for by the end of my degree. Thank you to Kevin Davis, who laid the foundation for most of the work in our lab. To the current Henderson lab PhD members: Ariel Ash-Shakoor, Fred Donelson, Stephen Sawyer, Shelby Buffington, Kyle Bishop, Michelle Pede, Alex Jannini, Roland Beard, and Katy Pieri – you got this. As painful as some of the long nights and weekends are, I know that each one of you will make it to the finish line. An extra special thanks to all of the undergraduates and Master's students who helped me along the way: Alexis Peña, Dakota Jones, Ye He, Stephen Burke, Elliot Russell, Trent Searfoss, Kadye Moore, Lauryn Alexander, Leila Hart, Joyrie Dickerson, Donmanique Hardy, Alyssa Seunarine, and Brandyn White.

Thank you to my various adopted family in other labs and departments. Thank you Erin McMullin for your friendship and support during our parallel PhD journey. Thank you Melodie Lawton for always lending an ear when I needed to vent. Thank you Giuseppe Passucci for helping me sort out gigabytes of video data (and always being on the same page as me). Thank you Anushree Gulvady and Greg Goreczny for having as ridiculous of a schedule as me and always being willing to help in any way you could. Thank you also to the entire Chisholm lab.

Last, but certainly not least, thank you to my family and friends outside of Syracuse. Jes – I'm working on rebuilding your knees… just hold out a little longer. Thank you to my amazing mother who has been an inspiration my entire life. To my brother, Erin, my sister-in-law, Alex, and my baby nephew, Eli – you always know how to make me laugh. And thank you to Dan, my fiancé, who has kept me sane all along. I love you all.

Table of Contents

Chapter 3: ACT*IV*E Case Study Investigating Change in Motility Dynamics of Static Anisotropic and Isotropic Microenvironments[†,*] 72

List of Tables

List of Schemes

List of Figures

Chapter 1: Background and Motivation

1.1 Thesis Overview: Development and Application of an Automated Cell Tracking System for Cell Motility Analysis on Novel *In Vitro* Smart Material Platforms

Cell-extracellular matrix (ECM) interactions play a critical role in regulating important biological processes *in vivo*, including morphogenesis, tissue repair, and disease regulation. Native tissue is dynamic and complex: it is mechanically, electrically, and chemically tuned to function as part of a specific microenvironment, where various stimuli collectively guide important cellular processes fundamental to tissue development, homeostasis, repair, and disease. Researchers have extensively utilized *in vitro* platforms as a means to mimic native tissue, using these systems to identify mechanisms driving crucial cell behaviors, including cell adhesion, differentiation, and motility. While much has been learned from these carefully developed *in vitro* platforms, there is a knowledge gap regarding how cell responses in these static systems correlate to those observed within dynamic ECM microenvironments *in vivo*. Current advances at the intersection of material science, biophysics, and cell biology have led to the production of dynamic ECM mimics where cells can be directly exposed to controlled mechanical, electrical, or chemical stimulation within their microenvironments, similar to stimuli experienced *in vivo*. By decoupling these stimuli from the complex interactions associated with cell-cell and cell-environmental factors, it is possible to decipher new mechanisms driving tissue repair and develop novel diagnostic tools and therapies to target complicated disease states, such as cancer.

To address the current knowledge gap regarding how dynamic ECM stimulation affects cell behavioral responses, this thesis utilizes a combination of a novel cell tracking approach from the field of computational biology, statistical methods from the fields of physics and bioinformatics, and a subset of smart material designs from the field of biomaterials to investigate how mechanical changes in a cell's microenvironment regulate cell polarization and cell motility responses. This goal will be achieved by first characterizing the novel cell tracking approach in static systems, and then applying the technique to cell motility behaviors in a shape memory polymer microenvironment. Additional environmental complexities, including cell motility dynamics in co-culture microenvironments, and adhesive or motility dynamics of cells on static platforms with varying mechanical properties, will also be investigated. To motivate these studies, this chapter will first summarize fundamental cell mechanobiology and mechanotransduction processes with respect to current literature understanding. A brief synopsis of how researchers have previously employed static *in vitro* systems to study important *in vivo* processes will then be discussed. Dynamic *in vitro* platforms used to regulate mechanical stimulation or bulk shape will then be reviewed to demonstrate current progress in smart materials design to better mimic the complex *in vivo* microenvironment. The role of "big data" in time-lapse microscopy videos will then be outlined to frame how current researchers process complex live-cell data. Lastly, the scope of this dissertation will be described chapter-by-chapter to further understanding of mechanisms driving cell motility and cell polarization responses.

1.2 The Role of the Extracellular Matrix in Cellular Processes

Within the human body, various stimuli—provided by cells, extracellular matrix (ECM), or other environmental factors—can directly influence a single cell’s behavior. Disruption of the body's natural scaffolding structure, the ECM, can play critical roles in key biological processes, including tissue development, wound healing, and disease states. In this section, a summary of the fundamental components of ECM is initially provided to highlight important underlying biological principles of *in vivo* microenvironment design. The role of ECM remodeling, reorganization, or stimulation *in vivo* is then provided with respect to the three primary fields of study in synthetic ECM design: 1) developmental processes, 2) tissue repair, and 3) disease initiation and progression. These important *in vivo* examples motivate the need for additional investigation of dynamic *in vitro* platforms to further understanding of mechanisms associated with *in vivo* tissue development, repair, and disease.

1.2.1 Extracellular Matrix: Structure and Function in Cell Adhesion and Motility

Mammalian extracellular matrix (ECM) is fundamentally comprised of a heterogeneous mixture of water, proteins, and polysaccharides that cohesively work to provide a scaffolding structure for cells and regulate biochemical and biophysical interactions between cells and their microenvironment [1]. ECM contains a mixture of: 1) nano- and micron-sized fibrous proteins such as collagen, laminin, or fibronectin and 2) proteoglycans such as glycosaminoglycans or aggrecan [1, 2]. However, ECM composition varies based on tissue type. For example, type I collagen is the most abundant form of collagen found in mammalian tissue; it is a major component of the dermis, muscle encasings, tendons, and scar tissue, providing mechanical integrity due to its fibril structure [3]. It is not, however, found in cartilage tissue, which is primarily derived from type II collagen for tensile support and aggrecans for compressive mechanical properties [4]. The microenvironment that chondrocyte cells experience in cartilage tissue is therefore very different than the microenvironment that keratinocytes or fibroblasts experience in skin or connective tissue environments respectively, primarily because each cell type is interacting with different proteins and polysaccharides of varying structure, size, and mechanical properties.

Integrins are the primary class of cell surface receptors responsible for adhesion of cells to ECM. Integrins are composed of an α and β subunit, where each α and β combination has a binding specificity. While many integrins can interchangeably recognize multiple ECM proteins, appropriate binding sites must exist for cells to bind to ECM within a unique microenvironment [5]. Focal adhesion kinases (FAK) aggregate in integrin-ECM focal adhesion sites, generating a protein enriched focal contact that aids in the signaling cascade moderating cell morphology and migration dynamics [6-8]. Various other adapter proteins (for example α-actinin, talin, vinculin, or paxillin) collectively assemble at the focal adhesion site to reinforce cell-ECM binding, serve as sensitive mechanotransducers to the surrounding microenvironment, and stabilize the cell cytoskeleton at the integrin-ECM binding site [9, 10].

Cells actively probe their surroundings to guide their local adhesive and motility behaviors within a particular microenvironment. Myosin serves as the primary mechanosensor responsible for F-actin polymerization and thus cell cytoskeletal reorganization [9]. This molecular motor can be recruited to focal adhesion sites by an active form of Rac1 [11]. As focal adhesions stabilize, they can serve as traction sites to initiate cell migratory behavior. Collectively, the internal architecture of the cell polarizes to align with the direction of stable protrusions [12]. With respect to cell polarity, or the reorientation and reorganization of a cell's internal structure to promote large-scale behaviors such as motility, Cdc42 has been implicated as the master regulator responsible for concentrating the microtubule-organizing center (MTOC) and Golgi apparatus towards the front of the nucleus to facilitate directed migration [13-15]. Cell polarization can, however, vary based on cell type. Rearward nuclear polarization is more prominent in slower moving cells, such as fibroblasts, whereas faster moving cells, such as T-lymphocytes, tend to aggregate their MTOC and Golgi bodies behind the nucleus during migration [12, 15, 16]. These subtle differences in cell-ECM adhesion and motility characteristics are directly related to necessary cell functions within tissue-specific *in vivo* microenvironments. These processes remain not fully understood, as researchers actively continue to investigate mechanistic responses of cells to changes in their local ECM environments.

1.2.2 ECM in Developmental Processes

Cell-extracellular matrix interactions regulate fundamental developmental processes including gastrulation, right-left asymmetry, and organogenesis [17]. One of the most widely studied developmental events is neural crest cell migration. This early embryonic process involves disruption of the basal lamina via increased fibronectin and hyaluronan deposition that ultimately upregulates mesenchymal cell phenotypes and migratory capabilities by way of an epithelial to mesenchymal transition (EMT) [18, 19]. Increased motility allows the cells to separate towards different portions of the embryo, where they can then receive localized differentiation signals to tailor tissue development [20]. Similar ECM driven processes are also observed during organ growth. Integrin $\alpha5\beta1$, a major cell-surface receptor for fibronectin, has been shown to be a crucial regulator in left-right asymmetry during organ development in vertebrates [21]. Similarly, branching is an organ development phenomenon that can be regulated by cell-ECM interactions. Branching is found in the development of multiple organ structures including the vasculature, kidneys, lungs, and mammary glands [22-24]. Specifically, in mesenchymal tissues, branching events are regulated by ECM. When compared to epithelial tissues, developing mesenchyme have sparser cell densities resulting in ECM driven motility dynamics [23]. For example, fibronectin has been shown to regulate cleft formation and branching of the salivary glands, lungs, and kidneys [25]. Clearly, appropriate biophysical and biochemical regulation of cells by ECM components is essential for proper organism development.

1.2.3 Cell-ECM Interactions Drive Tissue Repair

Tissue repair is a complex process involving coordination of damage assessment in a particular microenvironment, foreign body identification and confinement, and cell recruitment and differentiation to repair a wound site. Cell-ECM interactions are critical in providing appropriate biochemical cues, regulating the inflammatory process, and ultimately guiding cells to appropriate regions to direct tissue repair [26]. In one of the most common *in vivo* wound scenarios, fibroblasts and keratinocytes cooperatively remodel their basement membrane composition via deposition of ECM proteins (e.g., laminin 1, collagen IV, and laminin 5) to promote collective cell migration to heal skin tissue [27]. Similarly, in angiogenesis, extracellular gradients of vascular endothelial growth factor mediate cell-ECM binding properties to dictate cell migratory patterns to re-form vessels, once cells have penetrated into the fibronectin and fibrin rich wound site [27, 28]. In studies with rats, liver necrosis induces hepatic stellate cells (HSCs) to activate into myofibroblast cells. Myofibroblast differentiation is partially driven by a decrease in the mechanical integrity of the ECM [29, 30]. Once differentiated, these myofibroblasts deposit additional ECM proteins to further healing of localized liver damage [31]. A similar process is also observed in skeletal muscle regeneration. Local inflammation of the damage site leads to increased production of matrix metalloprotease-14 (MMP-14). MMP-14 locally cleaves collagen I and fibronectin binding sites, facilitating myofibroblast differentiation and migration during muscle repair [32]. These diverse examples illustrate that cell-ECM interactions are critical in regulating wound healing behaviors and mitigating the tissue repair process *in vivo*. By improving understanding of the mechanisms associated with these essential biological processes, new treatment options such as improved skin grafts for burns, autologous stem cell differentiation for tissue replacement, and enhanced cell infiltration and improved immune recognition for implantable devices may be achieved.

1.2.4 The Role of ECM in Disease Progression

Disruption of ECM homeostasis has been shown to influence various pathological disease states including cancer progression, fibrotic diseases, cardiomyopathies, and genetic disorders [33-35]. For example, during collagen synthesis, lysyl oxidase (LOX) cross-links newly synthesized collagen. Upregulation of LOX leads to ECM stiffening and collagen reorientation, promoting integrin expression and focal adhesion binding to facilitate breast cancer tumorigenesis [36-38]. Similarly, reorganization of ECM surrounding breast tumors by deregulated stromal cells has shown to elicit metastatic potential [39-41]. Comparable cell-ECM mediated responses have also been observed with human melanoma cells. Haptotactic gradients in ECM proteins, including laminin, fibronectin, and type IV collagen, have been shown to regulate melanoma motility behaviors and thus metastatic potential [42]. Regardless of tumor type, remodeling of ECM proteins by host cells is a hallmark of cancer cell invasion [27, 43-45]. Similarly, ECM surrounding metastatic tumor sites tends to be stiffer than in healthy tissue [46]. By improving understanding of cell-ECM mediated interactions in cancer systems, novel ECM-based drug treatments may be employed. These potential targets include disrupting integrin binding, modifying ECM degradation, or controlling biomolecule gradients within various microenvironments.

Cell-ECM irregularities have also been implicated in fibrotic disorders. As previously discussed, changes in ECM stiffness drive HSC differentiation to initiate the liver healing process. If the differentiated myofibroblasts remain activated, continual deposition of type I and type III collagen results in sclerosis and eventual cirrhosis of the liver tissue [30, 31, 47]. Similar processes are also observed in cardiomyopathies. Following myocardial infarctions (also known as heart attacks), collagen is deposited by cardiomyocytes to heal tissue damage. If left unregulated, this collagen deposition can continue, creating micro or macroscopic scar tissue that can hinder normal cardiac functions [48]. More generally, mechanical tension generated by ECM remodeling, coupled with TGF-β1 signaling, primarily dictates myofibroblast differentiation. Consistently abnormal ECM stiffness levels lead to an increase in TGF-β1 presence, which ultimately develops into fibrotic conditions [49]. Just as with cancer systems, understanding the mechanisms driving fibrotic disorders could lead to novel drug therapy targets, including stiffness based local modification of ECM tissue or biomolecule regulation to alter cell-ECM binding affinities.

Perturbations in appropriate ECM structure have additionally been linked to various genetic and autoimmune disorders [50]. For example, while EMT are important regulatory processes driven by ECM in beneficial *in vivo* events such as neural crest cell migration, they can also be found in detrimental *in vivo* disease states such as cancer cell development [18, 51]. Furthermore, ECM knockouts in mice have demonstrated the necessity of various proteins in healthy development and ultimately organism survival. For example, removal of laminin-α3 causes lethal skin defects while exclusion of fibronectin or collagen-α1 results in fatal vascular complications [25]. These examples clearly demonstrate that ECM is an important regulator and crucial driver of appropriate organism development and that proper ECM signaling is a primary factor contributing to the development of various disease states.

1.3 Static Microenvironments: Exploration of Chemical, Mechanical, and Topographical Cues for Regulating Cell Behaviors

Researchers have extensively utilized *in vitro* synthetic platforms as a means to mimic native tissue microenvironments. By tailoring the surface chemistry, substrate rigidity, and topographical features of these systems, important insights into cell adhesive properties, migratory behaviors, and differentiation capacity have been achieved. This section summarizes current literature understanding of how static patterned features, including surface protein modification, comparisons of stiffness variations within a substrate (or substrate to substrate), and the use of micro- and nano- channels, ridges, wells, and grooves as topographical guides, dictate cell behavioral responses. Emphasis is placed on why careful consideration of static surface features is important for *in vitro* synthetic cell-ECM study design. Lastly, limitations of these static systems, and how they correlate to dynamic ECM microenvironments *in vivo*, is summarized as a precursor to the next section's discussion about progress in dynamic *in vitro* ECM synthetic designs.

1.3.1 Surface Chemistries Alter Cell Adhesion and Proliferation

One of the most fundamental components of synthetic biomaterial design is selection of an appropriate material chemistry that is both cytocompatible and biomimetic, as surface chemistry dictates whether a cell can adhere and function within a particular microenvironment. As previously described, integrins are the primary class of surface receptors responsible for cell-ECM adhesion and ultimately dictate cell polarization and motility responses, the target cell behaviors analyzed in this thesis. One of the most widely used techniques to improve cell adhesive properties to a synthetic surface *in vitro* is the inclusion of RGD peptide sequences [52]. RGD sequences are recognized by multiple integrin heterodimers, as they are one of the primary structures that aid in cells binding to ECM fibronectin [9]. For example, Alvarez-Barreto and colleagues observed improved rat mesenchymal stem cell (MSC) seeding and attachment on RGD modified poly(L-lactic acid) foams compared to unmodified controls [53]. Similarly, Shin and colleagues confirmed that RGD peptide incorporation in poly (L-lactide) scaffolds improved cell adhesive properties of human MSCs. Shin et. al also demonstrated that RGD presence led to increased proliferative capacities of human MSCs *in vitro*, due to favorable surface chemistry within the cellular microenvironment [54].

Coordination of surface modifications and adhesive ligands, such as fibronectin, hylauronan, or gelatin deposition, on synthetic surfaces have been used broadly for spatial patterning and cell behavioral control [55]. Magnani and colleagues chemically modified glass by micropatterning hylauronan lines on the material surface. When exposing NIH 3T3 fibroblasts, human primary fibroblasts, bovine aortic endothelial cells (BAEC), and human endothelial cells (hEC) to the patterned surfaces, each cell type responded differently to their microenvironment. The 3T3 and primary human fibroblasts selectively attached to the silanized glass regions, orienting themselves in an aligned fashion between the hylauronan strips. The cells' proliferative capabilities were hindered until hylauronan degradation was complete, after which they grew to cover the full glass surface with no preferential orientation. Similar behavior was observed for the BAEC and hEC lines initially. However, when the hylauronan micropatterns were sulphated to increase their negative charge (and thus alter the binding properties), the hEC preferentially adhered to the hyaluronan domains instead of the glass. Increasing or decreasing the stripe dimensions further altered cell polarization dynamics, where thinning the lines increased cell migration along the stripe direction. No change was seen in BAEC behavior with the sulphated hylauronan [56]. These examples demonstrate that careful consideration of surface chemistry properties are critical when developing synthetic *in vitro* platforms to mimic *in vivo* cell adhesive, proliferative, and motility responses. As such, the material chemistries utilized in this thesis, poly(tert-butyl acrylate-co-butyl acrylate), borosilicate glass, and poly(dimethylsiloxane), were carefully screened using multiple cell types to ensure appropriate adhesive properties, cytocompatibility, and cell type specific motility characteristics signature to known cell behaviors, before designing experiments investigating mechanisms driving cell polarization and motility responses.

1.3.2 Substrate Rigidity Controls Stem Cell Differentiation, Polarization, and Motility

ECM stiffness is another important regulatory factor that dictates tissue differentiation *in vivo* [57] and is therefore crucial to consider when developing *in vitro* biomimetic platforms. The Young's modulus of ECM can vary significantly within the body. For hard tissues such as bone, ECM typically has a high elastic modulus of 100kPa or more, while for more elastic tissues such as muscle or skin, the modulus tends to average ~10kPa. Furthermore, soft tissues, such as the brain or lungs, traditionally have an elastic modulus below 1kPa [57]. Correspondingly, researchers have observed that *in vitro* culture of mesenchymal stem cells on soft (<1kPa), moderate (1-20kPa), and stiff (>25kPa) surfaces results in neurogenic, myogenic, and osteogenic differentiation respectively [58, 59].

Durotaxis, the motility and behavioral response of cells exposed to a stiffness gradient, is a common ECM phenomenon used to guide organism development, direct tissue repair, and control disease progression [60]. Wong and colleagues demonstrated that NIH 3T3 fibroblasts are sensitive to changes in surface stiffness *in vitro*. By controlling the patterning of soft and stiff circular features, Wong et. al showed that fibroblasts initially extend filopodia to probe their microenvironment and then selectively bind and create focal adhesion sites only on stiff features [61]. Similar stiffness preferences were also observed by Gray and colleagues. By locally altering stiffness regimes in poly(dimethylsiloxane) (PDMS) substrates, NIH 3T3 fibroblasts and bovine pulmonary arterial endothelial cells preferentially migrated towards and accumulated on stiffer (34 ± 3kPa) versus softer (1.8 ± 0.3kPa) portions of the PDMS, despite uniform coating of the surface with fibronectin [62]. More recently, Saez and colleagues took this idea a step further, analyzing the effects of a microscopic stiffness gradient in PDMS on Madin-Darby canine kidney (MDCK) epithelial cells. They demonstrated that MDCK cells align and migrate along the stiffest direction, hypothesizing that this alignment is mediated by contact guidance [63]. To further understanding of these principles, biophysical models have also been developed to characterize and simulate durotaxis phenomenon [64]. These examples demonstrate the importance of material stiffness on cell behavioral responses. Within the scope of this thesis, these concepts were incorporated when selecting *in vitro* biomaterial platforms for cell-ECM interaction studies. In the case studies presented in **Chapters 2-6**, stiff (>25MPa) biomaterials were deliberately selected to mimic the stiff ECM structure native to fibrotic and disease prone microenvironments. In **chapter 7**, differences in soft (0.1MPa) versus moderately stiff (2.6MPa) microenvironments were investigated to analyze anti-fouling properties of bacterial attachment. Clearly, careful consideration of the mechanical properties of synthetic biomaterials is required to appropriately direct cell behaviors with respect to implantable devices or tissue repair treatments *in vivo*.

1.3.3 Surface Patterning as a Tool to Regulate Cell Motility Dynamics

Topographical surface patterning is one of the most widely studied tools for regulating cell morphology, polarization, and motility dynamics *in vitro*. Therefore, careful consideration of surface topography is required when developing synthetic *in vitro* platforms for cell-ECM interaction studies. Microscopic grooves, ridges, wells, and channels have been used for decades to study cell-ECM interactions in two dimensions, with more recent attention directed towards nanoscale topographical features and three dimensional synthetic designs [52]. More specifically, these surface and structural modifications have been used to assess how the cell polarization process occurs *in vitro* and whether varying pattern dimensions, widths, heights, or architectures contributes to enabling or hindering cell motility responses [60]. Teixeira and colleagues demonstrated the fundamentals of these principles by patterning silicon wafers with nano- and micron-sized ridges. Patterns with 800nm or larger pitches resulted in ~70% or more alignment of human corneal keratocyte cells (HCKCs) with the ridge direction, compared to ~35% alignment of human corneal epithelial cells (HCECs). When pitch size was reduced to 400nm, HCKC alignment dropped to ~45%, while HCEC alignment remained consistent. Nanoscale features also resulted in a reduction of stress fiber formation and focal adhesion sites for HCKCs when compared to microscale patterns, which the authors hypothesized may be related to regulation of myofibroblast differentiation of keratocytes *in vivo* [65]. Similar analyses have been conducted to examine the effects of swelling [66] and width changes [67] in grooved designs, as well as the effects of asymmetric pattern distributions [68] and density [69] and wavelength [70] gradients on cell polarization and motility responses. More recently, these principles have been expanded to three dimensional systems to better mimic the native microenvironment that cells experience *in vivo*. For example, Peela and colleagues demonstrated that microencapsulation of breast tumor cells within a GelMA hydrogel matrix allowed for the study of breast tumor development, growth, and invasion into the surrounding ECM when comparing healthy (MCF10A), non-invasive tumorigenic (MCF7), and invasive tumorigenic (MDA-MB-231) mammary epithelial cells [71]. These examples demonstrate that pattern type, size, and gradation can have lasting impacts on biomaterial response *in vitro*. Thus, the nano- and micron-sized topographical features selected in the synthetic designs in **Chapters 2-5** and **7** respectively, were first characterized as static systems to meticulously analyze cell morphology, adhesion, and motility properties with respect to the pattern features. Clearly, it is important that surface topographies are carefully designed to improve natural biomaterial integration and facilitate cell homing capabilities for implant design and treatment procedures *in vivo*.

1.4 Active Microenvironments as New Frontiers for Studying Cell Dynamics

While researchers have begun to unravel useful mechanisms associated with cell morphology, polarization, and motility responses *in vitro* using synthetic systems with specific surface chemistries, variable stiffness, and patterned topographical features, the microenvironment that cells experience *in vivo* is not static in nature. *In vivo*, ECM is often remodeled to produce mechanical, electrical, and chemical stimuli that collectively guide important cellular processes fundamental for tissue development, homeostasis, repair, and disease. As such, advances in materials science have led to the development of dynamic synthetic platforms that can simulate these remodeling events. Examples of how cells reorganize natural ECM platforms and respond to mechanical stimulation within their microenvironment are explored in this section to demonstrate that incorporating mechanical, electrical, and chemical cues in *in vitro* systems is the next step required for furthering understanding of crucial mechanisms driving developmental, tissue repair, and disease progression processes *in vivo*.

1.4.1 Cells Reorganize Cell-Derived and Natural Extracellular Matrices

Remodeling of ECM is a hallmark of collective cell invasion in three-dimensional *in vivo* microenvironments [27]. As previously mentioned, ECM remodeling is essential in advantageous biological processes such as neural crest development [18, 19], healing of skin tissue [27], and myofibroblast differentiation for muscle repair [31, 32]. It is also prominent in detrimental *in vivo* processes such as breast cancer metastasis [39-41] and cirrhosis of the liver [30, 31, 47]. Typically, ECM remodeling occurs through one of two processes: 1) local degradation of ECM proteins via protease activity (e.g., matrix metalloproteinases), or 2) deposition of new ECM components, such as collagen, fibronectin, or laminin, to alter ECM mechanical properties and binding affinities [27].

Cell derived or natural polymer models have widely been used *in vitro* to study how cells actively remodel their microenvironment to promote various biological processes. Collagen matrices are one of the most widely employed systems, partially due to their FDA approval [72]. Collagen applications include cartilage tissue repair [73], vascular constructs [74, 75], and skin repair [76]. For example, Starke and colleagues used a 3D collagen matrix to demonstrate that cell protrusions actively engage and manipulate collagen fibrils to generate forces necessary to elongate melanoma cells and ultimately propel them through 3D tissue microenvironments [77]. Fibrin (also FDA approved) and Matrigel, a commercially available mix of multiple ECM proteins, have also been extensively explored as standalone *in vitro* ECM platforms. As previously mentioned, ligand modification of synthetic materials incorporating natural ECM adhesive proteins such as fibronectin, vitronectin, and laminin have also widely been employed *in vitro* with varied therapeutic success [55].

Some of the most effective applications of cell derived or natural polymers for therapeutic designs are in the area of skin repair for burns and cutaneous wounds. The bacterial synthesized version of cellulose, also known as microbial cellulose (MC), has a unique nanostructure that yields high mechanical integrity with natural antimicrobial and biodegradable properties for wound dressings [78]. Park and colleagues demonstrated that MC treatments of full-thickness skin defects in rats resulted in faster wound healing, reduction of inflammation, no apparent toxicity effects, and improved vascularization of the wound site compared to a Vaseline gauze treatment [79]. Chitan and chitosan have similarly been used for wound healing applications due to their anti-bacterial, anti-inflammatory, and strong mechanical properties [78]. Bactericides have been incorporated into chitan scaffolds used in wound dressings to further help prevent infections from initiating [80]. Alginate, dextran, agar, silk, and many other natural polymers have additionally been explored for wound healing applications [78]. Through these various examples, it is clear that cells actively manipulate natural ECM microenvironments to promote important *in vivo* biological processes. Therefore, it is important to consider how cells will manipulate natural ECM scaffolds and incorporate natural polymers and ECM ligands as integral components of synthetic *in vitro* studies to improve understanding of cell responses and therapeutic designs in tissue repair applications. To incorporate these principles, the material system utilized in **Chapters 2-5** was soaked in fetal bovine serum prior to cell seeding, to promote favorable cell attachment due to surface protein adsorption.

1.4.2 Mechanical Stimulation as a Tool to Hone Cell Behavioral Responses

Mechanical properties (e.g., alterations in ECM stiffness or ECM architectural remodeling) are commonly used *in vivo* to functionally guide cell morphology, polarization, and motility responses, locally homing cells to perform a specific role within their microenvironment. Within the last two decades, incorporation of mechanical stimulation into biomaterial models *in vitro* has provided new insights into the mechanisms driving these phenomena, as previous static systems failed to capture this dynamic functionality. Uniaxial cyclic strain has been shown to disrupt stress fiber formation within the actin cytoskeleton, inhibiting reorientation of cells exposed to persistent changes in strain [81]. Wang and colleagues exposed human aortic endothelial cells to both uniaxial and bi-axial deformations of silicone membranes. They observed that the cells reoriented their cytoskeleton to align in the direction of minimal substrate deformation, reorganizing their stress fibers parallel to the same direction. Importantly, this reorientation was still observed after perturbing the overarching microtubule structure of the cells [82]. This indicates that the cells "feel" the change in their microenvironment and respond with changes in their cytoskeletal organization. Just as with durotaxis driven behaviors, biophysical models have been developed to improve understanding of the underlying strain patterns driving these cytoskeletal reorganization processes [83]. While much has already been revealed related to changes in cell morphology and polarization as a result of cyclic changes in strain, little is currently known about how cell migration responses vary with respect to these dynamic mechanical stimuli.

Structural disruptions of the cellular microenvironment have also been explored *in vitro* to dynamically manipulate cell morphology, differentiation, and migratory responses. Liu and colleagues demonstrated that pre-stretching poly(dimethysiloxane) (PDMS) locally altered substrate stiffness to induce MSC alignment along the pre-stretch direction. Furthermore, this pre-stretch induced early myofibroblast differentiation, which may have important implications in tissue repair and disease state studies [84]. Similarly, Guvendiren and colleagues used strain responsive PDMS substrates to preferentially control alignment of human MSCs [85]. Tibbit and colleagues showed that two-photon photodegredation of poly(ethylene glycol) hydrogels could be used to spatially control cell retraction processes. By locally perturbing micron scale patterning of surface features, Tibbit et. al demonstrated that MSCs retract ~6 fold slower on soft hydrogel surfaces compared to stiff synthetic platforms [86]. This is particularly important, as it highlights differences in polarization and motility of cells based solely on cell-ECM interactions within a local microenvironment. More recently, Khademolhosseini and colleagues used magnetically actuated micropillars to temporarily alter the topographical features of PDMS microchips. Using photolithography, multiple micropillar array designs were cast with embedded carbonyl iron magnetic particles. Human umbilical vein endothelial cells (HUVECs) were seeded onto the structures in a barrier set-up, which was removed prior to starting time-lapse imaging. When the chips were actuated at 1Hz or higher frequencies, a significant reduction of HUVEC migratory capacity (~5 fold) was observed compared to equivalent substrates with no magnetic micropillar structure [87]. These various examples highlight how spatial and mechanical manipulation of ECM environments significantly alter cell behavioral responses when compared to their static counterparts. In order to fully understand mechanisms driving fundamental *in vivo* processes, mechanical remodeling of the extracellular environment must be incorporated into *in vitro* synthetic designs.

1.4.3 Shape Memory Polymers Dynamically Reorganize Cell Morphology

Shape memory polymers (SMPs) are a class of smart materials capable of undergoing a programmed change in shape via thermal triggering [88]. Within the biomedical field, thermal shape memory functionality has been investigated for suture fixation [89], micro-actuators for stroke treatment [90], and stent applications [91]. In regards to mechanical stimulation for cell characterization, we [92-95] and others [96-99] have demonstrated that altering a cell's topographical or architectural surroundings influences cell morphology and nuclear orientation in two- and three-dimensions. While SMPs have already been employed to investigate cell morphology, nothing, to date, has been revealed with respect to how shape memory properties can be used to guide cell polarization and migratory responses in these dynamic microenvironments. The tunable nature of SMP platforms makes them highly attractive candidates for decoupling cell-ECM regulated dynamics from associated cell-cell or extracellular driven responses. Therefore, a poly(tert-butyl acrylate-co-butyl acrylate) SMP system will be investigated throughout a major portion of this dissertation to reveal novel cell polarization mechanisms and identify changes in migratory responses associated with local reorganization of *in vitro* ECM microenvironments.

1.5 Current Tools for Processing Large-scale Biological Datasets

Bioinformatics has emerged as an important field for understanding and processing complex biological data. Recently, the ability to accurately track cell motility behavior in time-lapse microscopy videos has been recognized as an important challenge in understanding essential biological phenomena, including cell developmental processes, tissue repair, and disease progression [100, 101]. Over the past few decades, advances in high-throughput instrumentation have revolutionized live-cell data capture, allowing even the smallest of research labs direct access to or the ability to generate terabytes of data for analysis [102]. This output is referred to as "big data": large biological data sets that need to be carefully analyzed to identify meaningful trends. With big data generation comes the challenge of creating new procedures to regulate, manage, and maintain big data storage and accessibility. As such, the field of biocuration has emerged as an important next step in standardizing big data publishing practices and helping to establish guidelines for curating accurate biological records [103]. With respect to *in vitro* cell cultures, "big data" can refer to a variety of formats ranging from live-cell time-lapse microscopy videos [104] to proteomics and genomics sequencing [105, 106].

A variety of challenges exist with respect to processing time-lapse microscopy cell data. One of the main limiting factors preventing automated analysis of cell motility is the absence of automated tools capable of accurately characterizing long-timescale cell behaviors [107]. Manual study remains the gold standard in the cell biology field [108]. Time and labor requirements associated with this manual analysis often limits studies to processing minimal cell numbers over small windows of time [e.g., 109, 110]. While semi- or fully-automated approaches exist, limitations dominate their applicability in studying long-term behavior. In particular, these fully automated systems vary significantly in their ability to accurately identify cells frame to frame, sort interaction points for dense cells, and precisely analyze natural cell proliferation events [111]. Furthermore, while one automated method may work effectively for an intended application [107], proper feature selection and processing methods are critical for accurate results. When comparing multiple automated techniques using the same datasets, wide variability in results is seen [100, 101], proving that accuracy of results is extremely sensitive to cell segmentation and linking criterion. Due to these limitations, a primary focus of this thesis was to develop novel automated image processing tools to accurately ($\geq$ 90%) measure long timescale ($\geq$ 24 hrs) cell data. These new tools will be used to advance understanding of long-term cell behaviors in traditional *in vitro* microenvironments.

1.6 Dissertation Scope

This dissertation utilizes a combination of a novel cell tracking approach from the field of computational biology, statistical methods from the fields of physics and bioinformatics, and a subset of smart material designs from the field of biomaterials to investigate how mechanical changes in a cell's microenvironment regulate cell polarization and cell motility responses. The fundamental goals of this thesis are to: 1) develop a modular image processing tool that can be applied to complex microenvironment platforms (e.g., smart material designs) and 2) to utilize that tool to advance knowledge of essential mechanobiology and mechanotransduction processes critical to development, tissue repair, and disease states. The chapter-by-chapter outline of how these goals are achieved is described below.

Chapter 1 highlights why cell-ECM interactions are essential in *in vivo* biological processes. It then summarizes the current body of literature related to *in vitro* static and dynamic platforms as well as the limitations associated with current image processing techniques that have prevented accurate analysis of long-term cell motility studies. **Chapter 2** presents a novel automated tool for cell tracking, termed automated contour-based tracking for *in vitro* environments (ACT*IV*E), and characterizes the accuracy associated with this tool when tracking cell motility behaviors in time-lapse microscopy data. **Chapter 3** then goes on to explore how ACT*IV*E can be used to tease out subtle differences in cell motility responses in static anisotropic and isotropic 2D microenvironments.

After establishing ACT*IV*E's use as an automated cell tracking platform, **Chapters 4 and 5** incorporate a dynamic change in surface topography as a means to control cell behavioral responses. More specifically, **Chapter 4** focuses on how this topographical transition influences cell motility dynamics over time, while **Chapter 5** emphasizes how the dynamic surface change impacts temporal cell polarization, which in turn dictates motility responses. In **Chapter 6**, ACT*IV*E application is then switched to a co-culture microenvironment. For this chapter, bovine aortic endothelial and bovine aortic smooth muscle cells are cultured together on glass surfaces to investigate whether clustering techniques can be applied to ACT*IV*E outputs to identify and characterize cell subpopulations in heterogeneous systems. Similarly, **Chapter 7** explores new applications for ACT*IV*E in anti-fouling applications, examining bacterial rotation and motility on PDMS surfaces. Finally, research achievements and proposed future work are conveyed in **Chapter 8** to summarize dissertation progress and list new avenues for further research.

1.7 References

1. Frantz, C., K.M. Stewart, and V.M. Weaver, *The extracellular matrix at a glance.* Journal of Cell Science, 2010. **123**(24): p. 4195-4200.
2. Rijal, G. and W. Li, *3D scaffolds in breast cancer research.* Biomaterials, 2016. **81**: p. 135-156.
3. Bosman, F.T.a.S.I., *Functional structure and composition of the extracellular matrix.* The Journal of Pathology, 2003. **200**(4): p. 423--428.
4. Buckwalter, J.A. and H.J. Mankin, *Articular cartilage. Part I: Tissue design and chondrocyte-matrix interactions.* Journal of Bone and Joint Surgery - Series A, 1997. **79**(4): p. 600-611.
5. Giancotti, F.G. and E. Ruoslahti, *Integrin signaling.* Science, 1999. **285**(5430): p. 1028-1032.
6. Guan, J.-L., *Role of focal adhesion kinase in integrin signaling.* The International Journal of Biochemistry & Cell Biology, 1997. **29**(8): p. 1085-1096.
7. Mitra, S.K., D.A. Hanson, and D.D. Schlaepfer, *Focal adhesion kinase: In command and control of cell motility.* Nature Reviews Molecular Cell Biology, 2005. **6**(1): p. 56-68.
8. Zhao, X. and J.-L. Guan, *Focal adhesion kinase and its signaling pathways in cell migration and angiogenesis.* Advanced Drug Delivery Reviews, 2011. **63**(8): p. 610-615.
9. Di Cio, S. and J.E. Gautrot, *Cell sensing of physical properties at the nanoscale: Mechanisms and control of cell adhesion and phenotype.* Acta Biomaterialia, 2016. **30**: p. 26-48.
10. Nagano, M., et al., *Turnover of focal adhesions and cancer cell migration.* International Journal of Cell Biology, 2012.

11. Pasapera, A.M., et al., *Rac1-dependent phosphorylation and focal adhesion recruitment of myosin IIA regulates migration and mechanosensing.* Current biology : CB, 2015. **25**(2): p. 175-186.

12. Ridley, A.J., et al., *Cell Migration: Integrating Signals from Front to Back.* Science, 2003. **302**(5651): p. 1704-1709.

13. Etienne-Manneville, S. and A. Hall, *Rho GTPases in cell biology.* 2002. **420**(6916): p. 629-635.

14. Rodriguez, O.C., et al., *Conserved microtubule-actin interactions in cell movement and morphogenesis.* 2003. **5**(7): p. 599-609.

15. Friedl, P., K. Wolf, and J. Lammerding, *Nuclear mechanics during cell migration.* Current Opinion in Cell Biology, 2011. **23**(1): p. 55-64.

16. Serrador, J.M., M. Nieto, and F. Sánchez-Madrid, *Cytoskeletal rearrangement during migration and activation of T lymphocytes.* Trends in Cell Biology, 1999. **9**(6): p. 228-233.

17. Adams, J.C. and F.M. Watt, *Regulation of development and differentiation by the extracellular matrix.* Development, 1993. **117**(4): p. 1183-1198.

18. Yang, J. and R.A. Weinberg, *Epithelial-Mesenchymal Transition: At the Crossroads of Development and Tumor Metastasis.* Developmental Cell, 2008. **14**(6): p. 818-829.

19. Rozario, T. and D.W. DeSimone, *The extracellular matrix in development and morphogenesis: A dynamic view.* Developmental Biology, 2010. **341**(1): p. 126-140.

20. Kalluri, R. and R.A. Weinberg, *The basics of epithelial-mesenchymal transition.* Journal of Clinical Investigation, 2009. **119**(6): p. 1420-1428.

21. Pulina, M.V., et al., *Essential roles of fibronectin in the development of the left-right embryonic body plan.* Developmental Biology, 2011. **354**(2): p. 208-220.
22. Wiseman, B.S. and Z. Werb, *Development: Stromal effects on mammary gland development and breast cancer.* Science, 2002. **296**(5570): p. 1046-1049.
23. Lubkin, S.R. and P.K.M.S.A.N.a.T.J.N. Santiago Schnell, *Branched Organs: Mechanics of Morphogenesis by Multiple Mechanisms*, in *Current Topics in Developmental Biology*. 2008, Academic Press. p. 249-268.
24. Nelson, C.M., et al., *Tissue geometry determines sites of mammary branching morphogenesis in organotypic cultures.* Science, 2006. **314**(5797): p. 298-300.
25. Kleinman, H.K., D. Philp, and M.P. Hoffman, *Role of the extracellular matrix in morphogenesis.* Current Opinion in Biotechnology, 2003. **14**(5): p. 526-532.
26. Olczyk, P., Ł. Mencner, and K. Komosinska-Vassev, *The role of the extracellular matrix components in cutaneous wound healing.* BioMed research international, 2014. **2014**.
27. Friedl, P. and D. Gilmour, *Collective cell migration in morphogenesis, regeneration and cancer.* Nature Reviews Molecular Cell Biology, 2009. **10**(7): p. 445-457.
28. Gerhardt, H., *VEGF and endothelial guidance in angiogenic sprouting.* Organogenesis, 2008. **4**(4): p. 241-246.
29. Hinz, B., et al., *The Myofibroblast: One Function, Multiple Origins.* The American Journal of Pathology, 2007. **170**(6): p. 1807-1816.
30. Schuppan, D., et al., *Matrix as a modulator of hepatic fibrogenesis.* Seminars in Liver Disease, 2001. **21**(3): p. 351-372.

31. Kawai, S., et al., *Vinculin: a novel marker for quiescent and activated hepatic stellate cells in human and rat livers.* (0945-6317 (Print)).
32. Snyman, C. and C.U. Niesler, *MMP-14 in skeletal muscle repair.* Journal of Muscle Research and Cell Motility, 2015. **36**(3): p. 215-225.
33. Cox, T.R. and J.T. Erler, *Remodeling and homeostasis of the extracellular matrix: Implications for fibrotic diseases and cancer.* DMM Disease Models and Mechanisms, 2011. **4**(2): p. 165-178.
34. Jaalouk, D.E. and J. Lammerding, *Mechanotransduction gone awry.* Nature Reviews Molecular Cell Biology, 2009. **10**(1): p. 63-73.
35. Paszek, M.J. and V.M. Weaver, *The tension mounts: Mechanics meets morphogenesis and malignancy.* Journal of Mammary Gland Biology and Neoplasia, 2004. **9**(4): p. 325-342.
36. Levental, K.R., et al., *Matrix Crosslinking Forces Tumor Progression by Enhancing Integrin Signaling.* Cell, 2009. **139**(5): p. 891-906.
37. Erler, J.T., et al., *Lysyl oxidase is essential for hypoxia-induced metastasis.* Nature, 2006. **440**(7088): p. 1222-1226.
38. Yu, H.M., J.K. Mouw, and V.M. Weaver, *Forcing form and function: biomechanical regulation of tumor evolution.* Trends in Cell Biology, 2011. **21**(1): p. 47-56.
39. Lu, P., V.M. Weaver, and Z. Werb, *The extracellular matrix: A dynamic niche in cancer progression.* Journal of Cell Biology, 2012. **196**(4): p. 395-406.
40. Gaggioli, C., et al., *Fibroblast-led collective invasion of carcinoma cells with differing roles for RhoGTPases in leading and following cells.* Nature Cell Biology, 2007. **9**(12): p. 1392-U92.

41. Amatangelo, M.D., et al., *Stroma-derived three-dimensional matrices are necessary and sufficient to promote desmoplastic differentiation of normal fibroblasts.* American Journal of Pathology, 2005. **167**(2): p. 475-488.

42. Stetler-Stevenson, W.G., S. Aznavoorian, and L.A. Liotta, *Tumor cell interactions with the extracellular matrix during invasion and metastasis.* Annual Review of Cell Biology, 1993. **9**: p. 541-573.

43. Liotta, L.A. and E.C. Kohn, *The microenvironment of the tumour - Host interface.* Nature, 2001. **411**(6835): p. 375-379.

44. Friedl, P. and S. Alexander, *Cancer invasion and the microenvironment: Plasticity and reciprocity.* Cell, 2011. **147**(5): p. 992-1009.

45. Barney, L.E., et al., *The predictive link between matrix and metastasis.* Current Opinion in Chemical Engineering, 2016. **11**: p. 85-93.

46. Holle, A.W., J.L. Young, and J.P. Spatz, *In vitro cancer cell-ECM interactions inform in vivo cancer treatment.* Advanced Drug Delivery Reviews, 2016. **97**: p. 270-279.

47. Poli, G., *Pathogenesis of liver fibrosis: role of oxidative stress.* Molecular Aspects of Medicine, 2000. **21**(3): p. 49-98.

48. Lijnen, P.J., V.V. Petrov, and R.H. Fagard, *Induction of cardiac fibrosis by transforming growth factor-β1.* Molecular Genetics and Metabolism, 2000. **71**(1-2): p. 418-435.

49. Wipff, P.J., et al., *Myofibroblast contraction activates latent TGF-β1 from the extracellular matrix.* Journal of Cell Biology, 2007. **179**(6): p. 1311-1323.

50. Gumbiner, B.M., *Cell adhesion: The molecular basis of tissue architecture and morphogenesis.* Cell, 1996. **84**(3): p. 345-357.

51. Thiery, J.P., et al., *Epithelial-Mesenchymal Transitions in Development and Disease.* Cell, 2009. **139**(5): p. 871-890.
52. Stevens, M.M. and J.H. George, *Exploring and Engineering the Cell Surface Interface.* Science, 2005. **310**(5751): p. 1135-1138.
53. Alvarez-Barreto, J.F. and V.I. Sikavitsas, *Improved mesenchymal stem cell seeding on RGD-modified poly(L-lactic acid) scaffolds using flow perfusion.* Macromolecular Bioscience, 2007. **7**(5): p. 579-588.
54. Shin, Y.M., et al., *Synergistic effect of dual-functionalized fibrous scaffold with BCP and RGD containing peptide for improved osteogenic differentiation.* Macromolecular Bioscience, 2014. **14**(8): p. 1190-1198.
55. Lutolf, M.P. and J.A. Hubbell, *Synthetic biomaterials as instructive extracellular microenvironments for morphogenesis in tissue engineering.* Nature Biotechnology, 2005. **23**(1): p. 47-55.
56. Magnani, A., et al., *Cell behaviour on chemically microstructured surfaces.* Materials Science and Engineering C, 2003. **23**(3): p. 315-328.
57. Chua, I.L.S., H.W. Kim, and J.H. Lee, *Signaling of extracellular matrices for tissue regeneration and therapeutics.* Tissue Engineering and Regenerative Medicine, 2016. **13**(1): p. 1-12.
58. Engler, A.J., et al., *Matrix elasticity directs stem cell lineage specification.* Cell, 2006. **126**(4): p. 677-689.
59. Discher, D.E., P. Janmey, and Y.L. Wang, *Tissue cells feel and respond to the stiffness of their substrate.* Science, 2005. **310**(5751): p. 1139-1143.

60. Haeger, A., et al., *Collective cell migration: Guidance principles and hierarchies.* Trends in Cell Biology, 2015. **25**(9): p. 556-566.
61. Wong, S., W.H. Guo, and Y.L. Wang, *Fibroblasts probe substrate rigidity with filopodia extensions before occupying an area.* Proceedings of the National Academy of Sciences of the United States of America, 2014. **111**(48): p. 17176-17181.
62. Gray, D.S., J. Tien, and C.S. Chen, *Repositioning of cells by mechanotaxis on surfaces with micropatterned Young's modulus.* Journal of Biomedical Materials Research Part A, 2003. **66A**(3): p. 605-614.
63. Saez, A., et al., *Rigidity-driven growth and migration of epithelial cells on microstructured anisotropic substrates.* (0027-8424 (Print)).
64. Allena, R., M. Scianna, and L. Preziosi, *A Cellular Potts Model of single cell migration in presence of durotaxis.* Mathematical Biosciences, 2016. **275**: p. 57-70.
65. Teixeira, A.I., P.F. Nealey, and C.J. Murphy, *Responses of human keratocytes to micro- and nanostructured substrates.* Journal of Biomedical Materials Research - Part A, 2004. **71**(3): p. 369-376.
66. Han, L., et al., *Unidirectional migration of single smooth muscle cells under the synergetic effects of gradient swelling cue and parallel groove patterns.* Colloids and Surfaces B: Biointerfaces, 2013. **111**: p. 1-6.
67. Kim, D.H., et al., *Mechanosensitivity of fibroblast cell shape and movement to anisotropic substratum topography gradients.* Biomaterials, 2009. **30**(29): p. 5433-5444.
68. Kandere-Grzybowska, K., et al., *Short-term molecular polarization of cells on symmetric and asymmetric micropatterns.* Soft Matter, 2010. **6**(14): p. 3257-3268.

69. Kim, D.H., et al., *Guided Cell Migration on Microtextured Substrates with Variable Local Density and Anisotropy.* Adv Funct Mater, 2009. **19**(10): p. 1579-1586.

70. Song, J.-M., et al., *DNA Vaccination in the Skin Using Microneedles Improves Protection Against Influenza.* Molecular Therapy, 2012. **20**(7): p. 1472-1480.

71. Peela, N., et al., *A three dimensional micropatterned tumor model for breast cancer cell migration studies.* Biomaterials, 2016. **81**: p. 72-83.

72. Gomes, S., et al., *Natural and genetically engineered proteins for tissue engineering.* Progress in Polymer Science (Oxford), 2012. **37**(1): p. 1-17.

73. Pabbruwe, M.B., et al., *Repair of meniscal cartilage white zone tears using a stem cell/collagen-scaffold implant.* Biomaterials, 2010. **31**(9): p. 2583-2591.

74. Amiel, G.E., et al., *Engineering of blood vessels from acellular collagen matrices coated with human endothelial cells.* Tissue Engineering, 2006. **12**(8): p. 2355-2365.

75. Cummings, C.L., et al., *Properties of engineered vascular constructs made from collagen, fibrin, and collagen-fibrin mixtures.* Biomaterials, 2004. **25**(17): p. 3699-3706.

76. Helary, C., et al., *Concentrated collagen hydrogels as dermal substitutes.* Biomaterials, 2010. **31**(3): p. 481-490.

77. Starke, J., et al., *Mechanotransduction of mesenchymal melanoma cell invasion into 3D collagen lattices: Filopod-mediated extension–relaxation cycles and force anisotropy.* Experimental Cell Research, 2013. **319**(16): p. 2424-2433.

78. Mogoşanu, G.D. and A.M. Grumezescu, *Natural and synthetic polymers for wounds and burns dressing.* International Journal of Pharmaceutics, 2014. **463**(2): p. 127-136.

79. Park, S.U., et al., *The possibility of microbial cellulose for dressing and scaffold materials.* International Wound Journal, 2014. **11**(1): p. 35-43.

80. Madhumathi, K., et al., *Development of novel chitin/nanosilver composite scaffolds for wound dressing applications.* Journal of Materials Science: Materials in Medicine, 2010. **21**(2): p. 807-813.

81. Tamiello, C., et al., *Heading in the Right Direction: Understanding Cellular Orientation Responses to Complex Biophysical Environments.* Cellular and Molecular Bioengineering, 2016. **9**(1): p. 12-37.

82. Wang, J.H.C., et al., *Specificity of endothelial cell reorientation in response to cyclic mechanical stretching.* Journal of Biomechanics, 2001. **34**(12): p. 1563-1572.

83. McGarry, J.P., B.P. Murphy, and P.E. McHugh, *Computational mechanics modelling of cell-substrate contact during cyclic substrate deformation.* Journal of the Mechanics and Physics of Solids, 2005. **53**(12): p. 2597-2637.

84. Liu, C., et al., *Effect of Static Pre-stretch Induced Surface Anisotropy on Orientation of Mesenchymal Stem Cells.* Cellular and molecular bioengineering, 2014. **7**(1): p. 106-121.

85. Guvendiren, M. and J.A. Burdick, *Stem Cell Response to Spatially and Temporally Displayed and Reversible Surface Topography.* Advanced Healthcare Materials, 2013. **2**(1): p. 155-164.

86. Tibbitt, M.W., et al., *Controlled two-photon photodegradation of PEG hydrogels to study and manipulate subcellular interactions on soft materials.* Soft Matter, 2010. **6**(20): p. 5100-5108.

87. Khademolhosseini, F., et al., *Magnetically actuated microstructured surfaces can actively modify cell migration behaviour.* Biomedical Microdevices, 2016. **18**(1): p. 1-11.

88. Liu, C., H. Qin, and P.T. Mather, *Review of progress in shape-memory polymers.* Journal of Materials Chemistry, 2007. **17**(16): p. 1543-1558.
89. Lendlein, A. and R. Langer, *Biodegradable, elastic shape-memory polymers for potential biomedical applications.* Science, 2002. **296**(5573): p. 1673-1676.
90. Maitland, D.J., et al., *Photothermal properties of shape memory polymer micro-actuators for treating stroke.* Lasers in Surgery and Medicine, 2002. **30**(1): p. 1-11.
91. Gall, K., et al., *Thermomechanics of the shape memory effect in polymers for biomedical applications.* Journal of Biomedical Materials Research Part A, 2005. **73A**(3): p. 339-348.
92. Davis, K.A., et al., *Dynamic cell behavior on shape memory polymer substrates.* Biomaterials, 2011. **32**(9): p. 2285-2293.
93. Davis, K., et al., *Shape Memory Polymers for Active Cell Culture*. 2011: Journal of Visualized Experiments.
94. Yang, P., et al., *In vitro wrinkle formation via shape memory dynamically aligns adherent cells.* Soft Matter, 2013. **9**(18): p. 4705-4714.
95. Tseng, L.F., P.T. Mather, and J.H. Henderson, *Shape-memory-actuated change in scaffold fiber alignment directs stem cell morphology.* Acta Biomaterialia, 2013. **9**(11): p. 8790-8801.
96. Le, D.M., et al., *Dynamic Topographical Control of Mesenchymal Stem Cells by Culture on Responsive Poly(epsilon-caprolactone) Surfaces.* Advanced Materials, 2011. **23**(29): p. 3278-+.
97. Ebara, M., et al., *Focus on the interlude between topographic transition and cell response on shape-memory surfaces.* Polymer (United Kingdom), 2014. **55**(23): p. 5961-5968.

98. Ebara, M., et al., *The taming of the cell: Shape-memory nanopatterns direct cell orientation.* International Journal of Nanomedicine, 2014. **9**(SUPPL.1): p. 117-126.
99. Zhang, D., et al., *A bioactive "self-fitting" shape memory polymer scaffold with potential to treat cranio-maxillo facial bone defects.* Acta Biomaterialia, 2014. **10**(11): p. 4597-4605.
100. Maska, M., et al., *A benchmark for comparison of cell tracking algorithms.* Bioinformatics, 2014. **30**(11): p. 1609-1617.
101. Chenouard, N., et al., *Objective comparison of particle tracking methods.* Nature Methods, 2014. **11**(3): p. 281-U247.
102. Marx, V., *The big challenges of big data.* Nature, 2013. **498**(7453): p. 255-260.
103. Howe, D., et al., *Big data: The future of biocuration.* Nature, 2008. **455**(7209): p. 47-50.
104. Masuzzo, P., et al., *An open data ecosystem for cell migration research.* Trends in Cell Biology, 2015. **25**(2): p. 55-58.
105. Schadt, E.E., et al., *Computational solutions to large-scale data management and analysis.* Nature Reviews Genetics, 2010. **11**(9): p. 647-657.
106. Friedberg, I., *Automated protein function prediction - The genomic challenge.* Briefings in Bioinformatics, 2006. **7**(3): p. 225-242.
107. Meijering, E., et al., *Tracking in cell and developmental biology.* Seminars in Cell & Developmental Biology, 2009. **20**(8): p. 894-902.
108. Huth, J., et al., *Significantly improved precision of cell migration analysis in time-lapse video microscopy through use of a fully automated tracking system.* Bmc Cell Biology, 2010. **11**: p. 12.

109. Strachan, L.R. and M.L. Condic, *Neural crest motility and integrin regulation are distinct in cranial and trunk populations.* Developmental Biology, 2003. **259**(2): p. 288-302.

110. Eilken, H.M., S.I. Nishikawa, and T. Schroeder, *Continuous single-cell imaging of blood generation from haemogenic endothelium.* Nature, 2009. **457**(7231): p. 896-900.

111. Meijering, E., O. Dzyubachyk, and I. Smal, *METHODS FOR CELL AND PARTICLE TRACKING*, in *Imaging and Spectroscopic Analysis of Living Cells: Optical and Spectroscopic Techniques*, P.M. Conn, Editor. 2012, Elsevier Academic Press Inc: San Diego. p. 183-200.

Chapter 2: Automated Contour-Based Tracking for *In-Vitro* Environments (ACT*IV*E) Development and Accuracy Assessment†,*

2.1 Synopsis

Understanding the dynamics of single and collective cell motility is important for tissue development, wound repair, and disease progression. *In vitro,* synthetic systems of increasing complexity have emerged as model platforms for investigating these critical research areas. Unfortunately, current analysis techniques do not efficiently or accurately capture cell motility phenomenon observed *in vitro*, particularly in systems involving long timescales or high cell densities. The goal of this chapter was to develop an automated cell tracking system capable of measuring motility behaviors of populations of adherent cells subject to nuclear staining, infection, or transfection. Focus was placed on improving key limitations of current automated systems (e.g. tracking cells with low signal to noise or accurately tracking cells at high densities) with emphasis on achieving greater than 90% accuracy of long timescale (at least 24 hours) cell data. This algorithm, termed Automated Contour-Based Tracking for *In-Vitro* Environments (ACT*IV*E), was

---

[†] Adapted (in part) with permission from R.M. Baker, M.E. Brasch, M.L. Manning, and J.H. Henderson, *Journal of The Royal Society Interface*, **2014**, 11, 20140386. **Copyright © The Royal Society 2014**

[*] ACT*IV*E code was developed, validated, and benchmarked by Megan Brasch. Material preparation, cell culture, and time-lapse video experiments were designed and executed by Dr. Richard Baker. Video analysis was completed in collaboration by Megan Brasch and Dr. Richard Baker. For more information, see: Baker, RM, "Shape Memory Polymers as 2D Substrates and 3D Scaffolds for the Study of Cell Mechanobiology and Tissue Engineering" (2015).

designed to identify and sort complex cell behaviors (e.g., division or merging events) and has been benchmarked against accepted gold standard techniques.

2.2 Introduction: Automated Tools for Cell Motility Analysis

Synthetic biomaterials are actively being employed as *in vitro* models to characterize cell behaviors critical to understanding biological functions and to treating disease states. These platforms are particularly attractive, as researchers can alter material biochemical or biophysical properties via changes in substrate stiffness [1-3], patterned surface chemistries [4, 5], or ordered topographies [6-10]. Recent advances in materials science have revolutionized the capabilities of these programmable synthetic approaches, leading to the ability to dynamically tailor material properties through external stimuli (e.g. temperature [11-13] or light [14-16]). These increasingly complex model platforms are now broadly being employed for cancer cell biology [17, 18], cell mechanobiology [19, 20], and developmental biology applications [21, 22].

Independently from materials development, bioinformatics has emerged as an increasingly important field to understand and process multifaceted data. The combination of increased complexity in synthetic systems, coupled with improved computing power, has led to the generation of “big data”: large biological data sets that need to be carefully analyzed to identify meaningful trends. With respect to *in vitro* cell cultures, “big data” can refer to data sets ranging from live-cell time-lapse microscopy videos to proteomics and genomics sequencing [23-25]. In order to process this temporally and spatially complex biological information accurately and efficiently, new automated image processing techniques are being developed. Recently, the ability to accurately track cell motility data in time-lapse microscopy videos has been recognized as an important challenge [26, 27] in understanding cell developmental processes [28, 29], tissue repair [30, 31], and disease progression [32-34].

Manual tracking, in which a trained user individually traces a single cell's body or nucleus centroid frame-by-frame in a time-lapse video (e.g., [35, 36]), remains the gold standard in the cell-tracking field, despite the labor-intensive nature and potential for human error. While some semi- or fully-automated approaches exist, their specificity for an intended goal limits broad applicability [26, 27], particularly to long timescale analyses on the order of day(s). Popular automated approaches include pixel thresholding [37, 38] to isolate cells and active contours [39, 40] to trace cell boundaries . While both methods have their respective strengths, they are limited to processing high contrast or high signal to noise ratio (SNR) images. Material (e.g. autofluorescence) and imaging restrictions (e.g. photobleaching) often limit contrast and resolution, making high contrast and high SNR images over long timescales difficult to acquire reliably. Additionally, inaccuracies associated with tracking complex cell behaviors, such as cell-cell interactions or cell proliferation, are accentuated over long timescales. In order to ensure accurate analysis of cell behavior in diverse experimental microenvironments, we sought to develop a new automated tracking system, termed automated contour-based tracking for *in vitro* environments (ACT*IV*E), specifically tailored to address these common limitations and to further understanding of long-term cell behavior in traditional and emerging *in vitro* platforms. Notably, successful development of the ACT*IV*E system enabled the research presented in the remainder of this thesis.

2.3 Development and Methodology of the ACT*IV*E Tracking Algorithm

2.3.1 ACTIVE Platform

ACT*IV*E was implemented using MATLAB® (MathWorks) version 2011a and requires a valid commercial license to utilize for research purposes. In addition to the standard built-in functions provided by MATLAB, ACT*IV*E requires access to the Image Processing Toolbox (MathWorks, http://www.mathworks.com/products/image/). A user manual detailing ACT*IV*E operation is available in Appendix 1. Briefly, the algorithm is equipped to analyze 8-bit or 16-bit grayscale Tiff formatted image stacks. The program can be initialized by running the main wrapper function, `run_tracking_contour2`:

```
[ xyzs_id, xyzs_id_columns, filename, framerate, new_dir] =
run_tracking_contour2(image_mat_in, inputfilename)
```

The wrapper function takes one required input, “image_mat_in”, and one optional input, “inputfilename”, which is used to determine the mode of operation. “image_mat_in” is a matrix specifying the pixel intensity range that ACT*IV*E should readjust pixel scaling to. This matrix is input into the built-in MATLAB function, `imadjust`, to rescale pixel values outside of the minimum and maximum range specified by the user. A matrix input of `image_mat_in = [0;1]` will result in no change in image scaling. “inputfilename” is the file directory location for a text file containing all of the parameters required to initiate ACT*IV*E analysis (Appendix 1.2). Operation of ACT*IV*E using the optional input will initiate batch processing mode. In batch processing mode, which is designed for server execution, no image output will be displayed. If no input file is provided to the algorithm, ACT*IV*E will instead execute in graphical user interface (GUI) mode. The GUI mode will prompt the user to specify all of the same parameters that would otherwise have been found in the optional input file. A short description and numerical values for operating parameters used in **Chapters 2 and 3** can be found in Table 2-1. Additionally, a schematic depicting the overall ACT*IV*E automated tracking process is provided in Scheme 2-1.

2.3.2 Cell Segmentation

ACT*IV*E was designed to analyze adherent cell populations subject to nuclear staining, infection, or transfection. All of the cell images utilized in this chapter were visualized using Hoechst 33342 nuclear stain. Cell segmentation was achieved through a contour profiling technique, originally developed by Idema and colleagues [41]. A Gaussian band-pass filter was first applied to remove noise in the nuclear signal and to smooth pixel intensities [42]. Contour profiling was then completed using a built-in MATLAB function, `contour`. Center of mass values were calculated for each resultant contour and cell profiles were established based on relationships between center of mass and contour level information (Figure 2-1). Each cell was then processed according to its profile at or above a user-defined fit height, where the standard was defined as half height. In the case of isolated cells, each profile was fit according to the Fitzgibbon method [43]. The remaining multi-peak instances were flagged as cell interactions and categorized as division or merging events based on a custom post-processing algorithm.

2.3.3 Particle Tracking

Following contour-based segmentation, ACT*IV*E utilizes an adaptation of the previously established Kilfoil linking protocol to relate cell information between consecutive frames [42]. In the adapted approach, the total number of segmented cells is first identified in each frame. Each image pair is then systematically compared using positional analysis, separating cell-cell identification matches into trivial or non-trivial classifications. Trivial cases exist when only one potential match is found frame-to-frame within a specified maximum radius of potential distance traveled. Non-trivial cases result from multiple potential matches and are sorted by minimizing the overall distance between center of mass values. After sorting, each particle is then assigned an identification tag (ID), which is subsequently used by ACT*IV*E to sort inaccuracies associated with cell-cell interactions. Of additional note, the linking process incorporates a "memory" parameter, indicating a maximum frame interval during which a cell's signal may occlude or completely disappear before a new ID tag would be assigned. This "memory" parameter was set to a value of 10 frames in the current work.

2.3.4 Identifying and Performing Merging Correction for Interacting Cells

When cells come in close contact with one another, nuclear signal from interacting cells can overlap (Figure 2-2). This signal overlap often results in inaccurate capture and tagging of cells frame-to-frame when utilizing the positional method described in section 2.3.3. To correct for these potential inaccuracies in the ACT*IV*E system, interaction events were first identified and classified as merging or division events based on their track history. Specifically, when a multi-peak profile was identified, prior track history was used to classify whether a division event (see section 2.3.5) or merging event had occurred. For a merging event to occur, both cells must have prior track history. The user must specify a maximum interaction interval (which is separate from the previously described memory parameter), defined as the total number of frames that one cell can completely occlude another cell while still being considered as part of the same merging event. As specified in Table 2-1, this value was set to 10 frames for all of the work performed in **Chapters 2 and 3**. ACT*IV*E traces the history profile between interaction pairings of the same two cells to build a merging profile for a single cell-cell event. This profile is then analyzed using a custom-built cost function. It is important to note that ACT*IV*E's post-processing system currently only addresses two-body cases. Additional work has separately been performed to improve accuracy associated with complex merging events, involving three or more cells interacting at one time [44].

ACT*IV*E's two-body cost function approach incorporates either a multi-frame positional or two-frame fingerprint analysis, depending on the characteristics of the merging event profile. A positional cost function is utilized when both cells have ID information present in consecutive or nearly consecutive frame pairs. The general equation for the positional cost function is defined as:

$$cost = \sqrt{(x_1 - x_2)^2 + (y_1 - y_2)^2} \qquad \text{(Eq. 2-1)}$$

where (x_1, y_1) and (x_2, y_2) represent the center of mass values for a cell in frames one and two, respectively. All possible combinations of the two cells IDs are tested and the minimum cost value is selected as the appropriate ID information for that case.

In merging profiles where cells occlude for multiple consecutive frames, positional cost function analysis results in decreased accuracy due to the gap in cell trajectory information. If a single cell occludes for more than a predetermined number of consecutive frames, specified as greater than three frames in the work from **Chapters 2 and 3**, an alternative fingerprint cost function is employed. This function utilizes nuclear signal and morphometric characteristics, including area, average intensity, integrated intensity, and cell aspect ratio, to identify a cell's "fingerprint" and assign appropriate ID information. The general equation for the fingerprint analysis is defined as:

$$Fingerprint = w_{II} * \left(\frac{II_i}{\overline{II}_i} - \frac{II_{i+1}}{\overline{II}_{i+1}}\right)^2 + w_{NI} * \left(\frac{NI_i}{\overline{NI}_i} - \frac{NI_{i+1}}{\overline{NI}_{i+1}}\right)^2 + w_A * \left(\frac{A_i}{\bar{A}_i} - \frac{A_{i+1}}{\bar{A}_{i+1}}\right)^2 + w_{AR} * \left(\frac{AR_i}{\overline{AR}_i} - \frac{AR_{i+1}}{\overline{AR}_{i+1}}\right)^2 + w_p * \left(\frac{\left[\sqrt{(x_i - x_{i+1})^2 + (y_i - y_{i+1})^2}\right]}{\frac{\bar{d}_i + \bar{d}_{i+1}}{2}}\right)^2 \quad \text{(Eq. 2-2)}$$

where *II* represents the integrated intensity for a cell nucleus, *NI* is the normalized intensity for a cell nucleus, *A* is the area of a cell nucleus, *AR* is the aspect ratio of a cell nucleus, *d* is the diameter of a cell nucleus, *w* represents a weighting factor for the aforementioned subscripted variables (with the addition of *P,* which represents the position as it relates to the positional cost function described in Eq. 2-1), and "i" and "i+1" subscripts denote frame numbers. For our analysis, w_{II}, w_{NI}, w_A, and w_{AR} were all set to a value of one, while w_P was set to a value of zero. Similar to the positional analysis, all possible cell ID combinations were tested in the fingerprint method and the resulting cell-cell pair with the lowest cost function value was selected as the correct ID set. In cases where the identified ID combination from either the positional or fingerprint methods was identical to the original ID classification, no additional steps were taken. However, for incorrect pairings, the corresponding cell ID information was entered into an ID map for subsequent processing. Once all of the tagged merging events were assessed, the cell IDs were reversibly updated by frame to ensure labeling consistency and appropriate overall final ID assignment.

2.3.5 Classifying and Improving Accuracy Associated with Cell Divisions

As discussed in section 2.3.4, division events were segmented by ACT*IV*E when nuclear signal overlap resulted in a single contour set containing multiple peak contours (Figure 2-2). These events were differentiated from merging events based on their track history: in the case of division events, no prior cell track information existed for one of the two cells identified in the multi-peak instance. Cell division information was also assessed, as erroneous flagging of division events often occurred due to cell-cell interactions at the beginning of the image stack (where track history had not been developed yet) or as a result of cell proximity to image boundary locations. To accommodate issues associated with cell-cell interactions occurring in the first few frames of imaging, an image frame preset was incorporated to reclassify division events occurring early in the image series. All division events occurring prior to the frame preset were removed from further division analysis. This was particularly important at high densities, as the number of cell-cell interactions at the onset of imaging would result in significant false division identification. This image frame preset value was set to 10 frames, equivalent to the memory parameter and the maximum interaction interval originally specified in sections 2.3.3 and 2.3.4, respectively. A border region was additionally incorporated to accommodate erroneous classification associated with boundary locations. When divisions were flagged within the border region, set to 30 pixels in the present work, cell-cell interaction IDs would not be processed. For events classified as divisions, an area constraint was further applied to differentiate false positives resulting from misclassified merging events. Division events in mammalian cell cultures are typically symmetric [45]. Therefore, the nuclear area of the two daughter cells should be similar within a tolerance interval. This tolerance difference was set to 70% in the current work; cells falling outside of the tolerance interval were reclassified as merging events. Once division event information was appropriately identified, parent information was duplicated so that both daughter cells contained complete trajectory information from their mother cell.

2.4 Results and Discussion: ACT*IV*E Accuracy Assessment

To measure the validity of the ACT*IV*E approach, multiple benchmark comparisons were made. First, ACT*IV*E was compared to the gold standard, manual tracking, to assess benefits associated with automating motility analyses. ACT*IV*E was then benchmarked against a widely used automated tracking algorithm [42] and assessed for accuracy in three ways: 1) cell segmentation, 2) merging event ID classification, and 3) division event identification. The methodology and results for the ACT*IV*E approach are discussed below.

2.4.1 Manual Tracking and Execution Time

Manual tracking remains the gold standard in the cell tracking field, despite how labor intensive the technique is and the potential for human error that manual tracking permits [46]. To measure the productivity associated with switching to a completely automated system, we performed an execution time comparison between manual tracking and two automated approaches (ACT*IV*E and the Kilfoil approach [42]). Image stacks were generated from two substrate environments: 1) an anisotropic polymer surface coated in gold, and 2) a flat tissue-culture treated polystyrene surface. Cells were seeded at a density of 10,000 cells/cm^2 and imaged every three minutes. Each image stack consisted of 50 consecutive frames with a pixel area of 300x300 (approximately 380μm x 380μm). Manual tracking was performed by the same trained user utilizing the semi-automated MTrackJ function in ImageJ (Figure 2-3). As shown in Table 2-2, ACT*IV*E was greater than 150 times faster than the manual approach. With respect to the number of cells identified, ACT*IV*E erred on the side of reduced segmentation, assuming that the number of cells identified in the manual approach was correct. Comparatively, the Kilfoil approach was greater than 500 times faster than the manual approach and demonstrated the same deviation in cell number (compared to ACT*IV*E) from the manual traces.

2.4.2 Characterizing Cell Segmentation Accuracy

To assess ACT*IV*E's segmentation accuracy, synthetic data simulating anticipated cell studies was generated using an active matter simulation with periodic boundary conditions [47]. Two data sets were generated at two different nuclear area densities, 11.1% and 17.1% (Figure 2-4). While the general motion of the active matter simulation mimicked cell motility behavior, no cell division or cell-cell occlusion criteria were incorporated. Particles were simulated for 4000 natural simulation time units using equations for overdamped dynamics reported by Henkes and colleagues [47]. In expansion of Henkes and colleagues' previous work, a drag coefficient was incorporated in the y-direction to simulate anticipated anisotropy in the proposed cell experiments. The y drag coefficient was set to four times the x drag coefficient. Additional model parameters included: a spring constant (K) of 1, a drag coefficient (b) in the x-direction of magnitude 1, a self-propelled velocity (v0) of magnitude 0.1, and a rotational noise (η) of magnitude 0.1, in simulation units. Synthetic images were generated on a black background by randomly placing oriented white ellipses (eccentricity equal to two) at active particle positions. Detailed x and y positional and time data were recorded for each set to validate the automated approaches. Due to the inability to incorporate occlusion and division events into the synthetic data, separate analyses were performed to assess merging and division event accuracy (see sections 2.4.3 and 2.4.4 respectively).

ACT*IV*E segmentation was benchmarked against the Kilfoil tracking system [42]. In both automated approaches, synthetic cells were segmented in the first frame and labeled with an identification (ID) tag. For each of the remaining 479 frames, this cell ID map was used to determine if the cell IDs assigned by the automated approaches accurately depicted the synthetic track data. Track accuracy was calculated as the percentage of cells assigned to the correct cell ID. This frame-by-frame accuracy was recorded and plotted over time to compare the two automated approaches (Figure 2-5). Track inaccuracies generally resulted from the inability to segment cells in a frame or inappropriate assignment of cell IDs frame to frame. Due to variations in signal produced by the band-pass filter, accuracy values fluctuated frame to frame. ACT*IV*E was capable of achieving a segmentation accuracy of 97.5% and 95.7% at low and high synthetic densities respectively, when measured through the entire 480 frame image stack. By comparison, the Kilfoil approach yielded 96.8% and 92.9% accuracy at low and high densities, respectively. This indicated that ACT*IV*E's contour segmentation method improved segmentation accuracy by approximately 1% and 3% for low and high synthetic cell densities respectively. Of note, the synthetic data represents an idealized case, as each synthetic data set was binary. No cell-to-cell fluctuation in intensity was incorporated (which is uncommon for biological data).

2.4.3 Investigating Merging Event Precision

Cell-cell interaction events often result in reduced tracking accuracy due to complexities associated with segmenting two or more distinct cells over multi-frame time periods. Through the use of ACT*IV*E's unique segmentation process, we sought to improve track accuracy by isolating merging event profiles and utilizing cell history to improve long-term cell identification. To compare the accuracy of ACT*IV*E in correctly categorizing cells associated with two-body merging events, videos displaying 1) the cell-cell interaction, 2) the tracked behavior as identified by ACT*IV*E, and 3) the tracked behavior as identified by the Kilfoil benchmark algorithm were compiled. An example image set is depicted in Figure 2-6. An expert user first identified whether the event could be manually discerned with confidence. If it could be manually tracked, the expert user then determined whether the two automated approaches correctly identified cells involved in the event. The resulting accuracy was determined as the number of events correctly identified by the automated approach, divided by the total number of events that could be manually traced with confidence. 100 events were randomly selected for each of the three experimental cell densities (5,000, 10,000, and 20,000 cell/cm^2) to compare the effects of density on merging accuracy.

Merging accuracy results are detailed in Table 2-3. As shown, the additional post-processing cost function analysis improved merging event accuracy by 43% at the lowest density, 9% at the medium density, and 0% at the highest density. We hypothesize that the merging accuracy decreases as density increases due to the coupled increase in the number of cell-cell interactions at higher densities. At higher densities, two-body interactions are less common, leading to the predominant use of positional analysis over the customized fingerprint analysis. The positional method is similar to the Kilfoil processing, resulting in comparable accuracy values at higher densities. Additional work has been performed to improve cell-cell interaction accuracy resulting from complex multi-cell interactions [44].

2.4.4 Quantifying Cell Division Accuracy

Understanding cell division behavior is important for assessing cell development and proliferative capacities. ACT*IV*E's ability and accuracy to identify and trace division behavior was assessed in two ways. First, a false positive analysis was performed using a similar method to the merging event accuracy. 100 cell track videos of events classified as divisions by ACT*IV*E were randomly generated at each of the three experimental densities (5000, 10,000, and 20,000 cells/cm^2). These videos were then manually evaluated for false positives, the number of events identified as divisions that were not actually divisions (Figure 2-7). ACT*IV*E achieved a false positive rate of 20% at the lowest experimental density, 29% at the medium density, and 65% at the highest cell density (Table 2-4). We hypothesized that the false positive rate significantly increases at a critical cell density due to a coupled increase in the number of complex cell interactions (three of more cells) and due to potential under-segmentation in dense environments, resulting in the loss of cell ID information. This critical density falls between the medium and high density selected, as is evident by the significant increase in the false positive rate from 29% to 65%. No benchmark was performed using the Kilfoil system, as the Kilfoil system has no method for differentiating cell division behavior during tracking. Division tracing is typically not incorporated into automated tracking software; only a select few algorithms, have attempted to incorporate this capability into their systems, due to the complexity associated with accurately tracking these events.

To complete the division assessment, we additionally measured the false negative accuracy. False negatives were defined as the number of divisions overlooked by the ACT*IV*E approach. To quantify this value, a red ellipse was overlaid onto nuclear signal to highlight ACT*IV*E-identified divisions (Figure 2-8). This overlay was compiled across an entire image stack at each of the three experimental densities. Each video was then separated into four quadrants for manual analysis. An expert viewer carefully progressed through each image stack, recording the number of cell divisions missed by the ACT*IV*E system. This expert viewer was the same individual who performed the manual track analysis in section 2.3.3. As shown in Table 2-4, 7.32% or less divisions were missed by ACT*IV*E at each density. This indicated that the selected segmentation method was capable of identifying the majority of manually discernible division events.

2.5 Conclusion

We have developed and validated a powerful new automated cell tracking system, ACT*IV*E, that was designed to efficiently and accurately track long-term motility behavior of adherent cell populations subject to nuclear staining or transfection. Through the implementation of a novel cell identification method, we have achieved greater than 95% segmentation accuracy at all densities tested. We have additionally utilized unique cell signal characteristics to improve error associated with two-body cell-cell interactions by up to 43% at the lowest densities tested. This improvement is particularly important for long timescale studies, as the likelihood of cells participating in a cell-cell interaction significantly increases with extended experimental duration. We have also incorporated a method to identify and track cell division behavior utilizing ACT*IV*E. This capability is innovative, as most current automated tracking systems have no means to classify division behavior. While refinement of false positive detection is still required at high densities, we have demonstrated that we can achieve successful division detection rates of 80% and 71% at low and medium cell densities respectively. This ability enables new studies in mother-daughter cell relationships, both for developmental and cell-ECM foundational studies. We are confident that the ACT*IV*E system will enable long timescale studies of spatial and temporal correlations of individual and collective cell behaviors, advancing understanding of how cell-cell and cell-material interactions drive biological processes including disease progression, general development, and tissue repair.

2.6 Acknowledgements

Development and application of ACT*IV*E was performed in collaboration with Dr. Richard Baker, a former member of the Henderson lab. We would also like to acknowledge Dr. Lisa Manning, who was instrumental in providing guidance during ACT*IV*E development and in providing feedback for tailoring the accuracy assessment for publication. We extend a special thank you to Forrest Smith, a previous member of the Manning lab, who generated the synthetic data sets used to validate the segmentation accuracy. I would also like to thank the undergraduate students who helped me with ACT*IV*E development, validation, and user assessment, including Kadye Moore, Elliot Russell, Alexis Peña, Alyssa Seunarine, and Brandyn White.

2.7 References

1. Gray, D.S., J. Tien, and C.S. Chen, *Repositioning of cells by mechanotaxis on surfaces with micropatterned Young's modulus.* Journal of Biomedical Materials Research Part A, 2003. **66A**(3): p. 605-614.
2. Discher, D.E., P. Janmey, and Y.L. Wang, *Tissue cells feel and respond to the stiffness of their substrate.* Science, 2005. **310**(5751): p. 1139-1143.
3. Engler, A.J., et al., *Matrix elasticity directs stem cell lineage specification.* Cell, 2006. **126**(4): p. 677-689.
4. Missirlis, D. and J.P. Spatz, *Combined Effects of PEG Hydrogel Elasticity and Cell-Adhesive Coating on Fibroblast Adhesion and Persistent Migration.* Biomacromolecules, 2014. **15**(1): p. 195-205.

5. Magnani, A., et al., *Cell behaviour on chemically microstructured surfaces.* Materials Science and Engineering C, 2003. **23**(3): p. 315-328.
6. Ann Dalton, B., et al., *Modulation of epithelial tissue and cell migration by microgrooves.* Journal of Biomedical Materials Research, 2001. **56**(2): p. 195-207.
7. Yim, E.K.F., et al., *Nanopattern-induced changes in morphology and motility of smooth muscle cells.* Biomaterials, 2005. **26**(26): p. 5405-5413.
8. Kim, D.H., et al., *Mechanosensitivity of fibroblast cell shape and movement to anisotropic substratum topography gradients.* Biomaterials, 2009. **30**(29): p. 5433-5444.
9. Kim, D.H., et al., *Matrix nanotopography as a regulator of cell function.* Journal of Cell Biology, 2012. **197**(3): p. 351-360.
10. Guvendiren, M. and J.A. Burdick, *Stem Cell Response to Spatially and Temporally Displayed and Reversible Surface Topography.* Advanced Healthcare Materials, 2013. **2**(1): p. 155-164.
11. Lendlein, A. and R. Langer, *Biodegradable, elastic shape-memory polymers for potential biomedical applications.* Science, 2002. **296**(5573): p. 1673-1676.
12. Maitland, D.J., et al., *Photothermal properties of shape memory polymer micro-actuators for treating stroke.* Lasers in Surgery and Medicine, 2002. **30**(1): p. 1-11.
13. Gall, K., et al., *Thermomechanics of the shape memory effect in polymers for biomedical applications.* Journal of Biomedical Materials Research Part A, 2005. **73A**(3): p. 339-348.
14. Baer, G.M., et al., *Fabrication and in vitro deployment of a laser-activated shape memory polymer vascular stent.* BioMedical Engineering Online, 2007. **6**.
15. Lendlein, A., et al., *Light-induced shape-memory polymers.* Nature, 2005. **434**(7035): p. 879-882.

16. Zheng, Y., et al., *Light-induced shape recovery of deformed shape memory polymer micropillar arrays with gold nanorods.* RSC Advances, 2015. **5**(39): p. 30495-30499.
17. Lu, P., V.M. Weaver, and Z. Werb, *The extracellular matrix: A dynamic niche in cancer progression.* Journal of Cell Biology, 2012. **196**(4): p. 395-406.
18. Bissell, M.J. and D. Radisky, *Putting tumours in context.* Nature Reviews Cancer, 2001. **1**(1): p. 46-54.
19. Plotnikov, S.V., et al., *Force fluctuations within focal adhesions mediate ECM-rigidity sensing to guide directed cell migration.* Cell, 2012. **151**(7): p. 1513-1527.
20. Tan, J.L., et al., *Cells lying on a bed of microneedles: An approach to isolate mechanical force.* Proceedings of the National Academy of Sciences of the United States of America, 2003. **100**(4): p. 1484-1489.
21. Nelson, C.M., et al., *Tissue geometry determines sites of mammary branching morphogenesis in organotypic cultures.* Science, 2006. **314**(5797): p. 298-300.
22. Aman, A. and T. Piotrowski, *Cell migration during morphogenesis.* Developmental Biology, 2010. **341**(1): p. 20-33.
23. Masuzzo, P., et al., *An open data ecosystem for cell migration research.* Trends in Cell Biology, 2015. **25**(2): p. 55-58.
24. Schadt, E.E., et al., *Computational solutions to large-scale data management and analysis.* Nature Reviews Genetics, 2010. **11**(9): p. 647-657.
25. Friedberg, I., *Automated protein function prediction - The genomic challenge.* Briefings in Bioinformatics, 2006. **7**(3): p. 225-242.

26. Chenouard, N., et al., *Objective comparison of particle tracking methods.* Nature Methods, 2014. **11**(3): p. 281-U247.
27. Maska, M., et al., *A benchmark for comparison of cell tracking algorithms.* Bioinformatics, 2014. **30**(11): p. 1609-1617.
28. Adams, J.C. and F.M. Watt, *Regulation of development and differentiation by the extracellular matrix.* Development, 1993. **117**(4): p. 1183-1198.
29. Rozario, T. and D.W. DeSimone, *The extracellular matrix in development and morphogenesis: A dynamic view.* Developmental Biology, 2010. **341**(1): p. 126-140.
30. Olczyk, P., Ł. Mencner, and K. Komosinska-Vassev, *The role of the extracellular matrix components in cutaneous wound healing.* BioMed research international, 2014. **2014**.
31. Friedl, P. and D. Gilmour, *Collective cell migration in morphogenesis, regeneration and cancer.* Nature Reviews Molecular Cell Biology, 2009. **10**(7): p. 445-457.
32. Cox, T.R. and J.T. Erler, *Remodeling and homeostasis of the extracellular matrix: Implications for fibrotic diseases and cancer.* DMM Disease Models and Mechanisms, 2011. **4**(2): p. 165-178.
33. Jaalouk, D.E. and J. Lammerding, *Mechanotransduction gone awry.* Nature Reviews Molecular Cell Biology, 2009. **10**(1): p. 63-73.
34. Paszek, M.J. and V.M. Weaver, *The tension mounts: Mechanics meets morphogenesis and malignancy.* Journal of Mammary Gland Biology and Neoplasia, 2004. **9**(4): p. 325-342.
35. Strachan, L.R. and M.L. Condic, *Neural crest motility and integrin regulation are distinct in cranial and trunk populations.* Developmental Biology, 2003. **259**(2): p. 288-302.

36. Eilken, H.M., S.I. Nishikawa, and T. Schroeder, *Continuous single-cell imaging of blood generation from haemogenic endothelium.* Nature, 2009. **457**(7231): p. 896-900.

37. Tonkin, J.A., et al., *Automated Cell Identification and Tracking Using Nanoparticle Moving-Light-Displays.* Plos One, 2012. **7**(7): p. 8.

38. Becker, T. and A. Madany, *Morphology-based Features for Adaptive Mitosis Detection of In Vitro Stem Cell Tracking Data.* Methods of Information in Medicine, 2012. **51**(5): p. 449-456.

39. Deng, Y., et al., *Efficient Multiple Object Tracking Using Mutually Repulsive Active Membranes.* Plos One, 2013. **8**(6): p. 11.

40. Xu, T., D. Vavylonis, and X. Huang, *3D actin network centerline extraction with multiple active contours.* Medical Image Analysis, 2014. **18**(2): p. 272-284.

41. Idema, T., et al., *Wavefronts and Mechanical Signaling in Early Drosophila Embryos.* Biophysical Journal, 2013. **104**(2): p. 329A-329A.

42. Gao, Y.X. and M.L. Kilfoil, *Accurate detection and complete tracking of large populations of features in three dimensions.* Optics Express, 2009. **17**(6): p. 4685-4704.

43. Fitzgibbon, A., M. Pilu, and R.B. Fisher, *Direct least square fitting of ellipses.* IEEE Transactions on Pattern Analysis and Machine Intelligence, 1999. **21**(5): p. 476-480.

44. He, Y., *Comparison of Cost Function Against Positional Analysis for Automated Tracking of Three-Cell Interactions.* 2015.

45. Shahriyari, L. and N.L. Komarova, *Symmetric vs. Asymmetric Stem Cell Divisions: An Adaptation against Cancer?* Plos one, 2013. **8**(10): p. e76195.

46. Huth, J., et al., *Significantly improved precision of cell migration analysis in time-lapse video microscopy through use of a fully automated tracking system.* Bmc Cell Biology, 2010. **11**: p. 12.

47. Henkes, S., Y. Fily, and M.C. Marchetti, *Active jamming: Self-propelled soft particles at high density.* Physical Review E, 2011. **84**(4): p. 4.

48. Meijering, E., O. Dzyubachyk, and I. Smal, *Methods for cell and particle tracking*, in *Methods in Enzymology*. 2012. p. 183-200.

49. Schneider, C.A., W.S. Rasband, and K.W. Eliceiri, *NIH Image to ImageJ: 25 years of image analysis.* 2012. **9**(7): p. 671-675.

Table 2-1: Operating parameters for ACT*IV*E tracking software

Parameter	**Value**	**Brief Description (units, where appropriate)**	**Tracking Step**
Plot Toggle	0	toggle to display contour plot information	segmentation
Number of Contours	15	number of contour levels for intensity map	segmentation
Half Particle Diameter	13	radius of particles (pixels)	segmentation
Noise Wavelength	2	length scale of noise (pixels)	segmentation
Maximum Area	260	maximum allowed nuclear cell area (pixels^2)	segmentation
Minimum Area	10	minimum allowed nuclear cell area (pixels^2)	segmentation
Maximum Displacement	20 or 17*	maximum allowed motility distance between two consecutive frames (pixels)	linking
Collision Plot Toggle	0	toggle to plot and display cell-cell collision videos	post processing
Frame Time	3	total time between consecutive frames (minutes)	post processing
Maximum Collision Time	10	number of frames a complete occlusion can occur	post processing
Merging Event Toggle	0	toggle to initiate the manual merging event GUI	post processing
Division Event Toggle	0	toggle to initiate the manual division event GUI	post processing

Asterik (*) denotes that all high density samples (seeding density of 20,000 cells/mL) in **Chapters 2 and 3** were run with a maximum displacement of 17 pixels, due to complex combinatorics issues that prevented tracking completion or resulted in significantly increased run time. All low (5000 cells/mL) and medium (10,000 cells/mL) density samples were run with a maximum displacement of 20 pixels.

Table 2-2: Execution time comparison of the three tracking approaches.

Tracking Method	**Stack Number**	**Number of Cells Identified**	**Execution Time for Analysis (seconds)**
Manual	1	48	3600
	2	38	2040
Kilfoil Method [42]	1	49	5
	2	36	4
ACTIVE Approach	1	46	13
	2	37	12

Comparison of number of cells identified and total required execution time for the gold standard (manual) and two automated tracking approaches. Manual tracking was performed by a trained operator using the MTrackJ plugin [48] in ImageJ [49]. ACT*IV*E reduced execution time by two orders of magnitude, while identifying similar cell numbers to the manual method. Similarly, the Kilfoil approach significantly reduced execution time (three orders of magnitude) while identifying similar cell numbers to the manual method.

Table 2-3: Merging accuracy results of the two automated approaches

Seeding Density	**Tracking Method**	**Number of Events Analyzed**	**Number of Correctly Identified Events**	**Number of Incorrectly Identified Events**	**Error (%)**
Low	Kilfoil	91	70	21	23
	ACTIVE	91	79	12	13
Medium	Kilfoil	98	76	24	22
	ACTIVE	98	78	22	20
High	Kilfoil	89	72	28	20
	ACTIVE	89	72	28	20

100 merging events were randomly selected at each experimental density to assess the two-body cell interaction accuracy of the two automated approaches. ACT*IV*E reduced error associated with merging events by up to 43% at the lowest cell density. Accuracy of the two approaches at higher densities was more comparable, most likely due to the increased number of cell-cell interactions as cells became more densely packed.

Table 2-4: Summary of division event accuracy

Cell Seeding Density	**Total Number of Divisions Identified by ACT*IV*E**	**False Positive Rate (%)**	**Number of False Negatives Identified**	**False Negative Rate (%)**
Low	275	20	11	3.85
Medium	206	29	15	6.79
High	114	65	9	7.32

100 division events were randomly selected to assess the false positive rate for ACT*IV*E's division identification system. ACT*IV*E was capable of accurately classifying 80%, 71%, and 35% of these events at low, medium, and high densities respectively. False negative rates were also investigated through manual analysis. After overlaying ellipse information for dividing cells onto original image stacks, an expert viewer manually identified the total number of missed divisions in each video analyzed. For each density, 15 or less divisions were missed, signifying that ACT*IV*E was capable of identifying the majority of manually discernible division events.

Scheme 2-1: Overview of the ACT*IV*E cell tracking system

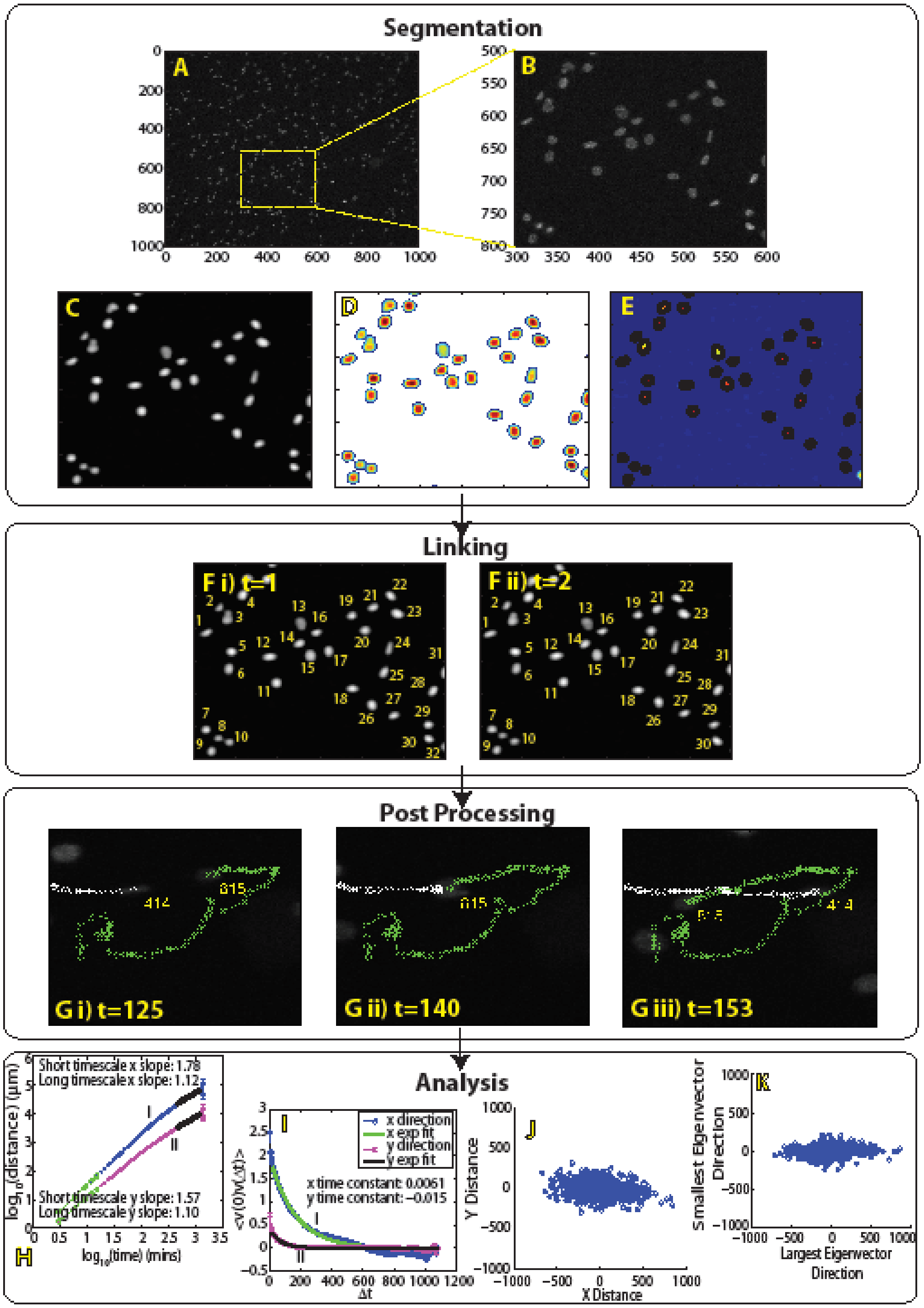

ACT*IV*E executes four major tasks: (A-E) nuclear segmentation, (F) nuclear linking, (G) cell division and merging event post-processing, and (H-K) individual and collective cell motility analyses. (A) Cells were stained with Hoechst 33342 and imaged for 24 hours; (B) image subsections exhibited variable intensity in nuclear staining. (C) Individual frames were first processed using a bandpass filter [42] and (D) contour profiles were established based on fluctuations in nuclear intensity. (E) Single peak contours were fit with an ellipse at half height, denoting cell identification. Multi-peak intensity profiles were tagged as either a division or merging event and reevaluated for accuracy during post-processing. (F-i) Once segmentation was complete, cell identification tags were established and (F-ii) cell track information was linked between consecutive frames. (G-i) Post tracking, cell-cell interaction events were identified, (G-ii) processed using a custom cost function, and (G-iii) track information was updated accordingly to improve track accuracy. Separately, division event track history was duplicated and parent-child relationships were established. Collective motility behavior was then characterized using (H) decomposed mean-squared displacement (I and II for x and y data, respectively), (I) velocity-autocorrelation analyses (I and II for x and y data, respectively), (J) diffusion plots of final cell track positions where the starting location for all cells was renormalized to the plot origin, and (K) final cell locations rotated by the principal axis of the gyration tensor.

Figure 2-1: Definition of single and multi-peak contour profiles

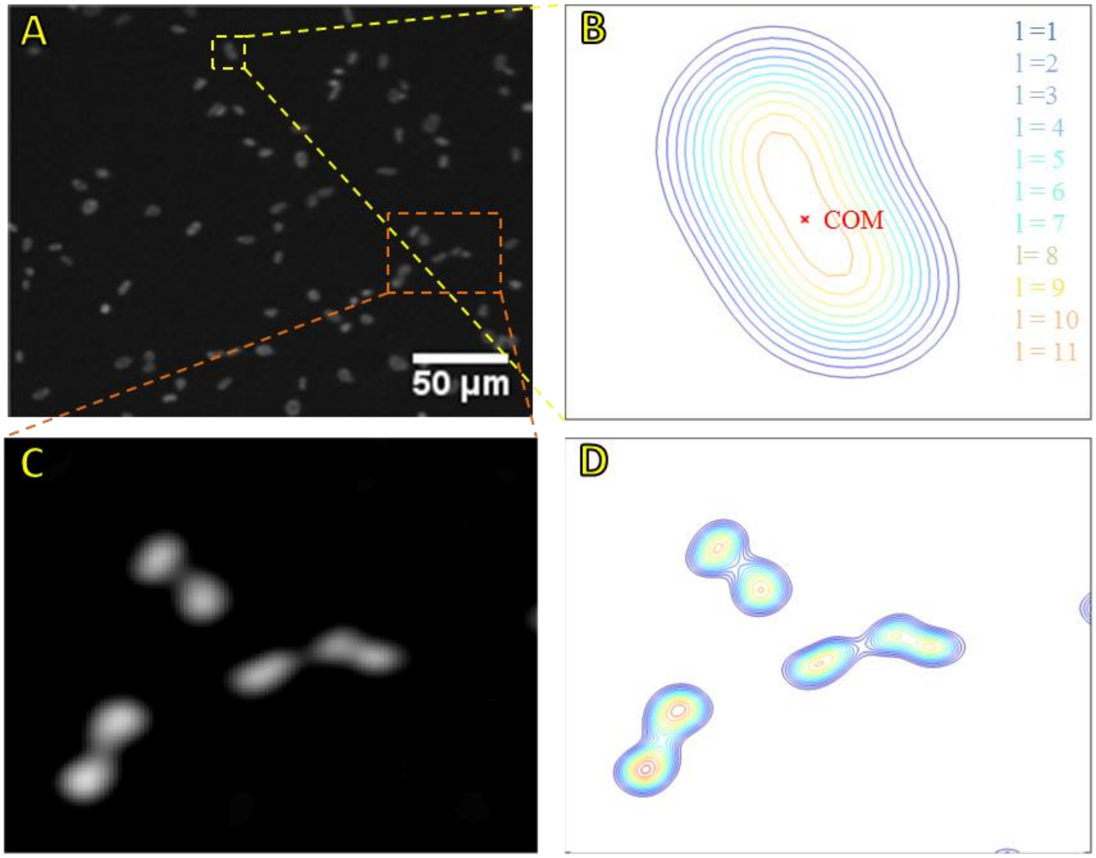

(A) Cells were stained with Hoechst dye to visualize nuclei. Intensity profile information was converted to a contour map to identify individual cells. (B) Relationships between contours were established according to their center of mass (COM), maximum radius, and level number (l). (C) In cases where signal from multiple cells intersected, (D) multiple peaks were identified and separately tagged to improve accuracy associated with interaction events.

Figure 2-2: Ellipse fitting for multi-peak instances

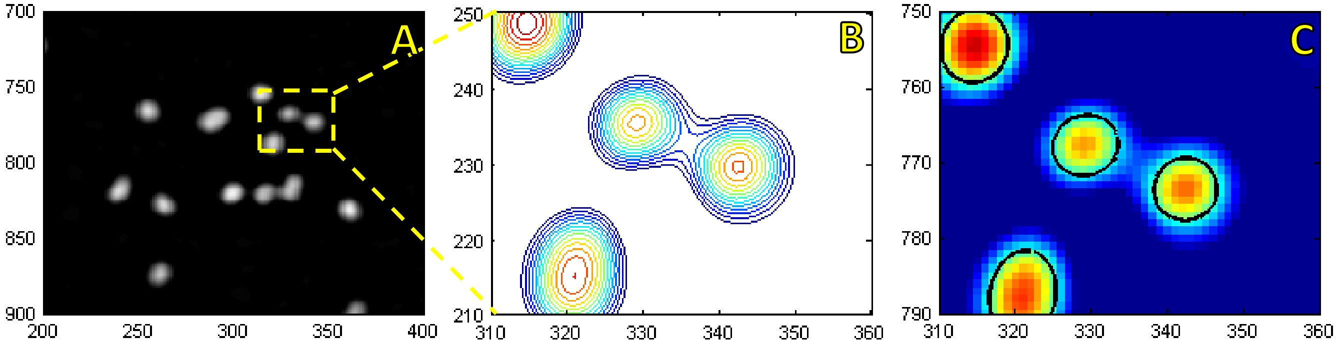

(A) After band-pass filtering was completed, nuclear signal from interacting cells overlapped. (B) This overlap resulted in multi-peak instances recognized by ACT*IV*E as either merging or division events. (C) Multiple peaks were fit as separate cells (denoted by the black outlines) and tracked through the same process as single peak instances. After tracking was completed, multi-peak instances were reassessed for accuracy utilizing a custom cost function.

Figure 2-3: Manual image stack comparison and example cell traces

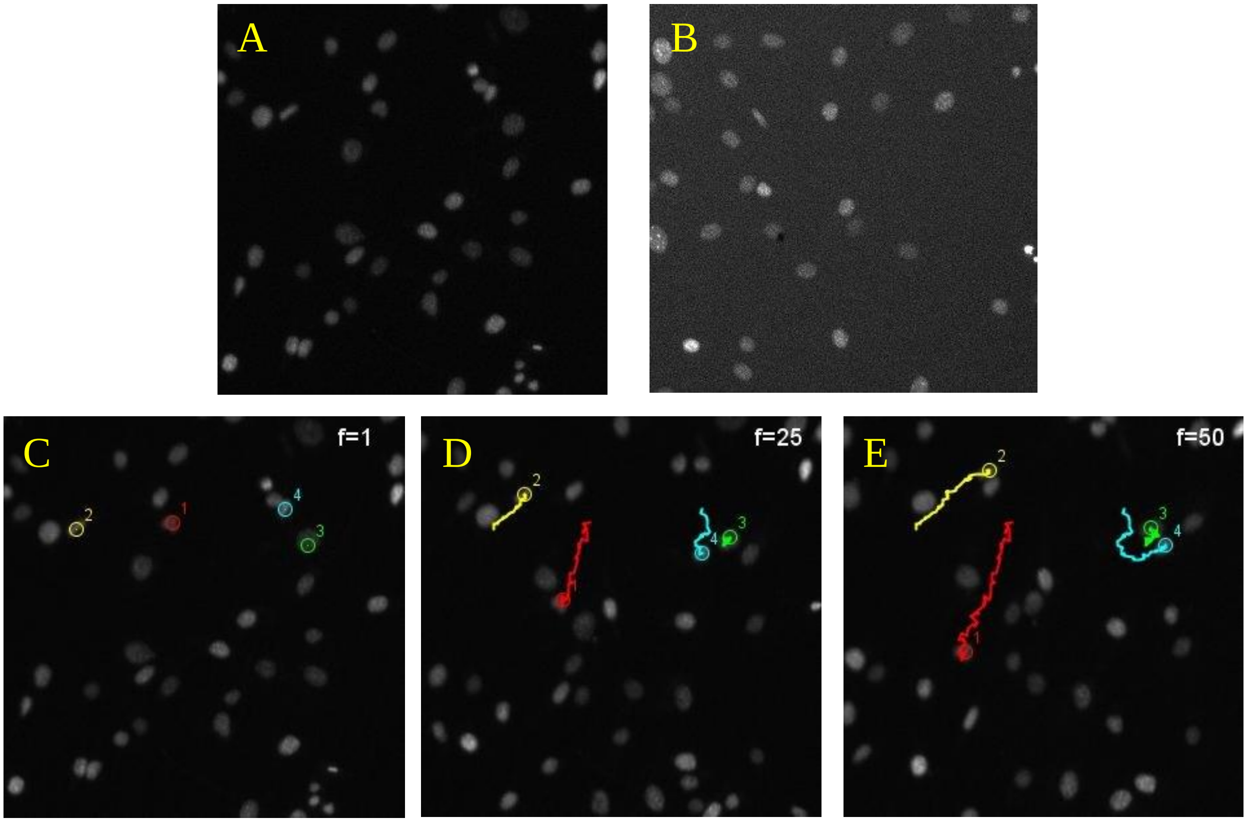

Cell image stacks were extracted from (A) static wrinkled polymer substrates and (B) tissue culture polystyrene materials seeded at 10,000 cells/cm^2. Analyzed stacks consisted of 50 frames, with a 300x300 pixel area. Manual tracking was performed using the MTrackJ [48] plug-in in ImageJ [49]. (C) Cells were individually identified by the user in the first frame, (D) manually traced through each consecutive frame of the image stack, and (E) visualized with track overlays to manually characterize cell motility dynamics.

Figure 2-4: Synthetic data depiction of low and high simulated cell densities

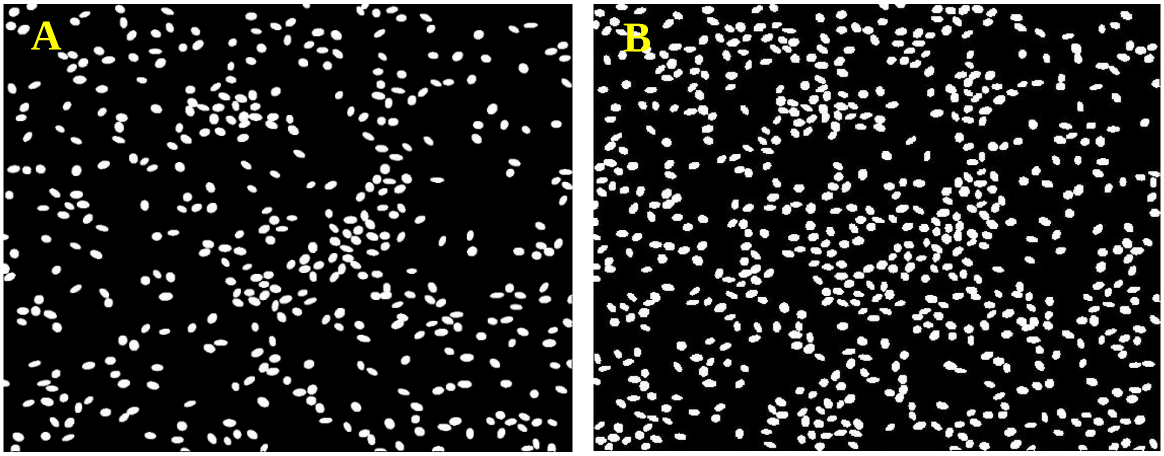

Example frames from (A) low (11.1% nuclear area coverage) and (B) high (17.1% nuclear area coverage) simulated cell densities. Motility dynamics were created using an active matter model [47] that was adapted to include a drag coefficient in the y-direction to simulate anisotropy of planned cell experimental groups.

Figure 2-5: Segmentation accuracy of the ACT*IV*E and Kilfoil approaches

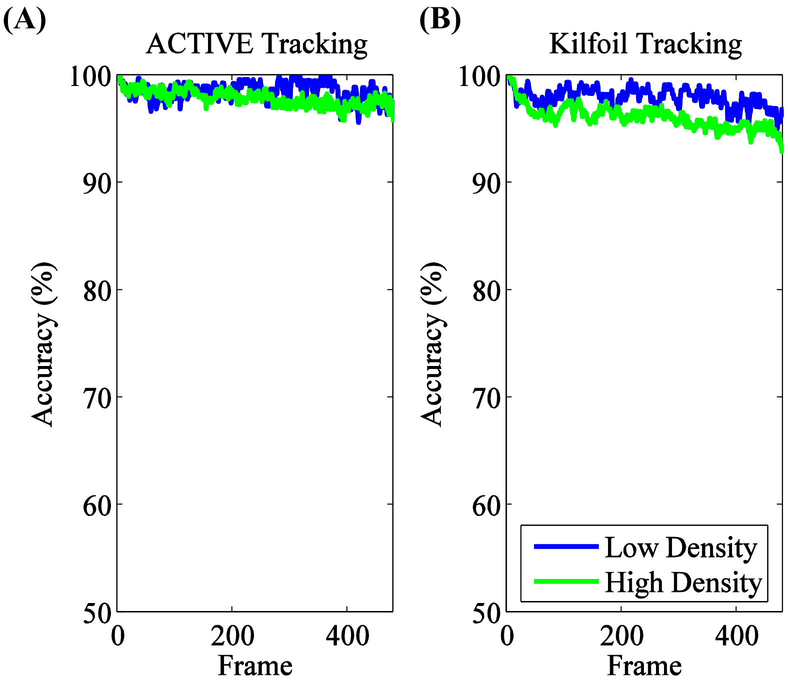

Segmentation accuracy was calculated as the percentage of cells assigned to the correct ID per frame when compared to the known simulated trajectory data. (A) ACT*IV*E achieved a segmentation accuracy of 97.5% and 95.7% at low and high synthetic densities respectively, when measured through the entire 480 frame image stack. (B) Comparatively, the Kilfoil approach yielded 96.8% and 92.9% accuracy at low and high densities, respectively. This validated that ACT*IV*E was capable of more accurately segmenting cells when compared to a benchmark program.

Figure 2-6: Example stills of merging accuracy assessment video

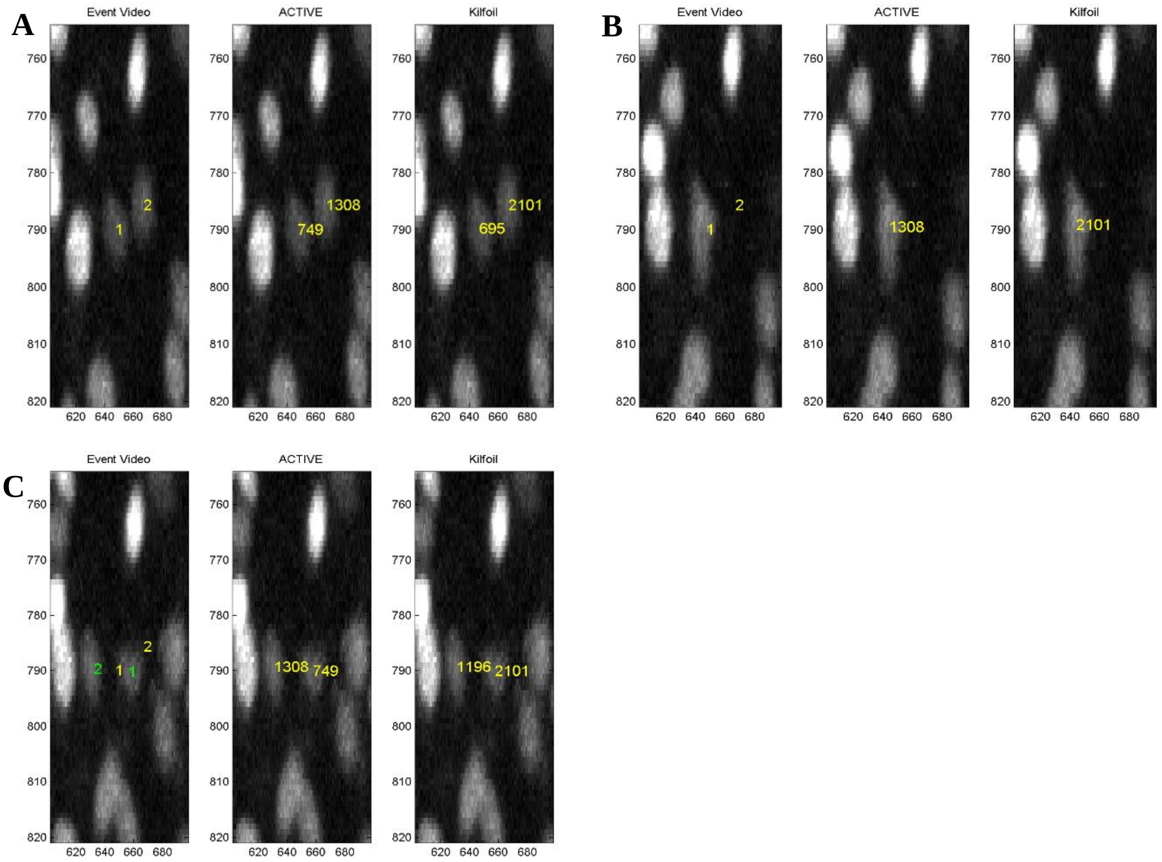

Sample stills from a selected merging event accuracy video. (A) Cells of interest were identified in the first frame of the "Event Video" column and (A-C) then traced by an expert user to determine manual tracking feasibility. If manual tracing was considered discernible, the user then assessed the ability of ACT*IV*E and of the Kilfoil approach, in the "ACT*IV*E" and "Kilfoil" columns respectively, to trace the cells appropriately through the interaction event. As shown in (A), the ACT*IV*E and Kilfoil methods first displayed cell IDs of interest. (B) One of these ID tags was often lost during the interaction event, as the two cells occluded. (C) After the signal separated, the original tags were re-assessed to determine track accuracy.

Figure 2-7: Example stills from false positive division accuracy assessment video

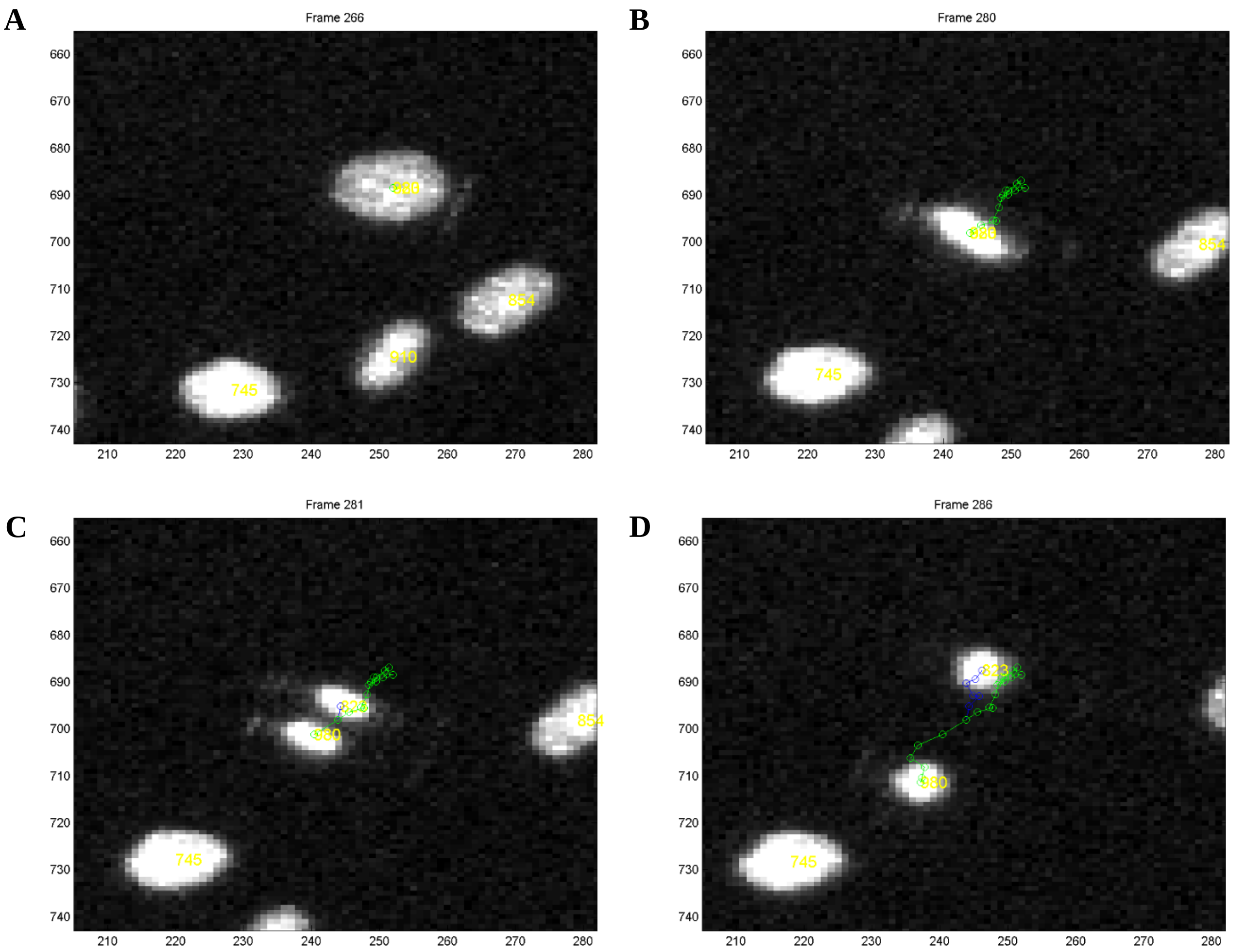

Division events were identified using ACT*IV*E's contour segmentation system and sample stills from videos analyses were plotted here to visualize the division process. (A) To assess false positive accuracy, 100 division events were randomly selected at each experimental density and videos of trajectory behavior were produced. (B) Trajectory information for the mother cell was recorded and (C) duplicated for each daughter cell to appropriately trace cell lineage progression. (D) Cell identification tags were manually assessed before, during, and after the division event to calculate false positive accuracy rates.

Figure 2-8: Example stills from false negative video analysis

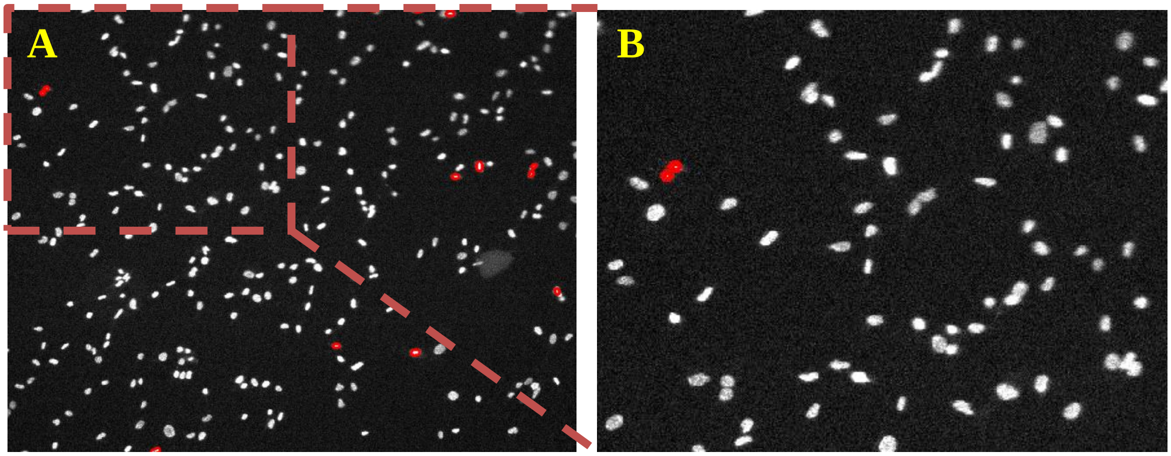

False negative videos were produced by overlaying cell division information onto nuclear signal videos. (A) Cell divisions identified by ACT*IV*E were highlighted using red ellipses. (B) Video overlays were then divided into four quadrants to enhance manual observation. An expert viewer performed a frame-by-frame analysis, tallying the total number of division events missed at each experimental density by the ACT*IV*E system.

Chapter 3: ACT*IV*E Case Study Investigating Change in Motility Dynamics of Static Anisotropic and Isotropic Microenvironments[†,*]

3.1 Synopsis

Substrate anisotropy has previously been used as a tool to manipulate and guide cell motility behaviors. More specifically, variations in topographical pattern size, shape, and spacing have been shown to dictate important functions that drive motility dynamics, including cell adhesion and polarization. This chapter focuses on a case study comparison of anisotropic and isotropic surfaces to apply the ACT*IV*E automated cell tracking system (described in **Chapter 2**) to long timescale (at least 24 hours) cell motility data. Cell motility atop wrinkled gold-coated, flat gold-coated, and flat tissue culture polystyrene (TCPS) surfaces was investigated. ACT*IV*E utilized physics-based statistical metrics, including mean-squared displacement, velocity autocorrelations, diffusion, gyration tensor, and asphericity measurements to tease out subtle differences in motility dynamics across all substrate types at multiple densities. Here, we demonstrate that gold coated anisotropic substrates induce directional cell motility parallel to the wrinkle angle, compared to random motion on the flat gold-coated and TCPS surfaces.

[†] Adapted (in part) with permission from R.M. Baker, M.E. Brasch, M.L. Manning, and J.H. Henderson, *Journal of The Royal Society Interface*, **2014**, 11, 20140386. **Copyright © The Royal Society 2014**

[*] ACT*IV*E code was developed, validated, and benchmarked by Megan Brasch. Material preparation, cell culture, and time-lapse video experiments were designed and executed by Dr. Richard Baker. Video analysis was completed in collaboration by Megan Brasch and Dr. Richard Baker. For more information, see: Baker, RM, "Shape Memory Polymers as 2D Substrates and 3D Scaffolds for the Study of Cell Mechanobiology and Tissue Engineering" (2015).

3.2 Introduction: Anisotropy Influences Directional Cell Migration

Cell-extracellular matrix (ECM) interactions play a crucial role in regulating important biological processes *in vivo*, including morphogenesis [1, 2], tissue repair [3, 4], and disease regulation [5-7]. ECM is composed of a mix of nano- and micron-sized fibrous proteins (e.g. collagen and fibronectin) and proteoglycans (e.g. aggrecan) that serve as physical scaffolding for cells, regulating biochemical and biomechanical cues critical for tissue homeostasis [8]. While it is widely recognized that cell-ECM interactions are fundamental in driving cell adhesion, polarization, and motility behaviors (e.g., [9]), decoupling cell-ECM regulated dynamics from associated cell-cell or extracellular driven responses in complex microenvironments has remained challenging.

Synthetic substrates serve as useful *in vitro* tools to investigate cell-ECM interactions, as researchers can regulate material stiffness [9-12], surface chemistry [13, 14], and topographical features [11, 13] to suit intended applications. Specific to cell motility, anisotropy of 2-D patterns (e.g. micro- and nano-ridges [15], micro- and nano-grooves [16, 17], and asymmetric micropatterns [18]) and controlled 3-D architectures (e.g. composition or alignment of electrospun fibers [19] or spatial structure and porosity control of scaffolds [20]) have been exploited to direct cell motility responses. For example, Kim and colleagues demonstrated that fibroblasts preferentially migrate along 2-D square lattice patterns and that pattern density can be used as a guide for homing cell motility behaviors [21]. With respect to 3-D, Li and colleagues represent one example where electrospinning a combination of natural and synthetic polymers (hyaluronan (HA), silk fibroin, and polycaprolactone) can be advantageous in stimulating fibroblast migration.

More specifically, Li and colleagues showed that the upregulation of CD44 expression from the synergistic incorporation of HA into the underlying synthetic fiber structure led to improved motility [22]. These examples demonstrate the power behind using synthetic substrates and scaffolds as tools to further understanding of initiation and regulation of cell motility responses as they relate to cell-ECM interactions.

Previous research confirms that anisotropic wrinkled patterns induce directional cell motility [17]. As previously shown, the degree of cell alignment and individual motility along the pattern direction varies substantially, based on cell type and feature size [15, 23]. While useful knowledge of attachment, polarization, and motility phenomenon have previously been deduced using substrates with nano- and micron-sized wrinkle topographies, the sample size of cells measured, specifically for elucidating cell-ECM motility dynamics, remains small (typically less than fifty cells per study) (e.g. [24]). With such small sample sizes, cells are measured individually with large variability study to study. This potentially fails to capture bulk population dynamics and behaviors at increased densities closer to confluent tissue scales. As previously discussed in **Chapter 2**, one of the major limitations influencing expansion of this analysis is that manual tracking remains the gold standard in the cell tracking field [25]. In order to improve understanding of long-term cell motility behavior (at least 24 hours or more) in anisotropic versus isotropic systems, we applied ACT*IV*E to carefully quantify subtle differences in 2D motility dynamics of hundreds of cells seeded atop wrinkled or flat shape memory polymer based or flat tissue culture polystyrene surfaces at multiple cell densities. Such large cell sample sizes enabled the application of several statistical physics-based metrics to tease out subtle motility differences present in the anisotropic versus isotropic 2-D microenvironments.

3.3 Experimental Design for Time-Lapse Imaging and Video Analysis[‡]

3.3.1 Substrate Preparation[1]

Shape memory polymer substrates were prepared as previously reported by Yang and colleagues [26]. 95:5 wt% *tert*-butyl acrylate, butyl acrylate (*t*BA-BA) films were prepared using 5 wt% tetraethylene glycol dimethacrylate (TEGDMA) as a cross-linker and 0.5 wt% 2,2-dimethoxy-2-phenylacetophenone (DMPA) as initiator. For anisotropic (wrinkled) substrates, *t*BA-BA samples were fixed with a 7% uniaxial strain and subsequently cut into 6x6 mm squares. Isotropic *t*BA-BA films were cut directly into 6x6 mm squares. All *t*BA-BA samples were then sputter coated with gold for 100 seconds (15 second intervals with 15 second breaks between coatings to ensure material did not heat prematurely) resulting in an approximately 33nm thick gold coating deposited on the material surface. Anisotropic substrates were then recovered at 55°C in an isothermal oven to induce surface buckling in the gold layer, resulting in a nanotopographic pattern with features on the order of 400nm in amplitude and 1-5µm in wavelength. An additional isotropic control group, tissue culture polystyrene (TCPS), was also prepared to compare surface chemistry effects. 6x6mm TCPS squares were cut from 100mm petri dishes using a razor blade. All three substrate groups were then UV sterilized for one hour on the non-gold or non TCPS

[‡] Cell experiments were executed by Dr. Richard Baker.

[1] Substrate characterization and optimization performed by Dr. Baker and Dr. Yang. Protocols were published in P. Yang, R.M. Baker, J.H. Henderson and P.T. Mather, *Soft Matter*, 2013, 9, 4705-4714

coated side and then sterilized for an additional 10 hours on the gold or TCPS treated side for subsequent cell culture.

3.3.2 Cell Culture Growth and Seeding Conditions

C3H10T1/2 mouse fibroblast cells (ATCC) were cultured in BME complete growth medium containing 10% fetal bovine serum (FBS, v/v), 1% penicillin/streptomycin (v/v), and 1% GlutaMAX (v/v). Cell expansion was performed in a 37°C humidified incubator with regulated 5% CO_2. Cells were passaged at 80% confluence using 0.25% Trypsin EDTA. For time-lapse experiments, cells were restricted to passage number 13-15.

Prior to seeding, gold coated wrinkled (W), gold coated non-wrinkled (NW), and tissue culture polystyrene (TCPS) samples were soaked in BME medium for 2 hours to promote FBS protein adsorption on the material surface to improve cell attachment. Solutions of 5,000 cells/cm^2, 10,000 cells/cm^2, or 20,000 cells/cm^2 were then prepared. Cells were seeded onto W, NW and TCPS substrates using a droplet seeding technique. In each case, a 20µL droplet of cell solution was carefully deposited on the surface of the substrates. Substrates were then transferred to a 37°C incubator for 2 hours to allow for initial cell attachment. After 2 hours, complete growth medium was added and the cells were cultured for an additional 22 hours at 37°C to establish equilibrium.

3.3.3 Live-Cell Nuclear Staining and Imaging

Cells were stained with Hoechst 33342 (Invitrogen), a vital nuclear marker, to visualize for ACT*IV*E analysis. Hoechst stock solutions (10mg/mL) were diluted to a final concentration of 0.01µg/mL in complete growth media. Of note, the selected concentration was one order of magnitude below the recommended range (0.2-5µg/mL) and was deliberately selected to ensure appropriate cell divisions persisted over the 24 hour imaging period; Hoechst staining at the recommended concentration suppressed division behavior. After the staining solution was prepared, W, NW, and TCPS substrates were transferred to LabTek borosilicate chamber slides (Fisher Scientific) for time-lapse imaging. 800µL of the staining solution was added to each of the four chamber wells and cells were then incubated at 37°C for 30 minutes to allow for nuclear uptake. Samples were then inverted and weighed down with a sterilized glass slide, cut to fit into the chamber wells. The glass weight acted as a stabilizer to prevent bulk sample movement during imaging. The chamber slide was then transferred to a live cell stage incubator (INC-2000, 20/20 Technology, Inc.) and imaged on a Leica DMI 6000B inverted microscope. The live cell stage incubator was connected to a temperature regulator set at 37°C and a gas regulator connected to a 5% CO_2/95% mixed air tank for the 24 hour imaging duration. Images were captured every three minutes with a 350ms exposure time using an A4 filter cube (excitation/emission peak of 360/470 nm) on an Andor Luca R camera with a 10x/0.63 NA objective.

3.3.4 Characterizing Cell Motility Behavior[2]

Cell motility behavior was characterized using several statistical physics-based metrics, including mean squared displacement, velocity autocorrelations, diffusion plotting, and asphericity measurements. This analysis was enabled by ACT*IV*E's ability to accurately track cells over long

---

[2] Video analysis completed in collaboration with Dr. Richard Baker

timescales and ACT*IV*E's capability to track hundreds of cells per frame in each substrate environment.

3.3.4.1 Mean Squared Displacement

Mean squared displacement (MSD) was used to quantify directional migration and diffusion characteristics. MSD was calculated as:

$$MSD(\Delta t) = \sum_{i=1}^{N} \frac{([r(t+\Delta t) - r(t)]^2)}{N} \qquad \text{(Eq. 3-1)}$$

where r was the [x,y] distance at a specific time point, Δt represented the time interval of interest and N signified the total number of cells analyzed [27]. MSD was calculated for each Δt and then plotted on a $\log_{10}$ Δt versus $\log_{10}$ MSD scale for each substrate and cell density tested. MSD decomposition was also performed in the x- and y-direction. In the decomposed case, the x-axis was rotated to align with the direction of anisotropy. Wrinkle direction was measured from the horizontal in phase contrast images using ImageJ [28, 29]. Once MSD information was plotted, a linear fit was applied to short and long timescale MSD data to compare cell motility behavior. The short timescale fit was based on the first five Δt intervals, whereas the long timescale fit was standardized to minimize fluctuations in the standard deviation at large Δt intervals. For this work, the upper 60 Δt intervals were disregarded for the long timescale fit. For MSD slope comparisons, a value of one represented diffusive ('random walk') motility while a value of two represented ballistic migration, where cells persist in a single direction at a constant velocity. A mobility parameter, δ, was further defined to describe how fast cells displace. δ represented the intercept of the line fit to the long timescale slope.

3.3.4.2 Velocity Autocorrelation

To investigate temporal correlations associated with cell velocity, a velocity autocorrelation function was used. This function was defined as:

$$C_v(t) = \langle v_i(0) \cdot v_i(t) \rangle \qquad \text{(Eq. 3-2)}$$

where $C_v(t)$ was the velocity autocorrelation for a specific time-step t, $v_i(0)$ was the initial velocity and $v_i(t)$ was the velocity at time t [27]. Cell velocities were calculated in x- and y-directions using the central finite difference approximation with an accuracy value of eight [30]. Velocity autocorrelation information was then calculated for each time-step and plotted as t versus $C_v(t)$. Similar to MSD calculations, the x-axis was rotated to align parallel to the wrinkle direction for anisotropic topographies. X- and y-velocity autocorrelation data were then fit with an exponential decay and a time constant was extracted to assess how long a single cell moved in a constant direction.

3.3.4.3 Diffusion Plots

Qualitative motility assessment was performed through diffusion plot characterization. For each substrate and cell density, track information was renormalized to a single starting location. Net displacement was then calculated for each cell and summed across the 24hr experimental duration. As with MSD and velocity autocorrelation calculations, the x-axis was rotated to align parallel with the wrinkle direction for anisotropic surfaces. Net displacement behavior was then recorded for the final frame and visualized to determine the directional distribution cells traveled.

Radial distributions indicated no directional bias while elongation along a particular axis allowed for qualitative assessment of preferential migration patterns.

3.3.4.4 Asphericity Measurements

Track asphericity was used to quantify cell track shape. To determine cell track asphericity, the gyration tensor was first calculated for each cell track:

$$S_{mn} = \frac{1}{2N^2} \sum_{i=1}^{N} \sum_{j=1}^{N} \left(m_i - m_j\right)\left(n_i - n_j\right) \tag{Eq. 3-3}$$

where *m* and *n* refer to the Cartesian coordinates (x or y respectively), *N* is the total number of track positions, and *i* and *j* are given track positions [31]. The largest and smallest eigenvalues for the gyration tensor, λ_2^2 and λ_1^2, respectively, were then extracted and used to calculate the cell track asphericity (*A*):

$$A = \frac{(\lambda_2^2 - \lambda_1^2)}{(\lambda_2^2 + \lambda_1^2)} \tag{Eq. 3-4}$$

As a result, asphericity values ranged from 0 to 1, with a larger asphericity indicating more directed cell migration. Average asphericity values were compared for each substrate tested.

3.3.5 Division Directional Analysis

Nuclear staining and ACT*IV*E division classification enabled assessment of division directionality, defined here as the angular direction in which two daughter cells pull apart. Immediately following the frame where two daughter cells split, the angle between the two daughter nuclear centroids and the horizontal axis was measured. The angular spread was then calculated using the truncated standard deviation, once all angle values were adjusted to a [-90°, 90°] range, centered around 0° [32]. To normalize between anisotropic and isotropic substrates, angle values were systematically rotated by 1° from 0° to 180° and corresponding angular spreads were calculated. For each substrate, the resulting reference angle with a minimum angular spread was used. For anisotropic substrates, this reference angle typically fell within ±10° of the direction of anisotropy, allowing conclusions to be drawn about the association of division directionality with the wrinkle angle. Using this approach, an angular spread of 52° indicates a completely random spread (no preferential directionality) while a decrease in the angular spread represents an increase in directionality.

3.3.6 Statistical Analysis

Statistical comparisons of MSD slopes and mobility parameters, velocity autocorrelation time constants, and asphericity parameters were performed using non-parametric analysis due to deviations in the assumption of normality revealed from Shapiro-Wilks testing. Spearman's rank correlation testing was used to assess the effects of density on motility behavior (n=12). Significance was determined through comparison of correlation coefficients using a 95% confidence level ($\alpha = 0.05$). Kruskal-Wallis one-way analysis of variance was conducted to analyze differences between substrates, followed by Wilcoxon rank-sum testing for individual comparisons. Multiple comparison testing was then performed using Holms-Sidak corrections for familywise error. MSD slope and velocity autocorrelation time constants within groups were performed using a paired t-test. All testing was completed using 95% confidence levels with $\alpha =$

0.05. For each of the three substrate combinations, four technical replicates were used, meaning that n=12 for density comparisons, while paired group testing consisted of n=4.

Statistical analyses of angular spread values were performed using one factor ANOVA with n=12 for each substrate group (W, NW, and TCPS). Individual comparison testing was performed using a student's t-test with a Holms-Sidak correction for multiple comparisons. Significance was determined at 95% confidence levels.

3.4 Results and Discussion: ACT*IV*E Case Study

Time-lapse microscopy was used to capture cell motility data of C3H10T1/2 mouse fibroblast cells at three different densities (5,000 cells/cm^2, 10,000 cells/cm^2, and 20,000 cells/cm^2) on three substrate surface types (W, NW, and TCPS). Overall, directed cell migration along the direction of anisotropy was observed on W substrates, while NW and TCPS cells displayed random cell motility.

3.4.1 Nuclear Imaging in Anisotropic and Isotropic Microenvironments

Biological variability led to fluctuations in the number of cells identified by ACT*IV*E at each of the three densities tested (5,000 cells/cm^2, 10,000 cells/cm^2, and 20,000 cells/cm^2). Representative fluorescent micrographs of cells seeded onto W substrates clearly demonstrate an increase in cell number when comparing low (5,000 cells/cm^2), medium (10,000 cells/cm^2), and high (20,000 cells/cm^2) seeding densities (Figure 3-1). As shown in Table 3-1, the average total number of cells identified by ACT*IV*E ranged from 716-956 cells, 1196-1558 cells, and 1627-2670 cells for low, medium, and high densities respectively, coupled with increasing standard deviations as the seeding density increased. This variability was attributed to biological fluctuations with cell attachment at lower densities, coupled with contact inhibition or varied proliferative responses at higher densities, leading to much more significant variability in cell density behavior at higher densities overall. The cell seeding technique may have also played a role in sample to sample variability, as droplet seeding promotes aggregation of the cells towards the center of the droplet due to surface tension effects. Regardless, as demonstrated in **Chapter 2**, ACT*IV*E was capable of accurately tracking cells at all three densities tested.

3.4.2 Cell Trajectory Data

Qualitative analysis of cell trajectory information revealed preferential migration (parallel to the wrinkle direction) of fibroblast cells on anisotropic W surfaces compared to random motility of cells on isotropic NW and TCPS surfaces (Figure 3-2). This provides evidence that cell motility behavior is directly linked to substrate topography, as similar bulk behavior was qualitatively observed on NW and TCPS materials despite changes in surface chemistries. Trajectory analysis confirmed that ACT*IV*E was capable of generating large, complete datasets useful for advanced statistical physics based tools that rely on ensemble-averaged functions such as MSD or velocity autocorrelations. In the future, pair correlation functions (e.g., [33]) could also be applied to these robust, large datasets to visualize new patterns in cell-cell interactions and explore phase transitions in collective cell behaviors (such as contact inhibition related responses).

3.4.3 Mean Squared Displacement Behavior

Mean squared displacement was plotted versus Δt on a $\log_{10}$-$\log_{10}$ scale to tease out subtle differences in cell motility behavior atop W, NW, and TCPS substrates. Surprisingly, analysis of non-decomposed MSD revealed that cell motility followed the same functional form at long timescales, irrespective of substrate type (Figure 3-3 and Table 3-2). In general, cell behavior was more diffusive at long timescales, independent of substrate topography or cell density. This suggests that motility of this particular cell type is not strongly influenced by cell-cell interactions.

When MSD behavior was further decomposed into x (parallel to anisotropy, where appropriate) and y (perpendicular to anisotropy, where appropriate) directions, the x-short timescale slope of W substrates was significantly higher than the x-short timescale slope for both NW and TCPS surfaces (Table 3-3). This quantitatively proves that cell motility is more ballistic on anisotropic substrates, parallel to the wrinkle direction. Further, when decomposed x and y behaviors were plotted on a $\log_{10}$ Δt versus $\log_{10}$ MSD scale, a clear separation of x and y behaviors was consistently seen atop W substrates, whereas x and y behaviors consistently overlapped on NW and TCPS substrates (Figure 3-4). This further demonstrates that cells preferentially migrate along the wrinkle direction for anisotropic surfaces. This trend was consistent across all cell densities, further confirming that C3H10T1/2 fibroblast motility is not strongly influenced by cell-cell interactions.

Interestingly, while both non-decomposed and decomposed MSD long timescale slopes were more diffusive at longer timescales, slopes never reached a value of 1, even after 24hrs of imaging. This is contrary to what has previously been reported in the biophysics literature and has recently started to gain recognition as an important biological phenomenon [34]. In general, a long timescale slope value of 1 would indicate purely diffusive cell motility. When applied to other cell types in a wound healing system, we have identified that this superdiffusive MSD behavior is a consistent trend (data not shown). We are continuing to explore and model this behavior to further understanding of mechanisms driving collective cell dynamics for biomechanics and wound healing applications.

3.4.4 Velocity Autocorrelation Analysis

Temporal velocity autocorrelations were used to assess trends in cell velocities on W, NW, and TCPS surfaces. Similar to decomposed MSD calculations, x (parallel to anisotropy, where appropriate) and y (perpendicular to anisotropy, where appropriate) velocity autocorrelation behaviors were decoupled to reveal differences in persistence with respect to the direction of anisotropy. Representative plots of velocity autocorrelation traces confirmed previous MSD results, indicating that cells preferentially migrate along the direction of anisotropy in W systems but had no preferential movement direction on NW and TCPS surfaces (Figure 3-5). In general, x- and y-velocity autocorrelation plots depicted longer decorrelation times on W substrates compared to NW and TCPS surfaces. This qualitatively indicates that cells are more likely to persist in the same direction on W surfaces for longer timescales, irrespective of density, indicating that cell-cell interactions play a minimal role in perturbing motility dynamics for this particular cell type.

Velocity autocorrelation data was fit with an exponential decay function to further determine differences in cell persistence with respect to direction-dependent motility. As shown in Table 3-4, comparison of the x- and y-rate constants revealed a statistically significant difference in autocorrelation behavior between W and TCPS surfaces. This again indicates that cell velocity is more persistent on W versus TCPS surfaces. While the rate constants for the W substrates were always larger than the rate constants for the NW substrates, there was no statistically significant difference observed.

3.4.5 Diffusion Characteristics

Diffusion plots were generated to qualitatively compare patterns in overall cell motility atop W, NW, and TCPS surfaces. For all substrates and densities, trajectory behavior was renormalized to the same starting location. Cell displacement information was then summed over the 24 hour imaging duration, resulting in a single final net displacement point plotted for each cell. Similar to MSD and velocity autocorrelation analyses, the x and y axes were reoriented to align parallel and perpendicular to the direction of anisotropy respectively, where appropriate. As shown in Figure 3-6, cells on W substrates move primarily along the direction of anisotropy. This is qualitatively depicted by the elongation of track behavior along the x-axis. For NW and TCPS substrates, the diffusion distribution is radial, indicating no preferential motility direction for the isotropic materials.

3.4.6 Asphericity Calculations

Asphericity calculations were used to quantitatively characterize cell trajectory shape. The largest gyration tensor eigenvector (or the largest principle direction of motility) was plotted parallel to the x-axis to reveal qualitative differences in asphericity. As shown in Figure 3-7, W substrates had the largest gyration tensor, followed by NW substrates, and finally TCPS surfaces.

This trend was quantitatively verified by comparing average asphericity values per substrate. As shown in Table 3-5, statistically significant differences were seen when comparing the anisotropic W substrate to both the isotropic NW and isotropic TCPS surfaces. Surprisingly, a significant difference in the isotropic controls was also noted, with a larger asphericity observed on the NW versus TCPS substrates. This indicates that ACT*IV*E was capable of determining subtle differences in even the "control" substrates.

When considering the results from the MSD analyses, it is unsurprising to note that cell tracks on all three surfaces exhibited asphericities much larger than that expected of a 2D random walk (0.57) [35]. With respect to biological phenomenon, this behavior could be attributed to proteolytic mechanisms. Previous literature has shown that mesenchymal (motile) cancer cells can degrade ECM components, leaving behind a track for invasive collective migration to follow [36]. Similarly, reorganization of ECM surrounding breast tumors by deregulated stromal cells has been shown to elicit metastatic potential [37, 38]. Manual inspection of ACT*IV*E cell traces suggest that cells tend to follow similar paths as previous cells. These potential "repeat" tracks could be a result of cell-derived matrix deposition, leading to non-random diffusive behavior. This may also be related to cell adhesion dynamics, as cell derived matrix would provide more favorable binding conditions on surfaces where cell adherence is traditionally weak. This could have important implications in tumor cell migration applications, where mesenchymal-amoeboid transitions are often dictated by changes in cell-ECM adhesion, inhibition of RHO signaling pathways, or inhibition of proteolysis [39, 40].

3.4.7 Division Angle Correlation

ACT*IV*E analysis enabled careful examination of cell division patterns, a capability often neglected in current automated cell tracking software. Cell division directionality was defined as the angle made between the centroids of the two dividing daughter cells and the horizontal axis. As shown in Figure 3-8, when comparing division directionality on W, NW, and TCPS surfaces at all densities, oriented divisions (parallel to the wrinkle direction) were observed atop W substrates. This is qualitatively depicted by the narrow distribution of division angles centered around 90°. Comparatively, no preferential division directionality was observed on NW and TCPS substrates, depicted by the broad distribution in division angles ranging from 0° to 180°. Average angular spread was used to quantitatively determine differences in cell division directionality. As shown in Table 3-6, cell divisions were more oriented on the W surfaces (41.0°) compared to the NW or TCPS surfaces (47.3° and 48.5° respectively). This difference was statistically significant for the anisotropic versus isotropic surfaces, but was not statistically significant for the two isotropic surfaces, indicating that substrate anisotropy can be utilized as a tool to guide cell division behavior. This has important implications for developmental biology, where oriented cell divisions play a critical role in shaping tissue development (e.g. neural crest).

3.5 Conclusions

ACT*IV*E analysis was successfully employed to tease out subtle differences in cell motility behavior atop anisotropic and isotropic surfaces at multiple cell densities. While directed motility has previously been observed on substrates with surface anisotropy, the large data sets generated by ACT*IV*E enabled the application of statistical physics techniques that require "big data" to reliably draw conclusions. These metrics included mean squared displacement, velocity autocorrelation analysis, diffusion characteristics, and asphericity calculations. Surprisingly, we demonstrated that mean squared displacement behavior follows the same functional form, regardless of surface topography type or cell density, and that this behavior remains superdiffusive over long timescales. After decomposing MSD and velocity autocorrelation behavior, we were able to prove quantitatively that cells on wrinkled substrates demonstrated a preferential movement direction (parallel to the direction of anisotropy) whereas cells on non-wrinkled and TCPS surfaces demonstrated similar x and y motility dynamics. This trend was qualitatively confirmed through trajectory and diffusion plotting. Interestingly, a significant difference was seen for the asphericity of cells on all surfaces, indicating that cell motility dynamics rely on both surface topography and cell-ECM interactions. Finally, ACT*IV*E enabled us to track cell division behavior, demonstrating that division directionality could be guided by the presence of surface topography. These findings demonstrate that ACT*IV*E can be applied to improve understanding of developmental biology, biophysical phenomenon, cell-material interface design, mechanisms guiding cell homing, and tissue engineering applications.

3.6 References

1. Adams, J.C. and F.M. Watt, *Regulation of development and differentiation by the extracellular matrix.* Development, 1993. **117**(4): p. 1183-1198.
2. Rozario, T. and D.W. DeSimone, *The extracellular matrix in development and morphogenesis: A dynamic view.* Developmental Biology, 2010. **341**(1): p. 126-140.

3. Olczyk, P., Ł. Mencner, and K. Komosinska-Vassev, *The role of the extracellular matrix components in cutaneous wound healing.* BioMed research international, 2014. **2014**.
4. Friedl, P. and D. Gilmour, *Collective cell migration in morphogenesis, regeneration and cancer.* Nature Reviews Molecular Cell Biology, 2009. **10**(7): p. 445-457.
5. Cox, T.R. and J.T. Erler, *Remodeling and homeostasis of the extracellular matrix: Implications for fibrotic diseases and cancer.* DMM Disease Models and Mechanisms, 2011. **4**(2): p. 165-178.
6. Jaalouk, D.E. and J. Lammerding, *Mechanotransduction gone awry.* Nature Reviews Molecular Cell Biology, 2009. **10**(1): p. 63-73.
7. Paszek, M.J. and V.M. Weaver, *The tension mounts: Mechanics meets morphogenesis and malignancy.* Journal of Mammary Gland Biology and Neoplasia, 2004. **9**(4): p. 325-342.
8. Frantz, C., K.M. Stewart, and V.M. Weaver, *The extracellular matrix at a glance.* Journal of Cell Science, 2010. **123**(24): p. 4195-4200.
9. Discher, D.E., P. Janmey, and Y.L. Wang, *Tissue cells feel and respond to the stiffness of their substrate.* Science, 2005. **310**(5751): p. 1139-1143.
10. Chua, I.L.S., H.W. Kim, and J.H. Lee, *Signaling of extracellular matrices for tissue regeneration and therapeutics.* Tissue Engineering and Regenerative Medicine, 2016. **13**(1): p. 1-12.
11. Haeger, A., et al., *Collective cell migration: Guidance principles and hierarchies.* Trends in Cell Biology, 2015. **25**(9): p. 556-566.
12. Engler, A.J., et al., *Matrix elasticity directs stem cell lineage specification.* Cell, 2006. **126**(4): p. 677-689.

13. Stevens, M.M. and J.H. George, *Exploring and Engineering the Cell Surface Interface.* Science, 2005. **310**(5751): p. 1135-1138.
14. Lutolf, M.P. and J.A. Hubbell, *Synthetic biomaterials as instructive extracellular microenvironments for morphogenesis in tissue engineering.* Nature Biotechnology, 2005. **23**(1): p. 47-55.
15. Teixeira, A.I., P.F. Nealey, and C.J. Murphy, *Responses of human keratocytes to micro- and nanostructured substrates.* Journal of Biomedical Materials Research - Part A, 2004. **71**(3): p. 369-376.
16. Han, L., et al., *Unidirectional migration of single smooth muscle cells under the synergetic effects of gradient swelling cue and parallel groove patterns.* Colloids and Surfaces B: Biointerfaces, 2013. **111**: p. 1-6.
17. Kim, D.H., et al., *Mechanosensitivity of fibroblast cell shape and movement to anisotropic substratum topography gradients.* Biomaterials, 2009. **30**(29): p. 5433-5444.
18. Kandere-Grzybowska, K., et al., *Short-term molecular polarization of cells on symmetric and asymmetric micropatterns.* Soft Matter, 2010. **6**(14): p. 3257-3268.
19. Fraley, S.I., et al., *Three-dimensional matrix fiber alignment modulates cell migration and MT1-MMP utility by spatially and temporally directing protrusions.* Scientific Reports, 2015. **5**.
20. Miron-Mendoza, M., J. Seemann, and F. Grinnell, *The differential regulation of cell motile activity through matrix stiffness and porosity in three dimensional collagen matrices.* Biomaterials, 2010. **31**(25): p. 6425-6435.

21. Kim, D.H., et al., *Guided Cell Migration on Microtextured Substrates with Variable Local Density and Anisotropy.* Adv Funct Mater, 2009. **19**(10): p. 1579-1586.
22. Li, L., et al., *The use of hyaluronan to regulate protein adsorption and cell infiltration in nanofibrous scaffolds.* Biomaterials, 2012. **33**(12): p. 3428-3445.
23. Berry, C.C., et al., *The influence of microscale topography on fibroblast attachment and motility.* Biomaterials, 2004. **25**(26): p. 5781-5788.
24. Rajnicek, A.M., L.E. Foubister, and C.D. McCaig, *Alignment of corneal and lens epithelial cells by co-operative effects of substratum topography and DC electric fields.* Biomaterials, 2008. **29**(13): p. 2082-2095.
25. Huth, J., et al., *Significantly improved precision of cell migration analysis in time-lapse video microscopy through use of a fully automated tracking system.* Bmc Cell Biology, 2010. **11**: p. 12.
26. Yang, P., et al., *In vitro wrinkle formation via shape memory dynamically aligns adherent cells.* Soft Matter, 2013. **9**(18): p. 4705-4714.
27. McQuarrie, D.A., *Statistical Mechanics*. 2003: Viva Books Private Limited.
28. Schneider, C.A., W.S. Rasband, and K.W. Eliceiri, *NIH Image to ImageJ: 25 years of image analysis.* 2012. **9**(7): p. 671-675.
29. Abràmoff, M.D., P.J. Magalhães, and S.J. Ram, *Image processing with ImageJ.* Biophotonics international, 2004. **11**(7): p. 36-42.
30. Levy, H. and F. Lessman, *Finite Difference Equations*. 1992: Dover Publications.
31. Šolc, K., *Shape of a random-flight chain.* The Journal of Chemical Physics, 1971. **55**(1): p. 335-344.

32. Davidson, P., et al., *Definition of a simple statistical parameter for the quantification of orientation in two dimensions: Application to cells on grooves of nanometric depths.* Acta Biomaterialia, 2010. **6**(7): p. 2590-2598.
33. Puliafito, A., et al., *Collective and single cell behavior in epithelial contact inhibition.* Proceedings of the National Academy of Sciences of the United States of America, 2012. **109**(3): p. 739-744.
34. Wu, P.H., et al., *Three-dimensional cell migration does not follow a random walk.* (1091-6490 (Electronic)).
35. Rudnick, J. and G. Gaspari, *The asphericity of random walks.* Journal of Physics A: Mathematical and General, 1986. **19**(4): p. L191-L193.
36. Wolf, K., et al., *Multi-step pericellular proteolysis controls the transition from individual to collective cancer cell invasion.* Nature Cell Biology, 2007. **9**(8): p. 893-904.
37. Amatangelo, M.D., et al., *Stroma-derived three-dimensional matrices are necessary and sufficient to promote desmoplastic differentiation of normal fibroblasts.* American Journal of Pathology, 2005. **167**(2): p. 475-488.
38. Gaggioli, C., et al., *Fibroblast-led collective invasion of carcinoma cells with differing roles for RhoGTPases in leading and following cells.* Nature Cell Biology, 2007. **9**(12): p. 1392-U92.
39. Paňková, K., et al., *The molecular mechanisms of transition between mesenchymal and amoeboid invasiveness in tumor cells.* Cellular and Molecular Life Sciences, 2010. **67**(1): p. 63-71.

40. Friedl, P. and K. Wolf, *Tumour-cell invasion and migration: Diversity and escape mechanisms.* Nature Reviews Cancer, 2003. **3**(5): p. 362-374.

Table 3-1: Average number of cells identified by ACT*IV*E for each substrate and density type.

Density (cells/cm^2)	*Material*	Average Number of Cells Segmented in First Frame	Average Number of Cells Segmented in Last Frame	Average Total Number of Cells Identified Over All Frames
5,000	*W*	327 ± 118	344 ± 171	760 ± 347
	NW	278 ± 61	308 ± 56	716 ± 112
	TCPS	405 ± 260	348 ± 213	956 ± 650
10,000	*W*	611 ± 145	597 ± 152	1196 ± 465
	NW	662 ± 130	590 ± 88	1519 ± 480
	TCPS	725 ± 239	636 ± 217	1558 ± 586
20,000	*W*	898 ± 389	746 ± 234	1627 ± 729
	NW	869 ± 316	652 ± 150	1943 ± 1164
	TCPS	1097 ± 347	780 ± 137	2670 ± 989

Comparison of the number of cells segmented by ACT*IV*E in the first and last video frames, as well as the average number of cells identified over all frames for each seeding density tested. Cell number increases with each cell seeding density, coupled with an increase in the standard deviation associated with the number of cells identified.

Table 3-2: Average MSD slope and mobility parameters for wrinkled, non-wrinkled and TCPS substrates

Substrate Type	**Short Timescale Slope**	**Long Timescale Slope**	**δ**
W	1.67[a] (0.09)	1.32[a] (0.13)	0.45 (0.52)
NW	1.53[a] (0.13)	1.32[b] (0.11)	0.18 (0.51)
TCPS	1.56 (0.16)	1.21[a,b] (0.12)	0.58 (0.59)

Average slopes and mobility parameters of non-decomposed MSD behavior on W, NW, and TCPS substrates. Standard deviations are listed in parentheses. For each metric, statistical comparisons were made between substrate types (e.g. W versus NW, W versus TCPS, etc.). Substrates sharing the same label (a, b) within a column were identified as statistically different from one another. No label indicates no statistically significant differences.

Table 3-3: Average decomposed MSD slope and mobility parameters for wrinkled, non-wrinkled and TCPS substrates.

Substrate Type	**X-Short Timescale Slope**	**X-Long Timescale Slope**	**X-δ**	**Y-Short Timescale Slope**	**Y-Long Timescale Slope**	**Y-δ**
W	$1.71^{a,b}$ (0.09)	1.33 (0.13)	0.37 (0.54)	1.52 (0.11)	1.23 (0.09)	-0.25 (0.42)
NW	1.53^{a} (0.12)	1.34^{a} (0.12)	-0.16 (0.55)	1.53 (0.14)	1.28 (0.12)	-0.07 (0.48)
TCPS	1.56^{b} (0.16)	1.21^{a} (0.15)	0.27 (0.60)	1.56 (0.16)	1.20 (0.12)	0.31 (0.65)

Average slopes and mobility parameters of decomposed MSD behavior on W, NW, and TCPS substrates. Standard deviations are listed in parentheses. Prior to analysis, the x-axis was rotated to align to the wrinkle direction, where appropriate. For each metric, statistical comparisons were made between substrate types (e.g. W versus NW, W versus TCPS, etc.). Substrates sharing the same label (a, b) within a column were identified as statistically different from one another. No label indicates no statistically significant differences.

Table 3-4: Average velocity autocorrelation rate constants for wrinkled, non-wrinkled and TCPS substrates.

Substrate Type	**X Rate Constant x 10^{-3} (min^{-1})**	**Y Rate Constant x 10^{-3} (min^{-1})**
W	4.85^{a} (1.29)	$9.99^{a,b}$ (3.24)
NW	5.79^{b} (1.31)	6.49^{a} (1.94)
TCPS	$8.35^{a,b}$ (2.04)	7.88^{b} (2.35)

Average decay constants for exponential fits to the velocity autocorrelation function for W, NW, and TCPS substrates. Similar to decomposed MSD, the x-axis was initially rotated to align parallel to the wrinkle direction, where appropriate. Standard deviations are reported in parentheses. For each metric, statistical comparisons were made between substrate types (e.g. W versus NW, W versus TCPS, etc.). Substrates sharing the same label (a, b) within a column were identified as statistically different from one another. No label indicates no statistically significant differences.

Table 3-5: Average asphericity measurements for wrinkled, non-wrinkled and TCPS substrates.

Substrate Type	**Asphericity**
W	$0.85^{a,b}$ (0.02)
NW	$0.81^{a,c}$ (0.02)
TCPS	$0.77^{b,c}$ (0.02)

Average asphericity measurements of cell tracks on W, NW, and TCPS substrate. Standard deviations are reported in parentheses. For each metric, statistical comparisons were made between substrate types (e.g. W versus NW, W versus TCPS, etc.). Substrates sharing the same label (a, b, c) were identified as statistically different from one another. No label indicates no statistically significant differences.

Table 3-6: Average angular spread of division angles on wrinkled, non-wrinkled, and TCPS surfaces.

	Wrinkled	**Non-Wrinkled**	**TCPS**
Angular Spread (°)	41.0 ± 3.7[a,b]	47.3 ± 3.1[a]	48.5 ± 2.9[b]

Average angular spread values were calculated for wrinkled, non-wrinkled, and TCPS materials. The average angular spread was lower on anisotropic surfaces when compared to the isotropic counterparts, indicating that cells divided parallel to the wrinkle direction in anisotropic environments, but had no preferential division direction for isotropic environments. Substrates sharing the same label (a, b) were identified as statistically different from one another. No label indicates no statistically significant differences.

Figure 3-1: Representative micrographs of wrinkled substrates at each cell density

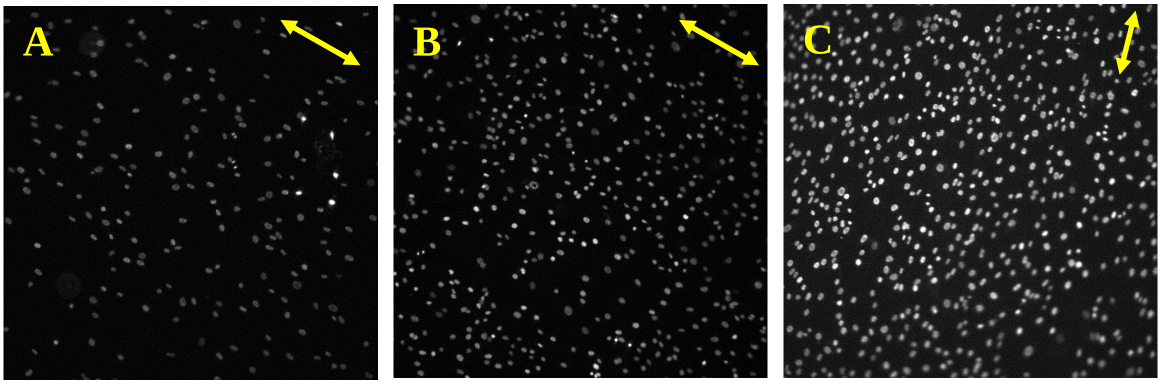

Representative fluorescent micrographs of C3H10T1/2 mouse fibroblasts seeded at A) low (5,000 cells/cm^2), B) medium (10,000 cells/cm^2), and C) high (20,000 cells/cm^2) cell densities. Cells were stained with Hoechst 33342 nuclear dye (0.01µg/mL) and image contrast was manually enhanced in ImageJ to improve cell visibility. Yellow double-headed arrows indicate wrinkle direction.

Figure 3-2: Trajectory behavior of cells on wrinkled, non-wrinkled, and TCPS surfaces

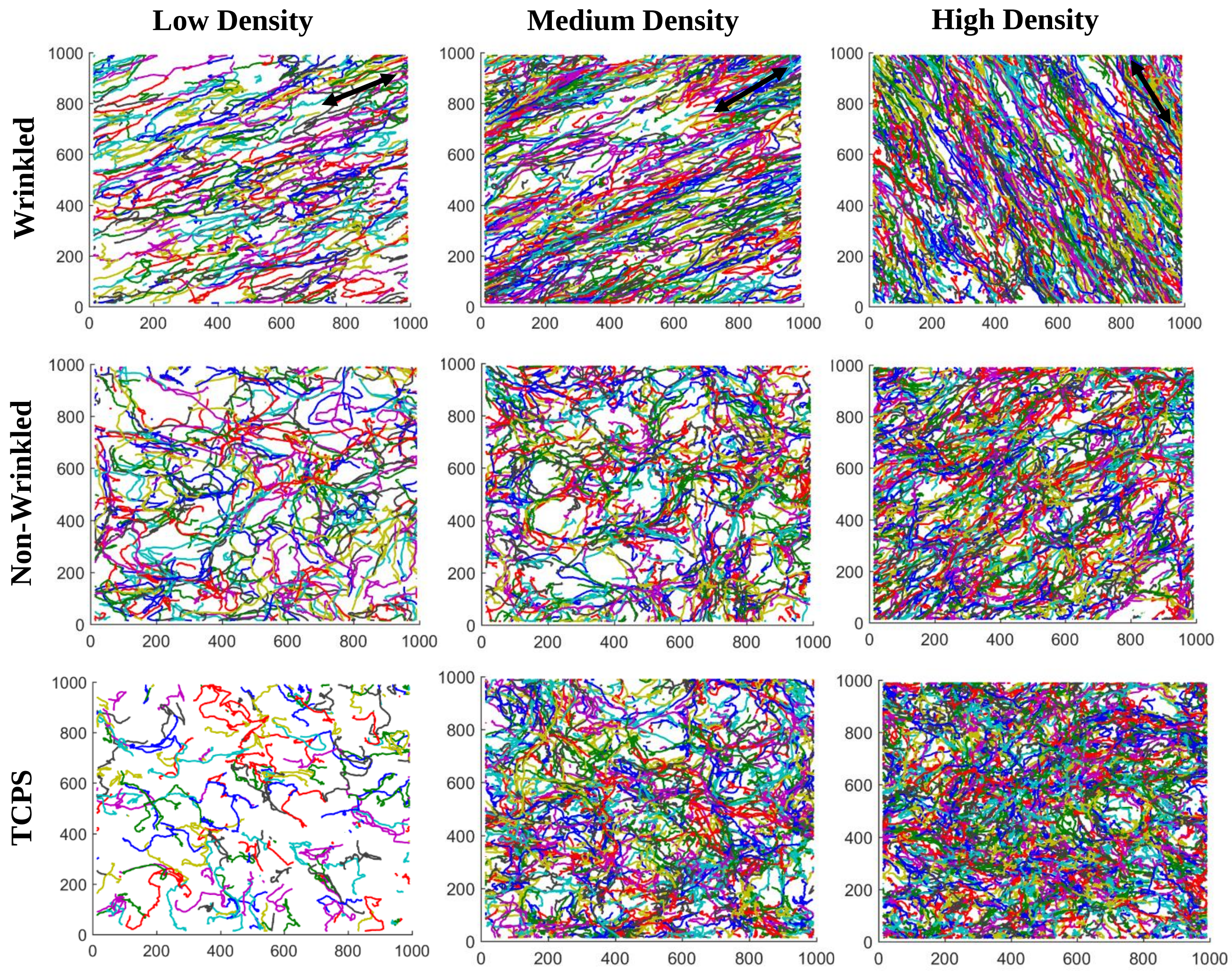

Representative cell tracks generated by ACTIVE of fibroblasts seeded on wrinkled (top), non-wrinkled (middle) and TCPS (bottom) surfaces at low (left), medium (middle), and high (right) cell densities. Qualitative analysis revealed preferential migration of cells on wrinkled surfaces (parallel to direction of anisotropy) compared to random motility of cells on non-wrinkled and TCPS surfaces. Black double headed arrows indicate direction of anisotropy, where appropriate.

Figure 3-3: Non-decomposed mean squared displacement behavior of cells on wrinkled, non-wrinkled and TCPS surfaces.

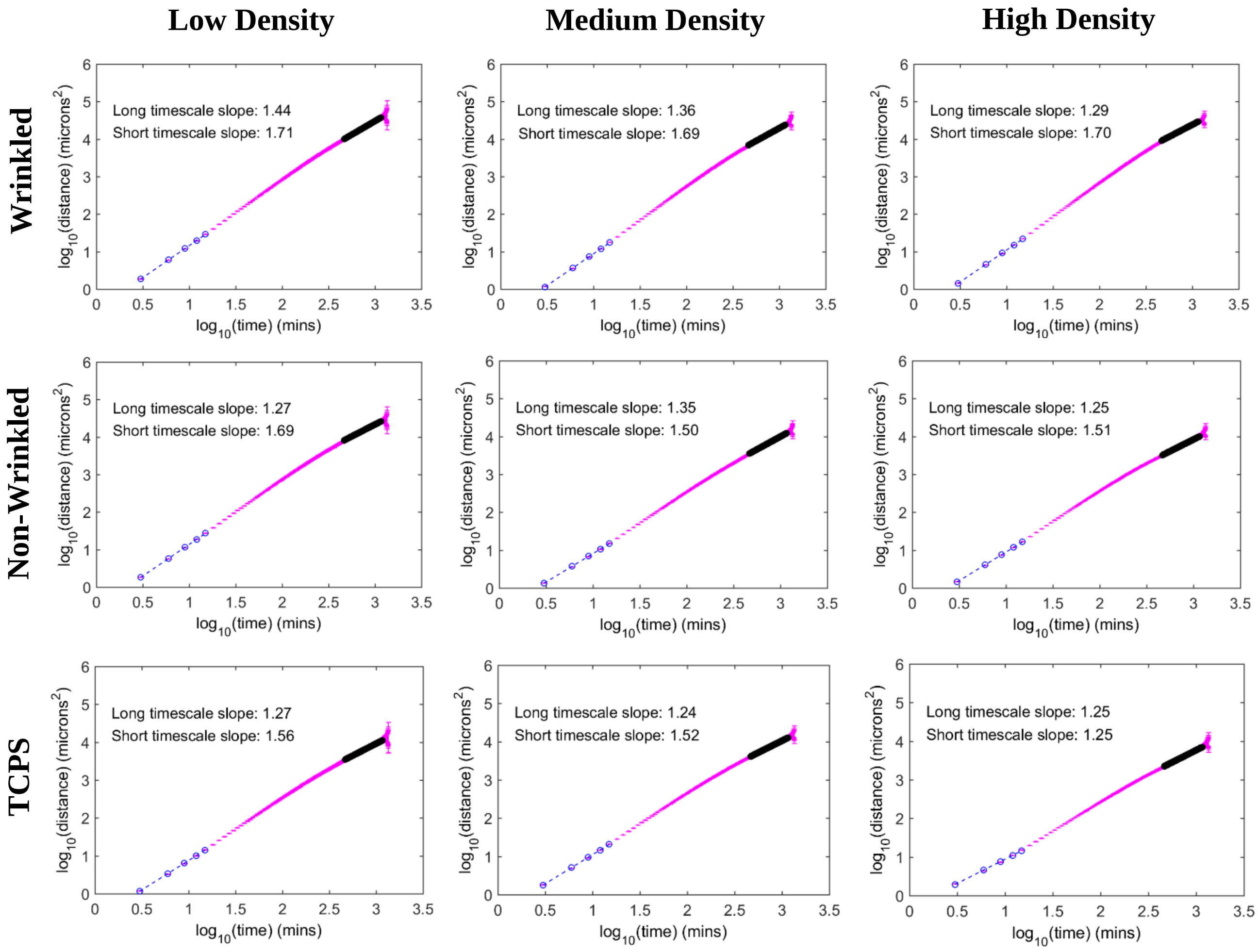

Representative mean squared displacement analyses obtained from ACT*IV*E for fibroblasts on wrinkled (top), non-wrinkled (middle) and TCPS (bottom) surfaces at low (left), medium (middle), and high (right) cell densities. A linear fit was applied to the first five Δt intervals (blue empty circles) and the final 60 Δt intervals were disregarded to assess short and long timescale (filled black circles) cell behaviors respectively. Surprisingly, analysis of non-decomposed MSD revealed that cell motility followed the same functional form at long timescales, irrespective of substrate type or cell density.

Figure 3-4: Decomposed mean squared displacement behavior of cells on wrinkled, non-wrinkled and TCPS surfaces.

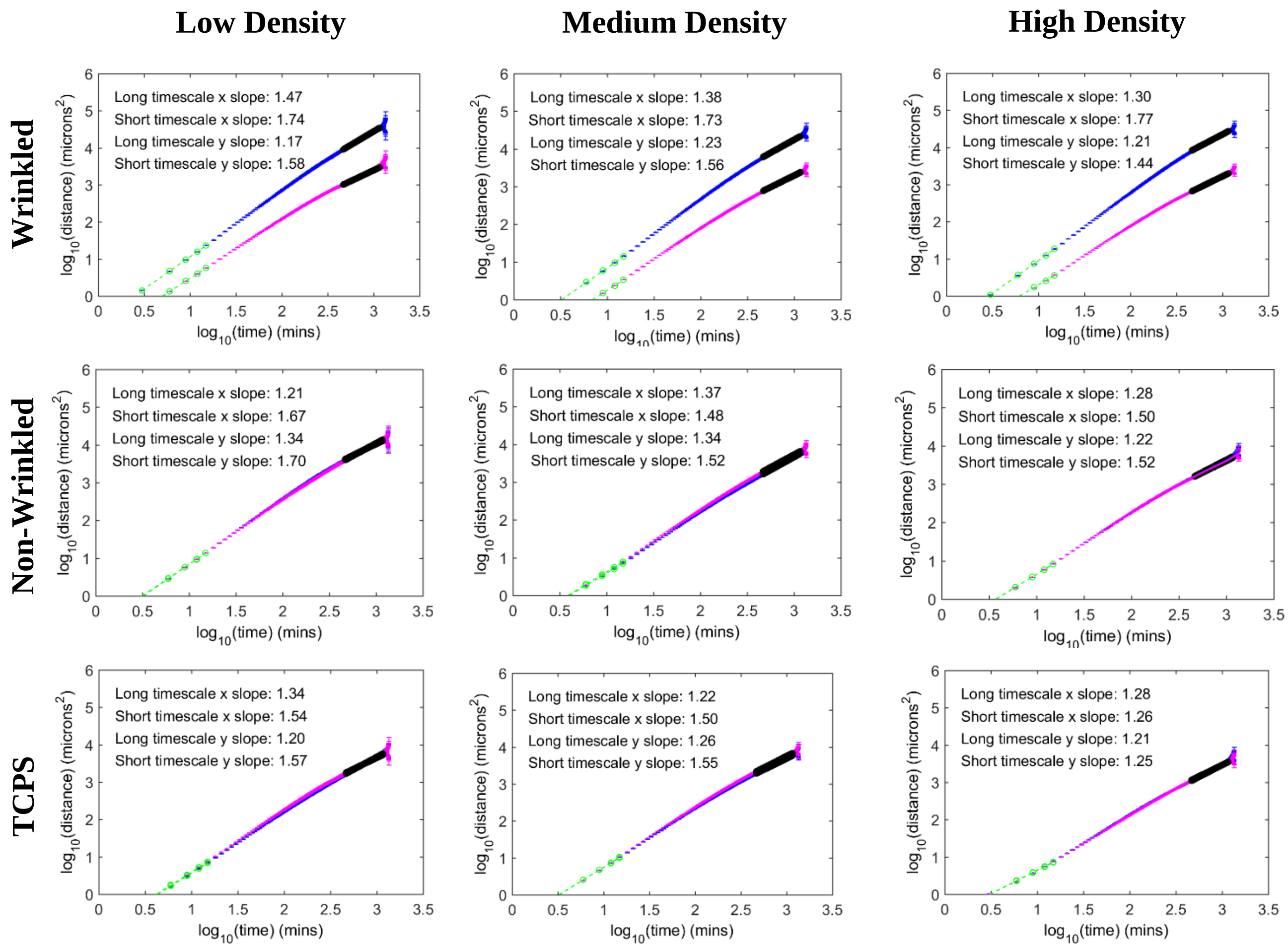

Representative decomposed mean squared displacement analyses obtained from ACT*IV*E for fibroblasts on wrinkled (top), non-wrinkled (middle) and TCPS (bottom) surfaces at low (left), medium (middle), and high (right) cell densities. A clear separation of x (parallel to anisotropy, where appropriate) and y (perpendicular to anisotropy, where appropriate) behaviors was consistently seen atop W substrates, whereas x and y behaviors consistently overlapped on NW and TCPS substrates demonstrating that cells preferentially migrate along the wrinkle direction for anisotropic surfaces.

Figure 3-5: Velocity autocorrelation behavior of cells on wrinkled, non-wrinkled and TCPS surfaces.

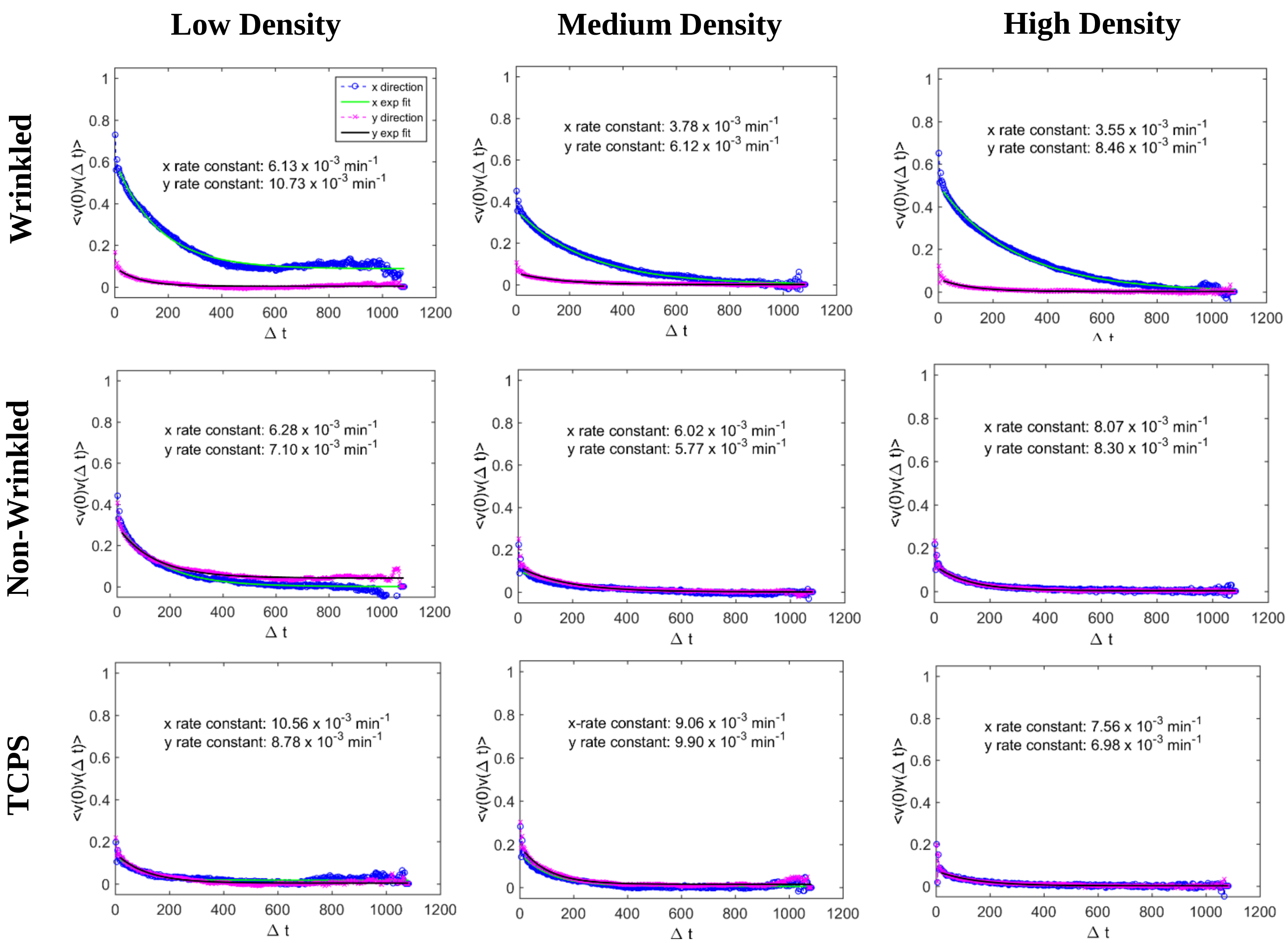

Representative decomposed velocity autocorrelation analyses obtained from ACT*IV*E for fibroblasts on wrinkled (top), non-wrinkled (middle) and TCPS (bottom) surfaces at low (left), medium (middle), and high (right) cell densities. A clear separation of x (parallel to anisotropy, where appropriate) and y (perpendicular to anisotropy, where appropriate) behaviors was consistently seen atop W substrates, whereas x and y behaviors consistently overlapped on NW and TCPS substrates demonstrating that cells preferentially migrate along the wrinkle direction for anisotropic surfaces.

Figure 3-6: Diffusion behavior of cells on wrinkled, non-wrinkled and TCPS surfaces.

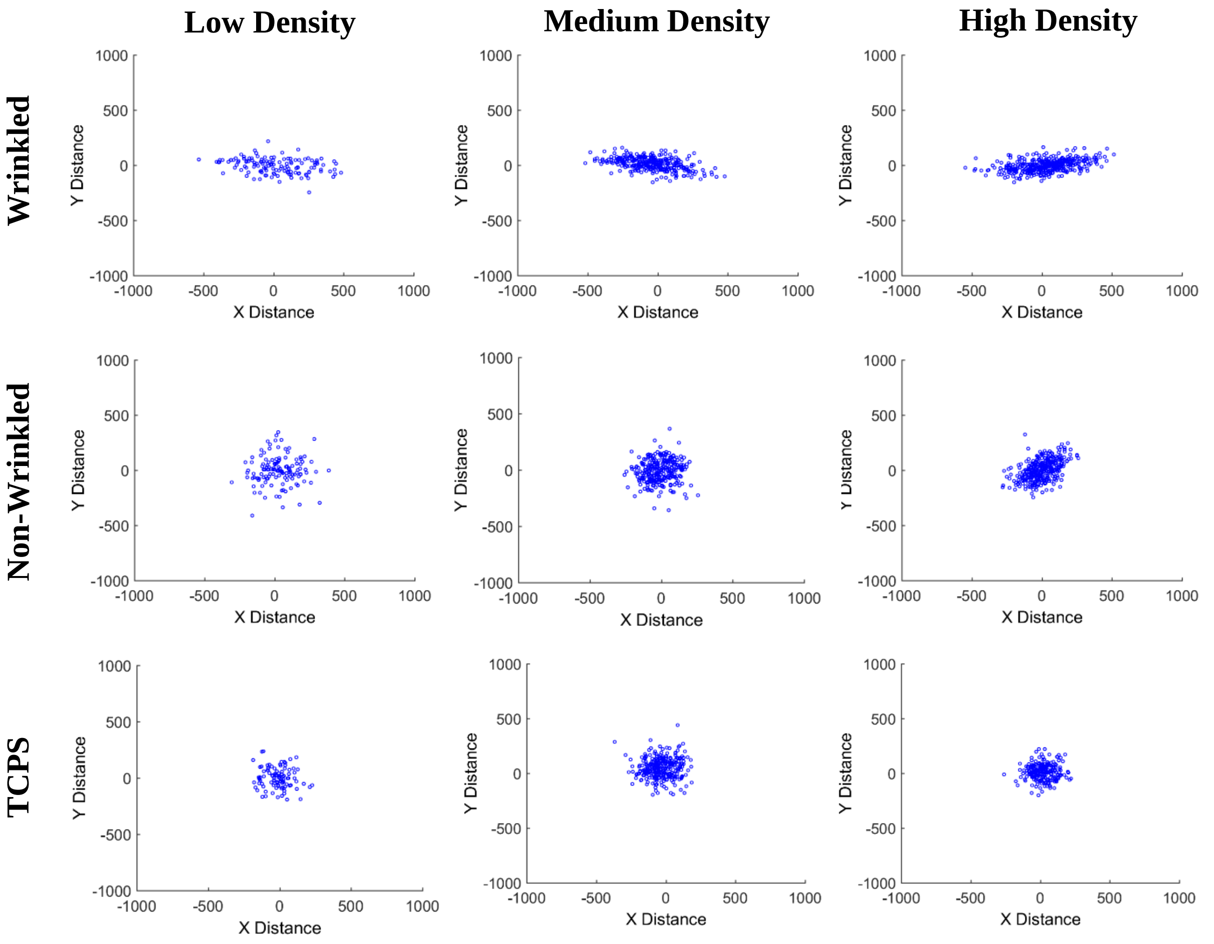

Representative diffusion plots obtained from ACT*IV*E after 24 hours for fibroblasts on wrinkled (top), non-wrinkled (middle) and TCPS (bottom) surfaces at low (left), medium (middle), and high (right) cell densities. The x-axis was rotated to align with the direction of anisotropy, where appropriate. Cells on wrinkled substrates moved primarily along the direction of anisotropy, depicted by the elongation of track behavior along the x-axis. For non-wrinkled and TCPS substrates, the diffusion distribution was instead radial, indicating no preferential motility direction for the isotropic materials.

Figure 3-7: Gyration tensor behavior of cells on wrinkled, non-wrinkled and TCPS surfaces.

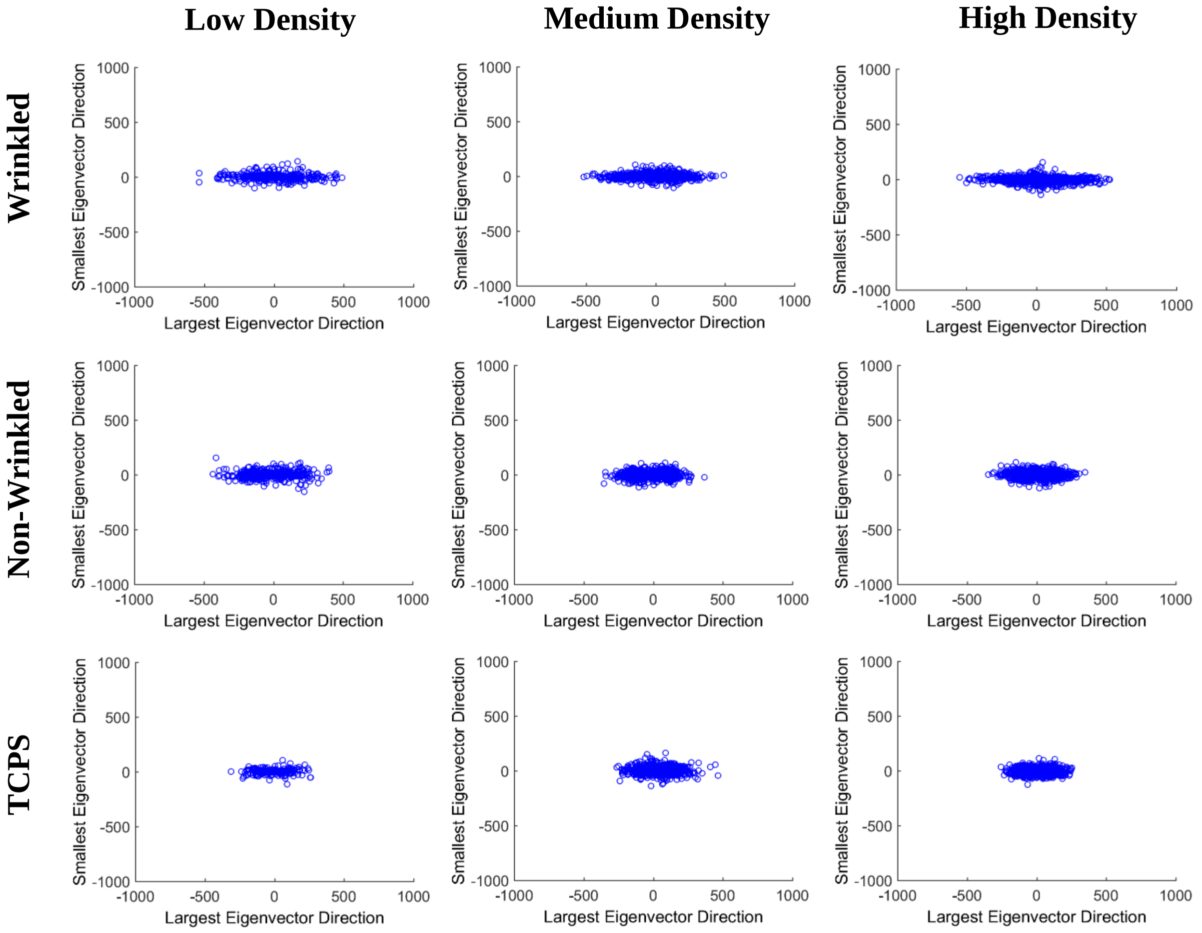

Representative gyration tensor plots obtained from ACT*IV*E for fibroblast motility on wrinkled (top), non-wrinkled (middle) and TCPS (bottom) surfaces at low (left), medium (middle), and high (right) cell densities. The largest eigenvector was plotted along the x-axis to visualize differences in cell asphericity. Wrinkled substrates had the largest asphericity, followed by non-wrinkled and then TCPS substrates. No significant difference was seen with respect to density across groups.

Figure 3-8: Division angle analysis on wrinkled, non-wrinkled, and TCPS surfaces.

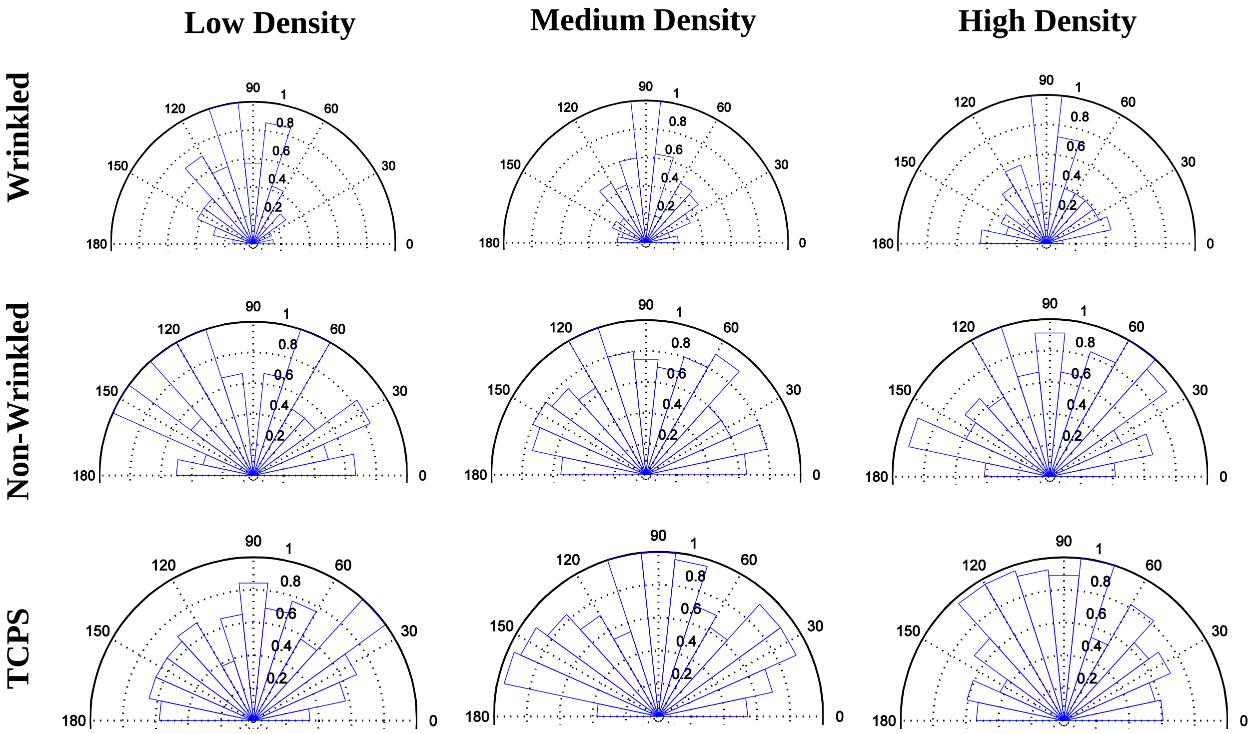

Division directionality on wrinkled (top), non-wrinkled (middle) and TCPS (bottom) surfaces at low (left), medium (middle), and high (right) cell densities, oriented divisions (parallel to the wrinkle direction) were observed atop wrinkled substrates. This is depicted by the narrow distribution of division angles centered around 90°. Comparatively, no preferential division directionality was observed on NW and TCPS substrates, depicted by the broad distribution in division angles ranging from 0° to 180°.

Chapter 4: Active Surface Wrinkling Alters Cell Motility Responses

4.1 Synopsis

Variations in a cell's local microenvironment can critically affect cell behavioral responses observed *in vitro*, such as cell orientation, polarization and motility. Static, anisotropic synthetic platforms have widely been used to demonstrate this effect, due to their ability to alter cell motility directionality and speed via topographical cues. Likewise, mechanical actuation of a cell's local microenvironment has separately been shown to alter cell adhesive, alignment, and motility responses. In this chapter, we sought to manipulate the cellular microenvironment via a developing topography, which could potentially be employed to direct and control cell motility dynamics. We utilized the shape memory functionality of the material system introduced in **Chapter 3** as a means to induce this local change. Here, we demonstrate that a nanotopographical transition of a cell's local microenvironment can elicit a change in cell motility directionality and nuclear orientation and further identify that pre-conditioning of the microenvironment hinders changes in expected cell velocity responses, potentially due to prior extracellular matrix (ECM) protein deposition.

4.2 Introduction: Topographical Features and Mechanical Stimulation Influence Cell Motility

Surface patterning is one of the most widely used techniques to regulate cell morphology, polarization, and motility responses *in vitro*. Nano- and microscopic grooves and channels have widely been used to study cell-ECM interactions in two-dimensions, with more recent emphasis on variations in three dimensional architectural designs [1]. For example, Kim and colleagues demonstrated that fibroblasts can sense nano- and microscopic gradients in channel features, altering cell migration directionality and speed via topographical cues [2]. Similar analyses have shown that swelling of grooved designs, [3], asymmetric pattern distributions [4], and density [5] and wavelength [6] gradients alter cell motility responses. At the intracellular level, protein patterning [7] and nano-features [8] have separately been shown to direct cell polarity responses which can, in turn, impact cell motility dynamics. Clearly, surface patterning is a powerful tool that can be used to manipulate cell motility responses in synthetic microenvironments.

Separate from topographical cues, mechanical stimulation (e.g., uniaxial stretching or changes in substrate stiffness) of a cell's local environment has emerged as an important field to elucidate mechanisms guiding cell reorganization and motility responses. Mechanical stimulation is a process commonly used *in vivo* to guide tissue homeostasis, locally homing cells to perform a specific role within their microenvironment. *In vitro*, uniaxial stretching [9, 10] and strain responsive materials [11] have been used to align cell morphology, while stiffness gradients [12, 13] have been employed to guide cell motility responses. More recently, we [14-17] and others [18-22] have utilized shape memory polymers (SMPs) to investigate how dynamically altering a cell's topographical or architectural surroundings influences cell morphology, alignment, and nuclear orientation in two- and three-dimensions. In this chapter we expand this SMP based approach to temporally analyze cell motility responses to a topographical surface transition. Unlike previous studies that focus on fixed time-points before or after the environmental change, this surface alteration was triggered to characterize cell motility dynamics *before, during,* and *after* a change in the cellular microenvironment in real time. Successful completion of this study demonstrates the first characterization of cell motility behavior during an SMP triggered topographical change, elucidating new mechanisms associated with dynamic reorganization of ECM that cells experience *in vivo*.

4.3 Experimental Design: Time-Lapse Imaging and Video Analysis of Cells on an Actively Wrinkling Surface

4.3.1 Substrate Preparation

Tert-butyl acrylate, butyl acrylate (*t*BA:BA) SMPs were prepared as previously reported [16]. 95:5 wt% *t*BA:BA films were fabricated using 5 wt% tetraethylene glycol dimethacrylate as a cross-linker and 0.06 wt% 2,2-dimethoxy-2-phenylacetophenone as initiator. Samples were extracted in a 1:1 methanol:distilled water solutions for 6 hours and then dried for 1 day in a 40°C vacuum oven prior to use. SMP films (T_g = ~37°C, hydrated) were processed in one of three ways: 1) as static flat controls (hereafter referred to as static non-wrinkled), 2) as static anisotropic controls (hereafter referred to as static wrinkled), or 3) as the active wrinkling experimental group (hereafter referred to as active wrinkling). Static non-wrinkled samples were cut into 6x6 mm squares using an 80°C hotplate. Static wrinkled and active wrinkling films were strained 7% in an

80°C isothermal oven for 10 minutes and subsequently cooled at -4°C for 5 minutes to fix in the strain. Wrinkled and active groups were then cut into 6x6 mm squares using a hammer and razorblade (no heat could be applied to cut samples). All static wrinkled, static non-wrinkled and active wrinkling samples were then sputter coated with gold for 100 seconds (15 second intervals with 15 second breaks to ensure samples did not heat prematurely) resulting in an approximately 33nm thick gold coating deposited on the material surface. Static wrinkled substrates were then recovered for 2 hours at 60°C, resulting in a nanotopographic pattern with features on the order of 400 nm in amplitude and 1-5 μm in wavelength [16]. All three substrate groups were then UV sterilized for one hour on each side in a biological safety cabinet (ThermoFisher, 1300 Series A2) for subsequent cell culture.

4.3.2 Cell Seeding and Culture Conditions

C3H10T1/2 mouse fibroblast cells (ATCC) were cultured in Basal Medium Eagle (BME) complete growth medium supplemented with 10% fetal bovine serum (FBS, v/v), 1% penicillin/streptomycin (v/v) and 1% GlutaMax (v/v). Cells were expanded in a 37°C humidified incubator with regulated 5% CO_2 and passaged at 80% confluence using 0.25% Trypsin EDTA. For time-lapse experiments, cells were restricted to passage numbers 11-16. Prior to seeding, static wrinkled, static non-wrinkled, and active wrinkling samples were soaked in BME medium for 2 hours to promote FBS protein adsorption on the material surface. Solutions of 4000 cells/cm^2 were then prepared. Each sample was transferred to an individual well in a 48-well plate and cells were solution seeded onto material surfaces. Cells were then incubated at 30°C for 16 hours to establish equilibrium prior to time-lapse image set-up.

4.3.3 Live-cell Nuclear Staining and Time-Lapse Imaging

Hoechst nuclear stain was prepared at a concentration of 0.01µg/mL in BME complete medium. The selected concentration was one order of magnitude below the manufacturer's recommended range, but was deliberately selected to ensure normal cell divisions (see **Chapter 3**, Section 3.3). 800uL of the staining solution was added to each well of a 4-well LabTek borosilicate chamber slide (Fisher Scientific). Static wrinkled, static non-wrinkled, and active wrinkling samples were then transferred into chamber slides and incubated at 30°C for one hour. Samples were then inverted and weighed down with a sterilized glass slide, cut to fit into the chamber wells. The chamber slide was transferred to a live cell stage incubator (INC-2000, 20/20 Technology, Inc.) and cells were imaged using a Leica DMI 6000B inverted microscope. The live cell stage incubator was equilibrated at 30°C with constant 5% CO_2. Five slice z-stack images were captured every five minutes in phase and A4 (excitation/emission peak of 360/470 nm) using 10 ms and 75 ms exposure times respectively on an Andor Luca R camera with a 10x/0.63 NA objective. After 8 hrs of imaging at 30°C, the temperature was increased to 37°C, triggering recovery in the active wrinkling group. Cells were then imaged for another 16 hours. Frame by frame z-stacks were compressed using an extended depth of field plugin [23] and compiled into a final tiff stack for processing. The resultant cell behavior was then characterized using the automated contour-based tracking for *in vitro* environments (ACT*IV*E) system [24] previously described in **Chapters 2 and 3**.

4.3.4 Characterizing Cell Motility

Careful consideration was required when analyzing cell motility behaviors in actively wrinkling microenvironments. Batch to batch kinetic variability, delayed heating in the time-lapse stage incubator set-up due to thermal transfer considerations, and the potential lag time between material and cell responses were all considered when establishing time frames for quantifying cell motility behaviors. Due to these factors, ACT*IV*E analysis was limited to cell trajectory plotting, diffusion dynamics, mean squared displacement assessment during equilibrium regimes, cell velocity comparisons, nuclear alignment characterization, and quantification of nuclear angular distributions.

4.3.4.1 Video Processing

ACT*IV*E was developed to analyze motility behaviors of adherent cell populations subject to nuclear staining, infection, or transfection [24]. Therefore, only the nuclear channel (A4) of the obtained time-lapse videos was analyzed by ACT*IV*E in this study. Overlays of phase and nuclear images revealed that cell nuclear behavior closely followed cell body dynamics in all three microenvironments, justifying nuclear processing (Figure 4-1). Nuclear videos were compiled into four different formats: 1) a 20 hr imaging duration including both the 30°C and 37°C environment, 2) a 6 hr pre-trigger portion where cells were only exposed to the 30°C microenvironment, 3) an 8 hr transitional region directly after the temperature increase to 37°C, and 4) a 6 hr post-trigger portion after the full material transition where the cells were in equilibrium at 37°C. The first 2 hrs of the 24 hr video were removed, due to poor signal to noise ratios in the 30°C environment. We hypothesize that Hoechst uptake was poor during the first 2 hrs due to temperature sensitivity, a principle previously described by Zhao and colleagues [25]. To accurately compare an equivalent time frame to the 30°C equilibrium videos (#2 above), the last 2 hrs of the post-trigger (#4 above) and full videos (#1 above) were also removed.

4.3.4.2 Cell Trajectory and Diffusion Plotting

Cell trajectories and diffusion behaviors were plotted using the same protocols described in **Chapter 3**, Section 3. Nuclear center of mass values were calculated and recorded for all cells in each video frame using ACT*IV*E's contour-based intensity segmentation system. Each cell was assigned a colored trajectory and displacement information was plotted for all frames where cells were present. All cell trajectory information was plotted on the same set of axes to visualize collective behaviors. For diffusion plotting, track information was initially renormalized to the same starting location (the origin). Net displacement was then calculated for each cell and summed across the imaging time frame. Net displacement behavior was recorded for the final frame and visualized to determine directional distribution. Where appropriate, the x-axis was rotated to align parallel to the direction of anisotropy.

4.3.4.3 Mean Squared Displacement

Mean squared displacement (MSD) was calculated as defined in **Chapter 3**:

$$MSD(\Delta t) = \sum_{i=1}^{N} \frac{([r(t+\Delta t) - r(t)]^2)}{N} \tag{Eq. 4-1}$$

where r was the [x,y] distance at a specific time point, Δt represented the time interval of interest and N signified the total number of cells analyzed [26]. Decomposed MSD was calculated in the x- and y-direction for each Δt and then plotted on a $\log_{10}$ Δt versus $\log_{10}$ MSD scale for each substrate type. In the decomposed case, the x-axis was rotated to align with the direction of anisotropy. Wrinkle direction was measured from the horizontal in phase contrast images using ImageJ [27, 28]. Once MSD information was plotted, a linear fit was applied to short and long timescale MSD data to compare cell motility behavior. The short timescale fit was based on the first five Δt intervals, whereas the long timescale fit was standardized to minimize fluctuations in the standard deviation at large Δt intervals. For this work, the upper 36 Δt intervals were disregarded for the long timescale fit. For MSD slope comparisons, a value of one represented diffusive ('random walk') motility while a value of two represented ballistic migration, where cells persist in a single direction at a constant velocity.

4.3.4.4 Cell Velocity Analysis

For each time-point, cell velocities were calculated in x- and y-directions using the central finite difference approximation with an accuracy value of two [29]. An overall average cell velocity per video was then calculated as:

$$\frac{\sum\left(\frac{\sum abs(v_f)}{n}\right)}{t} \qquad \text{(Eq. 4-2)}$$

where v_f = velocity value for a single cell in a single frame, n = number of cells in a single frame, and t = number of frames analyzed. Cell velocity distributions with average cell velocities per frame were additionally plotted to visualize collective data trends.

4.3.4.5 Nuclear Alignment and Nuclear Angular Distributions

To quantify cell nuclear alignment over the time-lapse duration, nuclear morphology information was extracted for all cells fit with an ellipse using ACT*IV*E's segmentation system. Nuclear angle data for each frame was then individually processed to determine nuclear alignment and angular standard deviation. Where appropriate, cell angles were first normalized to the wrinkle angle. A value of 90° was then subtracted from each cell angle to adjust the angle range to [-90°, 90°], centered on 0°. The truncated standard deviation about 0° was then calculated to yield the angular spread [30]. The reference angle was then incremented by 1°, calculating a new truncated standard deviation. This process was repeated until a reference angle of 180° was achieved. To normalize between topographical features, the reference angle that yielded the highest degree of alignment (which coupled with the lowest standard deviation) was selected as the alignment angle for comparisons. This reference angle was not always equivalent to the measured wrinkle angle, due to natural biological variability. The truncated standard deviation, or angular spread, was also recorded to compare the degree of alignment of cell nuclei during the active wrinkling process and to compare the cell nuclei degree of alignment substrate to substrate. For the angular spread, a random distribution of cell nuclei angles would generate a standard deviation of 52°, while perfect alignment would generate a standard deviation of 0°. Therefore, a smaller value for angular spread indicates more highly aligned cell nuclei. Cell nuclear alignment and angular spread data were recorded for each frame and plotted over the video duration to visualize collective trends.

4.3.5 Statistical Analysis

One-way ANOVA tests of pre-transition, during transition, and post-transition cell velocity, nuclear alignment, and angular spread behaviors were used to compare wrinkled, non-wrinkled, and active wrinkling substrate groups. Additional comparisons of pre, during and post transition groups were conducted for each substrate type to assess potential influences of temperature on velocity trends. Significance was determined at 90% and 95% p-values.

4.4 Results: The Role of Active Surface Wrinkling in Cell Motility Behaviors

Time-lapse microscopy was used to capture cell motility data of C3H10T1/2 mouse fibroblast cells on three substrate surface types (static wrinkled, static non-wrinkled, and active wrinkling) as the cells adjusted to a temperature change from 30°C to 37°C over a 24 hr imaging duration. The temperature was altered after 8 hours of imaging at 30°C, inducing a surface change in the active wrinkling topography from flat to wrinkled. No change in surface properties was observed in the static wrinkled or non-wrinkled groups, allowing these samples to serve as controls for cell motility in each microenvironment and temperature condition. Overall, directed cell migration was noted on static wrinkled surfaces, whereas random motility was observed on static non-wrinkled surfaces. For the active wrinkling group, cells transitioned from a random to oriented motion, directly related to the developing surface topography. Similarly, nuclear orientation rearranged to correspond with the direction of motion, suggesting that this process may be involved in coordinating the directed motility response. Cell velocity demonstrated an intermediate dynamic, indicating pre-conditioning of the microenvironment by ECM proteins may complicate the velocity responses observed.

4.4.1 Cell Trajectory Data

Qualitative analysis of cell trajectory information on static wrinkled and static non-wrinkled surfaces revealed similar trends to those seen in **Chapter 3**, despite the change in temperature employed. As shown in Figure 4-2, fibroblasts on static wrinkled surfaces preferentially migrated along the direction of anisotropy, whereas fibroblasts on static non-wrinkled surfaces moved with a random orientation. Cell motility on wrinkling SMP substrates showed a change from random to directional motility accompanying the change from an isotropic to anisotropic surface topography. Directional motility of cells on substrates with anisotropy has previously been reported [31, 32]. Similarly, biomaterials with reversible strain have been shown to align cells parallel to the strain direction [11]. However, to date, this analysis has not been extended to cell motility dynamics. This study represents the first investigation of how a developing nanotopographic pattern in the cellular microenvironment directly influences cell motility responses.

4.4.2 Diffusion Characteristics

Diffusion plots were used to further characterize the spatiotemporal nature of cell motility responses. As shown in Figure 4-3, cells atop static wrinkled topographies preferentially migrated parallel to the groove direction. This trend is apparent due to the elongated distribution of cell displacements along the x-axis. Cells atop the static non-wrinkled substrates displayed no preferential directionality, as is indicated by the circular shaped diffusion distribution. For the actively wrinkling materials, cells displayed no preferential motility direction prior to the topographical transition. Once the anisotropy was introduced, the diffusive pattern elongated along the x-direction, similar to what was observed in the static wrinkled case. This distribution however, was not identical to the wrinkled case, showing some remnants of circular motility behaviors unaligned to the direction of anisotropy. We hypothesized that this effect may be due to extracellular matrix deposition prior to the topographical transition. During the initial seeding process, the cells were given 16 hrs prior to imaging to equilibrate to their surrounding microenvironment. We speculate that the fibroblasts deposited ECM proteins during this duration in a random orientation, corresponding to the flat microenvironment they were interacting with. When the wrinkled topography was triggered during imaging, remnants of this ECM deposition combatted the developing topographic cue, allowing for a more mixed diffusive pattern compared to the static wrinkled control (in which the cells only saw the wrinkle at all times).

4.4.3 Mean Squared Displacement Behavior

Mean squared displacement (MSD) calculations were the first metric used to quantitatively characterize differences in cell motility responses atop static wrinkled, static non-wrinkled, and active wrinkling substrates. MSD analysis was concentrated on portions of the time-lapse sequence where the material and cell behaviors were considered to be in equilibrium. Decomposed MSD behaviors (where x and y are parallel and perpendicular to the direction of anisotropy respectively), revealed that cell motility on static wrinkled and static non-wrinkled surfaces followed similar trends to behaviors observed in **Chapter 3**, despite the change in temperature employed. As shown in Figure 4-4, when decomposed x and y behaviors were plotted on a $\log_{10} \Delta t$ versus $\log_{10}$ MSD scale, a clear separation of x and y responses was consistently seen atop static wrinkled substrates, whereas x and y behaviors consistently overlapped on non-wrinkled materials. With respect to the actively wrinkling surfaces, a shift in MSD behavior was observed. Initially, x and y MSD behaviors overlapped prior to the topographical transition. In general, after the topographical transition occurred, cells atop the actively wrinkling microenvironment showed an increase in the separation of x and y motility dynamics. This indicated that the cells were preferentially migrating along the direction of anisotropy, responding directly to the change in their microenvironment.

4.4.4 Cell Velocity Analysis

Cell velocity was used to tease out subtle differences in motility responses prior to, during, or after the potential topographic transition in each microenvironment. Instantaneous cell velocities were calculated for x (parallel to direction of anisotropy, where appropriate), y (perpendicular to the direction of anisotropy, where appropriate) and the overall magnitude, using finite differences theorem. Cell velocities were calculated for each cell in each frame, and then averaged over conditions of interest (prior to, during, or post transition) to obtain a single velocity value per video. For samples with multiple video positions per substrate (n = 2 or 3), conditional values were first averaged across all of the positions and then averaged across all technical replicates (n = 2 or 4) to produce a single biological replicate. Three biological replicates were used to produce final average velocity values and conduct statistical analyses for substrate and conditional comparisons.

Magnitude velocity distributions were first visualized to highlight potential trends in cell motility data prior to, during, or after the potential topographic transition. As shown in Figure 4-5, the average magnitude velocity value per substrate hovered around 0.5 μm/min, regardless of substrate type or condition. Distribution patterns revealed, however, significant deviation frame to frame in cell velocity behavior. In order to understand potential underlying trends in the velocity distributions, cell velocities were further decomposed into x and y dynamics. Static wrinkled samples demonstrated, on average, a higher x-velocity compared to the static non-wrinkled samples for all conditions. These average x-velocity values, displayed in Table 4-1, were 0.39 ± 0.10 μm/min, 0.49 ± 0.15 μm/min, and 0.40 ± 0.09 μm/min for the static wrinkled cases prior to, during, or after the potential topographic transition respectively, compared to 0.24 ± 0.07 μm/min, 0.33 ± 0.10 μm/min, and 0.28 ± 0.07 μm/min for the static non-wrinkled cases prior to, during, or after the potential topographic transition respectively. Statistical analysis revealed that wrinkled and non-wrinkled x-velocity values were significantly different from one another ($p < 0.05$), confirming that cells move faster on static materials when anisotropy was present.

When considering the actively wrinkling substrates, x-velocity dynamics demonstrated an interesting trend. The average x-velocity values prior to, during, or after the topographic transition were 0.28 ± 0.08 μm/min, 0.33 ± 0.12 μm/min, and 0.29 ± 0.08 μm/min respectively (Table 4-1). These values were similar to the x-velocities observed in the static non-wrinkled microenvironment, irrespective of the developing topography. Statistical analysis revealed that the x-velocity behaviors were significantly different ($p < 0.05$) from the static wrinkled microenvironment, even after the topography had fully developed and the cells had re-equilibrated to their surroundings. This was surprising, as the cytoskeletal organization of cells appeared similar in actively wrinkling microenvironments, post transition (Figure 4-6).

Average cell velocities in the y-direction (perpendicular to the anisotropy in wrinkled and active wrinkling samples) were also calculated for each substrate and condition type. As shown in Table 4-2, y-velocity values for all substrates and conditions were relatively consistent, with no apparent trend dominating any of the groups analyzed. When statistical analyses were performed, minor trends ($p < 0.1$) in the two static materials post transition and the active wrinkling versus static non-wrinkled group during transition were observed. The only significant difference ($p < 0.05$) in y-velocity values occurred post transition between the active wrinkling and static non-wrinkled groups. This supports our hypothesis that the cells recognize the developing topography. When combined with the x-velocity results, this further suggests that the velocity behavior on the actively wrinkling materials is falling into an intermediate dynamic after the transition occurs.

Lastly, cell magnitude was assessed to quantify overall trends in the cell velocity data on each substrate type and during each condition. Static wrinkled substrates demonstrated the highest cell magnitude velocities (Table 4-3), most likely due to the increased x-velocity observed parallel to the wrinkle direction. Similar to the decomposed values, average magnitude velocities for the active wrinkling group more closely mirrored the magnitude velocity of cells in the static non-wrinkled microenvironment, regardless of topographic condition. This was again confirmed with statistics, as no significant difference in the magnitude velocity for the active wrinkling and static non-wrinkled microenvironments was observed. Interestingly, the only significant ($p < 0.05$) difference in magnitude velocity was observed in the active wrinkling versus static wrinkled case, prior to the topographic transition. Weak differences ($p < 0.1$) in the magnitude velocities were also observed during and after the topographic transition between the active wrinkling and static wrinkled microenvironment. This further supports our claim that cells adapted an intermediate velocity response (with respect to the controls) during and after the topography was introduced.

Due to concerns of misleading velocity dynamics in response to the temperature change, statistical analyses of conditional comparisons were performed for x, y, and magnitude velocity values. No significant differences in any of the static comparisons were observed, indicating that temperature was not an influential factor in the motility results produced.

4.4.5 Nuclear Alignment and Orientation Dynamics

4.4.5.1 Nuclear Alignment

Frame-by-frame nuclear alignment calculations yielded a single angle value per frame representing the angle to which, on average, the greatest number of cell nuclei in that particular frame aligned. As shown in Figure 4-7, cell nuclei were consistently oriented in the direction of anisotropy for the static wrinkled surfaces. This coupled with a relatively small standard deviation in the nuclear angle of alignment. When comparing the static non-wrinkled group, no consistent angle of alignment was noted, highlighted by a large fluctuation in angle values frame to frame. As expected, nuclear alignment on the active wrinkling surfaces initially demonstrated a significant amount of fluctuation in the angle of alignment prior to the introduction of the surface topography. After the wrinkle pattern developed, the angle of alignment very closely mimicked the wrinkle angle, coupled with a decrease in the standard deviation over time. For average calculations, values were first averaged across positions (n = 2 or 3) and then across technical replicates (n = 2 or 4) to create a single value per substrate condition for biological replicate comparisons and statistical analyses.

The nuclear alignment angle was then compared to the wrinkle angle, where appropriate, to determine how aligned cell nuclei were to the wrinkle direction *before, during,* or *after* the potential topographic transition. We [16] and others [22] have previously demonstrated that inducing a topography via the shape memory effect dynamically alters cell nuclear alignment. However, to date, no quantification of nuclear reorganization *during* the change induced by shape memory has been reported. As shown in Table 4-4, the cell nuclear alignment for the static wrinkled surfaces was within approximately 4 ± 5° of the wrinkle direction, regardless of the temperature condition. Some of this variability may be a result of human error associated with measuring the wrinkle angle (the pattern is not a perfect wrinkle distribution and the angle is measured by eye from a phase image captured post time-lapse imaging), whereas other variability may be linked to local defects in the wrinkle pattern from the buckling phenomenon, resulting in a non-uniform pattern. When considering the static non-wrinkled surfaces, the calculated difference hovered closely around 90° (as there was no anisotropy) with a large standard deviation of approximately ± 44°. For the active wrinkling substrates, the calculated difference in nuclear alignment and wrinkle angle decreased from 7.65° ± 34.99° to 6.91° ± 27.39° to 5.89 ± 22.96°, prior, during, or post transition respectively. Statistical comparisons were performed on the *standard deviations* associated with the mean angle of orientation to characterize the angle distribution substrate to substrate. Cells atop active wrinkling surfaces had statistically different standard deviations compared to static wrinkled surfaces prior to the transition, whereas, post transition, cells atop active wrinkling surfaces had a statistically significant difference compared to the static non-wrinkled environment. This indicated that the angle distribution was getting narrower over time atop the active wrinkling substrates, orienting the cell nuclei in the direction of the developing wrinkle pattern.

4.4.5.2 Nuclear Angular Spread

The truncated standard deviation, or angular spread, was also calculated to compare the degree of alignment of cell nuclei during the active wrinkling process and to compare the angular spread substrate to substrate. As verified in methodology developed in [30], a perfectly random distribution of cell nuclei would generate a truncated standard deviation of 52°, while perfect alignment would result in an angular spread of 0°. Therefore, the smaller the angular spread value, the more highly aligned the cell nuclei are. Similar to angle of alignment, nuclear spread was first assessed on the individual video level. As shown in Figure 4-8, the angular spread for static wrinkled and static non-wrinkled substrates were approximately 36° and 47° respectively. With the active wrinkling sample, the angular spread was, at first, comparable to the static non-wrinkled group (Figure 4-8A, approximately 46° shown), prior to the topographic transition. Once the topography was introduced, this value steadily decreased until the post transition period, where the angular spread stabilized closer to the static wrinkled value (Figure 4-8A, approximately 38° shown). Similar to angle of alignment, angular spread values were first averaged across positions (n = 2 or 3) and then averaged for all technical replicates (n = 2 or 4) to create biological replicates for substrate comparisons and statistical analyses.

Average nuclear angular spread values were then compared for each substrate type in each topographic condition. As shown in Table 4-5, the average angular spread for the static wrinkled and static non-wrinkled groups were approximately 39° and 46° respectively, regardless of temperature. The active wrinkling group showed a steady decrease in angular spread as the topography was introduced, changing from 45.42° ± 1.81° to 43.80° ± 1.81° to 42.27° ± 1.71° respectively prior to, during, or after the topographic transition respectively. Statistical analysis revealed that angular spread was significantly different in the two static microenvironments, regardless of temperature condition. Interestingly, the active wrinkling substrates showed a consistent minor significant ($p < 0.1$) difference in angular spread for all potential topographic conditions, but only demonstrated a significant difference prior to or during the transition when compared to the static wrinkled microenvironment.

4.5 Discussion: Active Surface Wrinkling Enables Directed Migration and Nuclear Reorientation Along the Pattern Direction

This study represents the first investigation of how a developing nanotopography in the cellular microenvironment directly influences cell polarization and motility responses *before, during, and after* a topographic change was employed in real-time. The murine mesenchymal stem cell line C3H10T1/2 was selected due to their ability to exhibit classic fibroblastic motility, essential in both wound healing applications and metastatic cancer pathological development [34].

Here, we utilized a shape-memory induced transition in the cellular microenvironment as a means to generate the nanotopography [16] with controlled kinetics tailored to the thermal triggering conditions and time-frame applicable for time-lapse nuclear fluorescent imaging. Previously, we demonstrated that differences in cell motility of fibroblasts could be observed on the static versions of our nanotopographic surfaces at body temperature [24], but had not expanded the study to include the dynamic component of the shape memory response. The present study explored the spatiotemporal nature of cell trajectory, diffusion, mean squared displacement, velocity, and nuclear orientation responses *before, during, and after* the topographical transition in real-time and correlated that behavior to the static systems undergoing the same changes in environmental conditions. The results shown could not have been achieved by analyzing cell motility behaviors atop static substrates alone, or through time-point analyses of a combination of static and active materials.

Initial trajectory analysis of cells atop the static surfaces qualitatively revealed similar behaviors to those observed in **Chapter 3**. This was an important first step, as the temperature change used to employ the shape memory effect could potentially hinder motility responses (discussed below). As expected, cells atop the actively wrinkling surfaces demonstrated a switch in motility dynamics from random to oriented motion along the direction of anisotropy in response to the introduction of the wrinkled topography. In general, diffusion patterns of cells atop the actively wrinkling surfaces demonstrated a similar trend, however there was a clear increase in the diffusive spread along the y-direction (perpendicular to the direction of anisotropy) after the topography was introduced when compared to cell diffusion atop the static wrinkled surfaces. We speculate that when the wrinkled topography was triggered during imaging, remnants of ECM proteins deposited on the flat surface prior to the transition combatted the developing topographic cue, allowing for a more mixed diffusive pattern compared to the static wrinkled control (in which the cells only saw the wrinkle at all times).

Quantitative analysis of mean squared displacement characteristics further suggested that the cells were preferentially migrating along the direction of anisotropy once the topography was established in the actively wrinkling environments. Prior to the topographical transition, x and y decomposed MSD overlapped, indicating no preferential direction of motility. In some cases, there was some minor separation of x and y dynamics, though we hypothesize that this may be a consequence of the cells either responding to the underlying strain programmed into the substrate or pre-wrinkling of the material surface at 30°C. Further experiments looking at how increasing programmed strain influences motility dynamics would be required to validate this hypothesis. In all of the actively wrinkling samples, once the topography was fully developed, the x-directional MSD dominated, with a clear separation from the y-directional MSD dynamics. This is important to note, as it, in combination with the qualitative trajectory and diffusion plots, indicate that the cells were recognizing and responding to the topographical transition in their microenvironment.

One important consideration for using this SMP system as a platform for cell-ECM interactions is the potential influence that the temperature change (which triggers the change in topography for the actively wrinkling materials) has on cell structure and motility. For example, some forms of actin, the major component in cytoskeletal reorganization important to motility, are sensitive to thermal conditions [33]. Comparisons of cell velocity behaviors prior to and post transition for the static materials was of the most concern, as they would provide a direct comparison of cells in equilibrium at 30°C and 37°C. Statistical analyses revealed no significant difference in cell velocities atop static surfaces in the 30°C versus 37°C conditions, confirming that temperature was not a major factor influencing the motility responses shown.

Careful analysis of x-velocity behaviors revealed that cells moved faster along the direction of anisotropy in static wrinkled systems compared to static non-wrinkled systems. This is consistent with previous literature findings. For example, Qin and colleagues showed that human dermal fibroblasts migrated 60% faster on 8 micron-sized fibers of poly(methyl methacrylate) compared to a thin film of the same material. They hypothesized that the fibrillar structure caused an elongation of the cell cytoskeleton which led to less focal adhesion generation. This, in turn, enabled faster detachment of cells from the surface of the fibers compared to the thin film [35]. Kim and colleagues further noted that it is not only the presence of the pattern, but the size-scale of the anisotropic pattern that is an important factor dictating increased or decreased cell velocity responses parallel to the pattern direction [2]. Here, we have demonstrated that the presence of a static nanotopographical wrinkle pattern produces similar results, suggesting that less focal adhesions are generated for cells elongated along the pattern direction, leading to increased speed in the direction of anisotropy.

When analyzing the x-velocity behavior of cells atop the actively wrinkling surfaces, it was surprising to note that the values were not statistically significant from the non-wrinkled microenvironment, irrespective of the developing topography. We hypothesize that this effect is due to preconditioning from ECM deposition. In this case, the developing topography alone was not capable of inducing the expected change in x-velocity observed in the static wrinkled microenvironment versus the static non-wrinkled environment. As previously shown, cell trajectory, diffusion and mean squared displacement analysis revealed that the cells have recognized and are responding to the mechanical change in their surroundings. However, the x-velocity analysis suggests that the motility response is not identical to that observed in the static wrinkled case. With respect to Qin and colleagues' claim about cell elongation leading to less focal adhesion generation (and in turn faster cell velocities in the fiber direction) [35], deposition of ECM proteins on the flat substrate in a random orientation prior to wrinkle introduction would potentially increase the number of focal adhesion sites per cell, explaining why the cells do not adapt an increased x-velocity parallel to the wrinkle direction.

Nuclear alignment analyses revealed that there was a tight correlation between the nuclear alignment angle and the direction of anisotropy on static wrinkled surfaces. This was coupled with a small standard deviation (4 ± 5°). Conversely, no nuclear orientation preference was observed for the static non-wrinkled environment, coupled with a very large standard deviation (90 ± 44°). For the active wrinkling substrates, the calculated difference in nuclear alignment and wrinkle angle decreased from 7.65° ± 34.99° to 6.91° ± 27.39° to 5.89 ± 22.96°, prior, during, or post transition respectively. Two interesting trends were revealed in these values. First, the average difference in nuclear alignment angle and wrinkle direction was always less than 10°, regardless of the condition. This indicates that the cells may, to a certain extent, feel the underlying strain programmed into the material, partially aligning their nuclei in response. Similarly, the cells could be responding to pre-wrinkling of the surface that is nanotopographic, and thus, cannot be visualized in phase. Secondly, there is a large change in the standard deviation of this angle distribution. While the distribution in the active wrinkling environments does get narrower, it never achieves as tight of a distribution as observed in the static wrinkled microenvironment. Statistical analyses comparing the standard deviations of the angle of alignment confirm that there is a significant difference in nuclear distributions on static wrinkled and active wrinkling substrates prior to and during the topographic transition. However, the distribution is no longer significantly different once the developing topography has stabilized. Conversely, when comparing the active wrinkling and static non-wrinkled groups, a significant difference in the angle of alignment standard deviation is observed during and post topographic transition. This suggests that cell nuclei reorient in response to the developing topographical change.

Similar conclusions were drawn from the truncated standard deviation, or angular spread, results. The average angular spread for the static wrinkled and static non-wrinkled groups were approximately 39° and 46° respectively, regardless of temperature conditions. The active wrinkling group steadily decreased in angular spread as the topography was introduced, changing from 45.42° ± 1.81° to 43.80° ± 1.81° to 42.27° ± 1.71° respectively prior to, during, or after the topographic transition. While the angular spread of cells atop the static substrates were always statistically different, the active wrinkling substrates showed a consistent minor significant ($p < 0.1$) difference for all topographic conditions, but only demonstrated a significant difference ($p < 0.05$) prior to or during the transition when compared to the static wrinkled microenvironment. This suggests that the angular distribution is more tightly aligned after the topography is introduced, again reinforcing that the cell nuclei are aligning to the pattern direction.

4.6 Conclusions

Variations in a cell's local microenvironment have previously been shown to critically alter cell behavioral responses *in vitro*. Here, a shape memory polymer biomaterial was used as a platform for novel studies investigating mechanobiology responses of healthy fibroblasts to a developing topographical transition in the microenvironment. This study represents the first analysis of cell motility and nuclear alignment analysis *during* an active topographic change in the cellular microenvironment. Trajectory, diffusion, and mean squared displacement analyses revealed that cells transitioned from random to oriented motion with the introduction of a wrinkled pattern. Bulk motility metrics of cells atop the active wrinkling substrates appeared similar to those on static non-wrinkled substrates prior to the topographical transition. Conversely, the same metrics revealed that cells atop the active wrinkling substrates behaved similarly to cell behaviors atop static wrinkled substrates after the topographical transition had stabilized. Nuclear orientation analyses showed that cells reorient their nuclei in response to the developing surface pattern, suggesting that this process may be important for directed migration. Mouse fibroblasts cells adapted an intermediate velocity response when compared to the two static microenvironments, most likely due to pre-conditioning from ECM protein deposition. This analysis represents the first characterization of cell behaviors *during* a dynamic change in the microenvironment, providing important new insights into the underlying mechanisms guiding changes in cell motility responses. This new knowledge has important implications for *in vivo* applications, as it demonstrates that a mechanical change in the environment can alter directional motility and nuclear orientation responses.

4.7 References

1. Stevens, M.M. and J.H. George, *Exploring and Engineering the Cell Surface Interface.* Science, 2005. **310**(5751): p. 1135-1138.

2. Kim, D.H., et al., *Mechanosensitivity of fibroblast cell shape and movement to anisotropic substratum topography gradients.* Biomaterials, 2009. **30**(29): p. 5433-5444.
3. Han, L., et al., *Unidirectional migration of single smooth muscle cells under the synergetic effects of gradient swelling cue and parallel groove patterns.* Colloids and Surfaces B: Biointerfaces, 2013. **111**: p. 1-6.
4. Kandere-Grzybowska, K., et al., *Short-term molecular polarization of cells on symmetric and asymmetric micropatterns.* Soft Matter, 2010. **6**(14): p. 3257-3268.
5. Kim, D.H., et al., *Guided Cell Migration on Microtextured Substrates with Variable Local Density and Anisotropy.* Adv Funct Mater, 2009. **19**(10): p. 1579-1586.
6. Song, J.-M., et al., *DNA Vaccination in the Skin Using Microneedles Improves Protection Against Influenza.* Molecular Therapy, 2012. **20**(7): p. 1472-1480.
7. Missirlis, D. and J.P. Spatz, *Combined Effects of PEG Hydrogel Elasticity and Cell-Adhesive Coating on Fibroblast Adhesion and Persistent Migration.* Biomacromolecules, 2014. **15**(1): p. 195-205.
8. Kim, D.H., et al., *Matrix nanotopography as a regulator of cell function.* Journal of Cell Biology, 2012. **197**(3): p. 351-360.
9. Tamiello, C., et al., *Heading in the Right Direction: Understanding Cellular Orientation Responses to Complex Biophysical Environments.* Cellular and Molecular Bioengineering, 2016. **9**(1): p. 12-37.
10. Wang, J.H.C., et al., *Specificity of endothelial cell reorientation in response to cyclic mechanical stretching.* Journal of Biomechanics, 2001. **34**(12): p. 1563-1572.

11. Guvendiren, M. and J.A. Burdick, *Stem Cell Response to Spatially and Temporally Displayed and Reversible Surface Topography.* Advanced Healthcare Materials, 2013. **2**(1): p. 155-164.
12. Gray, D.S., J. Tien, and C.S. Chen, *Repositioning of cells by mechanotaxis on surfaces with micropatterned Young's modulus.* Journal of Biomedical Materials Research Part A, 2003. **66A**(3): p. 605-614.
13. Saez, A., et al., *Rigidity-driven growth and migration of epithelial cells on microstructured anisotropic substrates.* (0027-8424 (Print)).
14. Davis, K.A., et al., *Dynamic cell behavior on shape memory polymer substrates.* Biomaterials, 2011. **32**(9): p. 2285-2293.
15. Davis, K., et al., *Shape Memory Polymers for Active Cell Culture*. 2011: Journal of Visualized Experiments.
16. Yang, P., et al., *In vitro wrinkle formation via shape memory dynamically aligns adherent cells.* Soft Matter, 2013. **9**(18): p. 4705-4714.
17. Tseng, L.F., P.T. Mather, and J.H. Henderson, *Shape-memory-actuated change in scaffold fiber alignment directs stem cell morphology.* Acta Biomaterialia, 2013. **9**(11): p. 8790-8801.
18. Le, D.M., et al., *Dynamic Topographical Control of Mesenchymal Stem Cells by Culture on Responsive Poly(epsilon-caprolactone) Surfaces.* Advanced Materials, 2011. **23**(29): p. 3278-+.
19. Ebara, M., et al., *Focus on the interlude between topographic transition and cell response on shape-memory surfaces.* Polymer (United Kingdom), 2014. **55**(23): p. 5961-5968.
20. Ebara, M., et al., *The taming of the cell: Shape-memory nanopatterns direct cell orientation.* International Journal of Nanomedicine, 2014. **9**(SUPPL.1): p. 117-126.

21. Zhang, D., et al., *A bioactive "self-fitting" shape memory polymer scaffold with potential to treat cranio-maxillo facial bone defects.* Acta Biomaterialia, 2014. **10**(11): p. 4597-4605.
22. Mengsteab, P.Y., et al., *Spatiotemporal control of cardiac anisotropy using dynamic nanotopographic cues.* Biomaterials, 2016. **86**: p. 1-10.
23. Forster, B., et al., *Complex wavelets for extended depth-of-field: A new method for the fusion of multichannel microscopy images.* Microscopy Research and Technique, 2004. **65**(1-2): p. 33-42.
24. Baker, R.M., et al., *Automated, contour-based tracking and analysis of cell behaviour over long time scales in environments of varying complexity and cell density.* Journal of The Royal Society Interface, 2014. **11**(97).
25. Zhao, H., et al., *Induction of DNA damage response by the supravital probes of nucleic acids.* Cytometry Part A, 2009. **75**(6): p. 510-519.
26. McQuarrie, D.A., *Statistical Mechanics*. 2003: Viva Books Private Limited.
27. Schneider, C.A., W.S. Rasband, and K.W. Eliceiri, *NIH Image to ImageJ: 25 years of image analysis.* 2012. **9**(7): p. 671-675.
28. Abràmoff, M.D., P.J. Magalhães, and S.J. Ram, *Image processing with ImageJ.* Biophotonics international, 2004. **11**(7): p. 36-42.
29. Levy, H. and F. Lessman, *Finite Difference Equations*. 1992: Dover Publications.
30. Davidson, P., et al., *Definition of a simple statistical parameter for the quantification of orientation in two dimensions: Application to cells on grooves of nanometric depths.* Acta Biomaterialia, 2010. **6**(7): p. 2590-2598.

31. Mitchel, J.A. and D. Hoffman-Kim, *Cellular Scale Anisotropic Topography Guides Schwann Cell Motility.* PLoS ONE, 2011. **6**(9): p. e24316.
32. Kung, K.S., et al., *The development of anisotropic behaviours of 3T3 fibroblasts on microgrooved patterns.* European Physical Journal E, 2011. **34**(3).
33. Rosin, C., et al., *Exploring the Stability Limits of Actin and Its Suprastructures.* Biophysical Journal, 2014. **107**(12): p. 2982-2992.
34. Petrie, R.J. and K.M. Yamada, *Fibroblasts Lead the Way: A Unified View of 3D Cell Motility.* Trends in Cell Biology, 2015. **25**(11): p. 666-674.
35. Qin, S., et al., *Continual Cell Deformation Induced via Attachment to Oriented Fibers Enhances Fibroblast Cell Migration.* PLoS ONE, 2015. **10**(3): p. e0119094.

Table 4-1: Average x-velocities for active wrinkling, static non-wrinkled, and static wrinkled microenvironments prior, during or after the potential topographic transition.

	Active Wrinkling (μm/min)	**Static Non-Wrinkled (μm/min)**	**Static Wrinkled (μm/min)**
Prior to Transition	0.28 ± 0.08^{a}	0.24 ± 0.07^{b}	0.39 ± $0.10^{a,b}$
During Transition	0.33 ± 0.12^{c}	0.33 ± 0.10^{d}	0.49 ± $0.15^{c,d}$
Post Transition	0.29 ± 0.08^{e}	0.28 ± 0.07^{f}	0.40 ± $0.09^{e,f}$

Average x-velocities of fibroblasts atop active wrinkling (A), static non-wrinkled (NW), and static wrinkled (W) substrates. Prior to analysis, the x-axis was rotated to align to the wrinkle direction, where appropriate. For each metric, statistical comparisons were made between substrate types (e.g. A versus NW, A versus W, etc.) and between each temperature condition (e.g. A substrates prior to transition vs A substrates during transition, etc.). Substrates sharing the same label (a, b, etc.) were identified as statistically different from one another ($p < 0.05$) while conditional comparisons sharing the same numerical subscript (e.g., 1, 2, etc.) were identified as statistically different from one another ($p < 0.05$). No label indicates no statistically significant differences.

Table 4-2: Average y-velocities for active wrinkling, static non-wrinkled, and static wrinkled microenvironments prior, during or after the potential topographic transition.

	Active Wrinkling (μm/min)	**Static Non-Wrinkled (μm/min)**	**Static Wrinkled (μm/min)**
Prior to Transition	0.23 ± 0.07	0.25 ± 0.07	0.24 ± 0.06
During Transition	0.25 ± 0.09^{1}	0.32 ± 0.09	0.30 ± 0.10
Post Transition	0.19 ± 0.07^{a,1}	0.29 ± 0.08^{a}	0.23 ± 0.06

Average y-velocities of fibroblasts atop active wrinkling (A), static non-wrinkled (NW), and static wrinkled (W) substrates. Prior to analysis, the x-axis was rotated to align to the wrinkle direction, where appropriate. For each metric, statistical comparisons were made between substrate types (e.g. A versus NW, A versus W, etc.) and between each temperature condition (e.g. A substrates prior to transition vs A substrates during transition, etc.). Substrates sharing the same label (a, b, etc.) were identified as statistically different from one another ($p < 0.05$) while conditional comparisons sharing the same numerical subscript (e.g., 1, 2, etc.) were identified as statistically different from one another ($p < 0.05$). No label indicates no statistically significant differences.

Table 4-3: Average magnitude velocities for active wrinkling, static non-wrinkled, and static wrinkled microenvironments prior, during, or after the potential topographic transition

	Active Wrinkling (µm/min)	**Static Non-Wrinkled (µm/min)**	**Static Wrinkled (µm/min)**
Prior to Transition	0.40 ± 0.10[a,1]	0.39 ± 0.10	0.51 ± 0.12[a]
During Transition	0.47 ± 0.15[1]	0.51 ± 0.13	0.63 ± 0.17
Post Transition	0.38 ± 0.11	0.45 ± 0.11	0.51 ± 0.11

Average speed of fibroblasts atop active wrinkling (A), static non-wrinkled (NW), and static wrinkled (W) substrates. Prior to analysis, the x-axis was rotated to align to the wrinkle direction, where appropriate. For each metric, statistical comparisons were made between substrate types (e.g. A versus NW, A versus W, etc.) and between each temperature condition (e.g. A substrates prior to transition vs A substrates during transition, etc.). Substrates sharing the same label (a, b, etc.) were identified as statistically different from one another ($p < 0.05$) while conditional comparisons sharing the same numerical subscript (e.g., 1, 2, etc.) were identified as statistically different from one another ($p < 0.05$). No label indicates no statistically significant differences.

Table 4-4: Difference in nuclear angle of alignment compared to actual wrinkle direction for active wrinkling, static non-wrinkled, and static wrinkled microenvironments prior, during, or after the potential topographic transition

	Active Wrinkling (degrees)	**Static Non-Wrinkled (degrees)**	**Static Wrinkled (degrees)**
Prior to Transition	7.65 ± 34.99[a]	87.67 ± 42.58[b]	4.36 ± 5.31[a,b]
During Transition	6.91 ± 27.39[c,d]	91.71 ± 46.45[c,e]	4.50 ± 5.18[d,e]
Post Transition	5.89 ± 22.96[f]	82.35 ± 42.64[f,g]	3.69 ± 4.97[g]

Average nuclear angle of alignment (compared to wrinkle direction) atop active wrinkling (A), static non-wrinkled (NW), and static wrinkled (W) substrates. Prior to analysis, the x-axis was rotated to align to the wrinkle direction, where appropriate. For each metric, statistical comparisons of nuclear *standard deviations* were made between substrate types (e.g. A versus NW, A versus W, etc.). Substrates sharing the same label (a, b, etc.) were identified as statistically different from one another ($p < 0.05$). No label indicates no statistically significant differences.

Table 4-5: Nuclear angular spread for active wrinkling, static non-wrinkled, and static wrinkled microenvironments prior, during, or after the potential topographic transition

	Active Wrinkling (degrees)	**Static Non-Wrinkled (degrees)**	**Static Wrinkled (degrees)**
Prior to Transition	45.42 ± 1.81[a]	46.22 ± 1.70[b]	40.48 ± 1.80[a,b]
During Transition	43.80 ± 1.81[c,d]	46.63 ± 1.68[c,e]	38.70 ± 1.83[d,e]
Post Transition	42.27 ± 1.71	47.39 ± 1.52[f]	38.98 ± 1.74[f]

Average angular of fibroblasts atop active wrinkling (A), static non-wrinkled (NW), and static wrinkled (W) substrates. Prior to analysis, the x-axis was rotated to align to the wrinkle direction, where appropriate. For each metric, statistical comparisons were made between substrate types (e.g. A versus NW, A versus W, etc.). Substrates sharing the same label (a, b, etc.) were identified as statistically different from one another ($p < 0.05$). No label indicates no statistically significant differences.

Figure 4-1: Video stills of phase and nuclear overlays in static wrinkled, static non-wrinkled, and active wrinkling microenvironments.

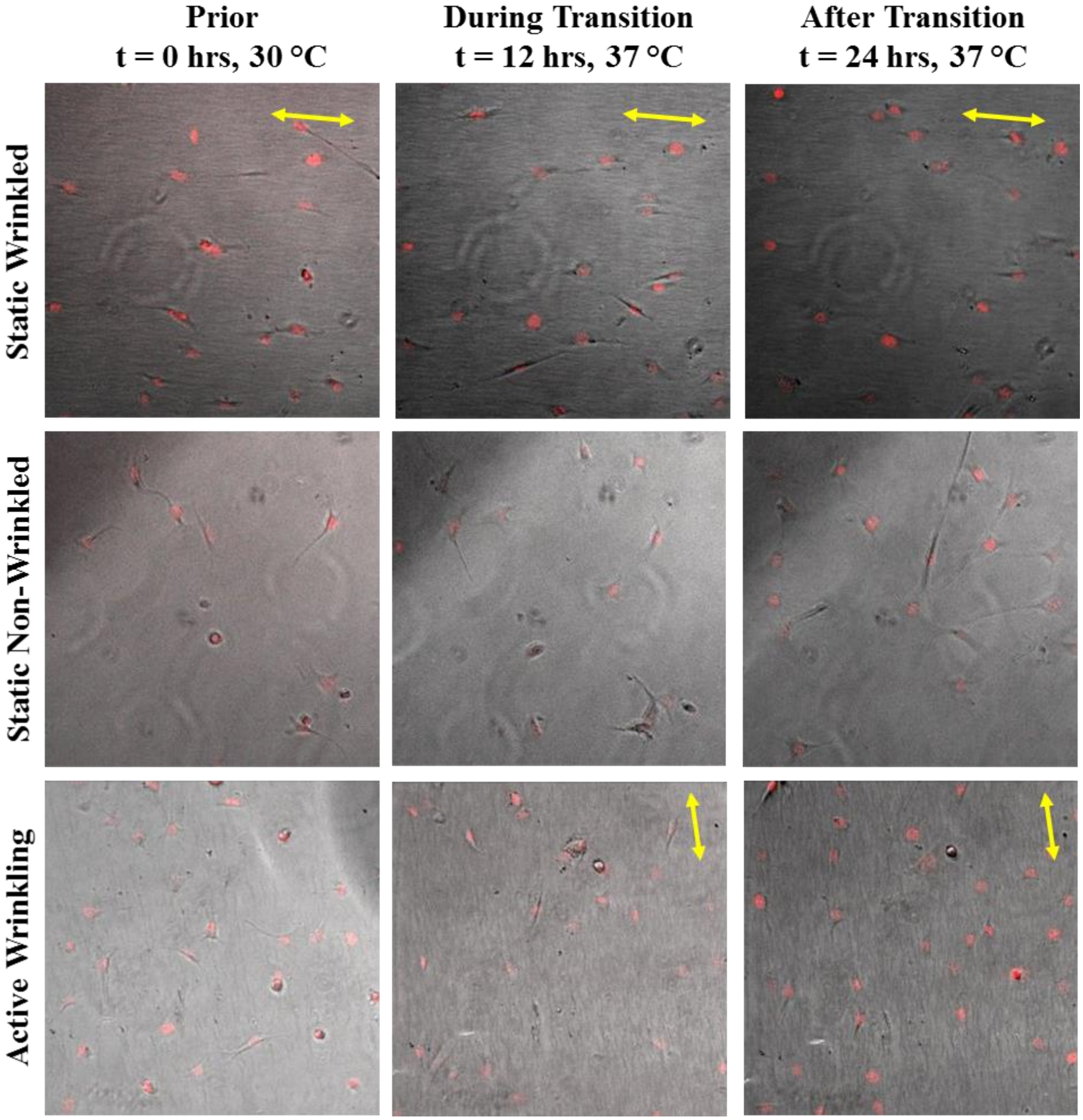

Representative micrographs of C3H10T1/2 mouse fibroblasts seeded at 4,000 cells/cm^2. Cells were stained with Hoechst 33342 nuclear dye (0.01μg/mL) and image contrast was manually enhanced in ImageJ to improve cell visibility. Overlays of phase (grayscale) and nuclear (red) channels demonstrate that cell nuclear behavior closely follows cell body dynamics, regardless of temperature and material conditions. Three time-points are shown: 1) “Prior” refers to before SMP triggering was initiated (frame 1 shown), 2) “During Transition” refers to a time-point during SMP wrinkling transition (frame 144 shown), and 3) “After transition” refers to a time-point after SMP wrinkling was completed (frame 288 shown). Yellow double-headed arrows indicate wrinkle direction, where appropriate. Image overlays have been cropped to enlarge cells displayed.

Figure 4-2: Trajectory behavior of cells atop active wrinkling, static non-wrinkled, and static wrinkled topographies prior to, during, or after the potential topographic transition

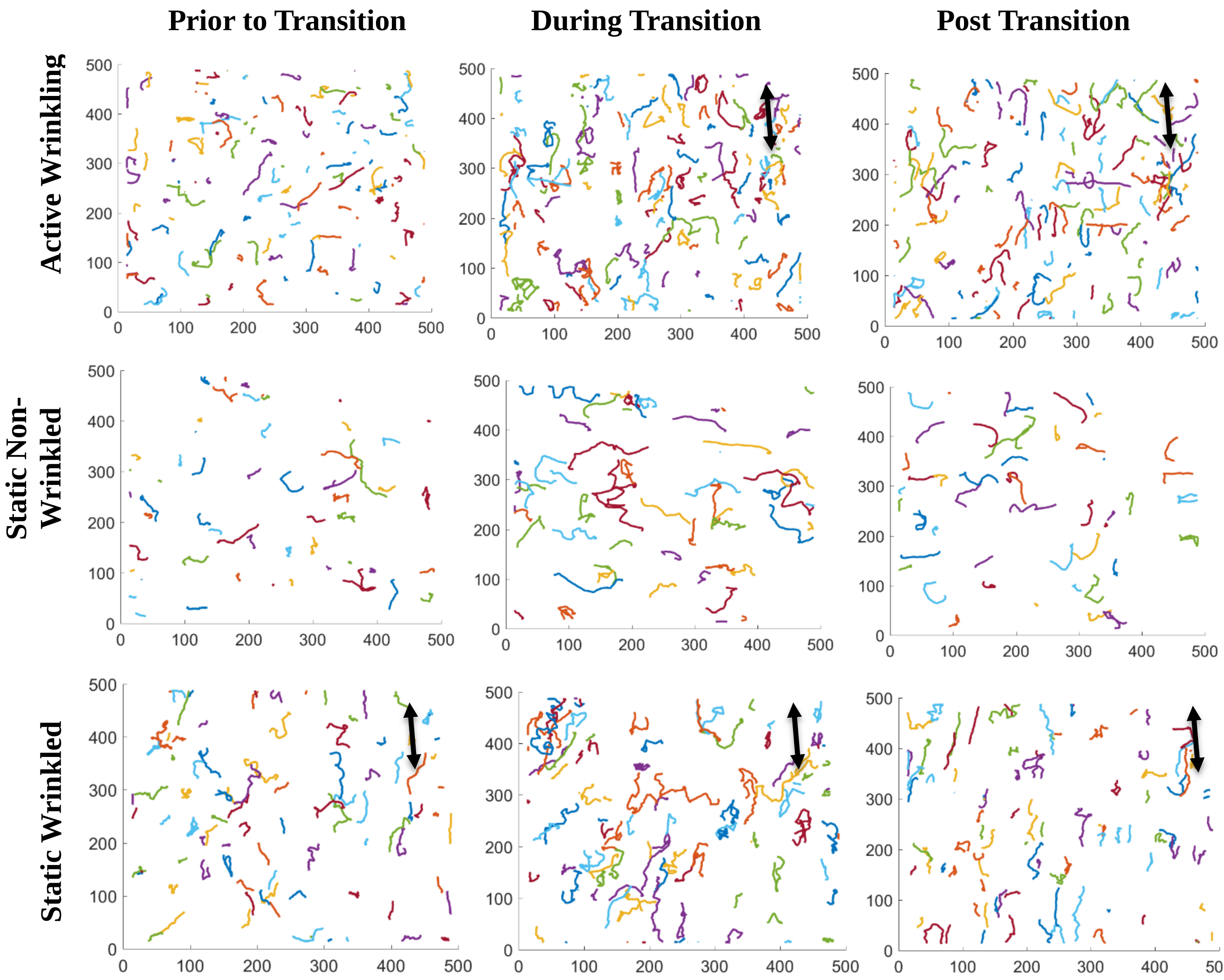

Representative trajectories of fibroblasts seeded on active wrinkling (top), static non-wrinkled (middle) and static wrinkled (bottom) surfaces prior to (left), during (middle), and post (right) the potential topographic transition. Qualitatively, cells preferentially migrated along the pattern direction on wrinkled surfaces compared to random motility atop static non-wrinkled surfaces. For active wrinkling surfaces, cells transitioned from random to oriented motion (parallel to new pattern). Black double headed arrows indicate direction of anisotropy, where appropriate.

Figure 4-3: Diffusion behavior of cells atop active wrinkling, static non-wrinkled, and static wrinkled microenvironments prior to, during, or after the potential topographic transition

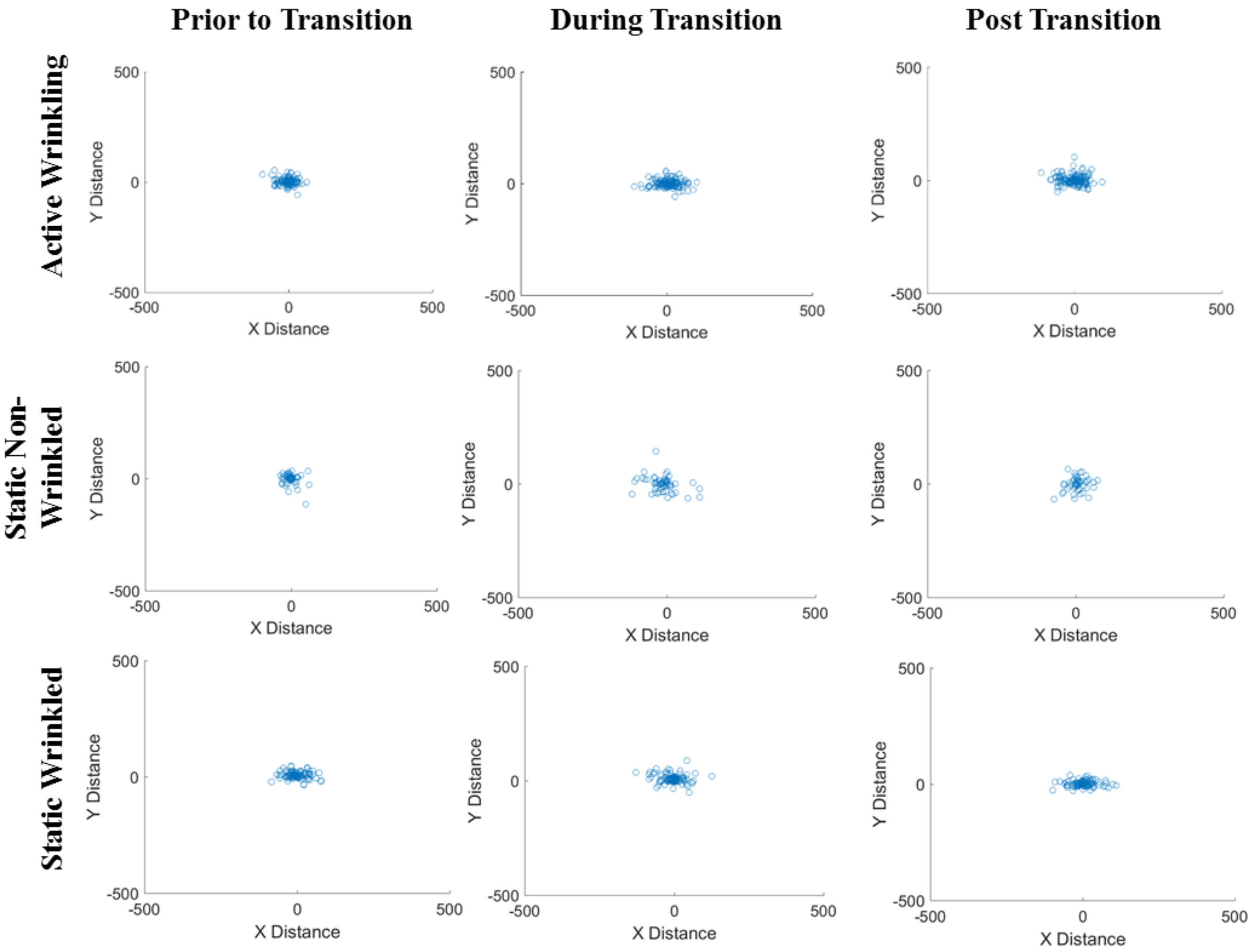

Representative diffusion of cells atop active wrinkling (top), static non-wrinkled (middle) and static wrinkled (bottom) surfaces prior to (left), during (middle), and post (right) the potential topographic transition. The x-axis was rotated to the direction of anisotropy, where appropriate. Cells on static wrinkled surfaces moved primarily along wrinkle direction, while cells atop static non-wrinkled substrates demonstrated a radial distribution, indicating no preferential motility. For active wrinkling surfaces, a change from radial to preferential x-axis motion was observed, indicating a switch from random to oriented motion in the direction of the developing anisotropy.

Figure 4-4: Decomposed mean squared displacement behavior of cells atop active wrinkling, static non-wrinkled, and static wrinkled topographies prior to or after the potential topographic transition

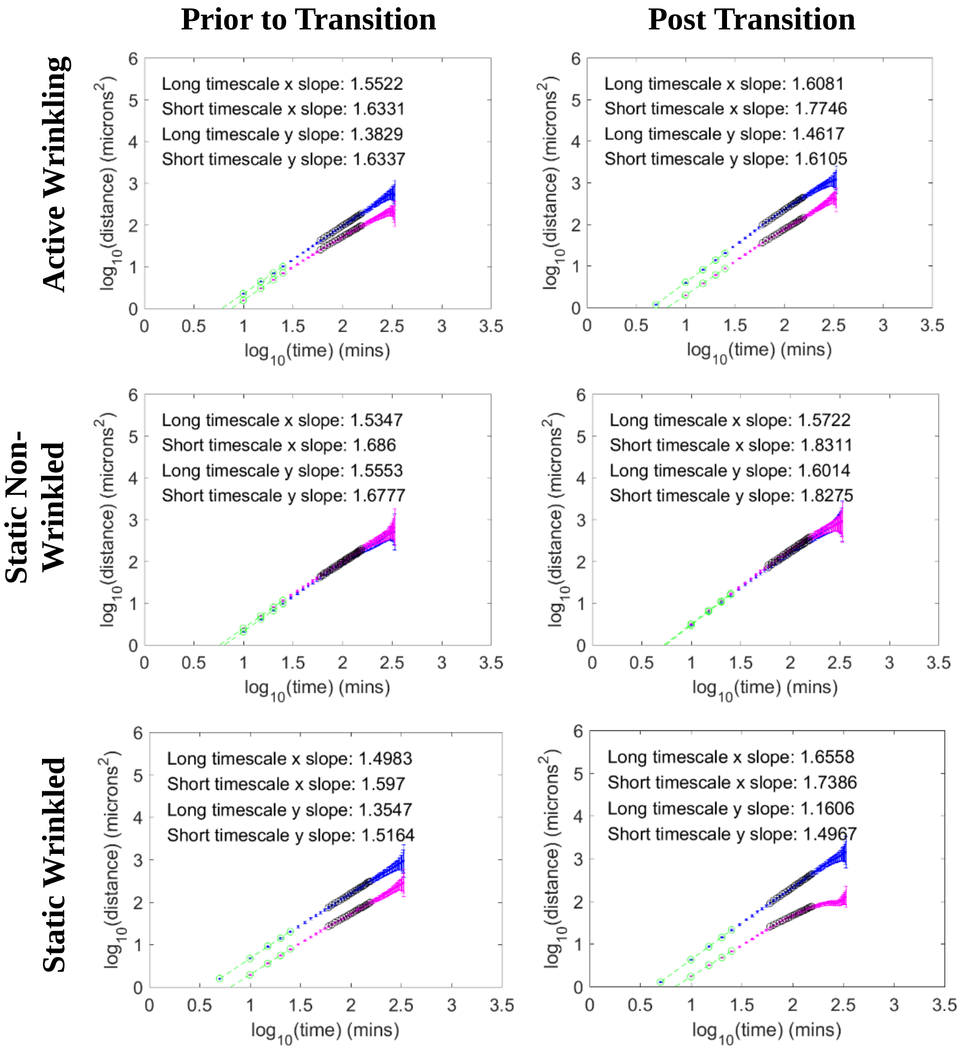

Representative decomposed mean squared displacement analyses of cells atop active wrinkling (top), static non-wrinkled (middle), and static wrinkled (bottom) microenvironments prior to (left) and after (right) the potential topographic transition. A clear separation of x (parallel to anisotropy, where appropriate) and y (perpendicular to anisotropy, where appropriate) behaviors was consistently seen atop static wrinkled substrates, whereas x and y behaviors consistently overlapped on static non-wrinkled topographies. For active wrinkling surfaces, x and y behaviors more closely followed behaviors seen in static non-wrinkled microenvironments prior to the topographic transition. After the topography stabilized, a switch in MSD behavior was observed, with a distinct separation in x and y behaviors.

Figure 4-5: Magnitude velocity distributions of cells atop active wrinkling, static non-wrinkled, and static wrinkled topographies prior to, during, or after the potential topographic transition

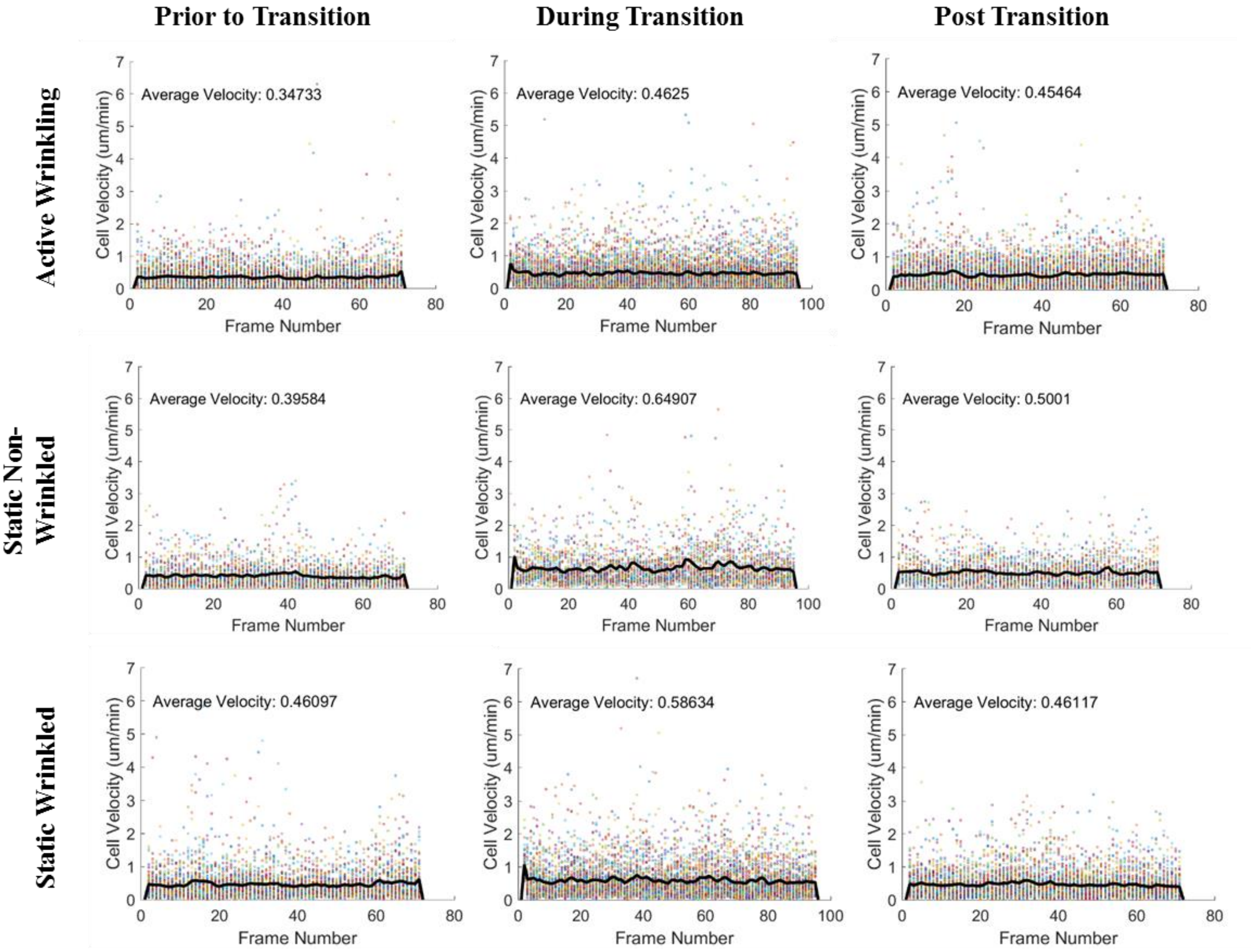

Example distributions of cell speeds atop active wrinkling (top), static non-wrinkled (middle) and static wrinkled (bottom) topographies prior to (left), during (middle), or after (right) the topographic transition. Each colored point corresponds to a single cell’s magnitude velocity in a frame. The average cell velocity per frame was calculated and displayed by the solid black line. Even though consistent average speeds were observed across all substrate types, plotting the distribution of cell behaviors per frame revealed the inherent variability of the underlying velocity distributions.

Figure 4-6: Representative micrographs of fixed fibroblasts with F-actin and nuclear staining on active wrinkling, static non-wrinkled, and static wrinkled surfaces after time-lapse imaging was completed.

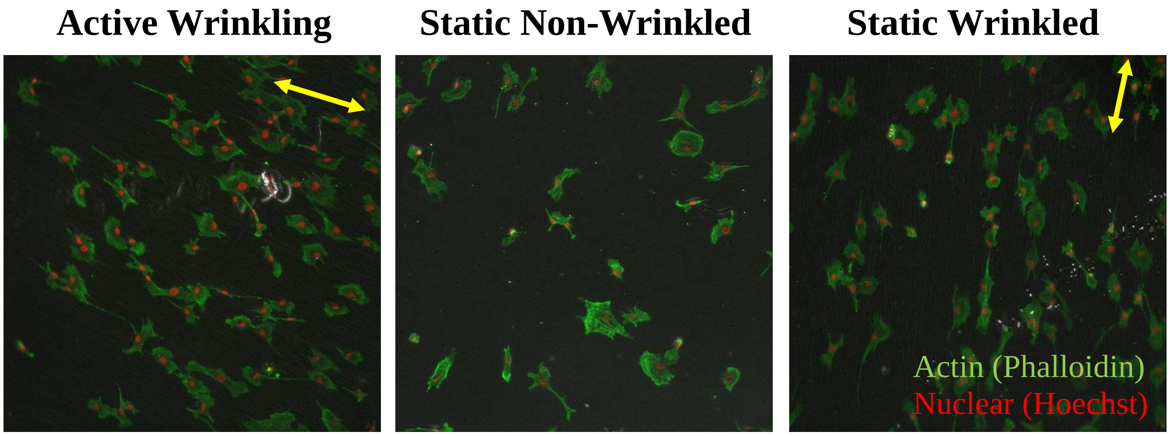

Representative micrographs of fibroblast cells atop active wrinkling (left), static non-wrinkled (middle), and static wrinkled (right) fixed and stained with Hoechst nuclear dye (red) and Phalloidin 647 (green) after 24 hrs of time-lapse imaging. Qualitatively, the cytoskeleton and nuclei of cells atop static non-wrinkled substrates show no preferential alignment or orientation. Conversely, cells atop static wrinkled substrates demonstrate more elongated cytoskeletons with nuclei aligned in the direction of the anisotropy. For cells on active wrinkling microenvironments, a mix in cytoskeletal and nuclear behavior is observed. Yellow double-headed arrows indicate wrinkle direction, where appropriate.

Figure 4-7: Angle of alignment for cells atop active wrinkling, static non-wrinkled, and static wrinkled microenvironments prior, during, or after the potential topographic transition

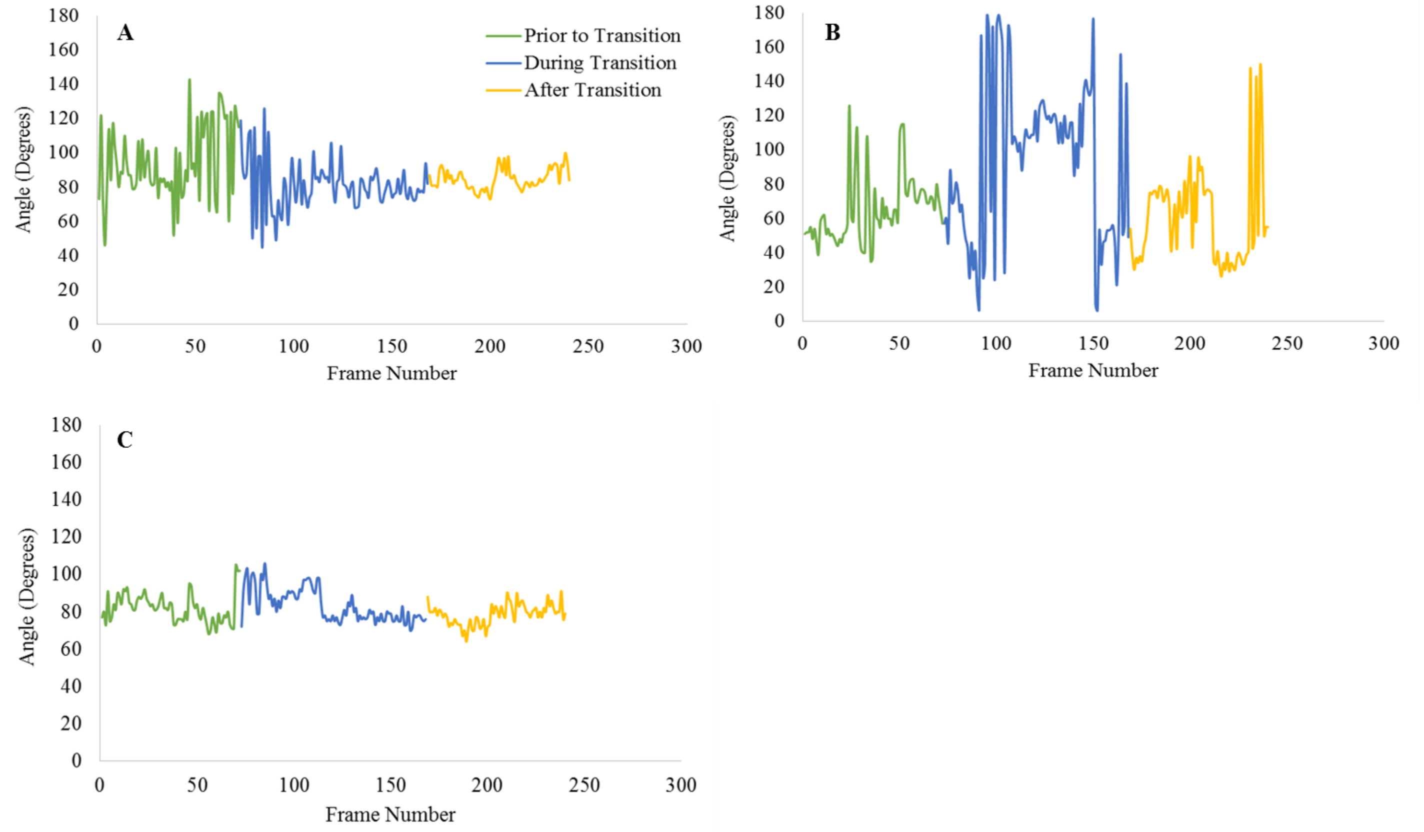

Representative example graphs of cell nuclear angle of alignment over the 20 hr video duration for A) active wrinkling, B) static non-wrinkled, and C) static wrinkled microenvironments. The static wrinkled sample (C) has a measured wrinkle angle of ~ 85.2°. The angle of alignment hovers closely around this value, indicating that nuclei preferentially align along the direction of anisotropy. Comparatively, the non-wrinkled sample (B) shows no alignment preference, as is indicated by the fluctuating nuclear alignment angle. For the active wrinkling surface (A), cell nuclei first demonstrated a significant fluctuation in their alignment until halfway through the transitionary period. After this point, the cell nuclei remained closely distributed to the direction of anisotropy (~86.0°), indicating that the nuclei have realigned to the pattern direction.

Figure 4-8: Nuclear angular spread of cells atop active wrinkling, static non-wrinkled, and static wrinkled microenvironments prior, during, or after the potential topographic transition

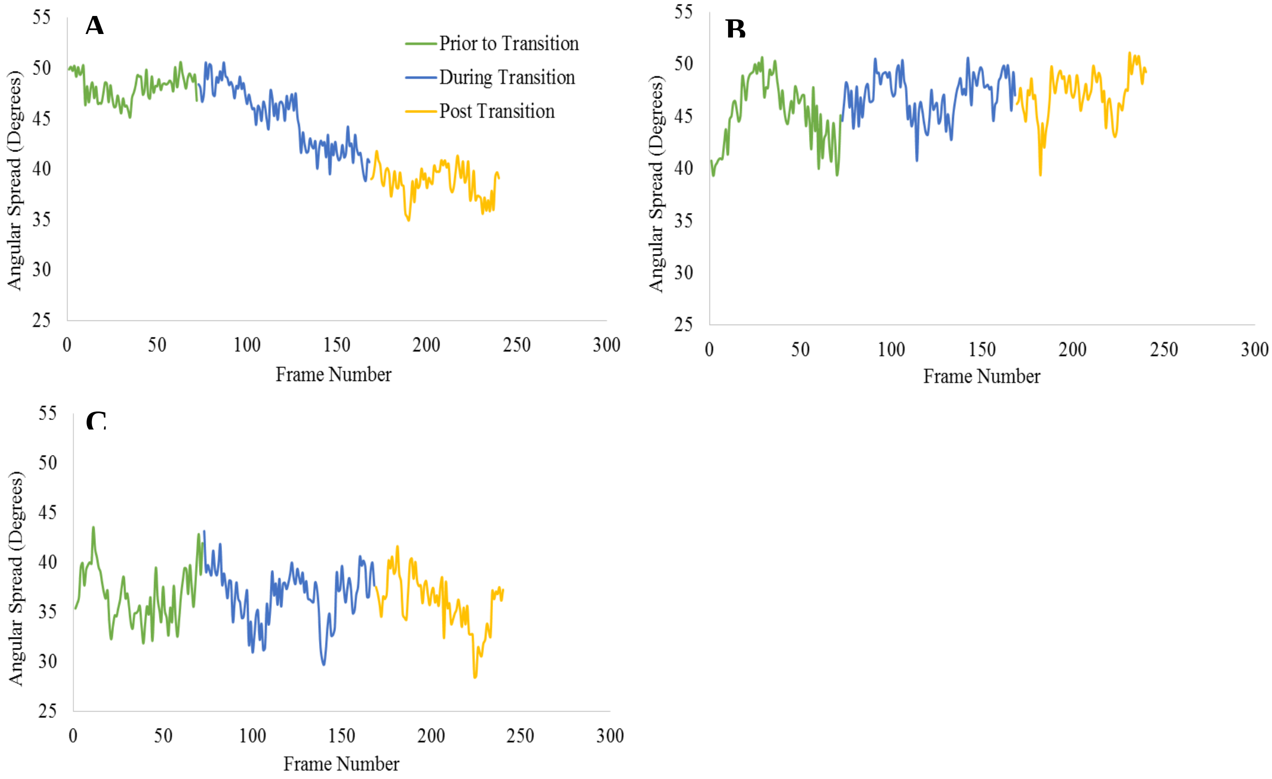

Representative graphs of nuclear angular spread over the 20 hr video duration for A) active wrinkling, B) static non-wrinkled, and C) static wrinkled microenvironments. While the static samples (B, C) demonstrated some natural fluctuations in their nuclear angular spread over time, the samples hovered around ~39° and ~45° for the static wrinkled and static non-wrinkled samples respectively. Cells on the active wrinkling surface showed a consistent angular spread to the non-wrinkled group prior to the topographical transition. Once the topography was initiated, the angular spread steadily decreased during the transitionary period. Post transition, the angular spread stabilized (similar to the static wrinkled topography) indicating that the cells had adapted to the change in their microenvironment.

Chapter 5: The Role of Intracellular Reorganization and ROCK Inhibition in Fibroblast Cell Motility Responses to a Developing Shape Memory Polymer Based Wrinkle Pattern†

5.1 Synopsis

Cell motility dynamics are governed by a mixture of physical, chemical, and electrical cues. In this chapter, we explored the relationship between a topographical surface change in a cell's microenvironment and its resulting influence on nuclear orientation, cell polarization, and, ultimately, cell migratory responses. Here, we employed the use of a shape memory polymer (SMP) biomaterial with the capability to dynamically wrinkle *during* culture with attached and motile cells. We further used multi-organelle automated tracking as a means to characterize cell polarization and motility responses via nuclear orientation, nuclear-Golgi polarization, trajectory, mean squared displacement, and velocity analyses *before, during,* and *after* an active surface change in the cellular microenvironment. We demonstrated that uninhibited fibroblast cells reorient their nuclei to align with a developing wrinkle pattern within an approximate 6 hr duration following the topographic change in their environment. This response was coupled with nuclear-

---

†This project is an ongoing collaborative effort between the Henderson, Manning, and Turner labs. Megan Brasch designed all cell experiments, executed all substrate preparation, and completed all time-lapse experiments. Anushree Gulvady infected fibroblast cells for RFP-Golgi imaging and helped with cell optimization. Giuseppe Passucci designed the Golgi tracking software. Megan Brasch and Giuseppe Passucci completed all data analysis.

Golgi polarization over a longer timescale. By examining the effects of ROCK inhibition on cell dynamics, we revealed that Rho is required for surface feature recognition by fibroblast cells. Furthermore, we demonstrated that inhibition of ROCK abolishes the cell’s directional motility bias, indicating that disruption of the ROCK pathway could be used to prevent cells from interpreting mechanical cues relevant to important biological processes, including those observed in morphogenesis, tissue repair, and disease progression.

5.2 Introduction: The Role of Cell-Material Interactions and Intracellular Organization in Cell Motility Dynamics

Cell motility is a complex biological process regulated by cell-material interactions and intracellular reorganization. Cells adhere to material surfaces through integrins [1], reinforced by focal adhesion kinases that aggregate at integrin-ECM binding sites to moderate cell motility responses [2-4]. Adaptor proteins reinforce cell-ECM binding, serving as mechanotransducers to the extracellular microenvironment while stabilizing the cell’s cytoskeleton at the integrin-ECM site [5, 6]. Mammalian cells actively probe their surroundings and subsequently migrate through constant cytoskeletal reorganization [5]. The migratory process consists of four major steps: 1) leading edge protrusions are generated in the direction of migration, 2) the new protrusions bind to the substrate’s surface through integrin binding and focal adhesion generation, 3) tension from new adhesion sites leads to traction force generation, and 4) the trailing edge of the cytoskeleton detaches allowing the cell body to propel in the direction of motion [7]. Mechanistically, this behavior is driven by the Rho signaling pathway [8, 9]. More specifically, there are three major

GTPases, RhoA, Rac1, and Cdc42, that have been studied extensively due to their role in cell motility responses. Rho has been shown to regulate the contraction process through filament formation, Rac controls polymerization of lamellipodial protrusions for substrate adhesion, while Cdc regulates polymerization of filopodia to enable directional migration [10]. Rho has additionally been linked to focal adhesion [11] and stress fiber formation [12].

On a larger scale, cytoskeletal reorganization is critical for many important cell motility driven biological processes. For example, epithelial to mesenchymal (EMT) transitions are essential for morphogenesis. During EMT transitions, epithelial cells alter their polarity (apico-basal to front-rear), reorganizing their cytoskeleton and redistributing their organelles to promote a more motile state. Cells can reestablish their epithelial phenotype through the reverse process, a mesenchymal to epithelial transition (MET), allowing for flexibility and reversibility in establishing tissues [13]. For example, neural crest cell migration has been linked to EMT [14, 15]. During neural crest formation, increased motility allows cells to separate towards different portions of the embryo, where they can then receive localized differentiation signals to tailor tissue development [16]. The EMT dedifferentiation process is also prominent in inducing cancer cell metastasis [17]. In this case, EMTs promote motility from the primary tumor site, aiding in cell dissemination and growth [18]. The Ras pathway, TGFβ [19], RhoA or RhoC GTPase expression through ROCK (rho associated kinase) mechanisms [20], and transcriptional modifiers have all been shown to influence EMT and MET dynamics [13].

Here, we sought to identify the mechanisms guiding a switch in cell motility responses observed atop an actively wrinkling shape memory polymer (SMP) biomaterial. As shown in **Chapter 4**, induction of a nanotopographical wrinkle feature during culture resulted in a switch from random to oriented motion (parallel to the wrinkle direction) of murine mesenchymal fibroblast cells. This was coupled with nuclear reorientation to the pattern direction and an intermediate response of cell velocity behaviors atop the wrinkling surface. To improve understanding of the cytoskeletal reorganization and cell polarization response associated with this process, we sought to track the relationship between cell nuclei and the Golgi apparatus. The Golgi apparatus is important for orienting the microtubule structure, coordinating with the centrosome to aid in cytoskeletal organization [21]. We hypothesized that the Golgi apparatus, which is important for establishing cell polarity and thus directed migration [22], are reorganizing in a similar timescale to promote this directed motility response. To explore this effect, we infected C3H10T1/2 mouse fibroblast cells with an RFP-Golgi marker, and tracked the nuclear-Golgi dynamics *before, during,* and *after* the active wrinkling transition. We further employed the use of a ROCK inhibitor to explore the relationship between cell motility mechanics and topographical recognition. Successful completion of this study demonstrates the first characterization of cell polarization responses *before, during,* and *after* an SMP driven topography change, while mechanistically determining how cytoskeletal reorganization and the ROCK pathway contribute to changes in cell motility responses observed as a result of dynamic rearrangement of the ECM microenvironment.

5.3 Methods: Cell Culture and Video Analysis

5.3.1 Substrate Preparation

Tert-butyl acrylate, butyl acrylate (*t*BA:BA) SMPs were prepared as previously reported in **Chapter 4** and [23]. Briefly, *t*BA:BA films were fabricated using 5 wt% TEG DMA and 0.06 wt% DMPA. Samples were cured for 30 minutes under UV light, followed by extraction in 1:1 methanol:distilled water overnight. Samples were then dried for at least 2 days in a 40°C vacuum oven prior to use. SMP films were then processed in one of three ways: 1) as static flat controls (hereafter referred to as static non-wrinkled), 2) as static anisotropic controls (hereafter referred to as static wrinkled), or 3) as the active wrinkling experimental group (hereafter referred to as active wrinkling). Static non-wrinkled samples were cut into 6x6 mm squares and then flattened using an 80°C hotplate. Static wrinkled and active wrinkling films were strained 7% in an 80°C isothermal oven for 10 minutes and subsequently cooled at -4°C for 5 minutes to fix in the strain. Wrinkled and active groups were then cut into 6x6 mm squares using a hammer and razorblade (no heat could be applied or the strain would recover prematurely). All sample types were then sputter coated for 100 seconds with gold, resulting in an approximately 33nm thick coating on the surface. Static wrinkled substrates were then recovered for 2 hours at 60°C in an isothermal oven, resulting in a nanotopographic pattern with features on the order of 400 nm in amplitude and 1-5 μm in wavelength [23]. All three substrate groups were then UV sterilized for one hour on each side in a biological safety cabinet (ThermoFisher, 1300 Series A2) for subsequent cell culture experimentation.

5.3.2 Cell Culture, Golgi Infections, and Cell Seeding Conditions

C3H10T1/2 mouse fibroblast cells (ATCC) were cultured in Basal Medium Eagle (BME) complete growth medium supplemented with 10% fetal bovine serum (FBS, v/v), 1% penicillin/streptomycin (v/v) and 1% GlutaMax (v/v). Cells were expanded in a 37°C humidified incubator with regulated 5% CO_2 and passaged at 80% confluence using 0.25% Trypsin EDTA. For time-lapse experiments, cells were restricted to passage numbers 12-18.

To enable Golgi tracking, cells were passaged using 0.25% Trypsin EDTA and plated at 50,000 cells/well in 1mL of media (per well) in a 6-well plate. Cells were then infected with 30 particles per cell of CellLight Golgi-RFP, BacMam 2.0 (ThermoFisher Scientific, Cat # C10593). 1μL of Bacmam Enhancer (ThermoFisher Scientific, Cat # B10107) was additionally added per well to improve infection efficiency to ~70% (data not shown). Infected cells were then cultured for 24 hrs in a 37°C humidified incubator with 5% CO_2.

Prior to cell seeding, SMP samples were soaked in room temperature BME medium for 6 hrs to promote FBS protein adsorption to the material surface. RFP infected cells were then passaged using 0.25% Trypsin EDTA warmed to 30°C. Each sample was transferred into an individual well in a 48-well plate and cells were solution seeded (500μL/well) at a density of 4000 cells/cm^2. Cell samples were then incubated at 30°C for 16 hours to establish equilibrium prior to time-lapse image set-up.

5.3.3 Live-cell Nuclear Staining, ROCK Inhibition, and Time-Lapse Imaging

Hoechst nuclear stain was prepared at a concentration of 0.01μg/mL in BME complete medium (30°C). Where appropriate, 10μM of Y-27632 ROCK inhibitor (Calbiochem) was additionally added to the prepared Hoechst solution to inhibit the p160ROCK (ROCK-I) pathway [24]. 800uL of the staining or staining/ROCK solution were added to each well of a 4-well LabTek borosilicate chamber slide (Fisher Scientific). Static wrinkled, static non-wrinkled, and active wrinkling samples were then transferred into chamber slides and incubated at 30°C for one hour. After 1 hr of incubation, samples were inverted and weighed down with sterilized glass slide inserts, cut to fit into the chamber wells. The chamber slide was then transferred to a live cell stage incubator (INC-2000, 20/20 Technology, Inc.) and cells were imaged using a Leica DMI 6000B inverted microscope. The live cell stage incubator was equilibrated at 30°C with constant 5% CO_2. Three slice (uninhibited RFP-Golgi data) or one slice (ROCK inhibited RFP-Golgi data) z-stack images were captured every five minutes in phase, A4 (excitation/emission peak of 360/470 nm), and N3 (excitation/emission peak of 546/600 nm) using 50 ms, 100 ms, and 50 ms exposure times respectively on an Andor Luca R camera with a 10x/0.63 NA objective. The number of z-slices used for the ROCK inhibited data was minimized due to concerns related to phototoxicity effects (see section 5.3.4.2 below). For the uninhibited biological replicates, the temperature was increased from 30°C to 37°C after 8 hrs of imaging, triggering the active wrinkling group. Cells were then imaged for an additional 16 hrs. For the ROCK inhibited data, this 30°C imaging timeframe was reduced to 4 hrs, to capture as much of the post wrinkling regime as possible without concern of phototoxicity. The cells were then imaged for an additional 20 hrs at 37°C. Where necessary, frame by frame z-stacks were compressed using an extended depth of field plugin [25] and compiled into a final tiff stack for processing. The resultant cell behavior was then characterized using the ACT*IV*E (automated contour-based tracking for *in vitro* environments) system [26] previously described in **Chapters 2-4**. A supplemental Golgi tracking code (detailed below in section 5.3.4.1), was used to correlate Golgi body motion to nuclear directional behaviors to track cell polarization over time.

5.3.4 Cell Motility Analysis

In **Chapter 4**, we observed that C3H10T1/2 mouse fibroblast cells altered their motility in response to a developing SMP induced topographical transition in their microenvironment. Here, our aim was to expand this analysis to examine how cell polarization changes over time in response to the developing surface topography. More specifically, we wanted to characterize the nuclear-Golgi polarization response and mechanistically determine the role of ROCK in identifying developing surface features. We chose to characterize the Golgi-nuclear response of cells *before, during,* and *after* the topographical transition as a means to quantify cell polarization. To do this, we developed a new Golgi tracking approach that could work in combination with the ACT*IV*E system to quantify cell polarization dynamics. We explored the cell polarization response through cell velocity, nuclear orientation, nuclear-Golgi orientation, nematic order parameters and directors as a means to quantify cell reorganization in uninhibited and ROCK inhibited fibroblast cells.

5.3.4.1 Video Processing: Golgi Tracking, Sample Translation, Photobleaching, and Phototoxicity

One of the most challenging features about tracking cell polarization dynamics over time was correlating the nuclear response to that of the Golgi bodies. As previously noted, the Golgi is important for establishing cell polarity and thus is critical in directed migratory responses [22]. We chose to couple the nuclei and Golgi to determine a “polarization vector”, as the Golgi typically orients towards the front, while the nucleus orients towards the back, of fibroblast cells during directed migration [27-30].

Golgi bodies vary in shape and density, preventing ACT*IV*E ellipsoidal tracking from being applied to their irregular designs. Instead, we utilized the clusterdata MATLAB function to group Golgi clusters [31]. Briefly, clusterdata minimizes the distance between points along each spatial dimension independently, using a minimum distance parameter to differentiate clusters appropriately. For our case, the minimum distance between each Golgi body was calculated from the seeding density, transfection efficiency, and an empirically determined constant of proportionality (based on the micron to pixel ratio and a user input parameter, the sensitivity). We incorporated a sensitivity parameter, which ranged from [0,1], to establish the relationship between the farthest points identified in a data set. Therefore, a high sensitivity value would yield fewer clusters, while a low sensitivity would increase the number of groups identified.

A thresholding technique was used to segment Golgi images. By comparison, the ACT*IV*E software utilizes a bandpass filter to smooth nuclear intensity for contour-based profiling. This technique was not viable for the Golgi body approach, as bandpass filtering led to loss of Golgi body shape and irregularity. These features were, in turn, important for establishing polarization. To determine the ideal threshold value, the image intensity histogram for each frame was fit to a Gaussian, from which a mean and standard deviation (sigma) were calculated. The MATLAB function im2bw with a threshold parameter of 5*sigma was then used to convert images to grayscale (where values above the threshold were mapped to white and values below were mapped to black).

To avoid false-positives (where a single Golgi body is split into multiple complexes), a low sensitivity was selected for Golgi identification. Additionally, post-processing code was implemented to finalize the number of clusters identified. The post-processing code sorts Golgi clusters based on pixel area, identifying the largest cluster as the reference cluster. Cluster boundaries were defined and false positives were further reduced by minimizing the distance between clusters and cluster areas. Following Golgi body identification, Kilfoil linking was used to assign identification (ID) tags for each cluster [32]. ACT*IV*E nuclear and Golgi ID tags were then combined using a weighted distance minimization technique. This required the user input parameter maximum distance, which represented the farthest distance a nucleus and Golgi cluster could be from one another to be coupled together. This parameter was important for accurate results, as the RFP infection efficiency was not 100%.

Three additional concerns emerged after establishing the Golgi-nuclear tracking technique, post experimentation: 1) sample translation, 2) photobleaching, and 3) phototoxicity. To address minor sample translations, the change in the mean center of mass (for all cell nuclei) was identified and plotted over time. Sample translation resulted in a large increase in the center of mass, allowing isolation of the frames where this shift occurred. By calculating the displacement vector caused by this shift, we could remove this error from our aggregate calculations (namely cell velocity).

Photobleaching and phototoxicity are well documented concerns resulting from consistent cell imaging over time. From a tracking standpoint, photobleaching results in a loss of signal intensity, while phototoxicity results in cell death from excessive fluorescent exposure. To combat photobleaching, we adjusted ACT*IV*E to incorporate image scaling on a frame by frame basis. A probability distribution function was used to map the pixel intensities of importance for each frame, improving ACT*IV*E's ability to consistently identify nuclei over time. In regards to phototoxicity, nuclear speed was used as a determining factor for cell death. Fibroblasts with a maximum speed of less than 0.125 µm/min were removed from our analysis, as they did not contribute useful data regarding cell orientation dynamics. We then calculated a moving average of nuclear displacement over 20 frames for each cell, deriving the speed and acceleration as a function of frame. We noted that immotile or dead cells had little change in their speed frame to frame, corresponding to an acceleration of approximately zero. After normalizing by the number of frames, we calculated the standard deviation of the acceleration. Immotile or dead cells yielded a drastic decrease in this standard deviation over time, allowing us to flag and remove dead cell data from our analysis, where necessary.

5.3.4.2 Uninhibited versus Inhibited Cell Experiments

Data analysis was broken down into two categories: 1) uninhibited RFP-Golgi tagged videos (hereafter referred to as the uninhibited data sets), and 2) ROCK inhibited RFP-Golgi tagged videos (hereafter referred to as the inhibited data sets). In both cases, cell nuclei were stained with Hoechst 33342 and Golgi bodies were infected with CellLight Golgi-RFP, BacMam 2.0. However, culture treatment, imaging, and triggering conditions were slightly different in each set. As shown in Scheme 5-1A, samples in uninhibited data sets included two static wrinkled controls, two static non-wrinkled controls, and four active wrinkling experimental samples. A larger number of active wrinkling samples were imaged compared to the controls, due to a higher chance that the active wrinkling samples would move macroscopically from the strain recovery during the imaging process (which cannot be resolved through post-processing). This meant that each biological replicate had up to two static wrinkled technical replicates, two static non-wrinkled technical replicates, and four active wrinkling technical replicates. Each sample was additionally imaged at two locations to increase the total number of cells tracked per substrate. To compensate when aggregating data, features of interest were first averaged across positions within a technical replicate, followed by averaging across all technical replicates to obtain one static wrinkled, static non-wrinkled, and active wrinkling value per biological replicate. Uninhibited experiments were repeated three times (three biological replicates). With regards to video capture, uninhibited data sets were imaged for 8 hrs at 30°C, followed by an additional 16 hrs at 37°C, similar to imaging conditions presented in the nuclear only data in **Chapter 4**. Similar to **Chapter 4**, final videos were truncated to 20 hrs total (imaging hours 2-22), due to poor Hoechst uptake during the first two hours of imaging. This allowed us to verify that RFP-Golgi infections did not affect bulk motility metrics (data not shown).

For the inhibited data sets, 10µM of Y-27632 ROCK inhibitor was added to 2mL of the prepared Hoechst solution prior to image set-up to inhibit the p160ROCK (ROCK-I) pathway. Samples were then arranged in the chamberslide as depicted in Scheme 5-1B. Notably, both uninhibited and inhibited samples were imaged from each group, allowing for a direct comparison to be made between cells and material from the same experimental conditions. In this case, samples were instead divided into one static wrinkled, one static non-wrinkled, two active wrinkling, one ROCK inhibited static wrinkled, one ROCK inhibited static non-wrinkled, and two ROCK inhibited active wrinkling samples. To compensate for the limited number of technical replicates, three positions were imaged per sample. Similar to the uninhibited data sets, features of interest were first averaged by position and then by technical replicate, where appropriate, to grant one static wrinkled, one static non-wrinkled, one active wrinkling, one ROCK inhibited static wrinkled, one ROCK inhibited static non-wrinkled, and one ROCK inhibited active wrinkling biological replicate value. Just as with the uninhibited data sets, the inhibited experiments were repeated three times (three biological replicates). With regards to video capture, uninhibited data sets noted some phototoxicity and photobleaching issues towards the end of the 24 hr imaging period. Therefore, the 30°C imaging period was reduced to 4 hrs for the inhibited data, followed by an additional 20 hrs of imaging at 37°C.

5.3.4.3 Calculating Cell Velocity

Cell speed was calculated from changes in nuclei center-of-mass frame-to-frame. This positional data was obtained from the ellipses fit by the ACT*IV*E tracking package. As previously described in **Chapter 2**, **t**he ACT*IV*E software contains a "memory" parameter, which represents the number of frames the linking code will allow between positions for a nucleus to retain the same identification number. Due to this feature, gaps in positional data as a function of time may occur. Since the speed represents a change in position, we filled these gaps by assuming that, while a nucleus was missing, it was travelling in a straight line between the last known position before it disappeared and the first position after it reappeared. Given the small number of frames (memory parameter = 10), the distance interpolated was negligible and allowed us to smoothly calculate the speed for particles with these filled in trajectories. We then examined the absolute value of change in the x-direction to calculate the x-component of the velocity and perform an analogous process for the y-direction. Finally, we combined these results to calculate the speed at which the nuclei centers-of-mass were moving.

5.3.4.4 Nuclear and Nuclear-Golgi Alignment

One of the most important metrics for characterizing cell polarization responses to the surface topography change was understanding the nuclear orientation and nuclear-Golgi polarization vector formed by pairing the nucleus and Golgi body orientation from the same cell. As previously noted, in uninhibited fibroblasts, the Golgi bodies orient toward the leading edge while the nucleus orients towards the rear of the cell. This provided for a simple method to compare cell orientation to the nuclei shape definition. For our experimental data, we treated all of the directions as apolar as we were primarily concerned about whether the cells were aligning to the surface topography. To calculate the nuclear and nuclear-Golgi orientation, we used the same technique described in **Chapter 4**. First, all angles were wrapped between [1°, 180°]. Next the standard deviation, σ, of this distribution was calculated. From this, the truncated standard deviation, σ_t, was determined using Equation 5-1 [33]:

$$\sigma_t = \frac{52}{1 + 543 * \sigma^{-1.96}} \qquad \text{Eq. 5-1}$$

The truncated standard deviation (hereafter referred to as the angular spread) was used to determine the degree of overall alignment of the cells atop patterned or unpatterned surfaces. As previously described in **Chapter 4**, a random distribution would generate an angular spread of 52°, while perfect alignment would result in an angular spread of 0°. Therefore, smaller values indicated more highly aligned cells. After calculating the angular spread, the distribution was shifted by one degree and re-wrapped from [1°, 180°]. The mean of the distribution was calculated and the process was repeated until the reference angle reached 180°. The mean distribution with the smallest truncated standard deviation was identified as the mean orientation for the system (hererafter referred to as the angle of alignment).

5.3.4.5 Nematic Order Parameter and Director

Nematic systems (as defined here by a collection of apolar objects) are prevalent in the field of liquid crystals. A common order parameter used to describe these systems is:

$$Q_{\alpha\beta} = \frac{1}{N}\sum_{i=1}^{N}\frac{3}{2}\hat{u}_{i,\alpha}\hat{u}_{i,\beta} - \frac{1}{2}\delta_{\alpha,\beta} \qquad \text{Eq. 5-2}$$

where α and β are reference directions, i is the cell index, N is the total number of cells, $\hat{u}_{i,\alpha}$ is the unit vector direction of cell i in dimension α, $\hat{u}_{i,\beta}$ is the unit vector direction of cell i in dimension β, and $\delta_{\alpha,\beta}$ is the Kronecker delta. Using this concept, we could then look at the eigenvalues and eigenvectors of tensor $Q_{\alpha\beta}$ to determine axial alignment of the system. The largest eigenvalue was an order parameter directly related to the system alignment, where 0 signifies no alignment and 1 signifies perfect axial alignment. The eigenvector related to the largest eigenvalue was the director, or mean orientation of the system. This director metric allowed for a secondary check to the mean orientation, while additionally providing an alignment order parameter.

5.3.4.6 Statistics

One-way ANOVA tests of pre-transition, during transition, and post-transition cell velocity, nuclear alignment, nuclear angular spread, nuclear-golgi alignment, nuclear-golgi angular spread, nematic order parameters, and alignment director behaviors were used to compare wrinkled, non-wrinkled, and active wrinkling substrate groups in the healthy data sets. For the inhibited data sets, three additional groups, ROCK static wrinkled, ROCK static non-wrinkled, and ROCK active wrinkling were also included. Significance was determined at 90% and 95% p-values.

5.4 Results: ROCK Inhibition Abolishes Fibroblast Directional Motility Atop Patterned Surfaces in Dynamic Microenvironments

5.4.1 Intracellular Reorganization Polarizes Cells for Directed Migration After a Topographical Surface Transition

Trends in nuclear orientation, nuclear-Golgi polarization, and cell velocity dynamics of the uninhibited data revealed that fibroblasts reorganize their internal structure to polarize cells to realign over time with the developing surface topography. Similar to data presented in **Chapter 4**, analysis was broken down into three categories: 1) a 6 hr pre-trigger portion where cells were only exposed to the 30°C microenvironment (hereafter referred to as "before the potential transition"), 2) an 8 hr region directly after the temperature increase to 37°C (hereafter referred to as "during the potential transition"), and 3) a 6 hr post-trigger portion after the transition where the cells were in equilibrium at 37°C (hereafter referred to as "after the potential transition"). Nuclear alignment was examined first using ACT*IV*E to determine whether RFP-Golgi infection had any impact on general alignment dynamics. Nuclear angle of alignment showed consistent results to those presented in **Chapter 4**. Cells atop static wrinkled substrates aligned their nuclei to the wrinkle direction. This was evident in plots of the mean orientation angle over time (Figure 5-1, top row), as well as the difference in the mean orientation angle as it compared to the wrinkle direction (Table 5-1). Conversely, cells atop the static non-wrinkled substrates had randomly oriented nuclei, with no particular angle identified as the primary angle of alignment frame to frame. For the active wrinkling substrates, cells reoriented their nuclei to align to the pattern direction shortly following wrinkle introduction. This was evident in the difference between the primary angle of alignment and the measured wrinkle direction (12.66° ± 21.06° before, 7.51° ± 17.67° during, and 9.73° ± 13.42° after the topographical transition; Table 5-1) and by plotting the mean nuclear orientation angle over time (Figure 5-1, top row).

The angular spread was further quantified using the truncated standard deviation to characterize cell-to-cell nuclear alignment over time. As shown in Table 5-2, static wrinkled substrates had an average angular spread of approximately 37° regardless of temperature condition, compared to approximately 46° for the static non-wrinkled case. Comparisons of static wrinkled and static non-wrinkle cells revealed that this difference in nuclear orientation was statistically significant ($p < 0.05$) for each time period of interest. Cells atop actively wrinkling surfaces showed an increase in nuclear alignment with the developing surface topography, as was demonstrated by a decrease in the average nuclear angular spread from 42.87° ± 3.36° before to 39.62° ± 4.21° during to 36.40° ± 4.34° after the surface change. This was validated by a statistically significant difference in nuclear angular spread for the active vs non-wrinkled substrates in all cases, but a statistically similar nuclear angular spread after the transition when compared to static wrinkled substrates. Again, these results were corroborated by plotting the nuclear angular spread over time for each surface type (Figure 5-1, bottom row).

Plots of the nematic angle (Figure 5-2, top row) and the alignment parameter (Figure 5-2, bottom row) over time further confirmed the trends reflected in the angle of alignment and angular spread data. As shown in Table 5-3, the nematic angle had a tight distribution centered around 90° for the static wrinkled case. Conversely, cells atop the static non-wrinkled substrates showed a large spread in their nematic angle. Cells atop actively wrinkling surfaces showed a decrease in the deviation over time of the nematic angle (88.21° ± 17.96° before, 84.79° ± 14.38° during, and 95.54° ± 9.01° after the surface transition), coupled with a tighter distribution about 90°. The alignment parameter further confirmed these trends. As shown in Table 5-4, cells atop static wrinkled surfaces had an alignment of approximately 0.59. Comparatively, cells atop static non-wrinkled surfaces had an alignment of approximately 0.37. For the actively wrinkling substrates, cells quickly transitioned from an alignment of 0.46 ± 0.07 before, to 0.53 ± 0.08 during, and 0.60 ± 0.08 after the surface change. Collectively, nuclear angle, angular spread, nematic angle, and the alignment data confirmed that cells reorient their nuclei to align to the developing topography within an approximate 6 hour duration following the surface change.

Nuclear-Golgi polarization was next considered to determine whether a link existed between nuclear and cytoskeletal reorganization over time in response to the developing surface topography. Angle of alignment and angular spread analyses were applied to the nuclear-Golgi polarization vector data. In general, nuclear-Golgi polarization vectors had a large standard deviation, regardless of substrate type. This was partially attributed to inconsistencies in Golgi fragmentation frame to frame, which led to a large deviation in the calculated polarization angle. This variability was also attributed to a reduced number of Golgi-nuclei pairs, as the infection efficiency was not 100% for RFP-Golgi tagging. Regardless, we demonstrated that cell nuclei and

Golgi bodies align in the same direction atop static wrinkled substrates (parallel to the pattern direction), while cells atop static non-wrinkled substrates show no similar orientation preference (Figure 5-3). The polarization angle of cells atop static wrinkled substrates deviated from the measured wrinkle angle by 10.72° ± 22.70° before, 11.70° ± 24.87° during, and 10.51° ± 21.89° after the potential surface transition (Table 5-5), confirming that this orientation was in the pattern direction. Comparatively, the polarization angle of cells atop non-wrinkled surfaces had a much larger standard deviation, with erratic mean angle of alignment values of 60.33° ± 41.01° before, 95.25° ± 31.45° during, and 70.58° ± 32.29° after the potential transition. Unsurprisingly, cells atop the active wrinkling surfaces displayed the greatest change in the polarization alignment during the transition region. As shown in Table 5-3, the polarization vector angle differed from the measured wrinkle angle in the active wrinkling system by 17.61° ± 26.05° before, 16.08° ± 28.46° during, and 23.00° ± 29.51° after the topography developed.

Angular spread trends were less pronounced in the nuclear-Golgi polarization analysis compared to the nuclear only plots (Figure 5-3, bottom row), however there was still a slight increase in nuclear-Golgi alignment over time atop the actively wrinkling surfaces (Table 5-6). It is interesting to note that a decrease in nuclear-Golgi angular spread over time was observed for all substrates. We hypothesize that this may partially be due to temperature effects, as actin polymerization is temperature dependent in some cell types [34, 35]. An increase in orientation over time could also be explained by ECM deposition over time, as cells would preferentially move along ECM “tracks”, most likely polarizing to achieve this motion. Collectively, the presented nuclear-Golgi polarization evidence suggests cytoskeletal rearrangement occurs on a much longer scale compared to nuclear reorientation. This rearrangement is much more prone to variability due to inconsistencies in Golgi fragmentation and a reduced number of nuclei-Golgi pairs (compared to nuclei alone) but clearly demonstrates that a polarization response is coupled with the surface topography change.

Cell velocity behaviors revealed that cells atop static wrinkled and active wrinkling surfaces preferentially migrated along the x-direction (parallel to substrate topography), while cells atop static non-wrinkled surfaces had equivalent x- and y-velocities (perpendicular to substrate topography). Overall speeds were consistent across all substrate types. Cell velocity values were calculated differently from those presented in **Chapter 4** to account for noise and phototoxicity effects. More specifically, cells with frame gaps were interpolated to smooth velocity values, cells with a maximum speed of less than 0.125 μm/min were removed from the analysis to reduce noise, and cells with a significant decrease in their standard deviation of acceleration over time were removed to accommodate phototoxicity. Representative plots of average cell velocities over time revealed that cells atop patterned surfaces moved faster in the x-direction, compared to the y-direction (Figure 5-4). When looking at the overall speed, cells atop all substrates had an approximate average speed of 0.40 μm/min before, 0.40 μm/min during, and 0.27 μm/min after the potential surface transition (Table 5-7 and Figure 5-4, bottom row). This average value decreased drastically over the final time interval of interest, indicating that phototoxicity was a concern. In regards to the decomposed velocity, cells atop the static non-wrinkled surfaces showed equivalent velocity behaviors in x (Table 5-8) and y (Table 5-9) directions. Conversely, cells atop static wrinkled and active wrinkling surfaces showed a bias towards motion in the x direction, as is evident in a larger ratio of average x:y velocity values (Table 5-10). It was surprising to note that cells atop the actively wrinkling surfaces had a faster x-velocity prior to the surface transition.

We hypothesized that the cells may “feel” the underlying substrate strain, causing faster motion along the x-direction. These behaviors contradict results shown in **Chapter 4**. We assumed that this is mostly due to additional constraints on velocity calculations to accommodate noise and phototoxicity effects.

5.4.2 ROCK Inhibition Abolishes Directional Motility on Actively Changing Surfaces

ROCK inhibition of fibroblasts abolished the cell’s ability to recognize the topographical transition, subsequently resulting in no significant alignment of the cell’s internal structure or motility preferences after the wrinkle pattern fully developed. Similar to the uninhibited data, inhibited analysis was broken down into three categories: 1) a 4 hr pre-trigger portion where cells were only exposed to the 30°C microenvironment (hereafter referred to as “before the potential transition”), 2) an 8 hr region directly after the temperature increase to 37°C (hereafter referred to as “during the potential transition”), and 3) a 12 hr post-trigger portion after the full material transition where the cells were in equilibrium at 37°C (hereafter referred to as “after the potential transition”). Cell trajectory behavior of uninhibited versus ROCK inhibited cells was visualized to illustrate differences in bulk motility dynamics. As shown in Figure 5-5, cells atop uninhibited active wrinkling and static wrinkled substrates showed preferential motion along the direction of anisotropy. Conversely, cells atop uninhibited non-wrinkled, ROCK active wrinkling, ROCK non-wrinkled, and ROCK wrinkled substrates demonstrated random motion. This was immediately interesting, as it signified that the cells were no longer responding to topographical cues. Further analysis of mean squared displacement (MSD) and velocity autocorrelation function (VACF) dynamics over time revealed that cell movement was persistent over at least a decade. Plots of the

MSD over time demonstrated quasi-ballistic (slope = ~1.5) cell motion across all substrate types for at least a 10 hr duration (Figure 5-6). Similar dynamics were observed in the VACF plots over time (Figure 5-7). In the case of the VACF, a nearly straight-line fit on the log-log plots was observed, suggesting almost power law behavior for one decade. Again, this indicated persistent motion of the fibroblast cells over long timescales, regardless of surface type or ROCK inhibition.

To understand the mechanisms driving this ROCK-based motility modification, nuclear alignment, nuclear-Golgi polarization, and cell velocity dynamics were characterized before, during, and after the potential shape change. Clear differences in nuclear alignment of uninhibited versus ROCK inhibited cells were immediately apparent. As shown in Figure 5-8, cells atop all of the ROCK inhibited microenvironments demonstrated large fluctuations in the mean nuclear angle of alignment over time, coupled with large standard deviations of these angle values. ROCK inhibited non-wrinkled substrates showed the same trends as uninhibited non-wrinkled substrates ($p > 0.1$ in all condition comparisons), with an average angle of alignment of 81.17° ± 25.18° before, 96.67° ± 30.61° during, and 97.33° ± 30.00° after the potential transition (Table 5-11). Cells atop ROCK inhibited active wrinkling substrates showed comparable alignment behaviors, with an average difference in the nuclear angle and the measured wrinkled angle of 25.07° ± 28.88° before, 31.55° ± 31.97° during, and 22.93° ± 35.60° after the surface transition. Interestingly, cells atop ROCK inhibited wrinkled substrates slowly lost their nuclear orientation, as is evident by an increase in the standard deviation and the difference between the nuclear angle and measured wrinkle angle over time (5.76° ± 10.54° before, 6.07° ± 18.56° during, and 29.24° ± 20.26° after the potential transition). This suggested that the cells, which were previously polarized to the substrate topography, were slowly de-polarizing due to ROCK inhibition. Plots of nuclear angular spread over time reinforced these claims (Figure 5-9). Cells atop ROCK inhibited non-wrinkled substrates showed a consistent nuclear angular spread of approximately 47° (Table 5-12). While nuclear angular spread was more deviated on ROCK inhibited active wrinkling substrates, similar average results (46.54° ± 2.43° before, 46.57° ± 2.57° during, and 46.15° ± 2.86° after the shape change) were observed for the aggregate data. For ROCK inhibited wrinkled substrates, cells slowly lost orientation over time, as was indicated by an increase in angular spread from 43.30° ± 2.12° before, 43.56° ± 2.09° during, and 44.50° ± 2.32° after the potential shape change. Nematic angle (Figure 5-10 and Table 5-13) and alignment parameter (Figure 5-11 and Table 5-14) results further echoed these trends. In summary, it was evident that ROCK inhibition abolished the fibroblast's ability to recognize and orient (or reorient) cell nuclei to the pattern direction.

Nuclear-Golgi polarization was then measured to assess the role of cytoskeletal reorganization in ROCK inhibited cells subjected to a change in surface topography. As shown in Figure 5-12, ROCK inhibition abolished the cell's ability to polarize, regardless of surface type. This was clear in the aggregate nuclear-Golgi polarization angle and wrinkle angle difference values calculated (Table 5-15). For example, when measuring the difference between the polarization angle and the measured wrinkle direction, cells atop ROCK inhibited non-wrinkled substrates had values of 61.67° ± 23.51° before, 102.33° ± 33.37° during, and 135.17° ± 33.86° after the potential transition. For cells atop the active wrinkling surfaces, a minor decrease in the difference between the polarization and wrinkle angle was observed during the transition (39.86° ± 36.73° before and 26.48° ± 34.72° during the transition). However, this temporary alignment was lost after the surface stabilized (32.40° ± 31.08° after the transition), indicating that the cells could not recognize the surface change. Comparatively, cells atop the ROCK inhibited wrinkled surfaces slowly lost their polarization over time (13.22° ± 23.50° prior, 15.23° ± 25.36° during, and 17.03° ± 21.89° after). Nuclear-Golgi angular spread confirmed that cells still had the ability to polarize, but that these dynamics were not linked with the wrinkle direction (Table 5-16). In general, ROCK inhibited cells exhibited less deviation in the nuclear-Golgi polarization angular spread (Figure 5-13). Collectively, these results indicated that ROCK inhibition abolishes the fibroblast's ability to polarize in response to the changing surface topography and that previously aligned cells slowly lose their preferential wrinkle orientation over time.

ROCK inhibition yielded no significant differences in cell speeds across all substrate types. As shown in Figure 5-14 and Table 5-17, the average speed of fibroblasts was approximately 0.40 μm/min regardless of surface topography or ROCK inhibition. While reduction of the number of z-slices acquired per time-point resulted in improvement of phototoxicity, there was still some evidence of reduction in speeds during the "post transition" region. When looking at decomposed x- (Table 5-18 and Figure 5-15) and y-velocity (Table 5-19 and Figure 5-16) values, it was interesting to note that all of the substrates with a topography (active wrinkling, static wrinkled, ROCK inhibited active wrinkling, and ROCK inhibited wrinkled) demonstrated preferential motion in the x-direction (Table 5-20). Conversely, cells atop non-wrinkled and ROCK inhibited non-wrinkled substrates showed no preferential motion. This indicates that the cells, to some effect still sense the surface topography, however they cannot polarize to direct motility responses in the direction of anisotropy. In summary, ROCK inhibition led to a complete loss of nuclear and nuclear-Golgi rearrangement of cells atop active wrinkling surfaces, while cells atop static wrinkled surfaces showed a decrease in nuclear and nuclear-Golgi orientation over time.

5.5. Discussion: Rho Signaling is Required for Topographic Recognition

This research shows the effects of rock inhibition on nuclear orientation, cell polarization, and motility responses of fibroblast cells, through the use of the first reported example of multi-organelle tracking. Here, we demonstrated that cells on static wrinkled topographies align their nuclei to the pattern direction, whereas cells atop static non-wrinkled surfaces displayed random nuclear orientation (Figures 5-1 and 5-2, Tables 5-1 through 5-4). We additionally showed that the nuclear-Golgi polarization angle was closely aligned to the wrinkle direction in static wrinkled systems, whereas no preferential orientation was observed atop static non-wrinkled surfaces (Figure 5-3, Tables 5-5 and 5-6). This was coupled with preferential motion along the wrinkle direction in the static wrinkled case, while random motion was observed in the static non-wrinkled case. With ROCK inhibition, this preferential movement direction atop static wrinkled substrates was lost (Figure 5-5), most likely due to the cell's inability to reorient their nuclear-Golgi axis to accommodate directional motion. This was noted only as a directional loss, as cell motion was consistently persistent regardless of substrate type or ROCK inhibition status (Figures 5-6 and 5-7), indicating that ROCK plays a role in surface pattern recognition, but not in general fibroblast motility persistence. We further demonstrated that nuclear orientation is directly related to ROCK, as ROCK inhibition slowly abolished nuclear alignment (Figures 5-8 through 5-11 and Tables 5-11 through 5-14) and nuclear-Golgi polarization atop the static wrinkled substrates over time (Figures 5-12 and 5-13 and Tables 5-15 and 5-16).

This study also represents the first successful characterization of the relationship between cell motility, nuclear reorientation, and nuclear-Golgi polarization in uninhibited and ROCK inhibited fibroblast cells responding to a dynamic surface change in their microenvironment. We showed that cells atop actively wrinkling substrates altered their motility by switching from random to preferential migration along the pattern direction, post transition. This was associated with nuclear reorientation and nuclear-Golgi polarization over time. Uninhibited fibroblasts atop actively wrinkling surfaces reoriented their nuclei to the developing pattern direction over a 6 hr time-period. The nuclear-Golgi polarization timescale was found to be much longer, with cells showing a difference in angular spread approximately 10 hrs after the material started to transition. Just as with the static systems, ROCK activity was critical in identifying this topographical change. ROCK inhibited cells moved with random trajectories, even after the pattern fully developed. Again, this was associated with the inability to reorient their nuclei or polarize their nuclear-Golgi structures, as was evident in the mean nuclear angle of alignment, nuclear angular spread, mean nuclear-Golgi angle of alignment, and nuclear-Golgi angular spread results. These novel claims could not have been resolved through time-point analyses or by investigating static substrates in time-lapse alone.

Previous literature demonstrates that ECM organization, cell polarization, and cell motility dynamics regulate critical biological processes, including contact guidance, EMT and MET, cell-ECM and cell-cell signaling, mechanotransduction, and phenotypic and differentiation responses [36]. Rajnicek and colleagues reported that Rho guides corneal epithelial alignment on grooved (<100 nm) quartz slides [37]. These results reinforced our findings for C3H10T1/2 fibroblasts. Totsukawa and colleagues investigated the role of ROCK in 3T3 fibroblast motility and its implication in focal adhesion generation and disassembly. More specifically, they showed that ROCK inhibited cells (cultured on a coverslip) moved both faster and in a straighter path due to myosin light chain kinase inhibition towards the center, but not on the periphery of the cells [38].

Our velocity results indicated no comparable increase in speed, suggesting that these dynamics may be based on cell-ECM or phenotypic responses. However, our MSD and VACF results revealed comparable fibroblast persistence in the direction of motion, though no significant difference in uninhibited versus ROCK inhibited cells was observed. We hypothesize that our larger sample size and tracking duration, enabled by ACT*IV*E nuclear and Golgi body coupling, revealed aggregate trends incapable of being resolved through manual tracking methods. Gaggioli and colleagues further showed that ECM remodeling by stromal fibroblasts was a Rho-mediated process. ROCK inhibition prevented stromal fibroblasts from creating tracks in the ECM to promote squamous cell carcinoma invasion [39]. This was an interesting comparison to make with our system because it implied that ROCK inhibited C3H10T1/2 fibroblasts lose their ability to manipulate or deposit ECM proteins in their changing extracellular environment. This in turn alters their motility dynamics and their ability to polarize, suggesting that ECM manipulation by cells is necessary to recognize and respond to physical changes in their surroundings.

We recognize that there were a few limitations of the current study and expansions that could be executed to reinforce or build upon the work presented in this chapter. First, phototoxicity was evident in the uninhibited data presented. To reduce phototoxicity, the number of z-slices was reduced for the inhibited data sets at the cost of lower z-resolution (particularly on the surfaces with a topography). Reducing the imaging frequency may be useful in resolving this issue. Similarly, the selected cell density (4000 cells/cm^2) was originally chosen based on the number of nuclei tracked in **Chapter 4** (~30-50 cells per video). However, RFP-Golgi infections were not 100%, so linking nuclei-Golgi pairs resulted in 15-30 viable cells for tracking per position imaged. To improve the statistics associated with the nuclear-Golgi polarization analysis and decrease some of the variability in the system, cell density could be increased and the experiments repeated. As previously mentioned, the use of a thermal trigger was potentially problematic when measuring Golgi body responses, as actin polymerization [34, 35] and microtubule assembly can be sensitive to temperature conditions. While we were able to quantify a change in nuclear-Golgi polarization, reducing the temperature range that the cells experience (so that the pre-trigger condition falls closer to body temperature) would improve overall characterization. In regards to future work, expansion of this study to investigate a metastatic cancer line could provide direct insight into how ECM reorganization influences EMT responses. Similarly, investigating the effects of inhibiting additional pathways (e.g. Rac or Cdc42) could provide further information about how the cell machinery is responding to the developing topography. Lastly, quantifying focal adhesion formation over time could provide further insight into cell-ECM interaction dynamics.

5.6 Conclusions

Cell motility is a complex biological process dictated by cell-ECM interactions and intracellular reorganization. Here, we used a shape memory biomaterial as a platform for investigating intracellular reorganization and the mechanistic responses of inhibiting the Rho pathway in fibroblast cell motility. This study represents the first example of multi-organelle tracking as a means to characterize the *relationship between surface topography and its role on uninhibited and ROCK inhibited fibroblast* nuclear orientation, cell polarization, and motility responses. This study also represents the first example of cell motility, nuclear reorientation, and nuclear-Golgi polarization responses in uninhibited and ROCK inhibited fibroblast cells *responding to a dynamic surface change* in their microenvironment. Nuclear orientation results revealed that cells on static wrinkled surfaces orient their nuclei and polarize their nuclear-Golgi axis in the pattern direction, compared to random nuclear and nuclear-Golgi orientation on static flat surfaces. In the dynamic environment, uninhibited fibroblasts reoriented their nuclei to the developing pattern direction within an approximate 6 hr duration following the topographic change. This was coupled with nuclear-Golgi polarization along the wrinkle direction across a much longer timescale, with an increase in alignment ~10 hrs post-trigger. We further demonstrated that the ability for the cells to reorganize their internal structure in response to this surface change was directly dictated by Rho-mediated processes. ROCK inhibition completely abolished the cell's ability to recognize the developing surface pattern by preventing nuclear and Golgi reorganization. This led to consistently persistent migration of the cells (even under ROCK inhibition), but loss of the ability to align cell motion to pattern direction. These dynamics may further be linked to a loss in the ability to locally manipulate ECM deposition or reorganization by the cells, suggesting that fibroblasts use Rho to relay information regarding physical environmental cues. This new knowledge has important implications for *in vivo* applications, as it demonstrates that disruption of the ROCK pathway prevents cells from interpreting mechanical cues relevant in developmental, tissue repair, and disease progression responses.

5.7 References

1. Giancotti, F.G. and E. Ruoslahti, *Integrin signaling.* Science, 1999. **285**(5430): p. 1028-1032.
2. Guan, J.-L., *Role of focal adhesion kinase in integrin signaling.* The International Journal of Biochemistry & Cell Biology, 1997. **29**(8): p. 1085-1096.

3. Mitra, S.K., D.A. Hanson, and D.D. Schlaepfer, *Focal adhesion kinase: In command and control of cell motility.* Nature Reviews Molecular Cell Biology, 2005. **6**(1): p. 56-68.
4. Zhao, X. and J.-L. Guan, *Focal adhesion kinase and its signaling pathways in cell migration and angiogenesis.* Advanced Drug Delivery Reviews, 2011. **63**(8): p. 610-615.
5. Di Cio, S. and J.E. Gautrot, *Cell sensing of physical properties at the nanoscale: Mechanisms and control of cell adhesion and phenotype.* Acta Biomaterialia, 2016. **30**: p. 26-48.
6. Nagano, M., et al., *Turnover of focal adhesions and cancer cell migration.* International Journal of Cell Biology, 2012.
7. Gupton, S.L., et al., *Cell migration without a lamellipodium: Translation of actin dynamics into cell movement mediated by tropomyosin.* Journal of Cell Biology, 2005. **168**(4): p. 619-631.
8. Moore, S.W., P. Roca-Cusachs, and M.P. Sheetz, *Stretchy proteins on stretchy substrates: The important elements of integrin-mediated rigidity sensing.* Developmental Cell, 2010. **19**(2): p. 194-206.
9. Schwartz, M., *Rho signalling at a glance.* Journal of Cell Science, 2004. **117**(23): p. 5457.
10. Raftopoulou, M. and A. Hall, *Cell migration: Rho GTPases lead the way.* Developmental Biology, 2004. **265**(1): p. 23-32.
11. Ishizaki, T., et al., *p160(ROCK), a Rho-associated coiled-coil forming protein kinase, works downstream of Rho and induces focal adhesions.* FEBS Letters, 1997. **404**(2-3): p. 118-124.
12. Parri, M. and P. Chiarugi, *Rac and Rho GTPases in cancer cell motility control.* Cell Communication and Signaling, 2010. **8**.

13. Thiery, J.P., *Epithelial-mesenchymal transitions in development and pathologies.* Current Opinion in Cell Biology, 2003. **15**(6): p. 740-746.

14. Yang, J. and R.A. Weinberg, *Epithelial-Mesenchymal Transition: At the Crossroads of Development and Tumor Metastasis.* Developmental Cell, 2008. **14**(6): p. 818-829.

15. Rozario, T. and D.W. DeSimone, *The extracellular matrix in development and morphogenesis: A dynamic view.* Developmental Biology, 2010. **341**(1): p. 126-140.

16. Kalluri, R. and R.A. Weinberg, *The basics of epithelial-mesenchymal transition.* Journal of Clinical Investigation, 2009. **119**(6): p. 1420-1428.

17. Brabletz, T., *EMT and MET in Metastasis: Where Are the Cancer Stem Cells?* Cancer Cell. **22**(6): p. 699-701.

18. Thiery, J.P., et al., *Epithelial-Mesenchymal Transitions in Development and Disease.* Cell, 2009. **139**(5): p. 871-890.

19. Oft, M., R.J. Akhurst, and A. Balmain, *Metastasis is driven by sequential elevation of H-ras and Smad2 levels.* Nature Cell Biology, 2002. **4**(7): p. 487-494.

20. Sahai, E. and C.J. Marshall, *ROCK and Dia have opposing effects on adherens junctions downstream of Rho.* Nature Cell Biology, 2002. **4**(6): p. 408-415.

21. Etienne-Manneville, S., *Microtubules in cell migration*, in *Annual Review of Cell and Developmental Biology*. 2013. p. 471-499.

22. Yadav, S., S. Puri, and A.D. Linstedt, *A Primary Role for Golgi Positioning in Directed Secretion, Cell Polarity, and Wound Healing.* Molecular Biology of the Cell, 2009. **20**(6): p. 1728-1736.

23. Yang, P., et al., *In vitro wrinkle formation via shape memory dynamically aligns adherent cells.* Soft Matter, 2013. **9**(18): p. 4705-4714.
24. Narumiya, S., T. Ishizaki, and M. Uehata, *Use and properties of ROCK-specific inhibitor Y-27632*, in *Methods in Enzymology*. 2000. p. 273-284.
25. Forster, B., et al., *Complex wavelets for extended depth-of-field: A new method for the fusion of multichannel microscopy images.* Microscopy Research and Technique, 2004. **65**(1-2): p. 33-42.
26. Baker, R.M., et al., *Automated, contour-based tracking and analysis of cell behaviour over long time scales in environments of varying complexity and cell density.* Journal of The Royal Society Interface, 2014. **11**(97).
27. Desai, R.A., et al., *Cell polarity triggered by cell-cell adhesion via E-cadherin.* Journal of Cell Science, 2009. **122**(7): p. 905-911.
28. Ridley, A.J., et al., *Cell Migration: Integrating Signals from Front to Back.* Science, 2003. **302**(5651): p. 1704-1709.
29. Friedl, P., K. Wolf, and J. Lammerding, *Nuclear mechanics during cell migration.* Current Opinion in Cell Biology, 2011. **23**(1): p. 55-64.
30. Serrador, J.M., M. Nieto, and F. Sánchez-Madrid, *Cytoskeletal rearrangement during migration and activation of T lymphocytes.* Trends in Cell Biology, 1999. **9**(6): p. 228-233.
31. Shoelson, B., *clusterData*. 2012: Mathworks File Exchange.
32. Gao, Y.X. and M.L. Kilfoil, *Accurate detection and complete tracking of large populations of features in three dimensions.* Optics Express, 2009. **17**(6): p. 4685-4704.

33. Davidson, P., et al., *Definition of a simple statistical parameter for the quantification of orientation in two dimensions: Application to cells on grooves of nanometric depths.* Acta Biomaterialia, 2010. **6**(7): p. 2590-2598.
34. Niranjan, P.S., et al., *The polymerization of actin: Thermodynamics near the polymerization line.* Journal of Chemical Physics, 2003. **119**(7): p. 4070-4084.
35. Fujiwara, S., et al., *Differences in internal dynamics of actin under different structural states detected by neutron scattering.* Biophysical Journal, 2008. **94**(12): p. 4880-4889.
36. Dalby, M.J., N. Gadegaard, and R.O.C. Oreffo, *Harnessing nanotopography and integrin-matrix interactions to influence stem cell fate.* 2014. **13**(6): p. 558-569.
37. Rajnicek, A.M., L.E. Foubister, and C.D. McCaig, *Alignment of corneal and lens epithelial cells by co-operative effects of substratum topography and DC electric fields.* Biomaterials, 2008. **29**(13): p. 2082-2095.
38. Totsukawa, G., et al., *Distinct Roles of Rock (Rho-Kinase) and Mlck in Spatial Regulation of Mlc Phosphorylation for Assembly of Stress Fibers and Focal Adhesions in 3t3 Fibroblasts.* The Journal of Cell Biology, 2000. **150**(4): p. 797.
39. Gaggioli, C., et al., *Fibroblast-led collective invasion of carcinoma cells with differing roles for RhoGTPases in leading and following cells.* Nature Cell Biology, 2007. **9**(12): p. 1392-U92.

Table 5-1: Difference in nuclear angle of alignment compared to actual wrinkle direction for active wrinkling, static non-wrinkled, and static wrinkled microenvironments prior, during, or after the potential topographic transition

	Active Wrinkling (degrees)	**Static Non-Wrinkled (degrees)**	**Static Wrinkled (degrees)**
Prior to Transition	12.66 ± 21.06	101.5 ± 34.78	4.49 ± 13.13
During Transition	7.51 ± 17.67	90 ± 35.14	6.52 ± 15.17
Post Transition	9.73 ± 13.42	90 ± 31.52	11.38 ± 17.59

Table 5-2: Nuclear angular spread for active wrinkling, static non-wrinkled, and static wrinkled microenvironments prior, during, or after the potential topographic transition

	Active Wrinkling (degrees)	**Static Non-Wrinkled (degrees)**	**Static Wrinkled (degrees)**
Prior to Transition	42.87 ± 3.36	47.26 ± 2.28	36.45 ± 4.44
During Transition	39.62 ± 4.21	46.25 ± 2.85	38.10 ± 3.95
Post Transition	36.40 ± 4.34	46.37 ± 2.66	37.30 ± 3.63

Table 5-3: Nematic angle results for active wrinkling, static non-wrinkled, and static wrinkled microenvironments prior, during, or after the potential topographic transition

	Active Wrinkling (degrees)	**Static Non-Wrinkled (degrees)**	**Static Wrinkled (degrees)**
Prior to Transition	88.21 ± 17.96	100.00 ± 31.87	91.17 ± 8.39
During Transition	84.79 ± 14.38	79.50 ± 33.98	92.00 ± 8.19
Post Transition	95.54 ± 9.01	108.50 ± 30.84	91.33 ± 13.51

Table 5-4: Alignment results for active wrinkling, static non-wrinkled, and static wrinkled microenvironments prior, during, or after the potential topographic transition

	Active Wrinkling	**Static Non-Wrinkled**	**Static Wrinkled**
Prior to Transition	0.46 ± 0.07	0.36 ± 0.05	0.60 ± 0.08
During Transition	0.53 ± 0.08	0.38 ± 0.07	0.58 ± 0.08
Post Transition	0.60 ± 0.08	0.38 ± 0.06	0.59 ± 0.07

Table 5-5: Difference in nuclear-Golgi polarization angle of alignment compared to actual wrinkle direction for active wrinkling, static non-wrinkled, and static wrinkled microenvironments prior, during, or after the potential topographic transition

	Active Wrinkling (degrees)	**Static Non-Wrinkled (degrees)**	**Static Wrinkled (degrees)**
Prior to Transition	17.61 ± 26.05	60.33 ± 41.01	10.72 ± 22.70
During Transition	16.08 ± 28.46	95.25 ± 31.45	11.70 ± 24.87
Post Transition	23.00 ± 29.51	70.58 ± 32.29	10.51 ± 21.89

Table 5-6: Nuclear-Golgi polarization angular spread for active wrinkling, static non-wrinkled, and static wrinkled microenvironments prior, during, or after the potential topographic transition

	Active Wrinkling (degrees)	**Static Non-Wrinkled (degrees)**	**Static Wrinkled (degrees)**
Prior to Transition	41.45 ± 5.67	42.69 ± 8.67	37.09 ± 6.86
During Transition	39.50 ± 7.42	41.00 ± 8.72	36.28 ± 8.18
Post Transition	38.69 ± 8.79	40.86 ± 8.34	33.99 ± 8.51

Table 5-7: Average speed of cells atop active wrinkling, static non-wrinkled, and static wrinkled microenvironments prior, during or after the potential topographic transition.

	Active Wrinkling (µm/min)	**Static Non-Wrinkled (µm/min)**	**Static Wrinkled (µm/min)**
Prior to Transition	0.42 ± 0.26	0.40 ± 0.21	0.40 ± 0.21
During Transition	0.42 ± 0.28	0.36 ± 0.21	0.41 ± 0.26
Post Transition	0.29 ± 0.20	0.23 ± 0.14	0.27 ± 0.18

Table 5-8: Average x-velocities of cells atop active wrinkling, static non-wrinkled, and static wrinkled microenvironments prior, during or after the potential topographic transition.

	Active Wrinkling (µm/min)	**Static Non-Wrinkled (µm/min)**	**Static Wrinkled (µm/min)**
Prior to Transition	0.35 ± 0.40	0.25 ± 0.26	0.36 ± 0.38
During Transition	0.36 ± 0.42	0.22 ± 0.25	0.37 ± 0.42
Post Transition	0.25 ± 0.29	0.15 ± 0.17	0.24 ± 0.28

Table 5-9: Average y-velocities of cells atop active wrinkling, static non-wrinkled, and static wrinkled microenvironments prior, during or after the potential topographic transition.

	Active Wrinkling (µm/min)	**Static Non-Wrinkled (µm/min)**	**Static Wrinkled (µm/min)**
Prior to Transition	0.11 ± 0.15	0.25 ± 0.26	0.05 ± 0.08
During Transition	0.09 ± 0.14	0.23 ± 0.24	0.05 ± 0.09
Post Transition	0.06 ± 0.10	0.15 ± 0.16	0.03 ± 0.06

Table 5-10: Ratio of average x and y velocities of cells atop active wrinkling (A), static non-wrinkled (NW), and static wrinkled (W) microenvironments prior, during, or after the potential topographic transition.

	Active Wrinkling (µm/min)	**Static Non-Wrinkled (µm/min)**	**Static Wrinkled (µm/min)**
Prior to Transition	3.18	1.00	7.20
During Transition	4.00	0.96	7.40
Post Transition	4.17	1.00	8.00

Table 5-11: Difference in nuclear angle of alignment compared to actual wrinkle direction for active wrinkling (A), static non-wrinkled (NW), ROCK inhibited active wrinkling (RA), ROCK inhibited static non-wrinkled (RNW), ROCK inhibited static wrinkled (RW), and static wrinkled (W) microenvironments prior, during, or after the potential topographic transition

	Prior to Transition (degrees)	**During Transition (degrees)**	**Post Transition (degrees)**
A	31.17 ± 26.98	10.70 ± 18.92	11.98 ± 16.53
NW	98.20 ± 33.00	77.43 ± 27.75	52.75 ± 26.57
RA	25.07 ± 28.88	31.55 ± 31.97	22.93 ± 35.60
RNW	81.17 ± 25.18	96.67 ± 30.61	97.33 ± 30.00
RW	5.76 ± 10.54	6.07 ± 18.56	29.24 ± 20.26
W	5.79 ± 10.72	4.93 ± 8.78	3.93 ± 10.93

Table 5-12: Nuclear angular spread of cells atop active wrinkling (A), static non-wrinkled (NW), ROCK inhibited active wrinkling (RA), ROCK inhibited static non-wrinkled (RNW), ROCK inhibited static wrinkled (RW), and static wrinkled (W) microenvironments prior, during, or after the potential topographic transition

	Prior to Transition (degrees)	**During Transition (degrees)**	**Post Transition (degrees)**
A	45.46 ± 2.79	41.70 ± 3.49	40.81 ± 3.82
NW	48.25 ± 1.50	47.38 ± 2.02	47.55 ± 1.95
RA	46.54 ± 2.43	46.57 ± 2.57	46.15 ± 2.86
RNW	47.95 ± 1.48	47.56 ± 1.79	46.92 ± 2.06
RW	43.30 ± 2.12	43.56 ± 2.09	44.50 ± 2.32
W	38.19 ± 3.32	34.30 ± 4.07	36.01 ± 3.60

Table 5-13: Nematic angle results for cells atop active wrinkling (A), static non-wrinkled (NW), ROCK inhibited active wrinkling (RA), ROCK inhibited static non-wrinkled (RNW), ROCK inhibited static wrinkled (RW), and static wrinkled (W) microenvironments prior, during, or after the potential topographic transition

	Prior to Transition (degrees)	**During Transition (degrees)**	**Post Transition (degrees)**
A	72.67 ± 26.06	86.67 ± 15.69	67.06 ± 11.64
NW	102.37 ± 32.92	100.07 ± 26.44	77.73 ± 26.37
RA	70.17 ± 26.61	94.39 ± 28.76	91.94 ± 34.53
RNW	79.33 ± 24.17	109.50 ± 29.99	125.50 ± 27.82
RW	86.17 ± 7.63	88.00 ± 14.96	100.83 ± 17.72
W	91.00 ± 8.50	90.33 ± 5.44	90.75 ± 6.23

Table 5-14: Alignment results for cells atop active wrinkling (A), static non-wrinkled (NW), ROCK inhibited active wrinkling (RA), ROCK inhibited static non-wrinkled (RNW), ROCK inhibited static wrinkled (RW), and static wrinkled (W) microenvironments prior, during, or after the potential topographic transition

	Prior to Transition	**During Transition**	**Post Transition**
A	0.40 ± 0.06	0.49 ± 0.07	0.51 ± 0.08
NW	0.33 ± 0.03	0.35 ± 0.05	0.34 ± 0.04
RA	0.37 ± 0.05	0.37 ± 0.06	0.38 ± 0.06
RNW	0.34 ± 0.04	0.35 ± 0.04	0.37 ± 0.04
RW	0.45 ± 0.04	0.45 ± 0.05	0.42 ± 0.04
W	0.56 ± 0.06	0.65 ± 0.08	0.64 ± 0.06

Table 5-15: Difference in nuclear-Golgi polarization angle of alignment compared to actual wrinkle direction for active wrinkling (A), static non-wrinkled (NW), ROCK inhibited active wrinkling (RA), ROCK inhibited static non-wrinkled (RNW), ROCK inhibited static wrinkled (RW), and static wrinkled (W) microenvironments prior, during, or after the potential topographic transition

	Prior to Transition (degrees)	**During Transition (degrees)**	**Post Transition (degrees)**
A	29.67 ± 28.73	15.31 ± 33.27	17.11 ± 31.94
NW	48.77 ± 31.87	103.03 ± 29.63	94.40 ± 29.72
RA	39.86 ± 36.73	26.48 ± 34.72	32.40 ± 31.08
RNW	61.67 ± 23.51	102.33 ± 33.37	135.17 ± 33.86
RW	13.22 ± 23.50	15.23 ± 25.36	17.03 ± 21.89
W	19.63 ± 20.26	12.91 ± 23.08	8.06 ± 15.69

Table 5-16: Nuclear-Golgi polarization angular spread of cells atop active wrinkling (A), static non-wrinkled (NW), ROCK inhibited active wrinkling (RA), ROCK inhibited static non-wrinkled (RNW), ROCK inhibited static wrinkled (RW), and static wrinkled (W) microenvironments prior, during, or after the potential topographic transition

	Prior to Transition (degrees)	**During Transition (degrees)**	**Post Transition (degrees)**
A	40.08 ± 7.41	38.83 ± 7.83	42.24 ± 5.61
NW	42.25 ± 7.28	39.72 ± 7.08	44.46 ± 4.75
RA	44.54 ± 5.56	41.80 ± 7.03	42.43 ± 6.33
RNW	43.68 ± 4.08	42.97 ± 5.65	42.86 ± 5.67
RW	40.79 ± 5.97	39.48 ± 7.23	37.78 ± 7.42
W	35.12 ± 8.52	37.36 ± 7.81	28.11 ± 9.33

Table 5-17: Average speeds of cells atop active wrinkling (A), static non-wrinkled (NW), ROCK inhibited active wrinkling (RA), ROCK inhibited static non-wrinkled (RNW), ROCK inhibited static wrinkled (RW), and static wrinkled (W) microenvironments prior, during, or after the potential topographic transition

	Prior to Transition (µm/min)	**During Transition (µm/min)**	**Post Transition (µm/min)**
A	0.45 ± 0.23	0.45 ± 0.29	0.38 ± 0.27
NW	0.46 ± 0.19	0.42 ± 0.19	0.36 ± 0.15
RA	0.42 ± 0.29	0.42 ± 0.23	0.40 ± 0.25
RNW	0.44 ± 0.18	0.38 ± 0.16	0.27 ± 0.13
RW	0.44 ± 0.15	0.44 ± 0.19	0.35 ± 0.19
W	0.50 ± 0.20	0.47 ± 0.23	0.41 ± 0.21

Table 5-18: Average x-velocities of cells atop active wrinkling (A), static non-wrinkled (NW), ROCK inhibited active wrinkling (RA), ROCK inhibited static non-wrinkled (RNW), ROCK inhibited static wrinkled (RW), and static wrinkled (W) microenvironments prior, during, or after the potential topographic transition

	Prior to Transition (µm/min)	**During Transition (µm/min)**	**Post Transition (µm/min)**
A	0.39 ± 0.43	0.40 ± 0.48	0.34 ± 0.40
NW	0.32 ± 0.29	0.29 ± 0.22	0.25 ± 0.18
RA	0.35 ± 0.37	0.37 ± 0.38	0.35 ± 0.39
RNW	0.27 ± 0.25	0.24 ± 0.21	0.17 ± 0.15
RW	0.40 ± 0.30	0.39 ± 0.33	0.31 ± 0.30
W	0.45 ± 0.39	0.42 ± 0.39	0.37 ± 0.35

Table 5-19: Average y-velocities of cells atop active wrinkling (A), static non-wrinkled (NW), ROCK inhibited active wrinkling (RA), ROCK inhibited static non-wrinkled (RNW), ROCK inhibited static wrinkled (RW), and static wrinkled (W) microenvironments prior, during, or after the potential topographic transition

	Prior to Transition (µm/min)	**During Transition (µm/min)**	**Post Transition (µm/min)**
A	0.09 ± 0.12	0.09 ± 0.14	0.08 ± 0.13
NW	0.26 ± 0.27	0.22 ± 0.24	0.18 ± 0.18
RA	0.11 ± 0.21	0.08 ± 0.10	0.08 ± 0.11
RNW	0.29 ± 0.24	0.24 ± 0.21	0.21 ± 0.15
RW	0.06 ± 0.07	0.07 ± 0.08	0.08 ± 0.10
W	0.08 ± 0.09	0.05 ± 0.09	0.05 ± 0.08

Table 5-20: Ratio of average x and y velocities of cells atop active wrinkling (A), static non-wrinkled (NW), ROCK inhibited active wrinkling (RA), ROCK inhibited static non-wrinkled (RNW), ROCK inhibited static wrinkled (RW), and static wrinkled (W) microenvironments prior, during, or after the potential topographic transition.

	Prior to Transition (µm/min)	**During Transition (µm/min)**	**Post Transition (µm/min)**
A	4.33	4.44	4.25
NW	1.23	1.32	1.39
RA	3.18	4.63	4.38
RNW	0.93	1.00	0.81
RW	6.67	5.57	3.875
W	5.625	8.40	7.4

Scheme 5-1: Experimental design for uninhibited and inhibited data

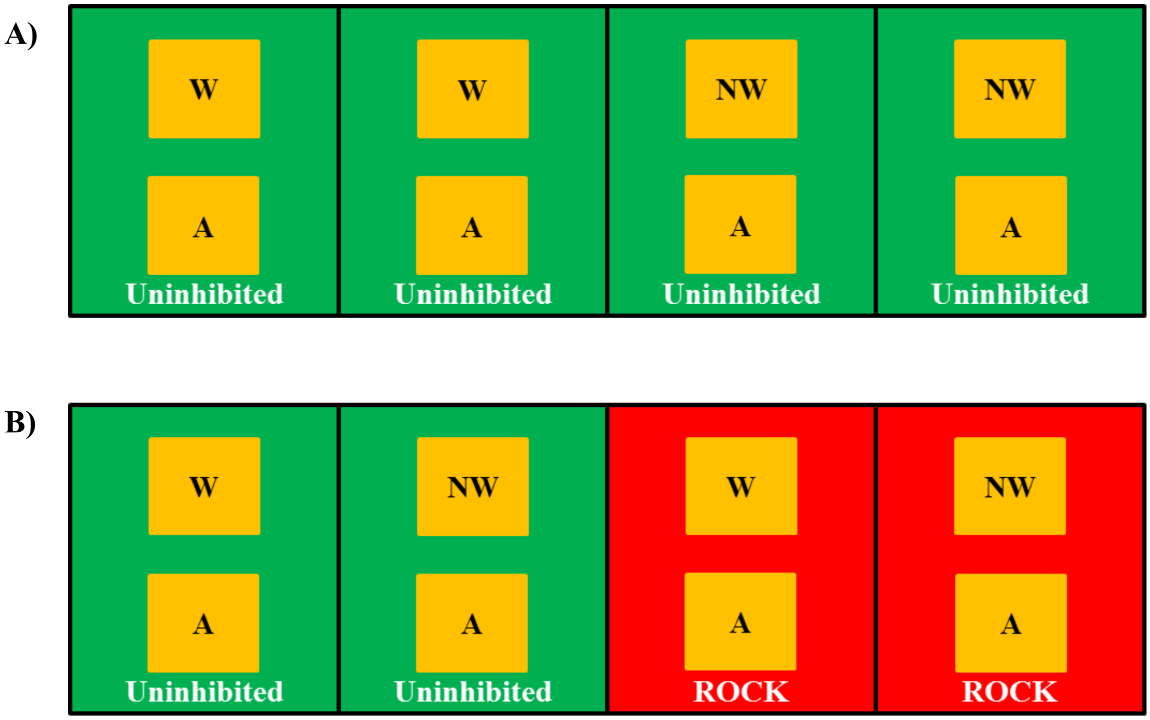

Experimental design set-up for A) uninhibited and B) inhibited time-lapse image capture. All cells were infected with an RFP-Golgi marker and stained 1hr prior to imaging with Hoechst nuclear dye for dual Golgi and nuclear tracking. The number of active wrinkling technical replicates was maximized due to potential issues associated with macroscopic sample motion. A) For the uninhibited data, this resulted in two static wrinkled, two static non-wrinkled, and four active wrinkling samples per biological replicate. B) For ROCK inhibited wells, this resulted in one static wrinkled, one static non-wrinkled, two active wrinkling, one ROCK inhibited static wrinkled, one ROCK inhibited static non-wrinkled, and two ROCK inhibited active wrinkling samples per biological replicate.

Figure 5-1: Representative nuclear orientation plots of cells atop active wrinkling, static non-wrinkled, and static wrinkled topographies prior to, during, or after the potential topographic transition

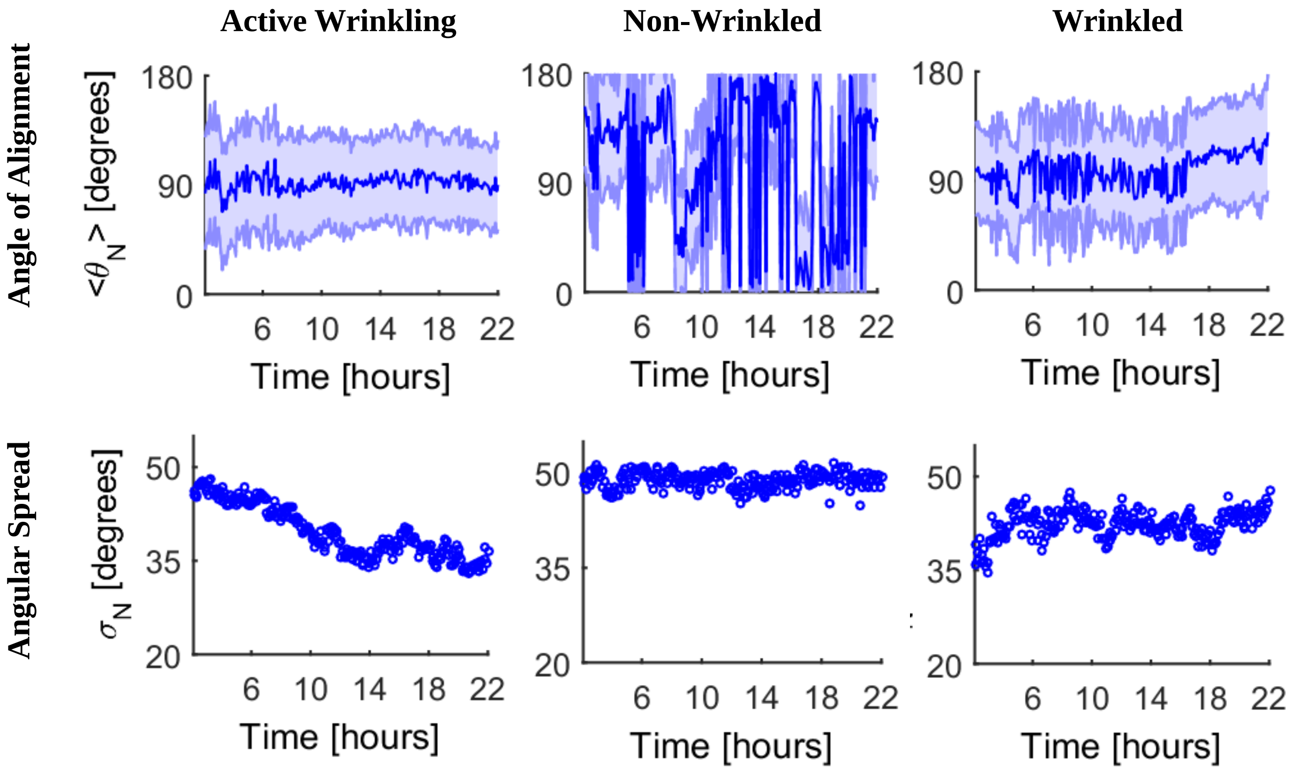

Representative plots (averaged aggregate data for one biological replicate shown) of nuclear angle of alignment (top row) and angular spread (bottom row) of cells atop active wrinkling (left column), static non-wrinkled (middle column), and static wrinkled surfaces (right column) over time. Cells atop static wrinkled substrates had highly aligned nuclei that correlated to the wrinkle direction (~90° in example shown). Conversely, cells atop static non-wrinkled surfaces showed no preferential orientation. For cells atop active wrinkling surfaces, a clear transition from unaligned to aligned nuclear behavior over an approximate 6 hr window of time was observed.

Figure 5-2: Representative nematic angle plots and orientation parameter over time of cells atop active wrinkling, static non-wrinkled, and static wrinkled topographies prior to, during, or after the potential topographic transition

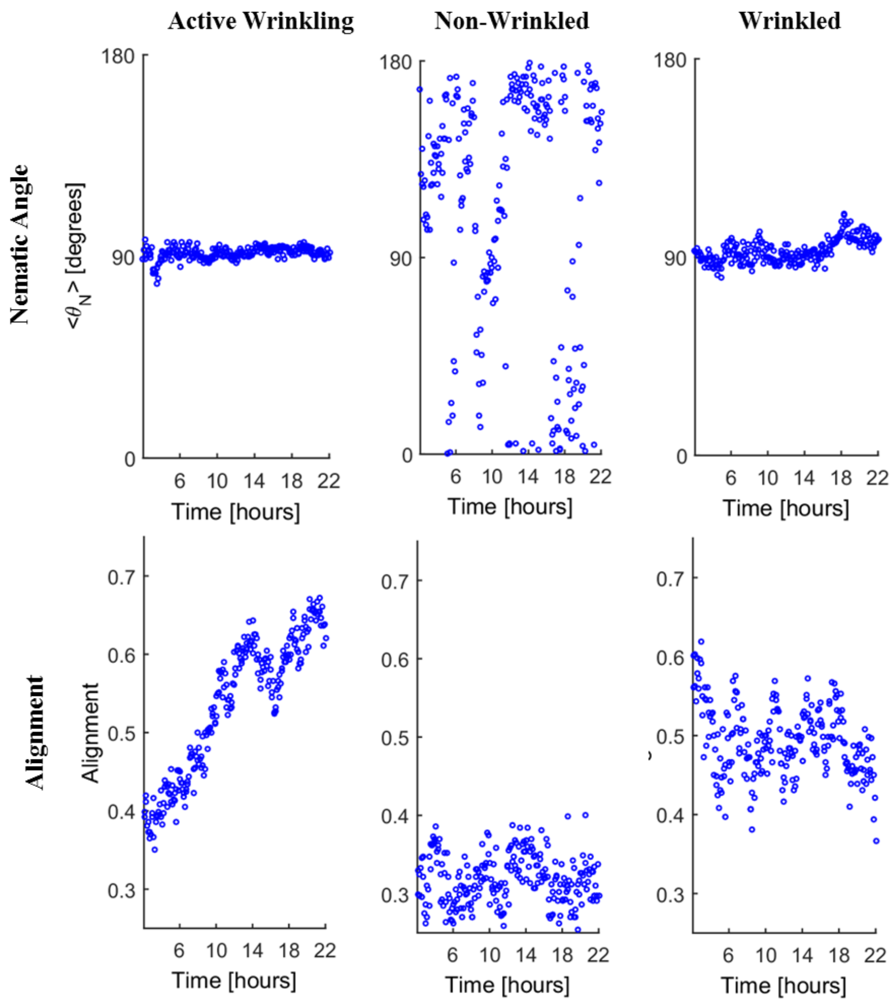

Representative (averaged aggregate data for one biological replicate shown) nematic angle (top row) and alignment parameter (bottom row) results of nuclear orientation atop active wrinkling (left column), static non-wrinkled (middle column), and static wrinkled surfaces (right column) over time. These results very closely mimicked behaviors observed in the nuclear alignment and angular spread over time, further demonstrating that cells atop active wrinkling surfaces increased their nuclear alignment (parallel to the developing wrinkle direction) over time.

Figure 5-3: Representative nuclear-Golgi polarization vector orientation of cells atop active wrinkling, static non-wrinkled, and static wrinkled topographies prior to, during, or after the potential topographic transition

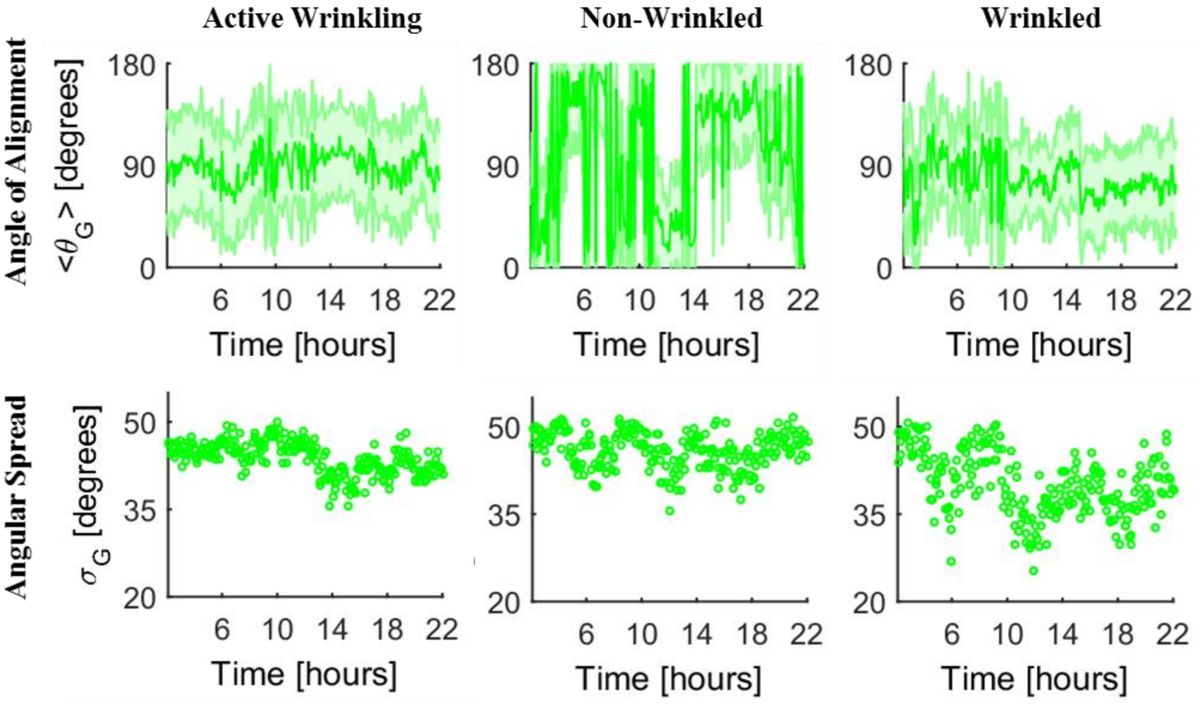

Representative plots (averaged aggregate data for one biological replicate shown) of nuclear-Golgi polarization angle of alignment (top row) and nuclear-Golgi polarization angular spread (bottom row) of cells atop active wrinkling (left column), static non-wrinkled (middle column), and static wrinkled surfaces (right column) over time. Cells atop static wrinkled substrates had polarization angles that correlated to the wrinkle direction (~90° in example shown). Conversely, cells atop static non-wrinkled surfaces showed no preferential orientation. For cells atop active wrinkling surfaces, a minor transition from unaligned to aligned behavior was observed.

Figure 5-4: Representative x-velocity, y-velocity, and speed plots of cells moving over time atop active wrinkling, static non-wrinkled and static wrinkled samples.

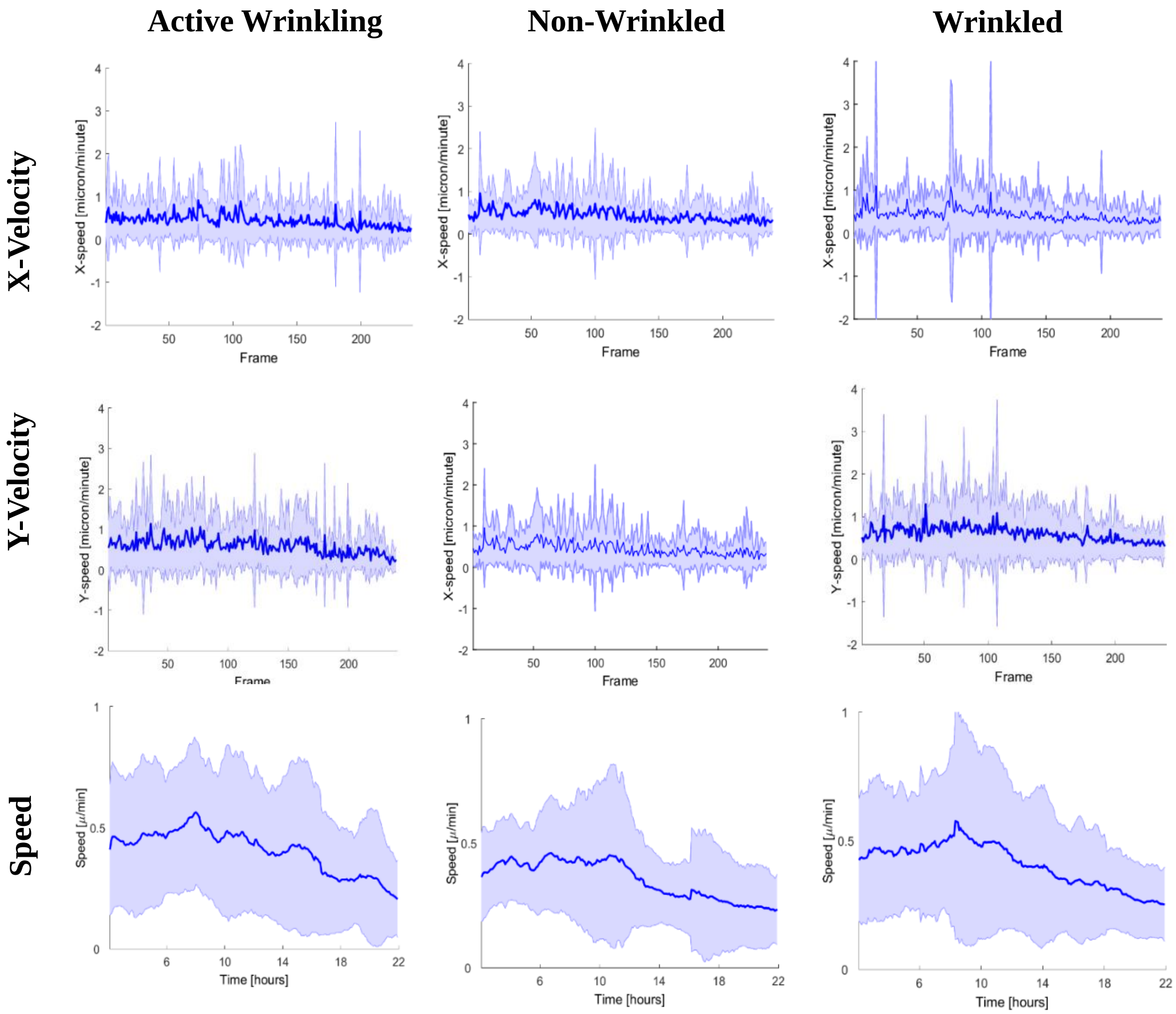

Representative plots of x-velocity (top row), y-velocity (middle row) and speed (bottom row) of cells atop active wrinkling (left column), static non-wrinkled (middle column), and static wrinkled surfaces (right column) over time. Cell speed was consistent regardless of substrate type. When decomposed, cells atop static wrinkled and active wrinkling surfaces showed preferential motion in the x-direction, whereas cells atop static non-wrinkled surfaces showed no direction preference.

Figure 5-5: Representative trajectory plots of cells moving over time atop active wrinkling, static non-wrinkled, ROCK inhibited active wrinkling, ROCK inhibited static non-wrinkled, ROCK inhibited static wrinkled, and static wrinkled samples.

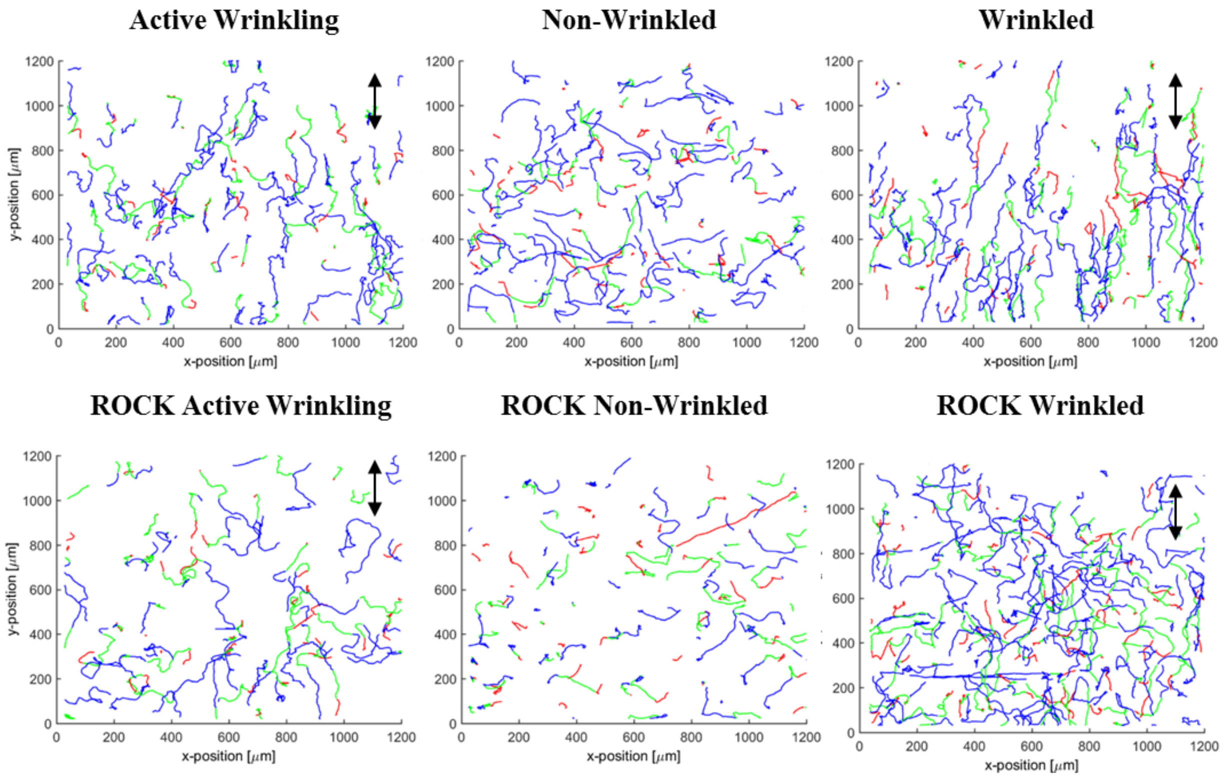

Active Wrinkling

Non-Wrinkled

Wrinkled

ROCK Active Wrinkling

ROCK Non-Wrinkled

ROCK Wrinkled

Representative plots of trajectory behaviors of cells atop uninhibited (top row) or ROCK inhibited (bottom row) active wrinkling (left column), static non-wrinkled (middle column), or static wrinkled surfaces (right column) over time. Red denotes the "pre-transition" region (hrs 0-4), green denotes the "during transition" region (hrs 4-12), and blue denotes the "post transition" region (hrs 12-24) of each trajectory as they relate to the different experimental conditions. Cells atop active wrinkling and static wrinkled surfaces showed preferential movement in the direction of anisotropy, whereas cells atop static non-wrinkled and all ROCK inhibited surfaces showed no directional preference. Black double headed arrows denote approximate wrinkle direction, where appropriate.

Figure 5-6: Representative mean-squared displacement plots of cells moving over time atop active wrinkling, static non-wrinkled, ROCK inhibited active wrinkling, ROCK inhibited static non-wrinkled, ROCK inhibited static wrinkled, and static wrinkled samples.

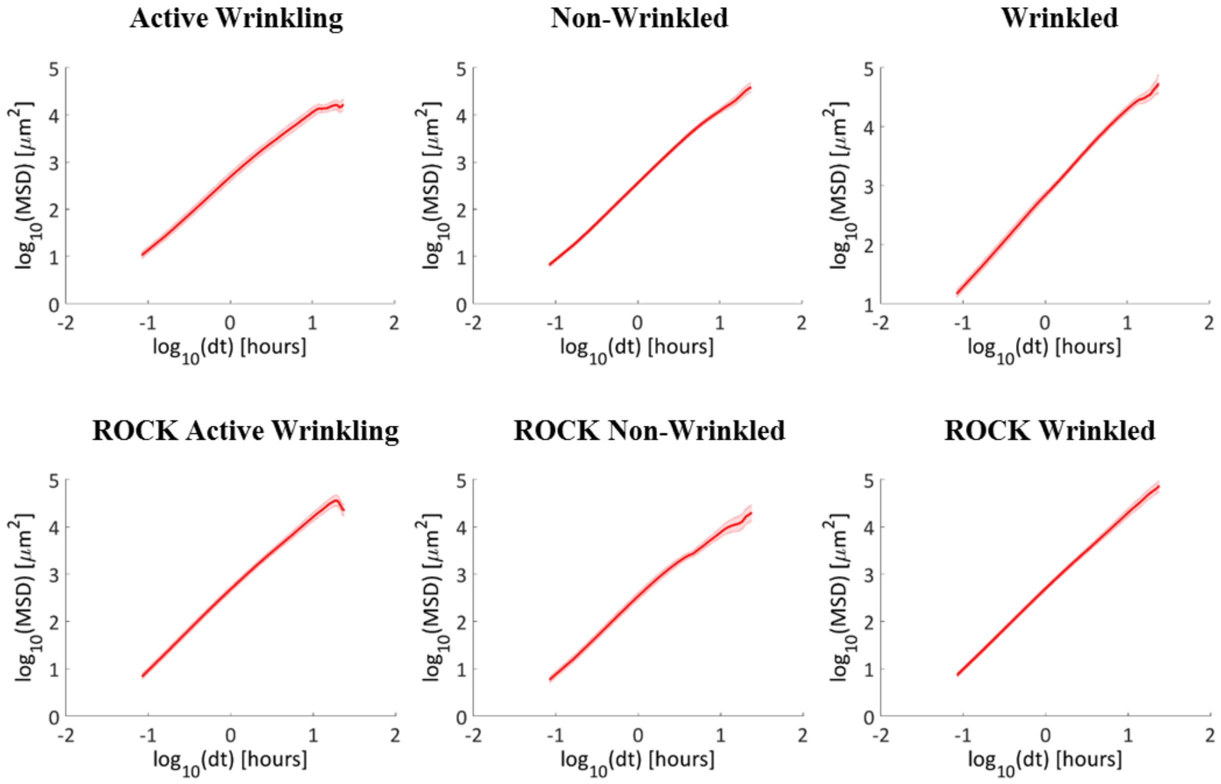

Active Wrinkling

Non-Wrinkled

Wrinkled

ROCK Active Wrinkling

ROCK Non-Wrinkled

ROCK Wrinkled

Representative plots of the mean squared displacement (MSD) of cells atop uninhibited (top row) or ROCK inhibited (bottom row) active wrinkling (left column), static non-wrinkled (middle column), or static wrinkled surfaces (right column) over time. Surprisingly, the MSD slopes were quasi-ballistic up to large timescales (10 hrs) across all substrate types, after which more diffusive behavior was observed.

Figure 5-7: Representative velocity autocorrelation plots of cells moving over time atop active wrinkling, static non-wrinkled, ROCK inhibited active wrinkling, ROCK inhibited static non-wrinkled, ROCK inhibited static wrinkled, and static wrinkled samples.

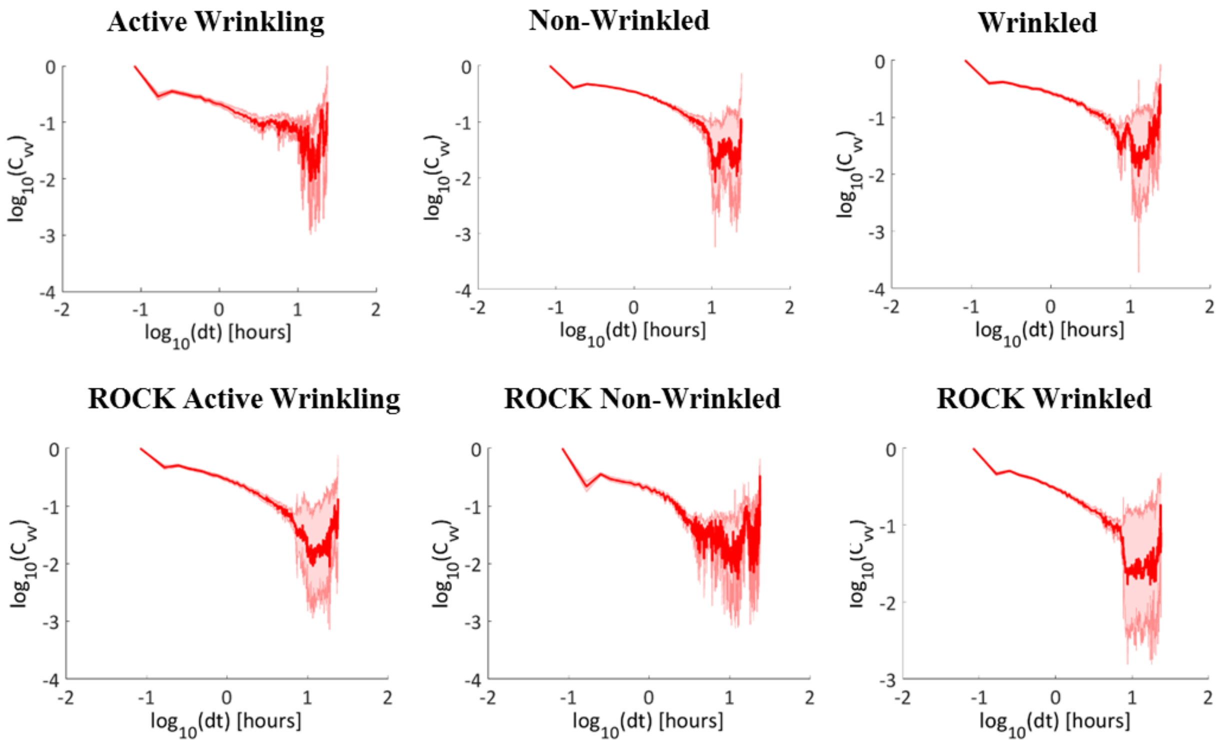

Active Wrinkling

Non-Wrinkled

Wrinkled

ROCK Active Wrinkling

ROCK Non-Wrinkled

ROCK Wrinkled

Representative plots of the velocity autocorrelation function of cells atop uninhibited (top row) or ROCK inhibited (bottom row) active wrinkling (left column), static non-wrinkled (middle column), or static wrinkled surfaces (right column) over time. Across all substrates, cells demonstrated persistent motion for approximately 10 hrs (as is evident by the linear decay observed for all samples), after which more diffusive behavior was observed.

Figure 5-8: Representative nuclear angle of alignment plots of cells over time atop active wrinkling, static non-wrinkled, static wrinkled, ROCK inhibited active wrinkling, ROCK inhibited static non-wrinkled, and ROCK inhibited static wrinkled samples.

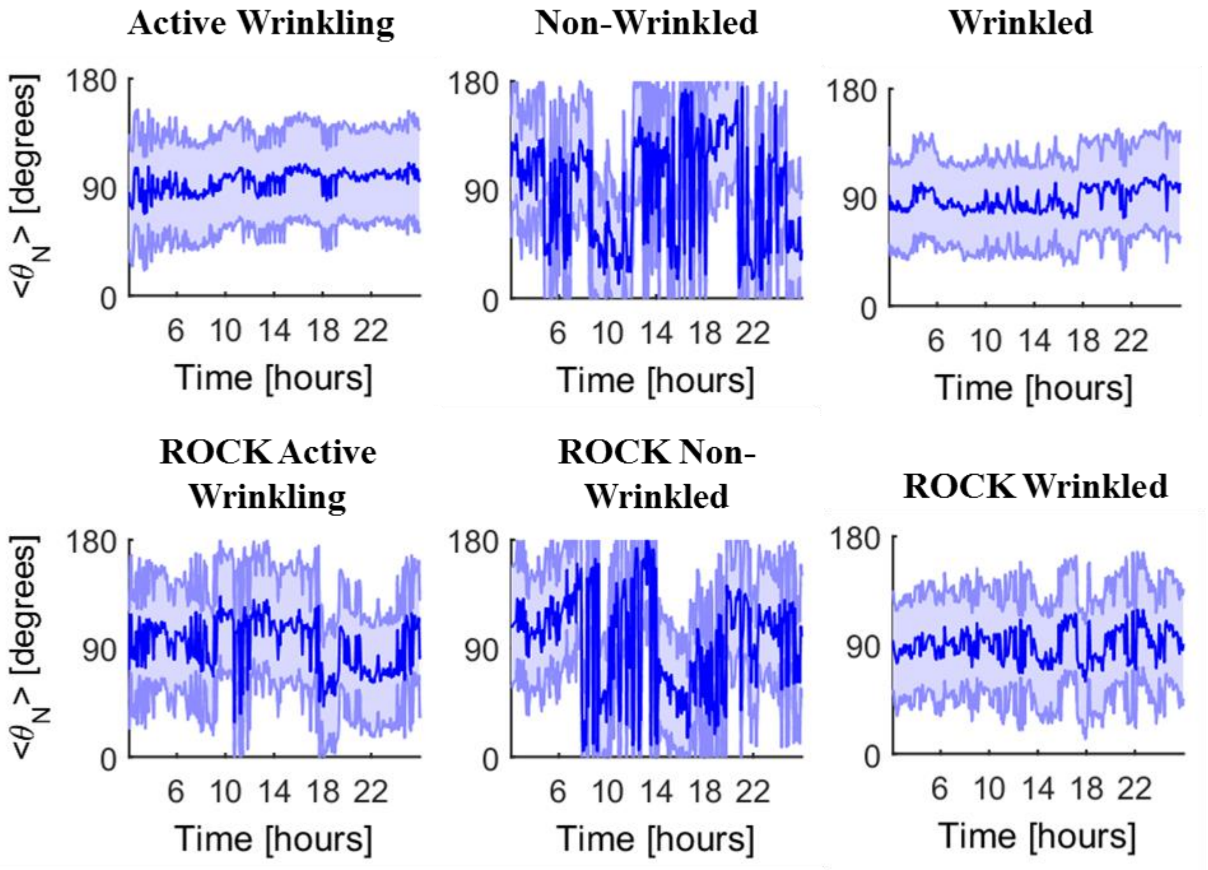

Representative plots (averaged aggregate data for one biological replicate shown) of the nuclear angle of alignment of cells atop uninhibited (top row) or ROCK inhibited (bottom row) active wrinkling (left column), static non-wrinkled (middle column), or static wrinkled surfaces (right column) over time. Cells atop active wrinkling and static wrinkled patterns displayed highly oriented nuclei, whereas no orientation preference was observed for cells atop non-wrinkled or ROCK inhibited surfaces

Figure 5-9: Representative nuclear angular spread of cells over time atop active wrinkling, static non-wrinkled, static wrinkled, ROCK inhibited active wrinkling, ROCK inhibited static non-wrinkled, and ROCK inhibited static wrinkled samples.

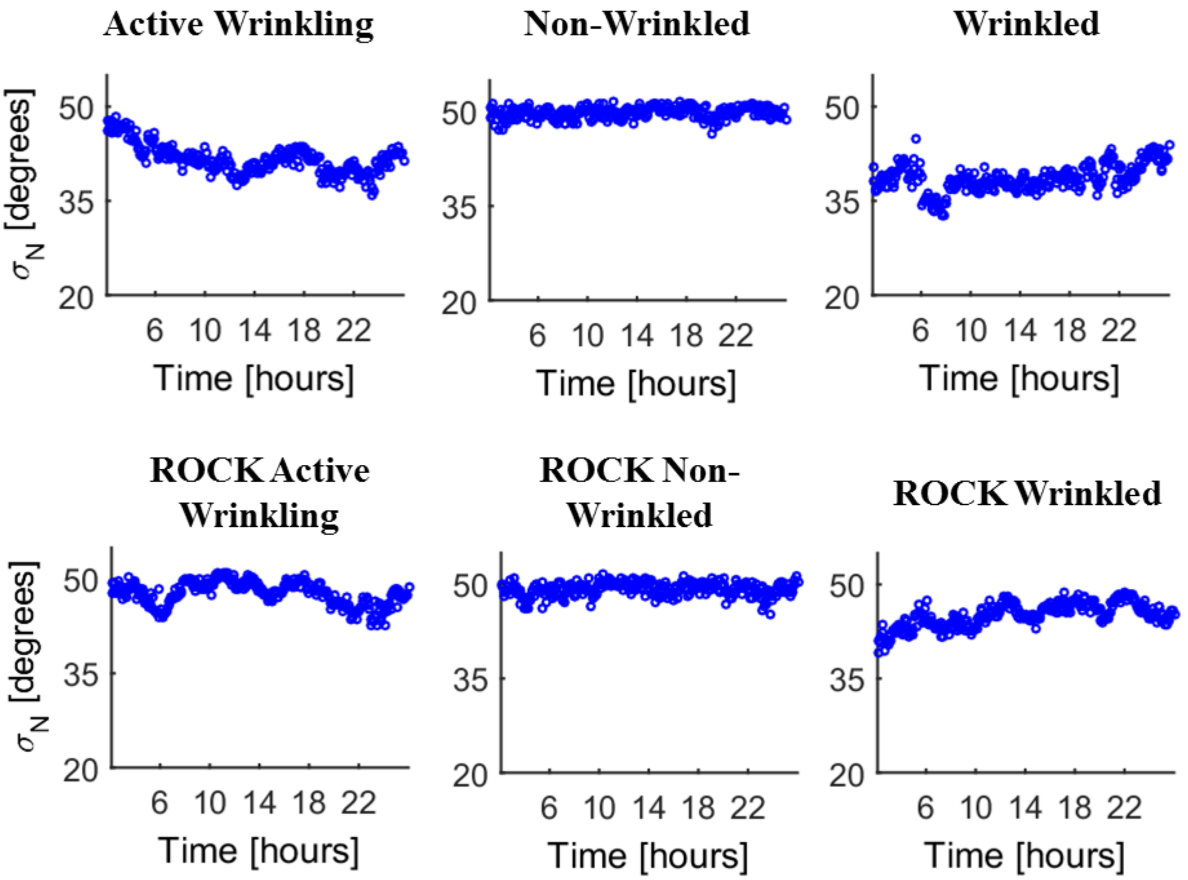

Active Wrinkling

Non-Wrinkled

Wrinkled

ROCK Active Wrinkling

ROCK Non-Wrinkled

ROCK Wrinkled

Representative plots (averaged aggregate data for one biological replicate shown) of the nuclear angular spread over time of cells atop uninhibited (top row) or ROCK inhibited (bottom row) active wrinkling (left column), static non-wrinkled (middle column), or static wrinkled surfaces (right column). Cells atop static wrinkled patterns displayed highly oriented nuclei. Cells atop actively wrinkling surfaces showed a decrease in the angular spread, signifying an increase in nuclear alignment. No nuclear orientation preference was observed for cells atop non-wrinkled or ROCK inhibited surfaces.

Figure 5-10: Representative nematic angle orientation of cells over time atop active wrinkling, static non-wrinkled, static wrinkled, ROCK inhibited active wrinkling, ROCK inhibited static non-wrinkled, and ROCK inhibited static wrinkled samples.

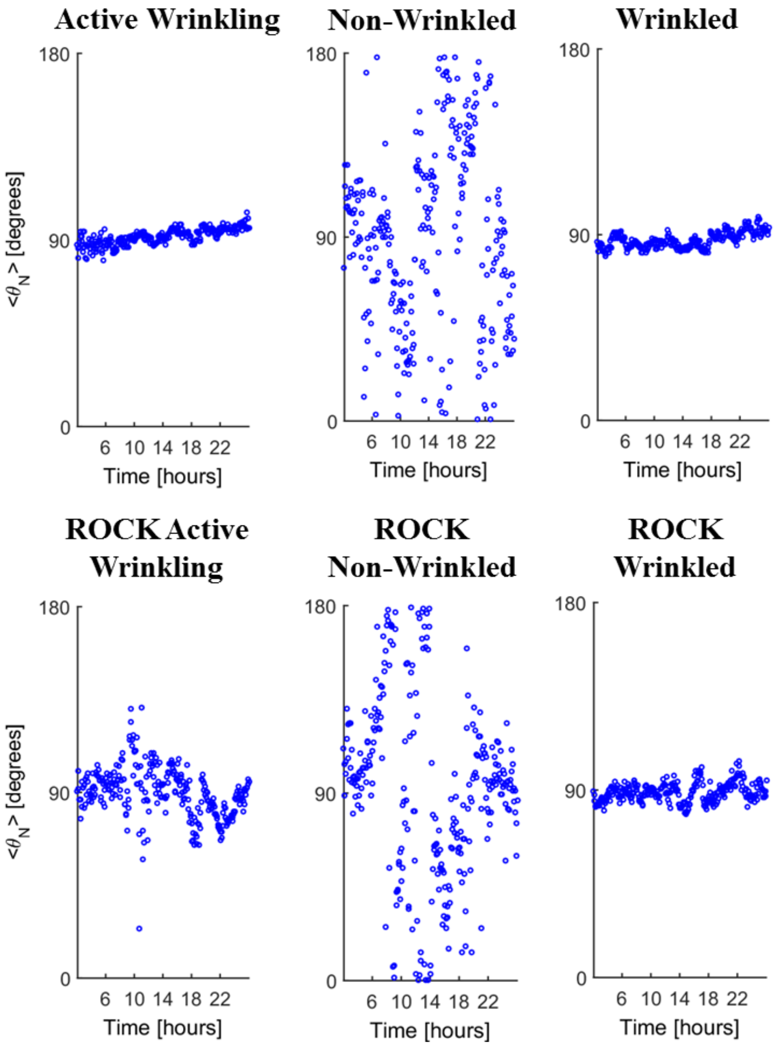

Representative plots of the nematic angle (averaged aggregate data for one biological replicate shown) over time of cells atop uninhibited (top row) or ROCK inhibited (bottom row) active wrinkling (left column), static non-wrinkled (middle column), or static wrinkled surfaces (right column). Cells atop static wrinkled patterns displayed highly oriented nuclei while cells atop actively wrinkling surfaces showed a decrease in the nematic angle standard deviation over time, signifying an increase in nuclear alignment. No nuclear orientation preference was observed for cells atop non-wrinkled, ROCK active wrinkling, or ROCK non-wrinkled surfaces. Cells atop ROCK wrinkled surfaces demonstrated a decrease in nuclear alignment about 90° (parallel to the wrinkle direction) over time.

Figure 5-11: Representative alignment of cells over time atop active wrinkling, static non-wrinkled, static wrinkled, ROCK inhibited active wrinkling, ROCK inhibited static non-wrinkled, and ROCK inhibited static wrinkled samples.

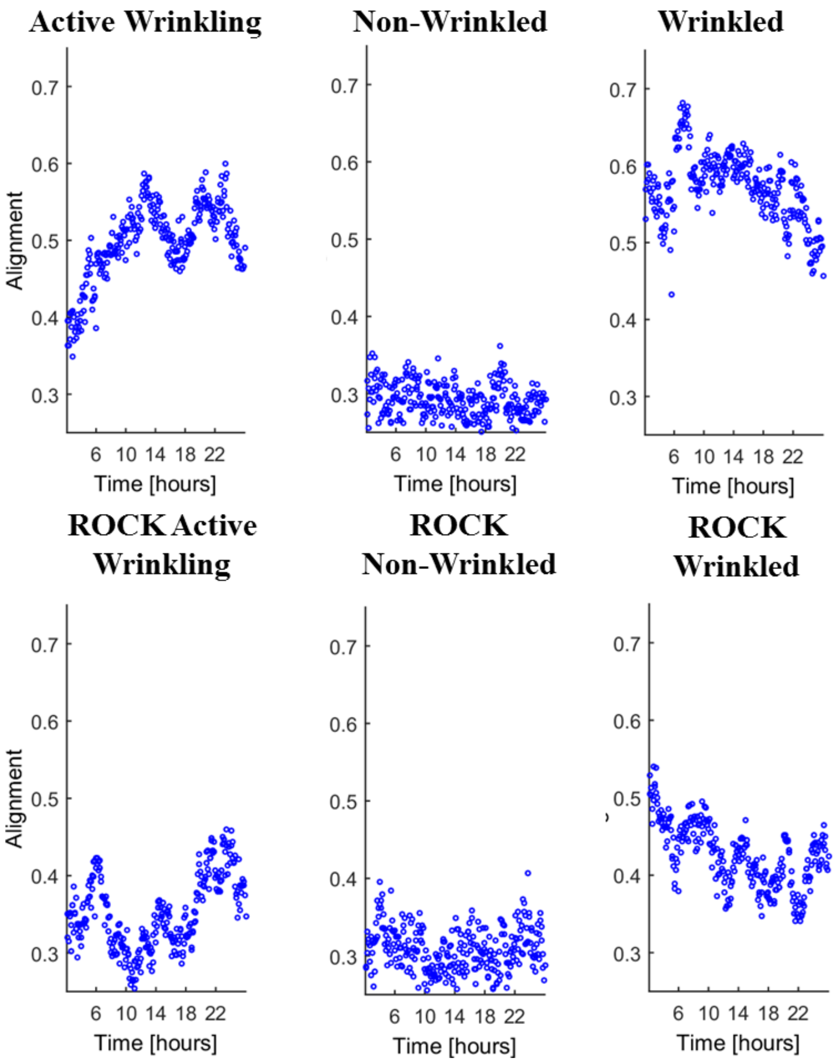

Representative plots of the alignment parameter (averaged aggregate data for one biological replicate shown) over time for cells atop uninhibited (top row) or ROCK inhibited (bottom row) active wrinkling (left column), static non-wrinkled (middle column), or static wrinkled surfaces (right column). Cells atop static wrinkled patterns displayed highly oriented nuclei (alignment parameter = ~0.6). For cells atop actively wrinkling surfaces, an increase in the alignment parameter over time was observed, signifying an increase in nuclear alignment. An alignment parameter of ~0.3 was observed for cells atop static non-wrinkled surfaces. Cells atop ROCK active wrinkling and ROCK non-wrinkled surfaces had similar alignment values to the static non-wrinkled case. For cells atop ROCK wrinkled surfaces, a decrease in the alignment parameter over time was observed.

Figure 5-12: Representative nuclear-Golgi polarization angle of alignment plots of cells over time atop active wrinkling, static non-wrinkled, static wrinkled, ROCK inhibited active wrinkling, ROCK inhibited static non-wrinkled, and ROCK inhibited static wrinkled samples.

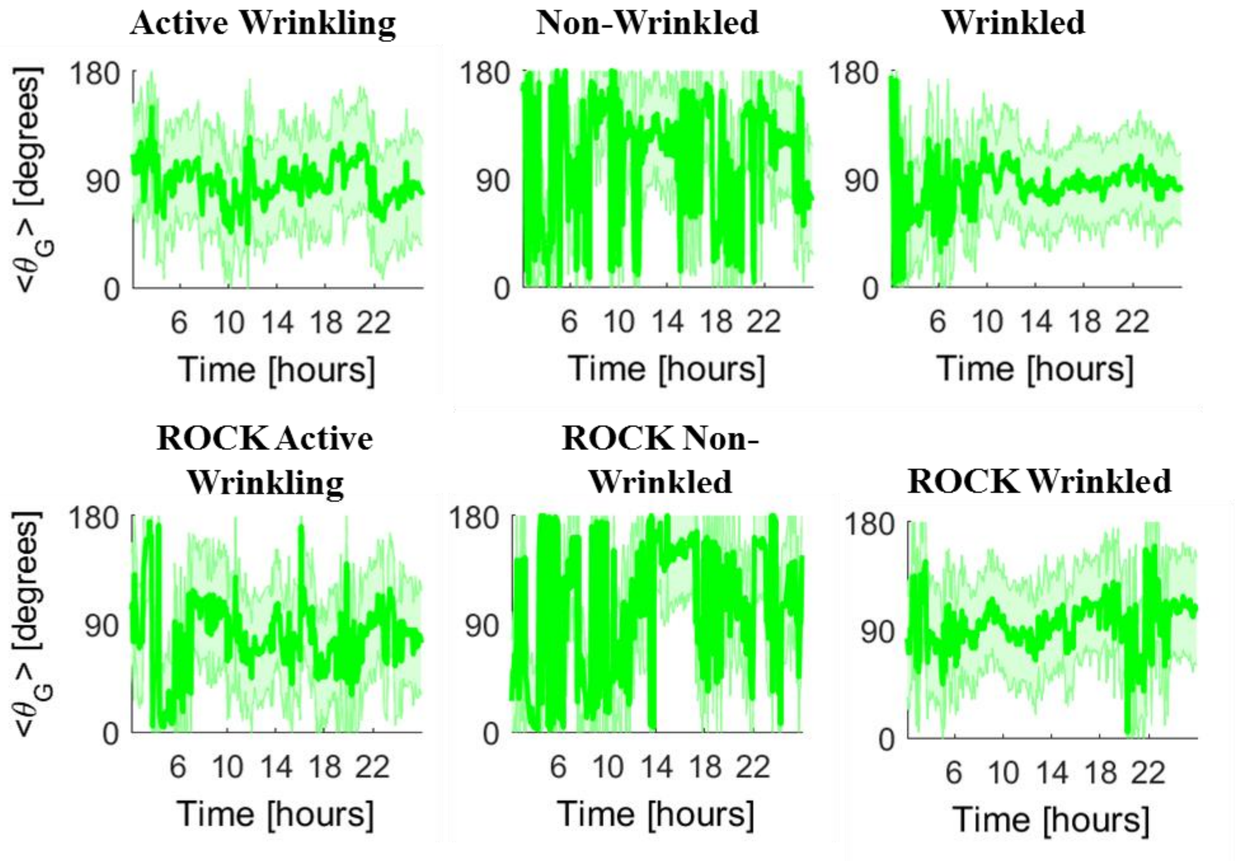

Active Wrinkling

Non-Wrinkled

Wrinkled

ROCK Active Wrinkling

ROCK Non-Wrinkled

ROCK Wrinkled

Representative plots of the nuclear-Golgi polarization angle (averaged aggregate data for one biological replicate shown) over time for cells atop uninhibited (top row) or ROCK inhibited (bottom row) active wrinkling (left column), static non-wrinkled (middle column), or static wrinkled surfaces (right column). Nuclear-Golgi polarization angle of alignment plots were noisy regardless of sample type. For cells atop static wrinkled surfaces, nuclear-Golgi polarization was oriented with the wrinkle direction. Cells atop actively wrinkling surfaces showed aligned polarization angles to the topography direction during the transition region. No polarization preference was noted on non-wrinkled or ROCK inhibited surfaces.

Figure 5-13: Representative nuclear-Golgi polarization angular spread of cells over time atop active wrinkling, static non-wrinkled, static wrinkled, ROCK inhibited active wrinkling, ROCK inhibited static non-wrinkled, and ROCK inhibited static wrinkled samples.

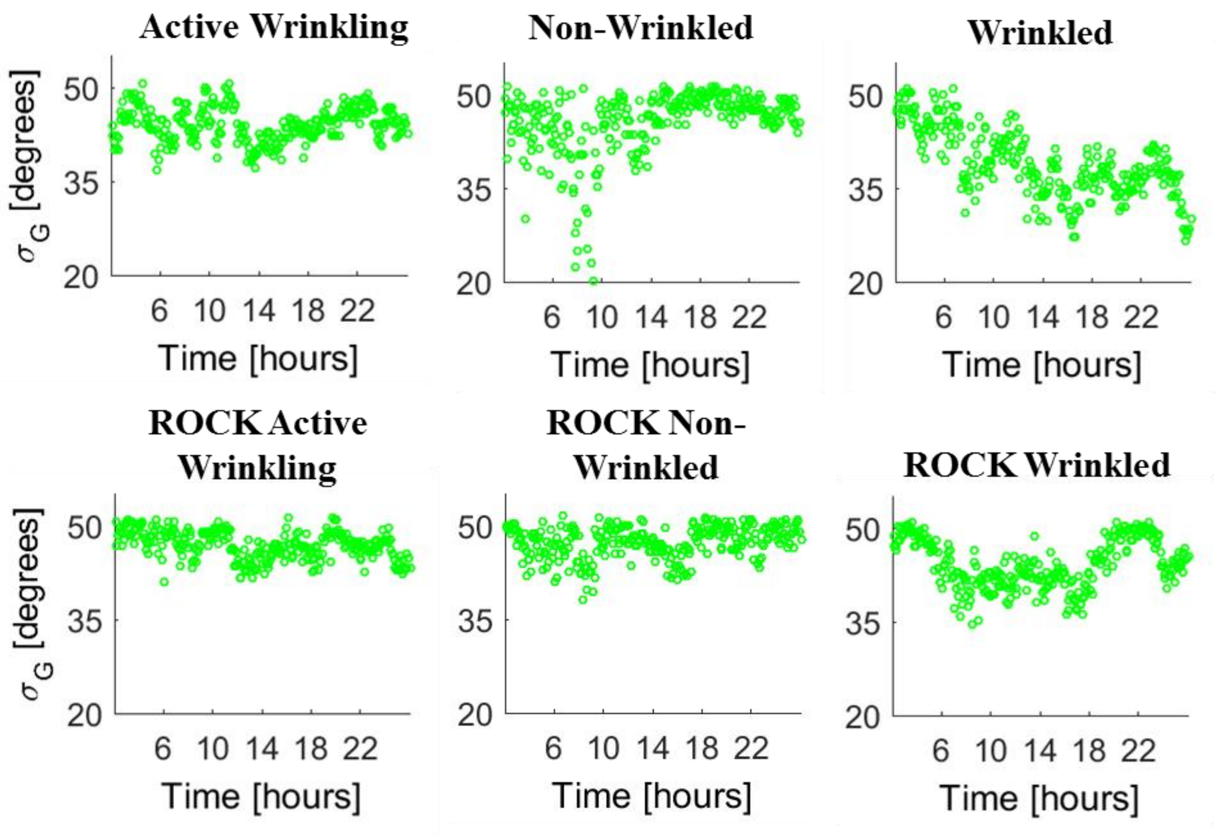

Representative plots of the nuclear-Golgi polarization angular spread (averaged aggregate data for one biological replicate shown) over time for cells atop uninhibited (top row) or ROCK inhibited (bottom row) active wrinkling (left column), static non-wrinkled (middle column), or static wrinkled surfaces (right column). Cells atop static wrinkled surfaces had the lowest nuclear-Golgi angular spread, indicating the greatest degree of alignment. Cells atop active wrinkling surfaces showed a decrease in nuclear-Golgi angular spread during the transition region, indicating increased polarization during the surface transition. For non-wrinkled, ROCK active wrinkling, and ROCK non-wrinkled surfaces, the nuclear-Golgi angular spread was consistently ~43°. Cells atop ROCK wrinkled substrates showed an average decrease in nuclear-Golgi angular spread over time, however, this alignment was not related to the wrinkle direction.

Figure 5-14: Representative speed of cells over time atop active wrinkling, static non-wrinkled, static wrinkled, ROCK inhibited active wrinkling, ROCK inhibited static non-wrinkled, and ROCK inhibited static wrinkled samples.

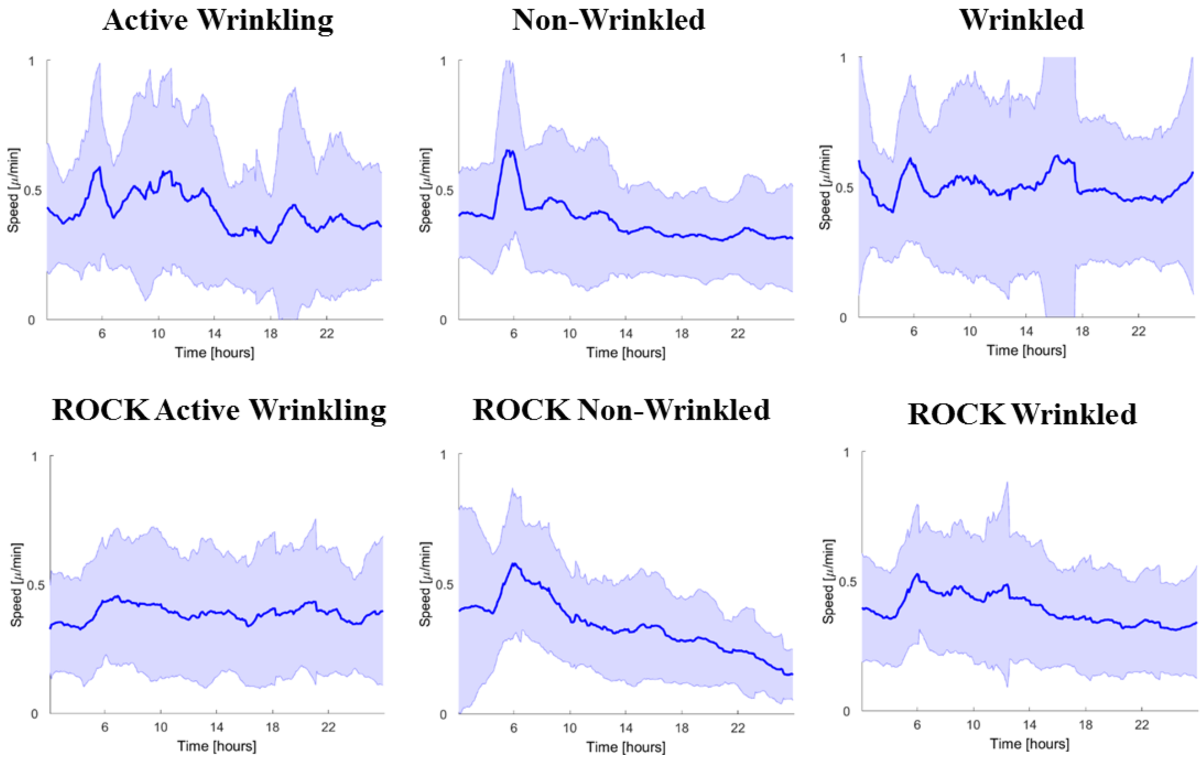

Representative plots of cell speed over time for cells atop uninhibited (top row) or ROCK inhibited (bottom row) active wrinkling (left column), static non-wrinkled (middle column), or static wrinkled surfaces (right column). Cells consistently moved with equivalent speeds, regardless of surface topography.

Figure 5-15: Representative x-velocities of cells over time atop active wrinkling, static non-wrinkled, static wrinkled, ROCK inhibited active wrinkling, ROCK inhibited static non-wrinkled, and ROCK inhibited static wrinkled samples.

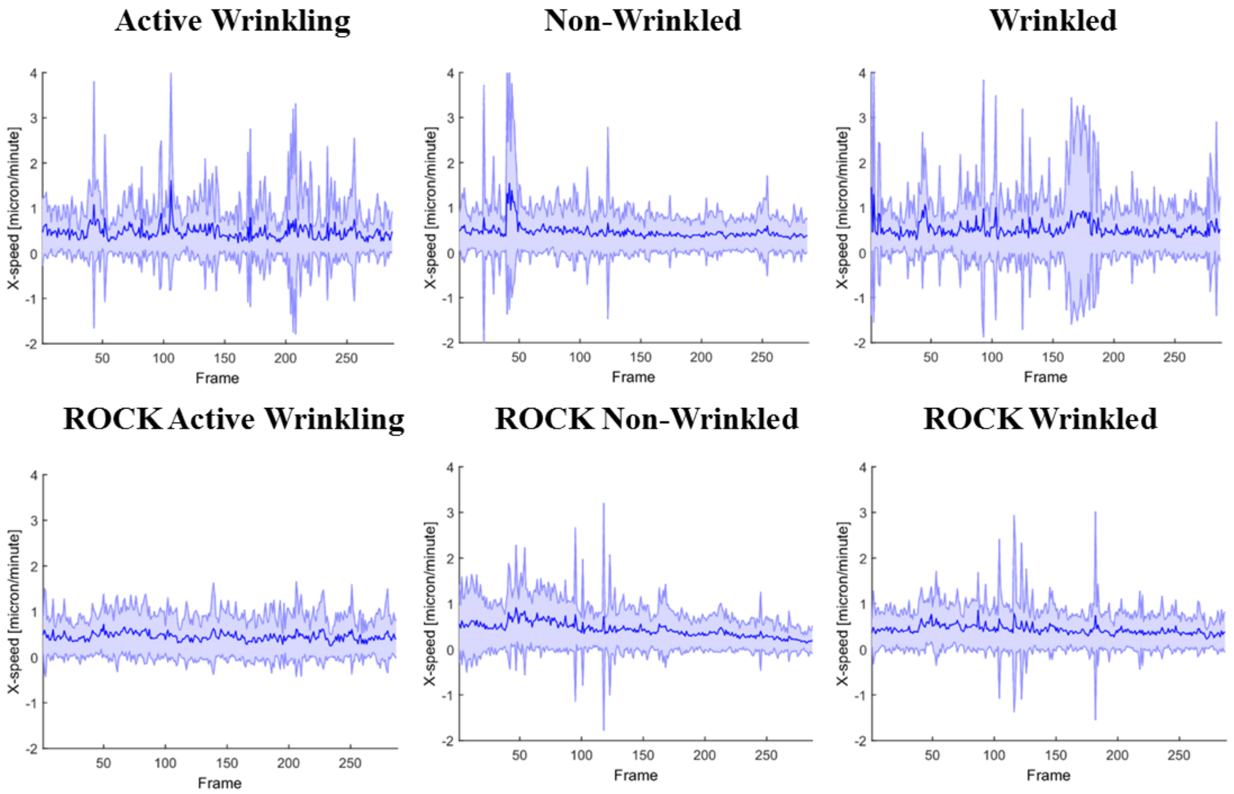

Active Wrinkling

Non-Wrinkled

Wrinkled

ROCK Active Wrinkling

ROCK Non-Wrinkled

ROCK Wrinkled

Representative plots of x-velocity dynamics over time for cells atop uninhibited (top row) or ROCK inhibited (bottom row) active wrinkling (left column), static non-wrinkled (middle column), or static wrinkled surfaces (right column). Cells atop anisotropic surfaces consistently moved with increased speeds in the x-direction (parallel to the direction of anisotropy).

Figure 5-16: Representative y-velocities of cells over time atop active wrinkling, static non-wrinkled, static wrinkled, ROCK inhibited active wrinkling, ROCK inhibited static non-wrinkled, and ROCK inhibited static wrinkled samples.

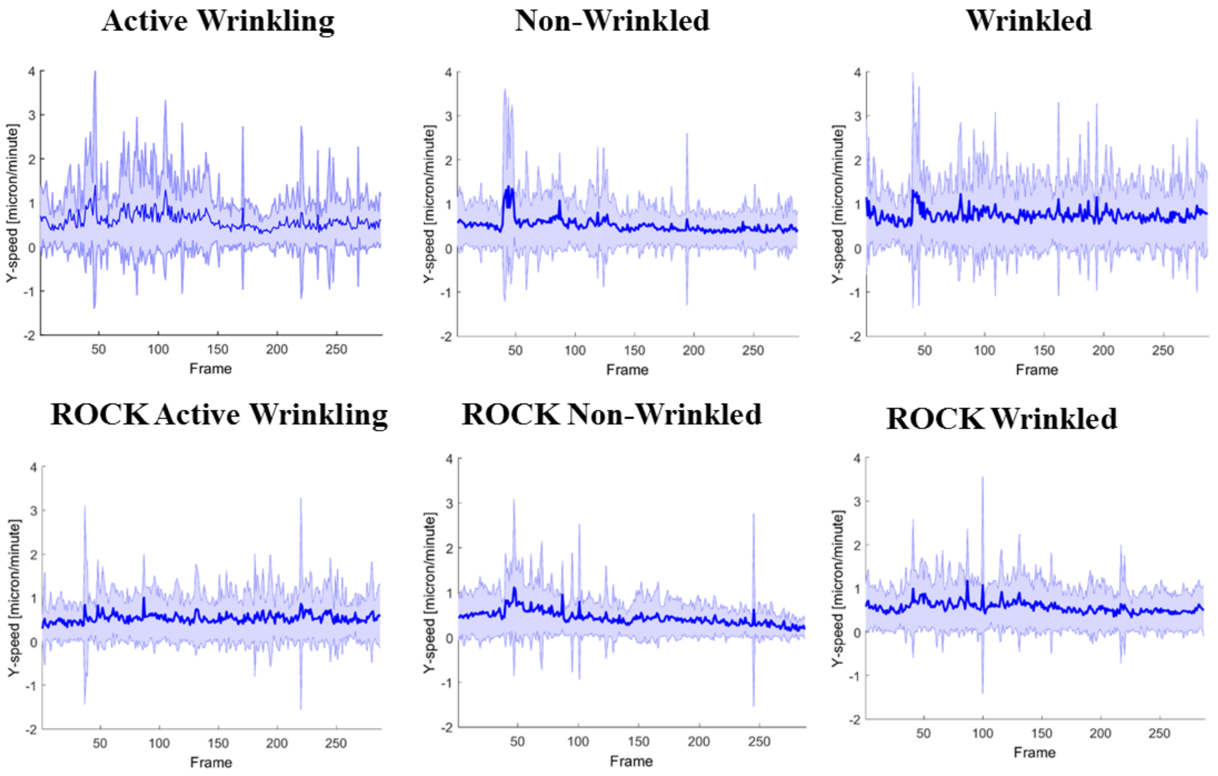

Representative plots of y-velocity dynamics over time for cells atop uninhibited (top row) or ROCK inhibited (bottom row) active wrinkling (left column), static non-wrinkled (middle column), or static wrinkled surfaces (right column). Cells atop isotropic surfaces moved with consistent x- and y-velocities, whereas cells atop anisotropic surfaces moved slower in the y-direction (perpendicular to anisotropy).

Chapter 6: Utilization of ACT*IV*E for Image-Based Cell Subpopulation Identification†

6.1 Synopsis

In vivo, cells often exist in a heterogeneous microenvironment where multiple phenotypes interact to coordinate cellular processes. *In vitro*, co-culture systems have emerged as important experimental designs to investigate these phenomena. Here, we present the use of a dual principle component analysis (PCA) and partitioning around medoids (PAM) technique to identify cell subpopulations in a non-destructive and non-invasive manner. To test the system, we imaged endothelial (EC) and smooth muscle cells (SMC) in mono or co-culture using live cell time-lapse fluorescence microscopy. By tagging the ECs with a cytoplasm specific marker and subsequently staining all of the cell nuclei, we utilized ACT*IV*E to quantify cell morphometric and motility features, while retaining the ability to manually discern EC and SMC cells. We first verified this technique by analyzing a test set, the Iris data set, and comparing results to current literature understanding. We then utilized cell morphometric, motility, and combined morphometric and motility data extracted from ACT*IV*E to reveal that: 1) morphometric clustering resulted in two primary groups, one with large nuclei and one with small nuclei, irrespective of culture condition, 2) cell subpopulations in co-culture adopt differences in movement rate that are not observed in

---

†This project was completed in collaboration with Alexis N. Peña, a former Henderson lab undergraduate student. Preliminary results were detailed in her Honors Capstone Report: Peña, AN. "Clustering Cell Populations in Heterogeneous *In Vitro* Model Cell Cultures via Application of Principle Component Analysis to Cell Motility Metrics" (2016). *Syracuse University Honors Capstone Projects.*

monoculture subpopulations, and 3) combined morphometric and motility data complicated clustering effectiveness, leading to subpar identification. We anticipate that the presented technique could be applied to co-culture or stem cell populations to further understanding of how heterogeneity alters cell migration patterns and to identify cell subpopulations using imaging modalities alone.

6.2 Introduction: Identifying Heterogeneity in Cell Populations

In vitro systems typically focus on culturing cells as individual monolayers to reduce complexity and focus on specific cellular processes [1]. However, cells rarely exist in homogeneous environments *in vivo*. For example, in cancer biology, the microenvironment of a breast tumor consists of a variety of phenotypes that all interact together, including fibroblasts, adipocytes, myoepithelial, and tumorigenic cells [2]. Co-culture systems have emerged as prominent mechanisms for studying cell-cell interactions, as they allow controlled physical contact and chemical exchange between cell types [3]. Similarly, the natural heterogeneity that exists within differentiating stem cell populations [4] is an important variable to consider when studying lineage pathways. Current methods used to characterize subpopulation behaviors are typically invasive and destructive to the cell populations involved. For example, immunohistochemistry, in which cells are typically fixed and stained using antibodies to bind to specific cell markers [5, 6], and real-time quantitative polymerase chain reaction, in which cells are lysed and DNA is harvested for quantitative genetic profiling [7, 8], are two techniques currently used to distinguish cell subpopulations within heterogeneous groups. In addition to their destructive nature, these techniques cannot be applied at the individual cell level *in situ*. As *in vitro* systems continue increasing in complexity for more accurate *in vivo* modeling, there is a critical need of identifying and analyzing cell subpopulations accurately and non-invasively to advance understanding of how cell-cell, cell-material, and cell-environmental factors dictate complex biological mechanisms *in vivo*.

A major challenge in dealing with these heterogeneous co-culture or stem cell populations in a non-invasive and non-destructive manner is the added complexity of variations in cell behavior amongst individual groups. Variations in some, but not all, cell subpopulation features (e.g., cell speed or cytoskeletal shape distributions) are often masked by bulk averaging methods common in current population analysis, leading to unclear interpretations of results using standard methodologies. Thus, automating the process used to classify population groups would be beneficial, reducing trends potentially overlooked by human analysis alone. Recent advances in the bioinformatics field have generated powerful computational approaches for reducing complexity and providing clustering techniques for analyzing biological data. For example, principle component analysis (PCA) has emerged as a popular technique for reducing data dimensionality. The technique isolates features within a data set that represent the most variability, defining these features as a series of "principle components" contributing to degrees of variance in the data. With PCA, a transformation is performed on the data features, allowing the number of variables used in the analysis to be reduced without losing pertinent information important to subpopulation identification [9]. Once features of interest in the data have been isolated, an assortment of clustering approaches, with varying benefits and limitations, have been developed to group subpopulations. Some of these approaches include gap criterion evaluation [10], dendrograms [9], quadtree decomposition [11], self-organized maps [12-16], and k-means or k-medoid partitioning [17, 18]. The k-medoids, also known as partitioning around medoids, technique is particularly attractive due to its versatility in building a similarity function that minimizes dissimilarity within a group but maximizes distances between medoid parameters group to group. As a k-medoid algorithm, the data is partitioned into subsets, iterating to improve clustering quality by minimizing the similarity function developed [19]. Silhouette widths can further be utilized to assess clustering effectiveness [20].

Here, we sought to apply the ACT*IV*E system to characterize cell behavior in a heterogeneous system, utilizing clustering techniques as a means to separate and characterize subpopulation morphology and motility patterns in a co-culture environment. We chose to use a direct co-culture of bovine aortic endothelial (ECs) and bovine aortic smooth muscle cells (SMCs) as our experimental system. ECs and SMCs are commonly found together in vasculature, with SMCs providing the contractive base and ECs coating the blood-contacting portion of vessel walls [21]. Co-culture of ECs and SMCs has previously been shown to improve EC adhesion and focal area contact, compared to monoculture [22]. For the clustering analysis, a combination of PCA pre-processing and subsequent partitioning around medoids was selected to reduce data dimensionality and cluster groups with a quantifiable metric (silhouette widths) for cluster verification, respectively. We anticipated that this technique would allow for accurate and efficient identification of cell clusters in both mono- and co-culture microenvironments, furthering understanding of how heterogeneous systems contribute to exhibited cell migration patterns.

6.3 Methods: Development and Analysis of a Co-culture Model[1,2]

6.3.1 Cell Culture and Seeding

Bovine aortic endothelial (ECs) and bovine aortic smooth muscle cells (SMCs) (ATCC) were cultured in Dulbecco's Modified Eagle Medium (DMEM) supplemented with 10% fetal bovine serum (v/v), 1% penicillin/streptomycin (v/v), and 1% GlutaMax (v/v). Cells were expanded in a 37°C humidified incubator with regulated 5% CO_2 and passaged at 80% confluence using 0.25% Trypsin EDTA at room temperature. For time-lapse experiments, ECs were restricted to passage 6-8 while SMCs were restricted to passage 12-16.

ECs and SMCs were directly seeded onto Lab-Tek borosilicate chamberglass slides (Fisher Scientific) that contained four individual wells (1.8 cm^2/well). The four wells were plated as follows: 1) co-culture of SMCs and ECs, 2) co-culture of SMCs and ECs, 3) SMC monoculture, and 4) EC monoculture (Scheme 6-1A). Directly seeding SMCs and ECs into the chamber wells increased cell attachment and even distribution along the base of the chamberglass slides (data not shown). To simulate native layering of cells observed *in vivo*, SMCs were plated first at a concentration of 3000 cells/cm^2, followed by a 24 hr incubation period at 37°C (Scheme 6-1B). ECs were then plated at a concentration of 10,000 cells/cm^2, followed by an additional 24 hr incubation period at 37°C. Cell densities for SMC and EC co-culture were optimized for approximately equivalent SMC and EC attachment (qualitatively assessed, manual verification).

---

[1] Co-culture and monoculture experiments designed and optimized by Megan Brasch and Alexis Peña. Final cell experiments were executed by Alexis Peña.

[2] PCA/PAM technique originally conceived by Alexis Peña

For consistency, cell densities for the respective monocultures were kept at the same seeding densities.

6.3.2 Live Cell Time-Lapse Imaging

Cells were stained with two separate live-cell markers for time-lapse image analysis (Figure 6-1, top row). An EC specific cytoplasm marker, DiI Acetylated Low Density Lipoprotein (DiI-Ac-LDL), was selected to differentiate EC and SMC populations for manual verification after clustering analysis. Cells were stained at a 1:40 dilution, after fluorescence optimization under anticipated imaging conditions. DiI-Ac-LDL was only added to one of the co-culture wells, to ensure consistent motility dynamics between the stained and un-stained co-culture populations (Scheme 6-1). DiI-Ac-LDL staining was separately confirmed to exhibit minimal uptake and undetectable fluorescence in SMC monocultures under anticipated imaging conditions, confirming that DiI-Ac-LDL could be used as an EC specific marker. Cells were incubated in DiI-Ac-LDL for 5 hrs at 37°C prior to image capture. After 5 hrs of incubation, DiI-Ac-LDL containing medium was removed and replaced with a DMEM solution containing Hoechst 33342 nuclear stain (0.01 μg/mL) in all wells. Cells were then incubated for an additional 20 mins at 37°C to allow for Hoechst uptake prior to time-lapse imaging set-up.

Chamberglass slides were then transferred into a live cell stage incubator (INC-2000, 20/20 Technology, Inc.) where the cells were imaged for 24 hrs using a Leica DMI 6000B inverted microscope with an Andor Luca R camera (10x/0.63x NA objective). The live cell stage incubator was equilibrated at 37°C with constant 5% CO_2. Five slice z-stack images were captured every three minutes in phase, A4 (excitation/emission peak of 360/470 nm), and N3 (excitation/emission peak of 546/600 nm) using 5 ms, 150 ms, and 50 ms exposure times respectively. Two representative locations were imaged per well. Image binning was set to 2, to improve signal clarity.

6.3.3 Characterizing Cell Motility using ACTIVE

Cell motility behaviors were characterized using the ACT*IV*E automated cell tracking system [23]. Co-culture and monoculture Hoechst images were processed using similar conditions to those presented in **Chapters 2-5** (Figure 6-1, bottom row). Cell features were then extracted from the ACT*IV*E data set, and standardized for equal consideration in principle component analysis (PCA). PCA results were then used to limit feature selection for partitioning around medoids (PAM) clustering and silhouette quantification. Details regarding ACT*IV*E, PCA, and PAM analysis are detailed below.

6.3.3.1 Video Processing and ACT*IV*E Analysis

Two biological replicates were used for cell subpopulation characterization. For the first replicate, two positions were selected for the co-culture and monoculture data. For the second replicate, position one was selected for the EC monoculture, while position two was selected for the co-culture and SMC monoculture (due to issues with the z-focal plane in position one). For all samples, co-culture and monoculture z-stacks were compressed using an extended depth of field plugin [24]. Tiff stacks were then compiled and truncated to visualize as many frames as possible for ACT*IV*E tracking analysis. All videos were truncated to 407 frames (20.35 hrs total of imaging) out of a potential 480 frames (24 hrs of imaging total), due to a combination of macroscopic and z-plane shifting in the imaging field of view, rendering ACT*IV*E analysis during those portions of the videos ineffective. Each video was then run using the ACT*IV*E tracking parameters detailed in Table 6-1. An additional requirement limiting the final analysis to cells present in 20% or more of the total number of frames was included to reduce noise and improve clustering capabilities.

6.3.3.2 Feature Selection: Morphometric, Motility, and Combined Analysis

ACTIVE output was broken down into three different categories for clustering analysis: 1) morphometric characterization, 2) motility characterization, and 3) combined morphometric and motility characterization (Table 6-2). Nuclear major axis, nuclear minor axis, nuclear aspect ratio, and nuclear area features were calculated using ACT*IV*E's built-in ellipse fitting function. Similarly, nuclear intensity was identified using ACT*IV*E's built-in ellipse mask function which calculates the integrated intensity based on the ellipse masking of cell nuclei. Motility metrics were obtained using cell trajectory information. As described in **Chapters 3 and 4**, x-, y-, and magnitude velocity values were calculated using central finite differences theorem. The straightness ratio, also known as the directionality ratio (DR), was calculated as:

$$DR = \frac{\sqrt{\left(x_f - x_0\right)^2 + \left(y_f - y_0\right)^2}}{\sum_{t_0}^{t_f} \sqrt{(x_t - x_{t+1})^2 + (y_t - y_{t+1})^2}} \qquad \text{(Eq. 6-1)}$$

where $[x_0, y_0]$ and $[x_f, y_f]$ represent the starting and ending locations for a cell's overall trajectory, $[x_t,\ y_t]$ represent a single time-point along that trajectory, $[x_{t+1},\ y_{t+1}]$ represent the next consecutive time-point along the same cell's trajectory, t_0 represents the starting frame and t_f

represents the ending frame for a cell [25-27]. As a result, values ranged from 0 to 1, with a larger value indicating a "straighter" or more direct trajectory between the starting and ending locations. As shown in **Chapter 3**, the asphericity was calculated using the gyration tensor for each cell track:

$$S_{mn} = \frac{1}{2N^2}\sum_{i=1}^{N}\sum_{j=1}^{N}(m_i - m_j)(n_i - n_j) \qquad \text{(Eq. 6-2)}$$

where *m* and *n* refer to the Cartesian coordinates (x or y respectively), *N* is the total number of track positions, and *i* and *j* are given track positions [28]. The largest and smallest eigenvalues for the gyration tensor, λ_2^2 and λ_1^2, respectively, were then extracted and used to calculate the cell track asphericity (*A*):

$$A = \frac{(\lambda_2^2 - \lambda_1^2)}{(\lambda_2^2 + \lambda_1^2)} \qquad \text{(Eq. 6-3)}$$

As a result, asphericity values ranged from 0 to 1, with a larger asphericity indicating more directed cell migration.

For each feature selected, the average value per cell was calculated across all frames for the nuclear morphometric and velocity features, while the straightness ratio and asphericity were calculated based on the overall cell trajectory. These cell-by-cell feature values were then used in the clustering analysis. For all cases, data features were standardized to the same interval range [0,1] prior to clustering using:

$$z_i = \frac{x_i - \min(x)}{\max(x) - \min(x)} \qquad \text{(Eq. 6-4)}$$

where x_i represents the original feature value, and $\min(x)$ and $\max(x)$ represent the minimum and maximum values for a feature respectively. Features were standardized to ensure equal weighting across PCA variance calculations.

6.3.4 Preprocessing and Data Reduction using Principle Component Analysis

Principle component analysis (PCA) was then used to reduce feature incorporation for PAM clustering. While a variety of complex techniques exist for statistically determining component inclusion [29], a cumulative threshold of 75% of the total variance was set to simplify cut-off determination. Component features were then extracted, with the maximum feature contributing to the variance highlighted. Any features falling within 10% of this major feature were additionally included, to account for instances where multiple features contribute to the majority of the variance. To ensure appropriate cut-offs for the novel co-culture and monoculture cell data, an accepted literature test data set (the Iris flower data set), was initially evaluated. PCA was performed in R using the FactoMineR: PCA package [30].

6.3.5 Clustering Data using a Partitioning Algorithm

PCA reduced features were then analyzed using a partitioning around medoids (PAM) clustering technique. The PAM technique arbitrarily selects a subset of the data, k, and identifies the medoids of each feature based on the designated number of clusters. A second subset of data, separate from k, is then selected and the cost associated with switching the data points is calculated. If the cost is less than the cost associated with the original values, data points are swapped and the process continues until no further change is identified [31]. Due to ambiguity associated with the number of ideal clusters in the co-culture and monoculture cell data, the pamk function, which additionally optimizes the number of clusters using silhouette width calculations [20], was employed from the flexible procedures for classification (fpc) package in R [32]. A silhouette width utilizes the average distance of a point from each other point within a cluster and the average distance of the same point to all points in the nearest secondary cluster to develop a quantitative metric for cluster effectiveness [20]. In our case, the optimal number of clusters chosen correlated with the highest average silhouette width. For our data, we adopted the ranges identified in [33], where silhouette widths of 0.7-1.0 indicated a strong structure, 0.5-0.7 indicated a reasonable structure, and 0.25-0.5 indicated a weak structure. In cases where silhouette widths were negative, we deduced that inappropriate clustering had been achieved.

6.3.6 Manual Verification of Co-Culture Populations

DiI-Ac-LDL staining was employed for differentiation of smooth muscle and endothelial cells in co-culture microenvironments. DiI-Ac-LDL is an EC specific stain that aggregates in the cell's cytoplasm. Preliminary experiments (data not shown) confirmed that SMCs did not uptake the DiI-Ac-LDL dye, allowing the N3 channel to be used for manual separation of EC and SMC cells. To identify cell types, A4 (Hoechst) and N3 (DiI-Ac-LDL) channel images were first overlaid in ImageJ [34]. Four frames (1, 135, 270, and 405) representing one early, two intermediate, and one late stage tracking frame, were then selected for manual analysis. Cell IDs, as identified by ACT*IV*E tracking, were then overlaid on each cell's center of mass. An expert user then classified each ACT*IV*E identified cell as an endothelial or smooth muscle cell. PAM cluster information was then matched to the manually identified cells and the percentage of each cell type per cluster was determined. It is of note that only a subset of the total number of cells per co-culture data set were evaluated, due to tracking complexities associated with cells moving in and out of the field of view, temporary loss of cell IDs from occlusion events, and potential relabeling of cell IDs due to erratic movements or mislabeled division or merging events.

6.4 Results: Combining Principle Component Analysis and Partitioning Clustering as a Means to Identify Cell Subpopulations

Cell subpopulation analysis was broken down into four distinct categories: 1) initial testing of a known data set to verify the PCA and PAM technique, 2) morphometric analysis of co-culture and monoculture EC and SMC data, 3) motility analysis of co-culture and monoculture EC and SMC data, and 4) a combined approach utilizing all morphometric and motility features to cluster EC and SMC subpopulations. Analysis of the Iris test data set revealed that the PCA and PAM technique could be utilized as a viable approach for effective clustering, based on current literature understanding. Application of the technique to cell morphometric features primarily identified two cell subpopulations: one with large nuclei and one with small nuclei. These groups were identified regardless of culture type, indicating that no major nuclear morphometric differences existed between the EC and SMC monoculture and co-culture groups. Conversely, clustering of motility parameters revealed that EC and SMC monocultures had relatively homogeneous movement rates (x-velocity, y-velocity, and speed), clustering into two groups primarily based on track shape (directionality ratio and asphericity). Co-culture groups also clustered into two distinct subpopulations, however these clusters were much more dependent on movement rate parameters, in addition to track shape features. This indicated that a mixed subset of the EC and SMC population adapted a faster movement rate in co-culture compared to monoculture. Combined analysis of the morphometric and motility features convoluted results, leading to poorer overall cluster separation. While two subpopulations were typically identified in the combined approach, subpar clustering and silhouette width values indicated that some of the subpopulations identified were most likely artificial. Overall, analysis of cell motility features demonstrated the greatest promise for identifying differences in cell subpopulations in mono versus co-culture.

6.4.1 Characterizing Clustering Effectiveness using the Iris Test Data Set

In order to verify appropriate use of the proposed clustering technique, Fisher's Iris data set was selected for methodology assessment [35]. The Iris data set contains 150 flowers, each stemming from one of three different species subpopulations: 1) Iris-Setosa, 2) Iris-Verisicolor, or 3) Iris-Virginica. Each flower has four features to consider for clustering classification: 1) sepal length, 2) sepal width, 3) petal length, and 4) petal width. This data set was selected as the test set because it is a standard in the bioinformatics literature and has been previously assessed with a variety of different clustering and machine learning techniques [36, 37]. While the Iris data set contains three known flower populations, two groups are identifiable using traditional clustering methods. This is due to characteristic overlap in the Versicolor and Virginica subpopulations, leading to ambiguous classification of one large cluster containing both Versicolor and Virginica species, and one small cluster containing the Setosa species [38].

Species attributes were first standardized to the interval range [0,1] for equivalent weighting in PCA classification and then analyzed in R using the freely available FactoMineR: PCA Package [30]. As shown in Table 6-3, PCA analysis identified four total components, with 95.80% of the variance attributed to the first two components. Further investigation of the dimensional breakdown by feature indicated that sepal length (27.28%), petal length (33.79%), and petal width (31.99%) primarily contributed to the variance in the first major component, while sepal width was the primary contributor (85.67%) to the variance associated with the second component (Table 6-4). Based on these results, all four features were included in the PAM clustering analysis.

Clustering analysis was performed using the flexible procedures for classification (fpc) package in R. More specifically, the partitioning around medoids with estimation of the number of clusters (pamk) function was utilized [32]. As shown in Figure 6-2A, two distinct clusters were identified for the Iris data set. Silhouette width analysis indicated that the smaller group (cluster 1) was considered a "strong" structure, as is indicated by a silhouette width of 0.76. The larger group (cluster 2), had a much lower silhouette width, with a value of 0.57, indicating "reasonable" classification (Figure 6-2B). After matching the cluster data to the original species data, cluster 1 was 100% Setosa species, while cluster 2 was 50% Versicolor and 50% Virginica species. This analysis is consistent with previous literature results [38], verifying that the PCA and PAM technique is a viable method for determining subpopulations. To determine whether more groups could be identified in cluster 2, Setosa data was removed and the clustering analysis was performed a second time. As shown in Figure 6-2C, two clusters were identified representing the Versicolor and Virginica subpopulations. The silhouette widths for these two subpopulations were 0.47 and

0.35 respectively, with 88% of the Versicolor and 92% of the Virginica groups appropriately clustered (Figure 6-2D). This corresponds well to literature understanding of how the iris data set should be clustered [38], indicating that our selected technique is a viable method for analyzing our co-culture and monoculture cell data.

6.4.2 Clustering Analysis of EC and SMC Co-Culture, SMC Monoculture, and EC Monoculture Morphometric Data

Dual PCA and PAM analysis was next used to identify subpopulation trends in the co-culture and monoculture SMC and EC data. Cell features classified as "morphometric" parameters were considered first (Table 6-2), as we hypothesized that SMCs and ECs may exhibit different nuclear morphology in co-culture leading to identification of two distinct SMC and EC clusters. The morphometric features selected included the nuclear major axis, the nuclear minor axis, the nuclear aspect ratio, the nuclear area, and the nuclear intensity. Overall, clustering analysis revealed that two subpopulations (one with large nuclei and one with small nuclei) were identified regardless of culture type.

More specifically, PCA analysis revealed that 94% or more of the variation in the co-culture and monoculture data sets could be resolved by examining the first two principle components (Table 6-5). Further examination yielded that all morphometric features should be taken into consideration, as the nuclear major axis, nuclear minor axis, nuclear area, and nuclear intensity were the major factors contributing to the variability of the first component, while the nuclear aspect ratio was the major feature contributing to the variability of the second component

(Table 6-6). These results were irrespective of culture type; therefore, no features were removed for the PAM clustering.

Subpopulation analysis of all replicates identified 2, 2, and 2 clusters (medians presented) for the co-culture, SMC monoculture, and EC monoculture morphometric data sets respectively. Point by point visualization of clusters from each experimental replicate further showed decent clustering across all groups analyzed (Figure 6-3). In comparison to the Iris test set (Figure 6-2), cluster classification of the co-culture morphometric features was poorer, but showed some promise for all groups tested. Cluster silhouette widths were plotted for each replicate to quantify clustering effectiveness (Figure 6-4). As shown in Table 6-7, average silhouette widths of 0.38 ± 0.01, 0.4 ± 0.05, and 0.38 ± 0.01 were observed for the co-culture, SMC monoculture, and EC monoculture groups respectively. This indicated that the clusters identified were relatively weak, but resembled the silhouette widths observed for the mixed Versicolor and Virginica clusters in the Iris data set. We attribute the low silhouette width values to shared characteristic overlap between subpopulations. Plotting feature distributions by subpopulation confirmed this trend (data not shown). Further manual characterization of the co-culture populations revealed that replicate 1 consisted mainly of ECs, representing 89.59% of the total cells identified. Comparatively, replicates 2 and 3 were much more balanced with respect to EC and SMC populations; replicate 2 was 53.52% ECs and 46.48% SMCs, while replicate 3 was 59.52% ECs and 40.48% SMCs.

After analyzing collective trends, replicate monocultures were individually considered to evaluate fluctuations within single cell populations. The morphometric data for the SMC and EC populations was predominately clustered into two subpopulations per replicate analyzed, with the exception of replicate 2 from both the SMC and EC monoculture groups (Figure 6-3). When individually considering the SMC monocultures, replicate 3 was the only sample with a "reasonable" identified cluster, according to silhouette width classification. After plotting average feature values by cluster, nuclear major axis, nuclear minor axis, nuclear area, and nuclear intensity demonstrated similar trends for replicates 1 and 3 for the SMC subpopulations (Figure 6-5). For replicate 2, the major feature averages for clusters 1 and 2 (which also had the lowest silhouette widths), fluctuated in similarity to clusters 3 and 4, depending on the feature investigated. These minor dissimilarities most likely accounted for the classification of the two additional weak SMC subpopulations. EC monocultures demonstrated similar trends to the SMC groups. As shown in Figure 6-6, aggregation of average feature values by subpopulation revealed similar trends for replicates 1 and 3. Replicate 2 clustered into 3 subpopulations, two very weak and one reasonable. This suggested that this replicate was actually a single population.

When evaluating morphometric clustering for the co-culture environments, each replicate was again individually considered. Replicate 1 clustered into two subpopulations: cluster 1 consisted of 88.51% ECs and 11.49% SMCs, while cluster 2 contained 90.30% ECs and 9.70% SMCs. Co-culture replicate 2 also clustered into two subpopulations, with 67.83% ECs and 32.17% SMCs in cluster 1 and 36.40% ECs and 63.60% SMCs in cluster 2. Replicate 3 was the only co-culture data set that clustered into three subpopulations, with 52.20% ECs and 47.80% SMCs in cluster 1, 79.28% ECs and 20.72% SMCs in cluster 2, and 47.37% ECs and 52.63% SMCs in cluster 3. For all of the co-culture data analyzed, cluster 1 from replicate 3 was the only subpopulation that had a "reasonable" silhouette width. Conversely, replicate 3 was also the only data set with an extremely low silhouette for cluster 2 (with a value of 0.18), indicating that this group was most likely artificial and should be split into clusters 1 and 3 only. When comparing average features across replicates, clusters, and cell types, replicates 1 and 2 had similar trends in cell subpopulations (Figure 6-7). Feature averages for replicate 3, cluster 2 consistently teetered back and forth, trending towards either cluster 1 or cluster 3 for nuclear major axis, nuclear minor axis, nuclear area, or nuclear intensity values. Unsurprisingly, no clear trends were observed for any of the subpopulations for the nuclear aspect ratio, as this feature was the only feature identified by PCA to not contribute to the first principle component. Overall, the morphometric co-culture and monoculture data suggested that two subpopulations (one with large nuclei, one with small nuclei) were identified regardless of culture type. This further indicated that there were no clear differences in nuclear morphometric features of EC and SMC cells co-cultured when compared to individual monocultures, disproving our initial hypothesis.

6.4.3 Expansion of Co-Culture Analysis to Cell Motility Data

Morphometric clustering of cell features demonstrated minor differences between co-culture and monoculture subpopulations. When clustering cell motility features, we hypothesized that much more pronounced subpopulations would be identified. More specifically, we hypothesized that a single migration mode would be observed in EC and SMC monocultures, while three modes would be identified in co-culture (SMC specific migration, endothelial specific migration, and intermittent behavior). Five motility parameters, x-velocity, y-velocity, speed, the directionality ratio, and asphericity (Table 6-2), were selected to compare clustering capabilities of co-culture and monoculture EC and SMC subpopulations. Overall, we observed that EC and SMC monocultures predominantly clustered based on track shape, while a portion of the EC and

SMC populations adapted a much higher movement rate in co-culture, which altered the clustering to be predominantly based on speed characteristics (instead of track behavior).

Similar to the morphometric data, PCA and PAM clustering of motility features was performed on three separate replicates for each experimental condition and then averaged across replicates to describe overall trends. As shown in Table 6-8, PCA identified that, on average, 84.59 ± 0.76%, 78.42 ± 2.01%, and 84.09 ± 0.90% of the overall variance could be described by the first two principle components for the co-culture, SMC monoculture, and EC monoculture motility data respectively. This signified that the SMC data had more variability in the cell features, as is indicated by a lower percentage of the variance conveyed in the first two principle components. Further analysis of feature contributions by dimension demonstrated that all five motility features should be considered for clustering in all three conditions tested. As shown in Table 6-9, the x-velocity, y-velocity, and speed contributed to the first principle component for all groups tested, while the directionality ratio and asphericity contributed to the second principle component for all groups tested. Similar to the morphometric data, this meant that all five features were considered for the motility PAM clustering, irrespective of culture condition.

PAM clustering revealed that 2, 2, and 2 subpopulations (medians presented) were observed for the co-culture, SMC monoculture, and EC monoculture groups respectively (Table 6-10). This corresponded to average silhouette widths of 0.29 ± 0.0047, 0.33 ± 0.05, and 0.29 ± 0.01, respectively. While these values were all lower than the average morphometric silhouette widths (indicating poorer clustering), they all still fell within the “weak” structure range. Point by point visualization of clusters from each experimental replicate further showed good separation across all groups analyzed (Figure 6-8). Silhouette plots further confirmed “weak” or borderline “weak” structure identification for all subpopulation groups identified (Figure 6-9).

Replicates from each experimental condition were then considered to evaluate unique trends in the co-culture versus monoculture data. The SMC monocultures were consistently clustered into two groups across all of the replicates analyzed. Average feature analysis by cluster revealed that the track shape (directionality ratio and asphericity) was more important than the cell movement rate (x-velocity, y-velocity, speed) in separating the SMC monoculture subpopulations (Figure 6-10). EC monocultures demonstrated similar motility trends. Overall, EC monoculture replicates were grouped into two clusters, with the exception of replicate three, which was clustered into three groups. When plotting average motility features by replicate, replicates 1 and 2 were clustered primarily based on track shape (directionality ratio and asphericity), and showed little difference in movement rate (x-velocity, y-velocity, and speed) features (Figure 6-11). Replicate three for the EC monocultures showed similar trends for the track shape parameters, but showed a large difference in movement rate features for cluster 2 compared to clusters 1 and 3 (while clusters 1 and 3 had very similar movement rate features). We hypothesize that there was a subset of ECs in replicate three that were highly motile, leading to the classification of three distinct clusters for this replicate, instead of two.

Co-culture replicates consistently clustered into two distinct subpopulations (Figure 6-8). For the motility features, replicate one had one cluster with 89.50% ECs and 10.50% SMCs and a second cluster with 89.69% ECs and 10.31% SMCs. Replicate two had one SMC dominant cluster, subpopulation 1, and one EC dominant cluster, subpopulation 2. In this case, subpopulation 1 consisted of 45.35% ECs and 54.65% SMCs. Comparatively, subpopulation 2 consisted of 69.06%

ECs and 30.94% SMCs. Similar to replicate two, replicate three was also grouped into one SMC dominant group (cluster 1) and one EC dominant group (cluster 2). In this case, subpopulation 1 had 40% ECs and 60% SMCs while subpopulation 2 had 69.35% ECs and 30.65% SMCs. Average feature plots revealed that, unlike the monoculture data, cell movement rate features were more important than track shape features for cluster determination in replicates one and two (Figure 6-12). For replicate three, movement rate features were still a factor in determining clusters, but track shape features dominated cluster identification. When examining the unscaled velocity values, cell movement rate features were greater than 66% faster in replicates 1 and 2 compared to replicate 3, while the track shape parameters were comparable across all replicates (Table 6-11). We hypothesize that these discrepancies in speed may be related to cell age or prolonged culture at high densities to accommodate experimental time constraints, leading to the minor inconsistencies associated with the co-culture average features observed. Overall, we observed that EC and SMC monocultures were predominantly clustered based on track shape (directionality ratio and asphericity). Interestingly, when in co-culture, a portion of the EC and SMC subpopulation adapted a much higher movement rate (x-velocity, y-velocity, and speed), which altered the clustering to be predominantly based on speed characteristics (instead of track characteristics).

6.4.4 A Combination Approach: Cluster Analysis of Morphometric and Motility Features

After identifying differences in the motility-based subpopulation analysis, morphometric and motility features were combined into a single data set to determine whether a combination approach could improve cell subpopulation identification. We hypothesized that four distinct clusters would be observed in co-culture: two overall clusters based on the movement rate motility differences, and two subgroups within these motility subpopulations of small and large nuclei. For the monocultures, we hypothesized a similar result, except that the motility features would be based predominantly on track shape, instead of movement rate features. In this case, two subgroups would still exist per motility subpopulation, representing cells with either large or small nuclei. Overall, performance of PAM clustering on the dual morphometric and motility parameters complicated clustering effectiveness, leading to poor subpopulation identification in the mono and co-culture data (Appendix 2). We concluded that, in order to more effectively determine trends, feature types should either be considered separately or more stringent feature inclusion parameters should be predetermined to minimize the number of features incorporated for more accurate and effective clustering.

6.5 Discussion: Application of PCA/PAM Classification of Mono and Co-Culture Cell Subpopulations

The original goal of this project was to develop a non-destructive, non-invasive method to identify subpopulations in heterogeneous cell cultures. Our claim is that this goal was achieved. The current study represents, to our knowledge, the first application of a combined principle component analysis (PCA) and partitioning around medoids (PAM) technique to identify differences in cell subpopulations of bovine aortic endothelial cells (ECs) and bovine aortic smooth muscle cells (SMCs) in mono and co-culture. Cells were imaged over a 24 hour duration using time-lapse microscopy to capture trends in nuclear morphometric and motility dynamics. Ten cell features were then selected for clustering analysis, including the nuclear morphometric features major axis, minor axis, aspect ratio, area, and intensity, and the cell motility parameters x-velocity, y-velocity, cell speed, the directionality ratio, and asphericity. Morphometric clustering revealed no major differences between cells in monoculture or co-culture, resulting in primarily two clusters identified (one with large nuclei and one with small nuclei). Interestingly, analysis of motility trends generally resulted in two subpopulations identified irrespective of culture type, however, clustering was based predominantly on cell track features (directionality ratio and asphericity) for the monoculture group but more heavily based on movement rate characteristics (x-velocity, y-velocity, and speed) for the co-culture groups. This signified that a portion of the EC and SMC population adapted enhanced movement rates in co-culture, leading to a substantial difference in average movement speeds for the identified co-culture subpopulations. Further expansion of the analysis to include both morphometric and motility parameters convoluted clustering results, leading to subpar classification of cell groups.

Experimentally, a co-culture of bovine aortic ECs and SMCs were chosen due to the natural synergy that exists between the two cell types in vasculature [21]. Long term co-culture of EC and SMC cells has been shown to improve cell proliferation and decrease protein deposition compared to cells in monoculture, indicating that strong interactions exist between SMCs and ECs [39]. The morphometric and motility features selected for this analysis were easily accessible based on ACT*IV*E's nuclear tracking capabilities [23]. The morphometric features selected, with exception of the nuclear intensity, were highly correlated with one another. Therefore it is not surprising that no major trends were observed to distinguish the mono and co-culture subpopulations identified within the morphometric characteristics. The motility metrics chosen were much more varied, enabling insight into differences in subpopulation dynamics based on movement rate or track shape features. In the future, inclusion of one or two morphometric features, one movement rate parameter, one track shape characteristic, and some additional descriptive behaviors, such as a cell's proliferative capacity or ECM deposition, could enable much more distinct cluster classifications, providing more detailed insight into the differences in mono and co-culture EC and SMC populations.

Here, we selected a combination approach of PCA to identify component variability and reduce feature size (where necessary) and PAM clustering to identify subpopulations from the reduced data set. This technique was first verified using the literature accepted Iris data set, where we verified 100% equivalent classification to accepted literature standards [36-38]. From there, PCA identified that all of the morphometric and motility parameters in the SMC and EC mono and co-cultures were important for clustering in their respective individual data sets, while only the aspect ratio was removed in the combined case when a 75% cumulative variance cut-off was employed. We recognize that this cumulative variance cut-off is not the most elegant approach for statistically determining component inclusion [29], however it provided an easy method for identifying cell features contributing substantially to the variance. To improve the subpopulation identification, a bootstrap [40], monte carlo [41], or eigenvector correlation analysis [29] could be performed instead to verify feature inclusion.

The Iris data set provided a baseline for silhouette width classification. While "strong" or "reasonable" clusters were observed in the initial analysis, "weak" classification was observed once the Setosa species, the group that consistently clusters into a single subpopulation, was removed. This was important, as it demonstrated that characteristic overlap results in weaker silhouette values, even though 88% or more of the flowers were appropriately clustered into their respective subpopulations. Therefore, it was unsurprising to see similar “weak” silhouette values in the cell subpopulation data (Figures 6-4 and 6-9). Outliers have been shown to significantly influence silhouette width values [20]. Noisy cell data or tracking inaccuracies could produce multiple outliers, resulting in weaker silhouette values for the experimental data used in the morphometric and motility clustering. Overall, while the silhouette values were considered “weak” in all of the clustering cases, more careful selection of the cells included for analysis may improve clustering effectiveness. One way to do this would be to alter the frame cut-off. In the presented work, cells had to be present for at least 20% of the total number of frames to be included in the final analysis. Similarly, removing cells with extremely large standard deviations in cell features (which are probably the result of tracking inaccuracies) could significantly improve clustering capabilities.

In addition to the ability to quantify clustering effectiveness using silhouette widths, the PAM technique was originally selected because it required no user bias for the target number of clusters identified [32]. Silhouette widths were instead used to determine the number of clusters, k. It is important to note that this technique will never identify a single population, as silhouette width classification is defined as the comparison of at least two subpopulations [10]. Therefore, careful consideration of cluster plots (e.g., Figure 6-3 and 6-8) and average features values per subpopulation (e.g., Figures 6-5, 6-6, and 6-7) were required to draw accurate conclusions. In the presented work, two dimensional plots of the cell data confirmed at least two distinct clusters for the individual morphometric or motility subpopulations. However, when analyzing the combined features, concerns about cluster inclusion arose due to subpopulation overlap. Expansion of the analysis to new features, data inclusion parameters, or PCA guidelines would require further examination to ensure appropriate cluster identification.

6.6 Conclusions

We successfully demonstrated that endothelial and smooth muscle cell mono and co-cultures could be imaged using time-lapse fluorescence microscopy, analyzed for morphometric and motility trends, and then clustered to reveal cell subpopulations. Our goal was to create a non-destructive, non-invasive method for analyzing heterogeneous microenvironments. This approach allows for just that, while directly linking morphometric or motility data to population composition. By adapting a combination approach of ACT*IV*E morphometric and motility analysis, principle component feature reduction, and partitioning around medoids, we demonstrated that the technique could be utilized to identify trends in EC and SMC live-cell data. The technique was proven robust and effective first through analyzing a known test set, the Iris data, to achieve results consistent with literature understanding. We then applied the technique to morphometric cell data, resulting in the identification of two major clusters, one with large nuclei and one with small nuclei, irrespective of culture condition. Interestingly, application of the technique to motility features identified that cells in co-culture adapted different movement rate parameters compared to those in monoculture, indicating that a subpopulation of the EC and SMC cells altered their speed in co-culture. A combinatory approach which pooled the morphometric and motility data revealed that the technique was sensitive to the features included, as poor clustering was noted for all cases when the data was combined. In general, this technique is modular and could be applied to any heterogeneous system without the need to sacrifice additional cultures to link morphometric or motility dynamics to population groups. Fully automating the approach further reduces bias associated with cluster classification, while retaining important information about each individual cell feature. We anticipate that application of this technique will further understanding of how heterogeneous systems contribute to exhibited cell migration patterns.

6.7 References

1. Duell, B.L., et al., *Epithelial Cell Coculture Models for Studying Infectious Diseases: Benefits and Limitations.* Journal of Biomedicine and Biotechnology, 2011: p. 9.
2. Casbas-Hernandez, P., J.M. Fleming, and M.A. Troester, *Gene Expression Analysis of In Vitro Cocultures to Study Interactions between Breast Epithelium and Stroma.* Journal of Biomedicine and Biotechnology, 2011: p. 12.
3. Goers, L., P. Freemont, and K.M. Polizzi, *Co-culture systems and technologies: taking synthetic biology to the next level.* Journal of the Royal Society Interface, 2014. **11**(96): p. 13.
4. Baer, P.C. and H. Geiger, *Adipose-Derived Mesenchymal Stromal/Stem Cells: Tissue Localization, Characterization, and Heterogeneity.* Stem Cells International, 2012: p. 11.
5. Duraiyan, J., et al., *Applications of immunohistochemistry.* Journal of pharmacy & bioallied sciences, 2012. **4**(Suppl 2): p. S307-9.
6. de Matos, L.L., et al., *Immunohistochemistry as an important tool in biomarkers detection and clinical practice.* Biomarker Insights, 2010. **2010**(5): p. 9-20.
7. Giulietti, A., et al., *An overview of real-time quantitative PCR: Applications to quantify cytokine gene expression.* Methods, 2001. **25**(4): p. 386-401.

8. Bustin, S.A., *Quantification of mRNA using real-time reverse transcription PCR (RT-PCR): Trends and problems.* Journal of Molecular Endocrinology, 2002. **29**(1): p. 23-39.
9. Quinn, G.P. and M.J. Keough, *Experimental Design and Data Analysis for Biologists*. 2002, Cambridge, U.K.: Cambridge University Press.
10. Tibshirani, R., G. Walther, and T. Hastie, *Estimating the number of clusters in a data set via the gap statistic.* Journal of the Royal Statistical Society. Series B: Statistical Methodology, 2001. **63**(2): p. 411-423.
11. Samet, H., *The Quadtree and Related Hierarchical Data Structures.* ACM Computing Surveys (CSUR), 1984. **16**(2): p. 187-260.
12. Kohonen, T., *Essentials of the self-organizing map.* Neural Networks, 2013. **37**: p. 52-65.
13. Ivanenkov, Y.A., et al., *Computational mapping tools for drug discovery.* Drug Discovery Today, 2009. **14**(15-16): p. 767-775.
14. Schneider, P., Y. Tanrikulu, and G. Schneider, *Self-Organizing Maps in Drug Discovery: Compound Library Design, Scaffold-Hopping, Repurposing.* Current Medicinal Chemistry, 2009. **16**(3): p. 258-266.
15. Beckonert, O., et al., *Visualizing metabolic changes in breast-cancer tissue using H-1-NMR spectroscopy and self-organizing maps.* Nmr in Biomedicine, 2003. **16**(1): p. 1-11.
16. Wang, Z.D., et al., *A novel neural network approach to cDNA microarray image segmentation.* Computer Methods and Programs in Biomedicine, 2013. **111**(1): p. 189-198.
17. Blekherman, G., et al., *Bioinformatics tools for cancer metabolomics.* Metabolomics, 2011. **7**(3): p. 329-343.

18. Van der Laan, M.J., K.S. Pollard, and J. Bryan, *A new partitioning around medoids algorithm.* Journal of Statistical Computation and Simulation, 2003. **73**(8): p. 575-584.
19. Rafsanjani, M.K.V., Zahra Asghari and N.E. Chukanlo, *A survey of hierarchical clustering algorithms.* The Journal of Mathematics and Computer Science 2012. **5**(3): p. 229-240.
20. Rousseeuw, P.J., *Silhouettes: A graphical aid to the interpretation and validation of cluster analysis.* Journal of Computational and Applied Mathematics, 1987. **20**(C): p. 53-65.
21. Wang, H.Q., et al., *Coculture with endothelial cells enhances vascular smooth muscle cell adhesion and spreading via activation of beta(1)-integrin and phosphatidylinositol 3-kinase/Akt.* European Journal of Cell Biology, 2007. **86**(1): p. 51-62.
22. Wang, Y.H., et al., *Vascular smooth muscle cells promote endothelial cell adhesion via microtubule dynamics and activation of paxillin and the extracellular signal-regulated kinase (ERK) pathway in a co-culture system.* European Journal of Cell Biology, 2009. **88**(11): p. 701-709.
23. Baker, R.M., et al., *Automated, contour-based tracking and analysis of cell behaviour over long time scales in environments of varying complexity and cell density.* Journal of The Royal Society Interface, 2014. **11**(97).
24. Forster, B., et al., *Complex wavelets for extended depth-of-field: A new method for the fusion of multichannel microscopy images.* Microscopy Research and Technique, 2004. **65**(1-2): p. 33-42.
25. Benhamou, S., *How to reliably estimate the tortuosity of an animal's path: Straightness, sinuosity, or fractal dimension?* Journal of Theoretical Biology, 2004. **229**(2): p. 209-220.

26. Codling, E.A., M.J. Plank, and S. Benhamou, *Random walk models in biology.* Journal of the Royal Society Interface, 2008. **5**(25): p. 813-834.

27. Gorelik, R. and A. Gautreau, *Quantitative and unbiased analysis of directional persistence in cell migration.* Nature Protocols, 2014. **9**(8): p. 1931-1943.

28. Šolc, K., *Shape of a random-flight chain.* The Journal of Chemical Physics, 1971. **55**(1): p. 335-344.

29. Peres-Neto, P.R., D.A. Jackson, and K.M. Somers, *How many principal components? stopping rules for determining the number of non-trivial axes revisited.* Computational Statistics and Data Analysis, 2005. **49**(4): p. 974-997.

30. Lê, S., J. Josse, and F. Husson, *FactoMineR: An R Package for Multivariate Analysis.* Journal of Statistical Software; Vol 1, Issue 1 (2008), 2008.

31. Han, J. and M. Kamber, *Data Mining: Concepts and Techniques*. 2 ed. The Morgan Kaufmann Series in Data Management Systems, ed. J. Gray. 2006, San Francisco, CA: Morgan Kaufmann Publishers.

32. Hennig, C. and T.F. Liao, *How to find an appropriate clustering for mixed-type variables with application to socio-economic stratification.* Journal of the Royal Statistical Society: Series C (Applied Statistics), 2013. **62**(3): p. 309-369.

33. *Innovation and Advances in Computer, Information, Systems Sciences, and Engineering*. Vol. 152. 2013, New York: Springer.

34. Schneider, C.A., W.S. Rasband, and K.W. Eliceiri, *NIH Image to ImageJ: 25 years of image analysis.* 2012. **9**(7): p. 671-675.

35. Fisher, R.A., *The use of multiple measurements in taxonomic problems.* Annual Eugenics, 1936. **7**(Part II): p. 179-188.

36. Klein, D., S.D. Kamvar, and C.D. Manning, *From Instance-level Constraints to Space-Level Constraints: Making the Most of Prior Knowledge in Data Clustering*, in *Proceedings of the Nineteenth International Conference on Machine Learning*. 2002, Morgan Kaufmann Publishers Inc. p. 307-314.

37. Ben-Hur, A., et al., *A support vector clustering method.* Proceedings - International Conference on Pattern Recognition, 2000. **15**(2): p. 724-727.

38. Sugar, C.A. and G.M. James, *Finding the Number of Clusters in a Dataset: An Information-Theoretic Approach.* Journal of the American Statistical Association, 2003. **98**(463): p. 750-763.

39. Williams, C. and T.M. Wick, *Endothelial cell-smooth muscle cell co-culture in a perfusion bioreactor system.* Annals of Biomedical Engineering, 2005. **33**(7): p. 920-928.

40. Jackson, D.A., *Stopping rules in principal components analysis: A comparison of heuristical and statistical approaches.* Ecology, 1993. **74**(8): p. 2204-2214.

41. Zwick, W.R. and W.F. Velicer, *Comparison of Five Rules for Determining the Number of Components to Retain.* Psychological Bulletin, 1986. **99**(3): p. 432-442.

Table 6-1: ACT*IV*E run parameters for co-culture and monoculture analysis

Parameter	**Description**	**Value**
Plot Toggle	Toggle to display segmentation plots	0
Number of Contours	Maximum number of contour levels for a single cell's intensity profile	15
Half Particle Diameter	Half the diameter of a typical cell (pixels)	13
Noise Wavelength	Characteristic noise for each image (pixels)	2
Collision Plot Toggle	Toggle to plot collision event videos	0
Maximum Area	Maximum area threshold for a cell (pixels)	260
Minimum Area	Minimum area threshold for a cell (pixels)	10
Maximum Displacement	Maximum distance a single particle moves, frame to frame (pixels)	15 or 10*
Frame Time	Time step between consecutive images (minutes)	3
Maximum Collision Time	Maximum duration cells can be completely occluded during a merging event (frames)	10
Division Toggle	Toggle to implement the manual division GUI	0
Merging Toggle	Toggle to implement the manual merging GUI	0

*Values of 15 and 10 were used for the first and second experimental data sets respectively

Table 6-2: Morphometric and motility parameters used for clustering analysis (averaged across all frames)

Parameter	**Description**	**Feature Type**
Nuclear Major Axis	Long-axis length of a fitted cell ellipse	Morphometric
Nuclear Minor Axis	Short-axis length of a fitted cell ellipse	Morphometric
Nuclear Aspect Ratio	Ratio of nuclear major axis to nuclear minor axis	Morphometric
Nuclear Area	Calculated area of a fitted ellipse	Morphometric
Nuclear Intensity	Calculated intensity for a fitted ellipse	Morphometric
X-Velocity	Speed in x-direction (horizontal)	Motility
Y-Velocity	Speed in y-direction (vertical)	Motility
Speed (Magnitude Velocity)	Average speed of a cell as defined by: $\sqrt{(X\_Velocity^2 + Y\_Velocity^2)}$	Motility
Straightness Ratio	Ratio of the straight line distance between the start and end point and the trajectory length scale: $DR = \frac{\sqrt{\left(x_f - x_0\right)^2 + \left(y_f - y_0\right)^2}}{\sum_{t_0}^{t_f} \sqrt{(x_t - x_{t+1})^2 + (y_t - y_{t+1})^2}}$	Motility
Asphericity	Cell track shape as defined by the gyration tensor: $A = \frac{(\lambda_2^2 - \lambda_1^2)}{(\lambda_2^2 + \lambda_1^2)}$	Motility

Table 6-3: Eigenvalue and variance PCA for the Iris data set

	Eigenvalue	Percentage of Variance (%)	Cumulative Percentage of Variance (%)
Component 1	2.91	72.77	72.77
Component 2	0.92	23.03	95.80
Component 3	0.15	3.68	99.48
Component 4	0.02	0.52	100.00

Table 6-4: Iris data set feature contributions by PCA dimension

Feature	**Dimension 1**	**Dimension 2**	**Dimension 3**	**Dimension 4**
Sepal Length	27.29%	13.86%	51.99%	6.86%
Sepal Width	6.94%	85.67%	5.86%	1.54%
Petal Length	33.79%	0.04%	1.99%	64.18%
Petal Width	31.99%	0.43%	40.17%	27.41%

Table 6-5: Average eigenvalue and variance PCA for the morphometric co-culture and monoculture SMC and EC data

		Eigenvalue	**Percentage of Variance (%)**	**Cumulative Percentage of Variance (%)**
Co-Culture	*Component 1*	3.54 ± 0.10	70.90 ± 1.94	70.90 ± 1.94
	Component 2	1.19 ± 0.13	23.85 ± 2.54	94.74 ± 0.63
SMC Monoculture	*Component 1*	3.40 ± 0.0.15	67.98 ± 3.07	67.98 ± 3.07
	Component 2	1.30 ± 0.03	26.06 ± 0.61	94.03 ± 2.52
EC Monoculture	*Component 1*	3.54 ± 0.08	70.83 ± 1.51	70.83 ± 1.51
	Component 2	1.22 ± 0.06	24.40 ± 1.18	95.23 ± 0.82

Table 6-6: Morphometric co-culture and monoculture feature contributions by PCA dimension (averaged across all replicates)

	Co-culture		**SMC Monoculture**		**EC Monoculture**	
	Dim. 1 (%)	**Dim. 2 (%)**	**Dim. 1 (%)**	**Dim. 2 (%)**	**Dim. 1 (%)**	**Dim. 2 (%)**
Major Axis	25.59 ± 0.36	6.27 ± 2.50	25.09 ± 0.17	10.02 ± 2.38	24.63 ± 1.51	8.30 ± 4.85
Minor Axis	21.81 ± 1.16	15.71 ± 3.10	22.15 ± 2.16	16.70 ± 3.69	22.99 ± 1.43	12.66 ± 3.59
Aspect Ratio	3.34 ± 2.56	72.87 ± 0.41	2.28 ± 1.61	70.25 ± 2.89	1.17 ± 1.11	78.22 ± 4.69
Area	27.19 ± 0.76	0.11 ± 0.15	28.63 ± 1.03	0.04 ± 0.06	27.52 ± 0.50	0.12 ± 0.09
Intensity	22.06 ± 2.07	5.04 ± 3.85	21.85 ± 1.43	2.99 ± 1.69	23.69 ± 1.01	0.70 ± 0.89

Highlighting indicates features with a majority percentage selected from each dimension for clustering analysis.

Table 6-7: Silhouette width analysis for morphometric co-culture and monoculture cell data (averaged across all replicates)

	Median Number of Clusters Identified	**Average Silhouette Width**	**Average Number of Cells Analyzed**
Co-Culture	2	0.38 ± 0.01	505 ± 75
SMC Monoculture	2	0.4 ± 0.05	303 ± 101
EC Monoculture	2	0.38 ± 0.01	297 ± 133

Table 6-8: Average eigenvalue and variance PCA for the motility co-culture and monoculture SMC and EC data

		Eigenvalue	**Percentage of Variance (%)**	**Cumulative Percentage of Variance (%)**
Co-Culture	*Component 1*	2.75 ± 0.03	54.90 ± 0.67	54.90 ± 0.67
	Component 2	1.48 ± 0.01	29.68 ± 0.12	84.59 ± 0.76
SMC Monoculture	*Component 1*	2.51 ± 0.08	50.30 ± 1.51	50.30 ± 1.51
	Component 2	1.41 ± 0.04	28.12 ± 0.78	78.42 ± 2.01
EC Monoculture	*Component 1*	2.77 ± 0.05	55.42 ± 0.93	55.42 ± 0.93
	Component 2	1.43 ± 0.02	28.67 ± 0.32	84.09 ± 0.90

Table 6-9: Motility co-culture and monoculture feature contributions by PCA dimension (averaged across all replicates)

	Co-culture		**SMC Monoculture**		**EC Monoculture**	
	Dim. 1 (%)	**Dim. 2 (%)**	**Dim. 1 (%)**	**Dim. 2 (%)**	**Dim. 1 (%)**	**Dim. 2 (%)**
X-Velocity	30.46 ± 0.49	1.30 ± 0.28	29.61 ± 0.51	0.13 ± 0.10	31.26 ± 0.08	0.73 ± 0.70
Y-Velocity	30.51 ± 0.62	0.68 ± 0.46	28.63 ± 0.74	0.78 ± 0.54	31.35 ± 0.42	0.20 ± 0.21
Speed	35.66 ± 0.47	1.37 ± 0.52	39.44 ± 1.14	0.11 ± 0.08	35.86 ± 0.70	0.37 ± 0.24
Directionality Ratio	1.36 ± 0.77	49.11 ± 1.19	1.47 ± 0.55	48.70 ± 1.66	0.90 ± 0.46	49.05 ± 1.17
Asphericity	2.02 ± 0.67	47.54 ± 0.88	0.86 ± 0.77	50.28 ± 1.48	0.62 ± 0.81	49.66 ± 1.99

Highlighting indicates features with a majority percentage selected from each dimension for clustering analysis.

Table 6-10: Silhouette width analysis for motility co-culture and monoculture cell data (averaged across all replicates)

	Median Number of Clusters Identified	**Average Silhouette Width**	**Average Number of Cells Analyzed**
Co-Culture	2	0.29 ± 0.0047	505 ± 75
SMC Monoculture	2	0.33 ± 0.05	303 ± 101
EC Monoculture	2	0.29 ± 0.01	297 ± 133

Table 6-11: Unscaled average feature values for co-culture motility replicates

Feature	**Replicate 1**	**Replicate 2**	**Replicate 3**
X-Velocity (µm/min)	0.20 ± 0.073	0.17 ± 0.060	0.12 ± 0.044
Y-Velocity (µm/min)	0.20 ± 0.070	0.17 ± 0.058	0.12 ± 0.044
Speed (µm/min)	0.29 ± 0.095	0.25 ± 0.077	0.17 ± 0.058
Directionality Ratio	0.34 ± 0.18	0.32 ± 0.18	0.31 ± 0.18
Asphericity	0.70 ± 0.21	0.72 ± 0.22	0.73 ± 0.21

Scheme 6-1: Time-line and seeding conditions for time-lapse image set-up

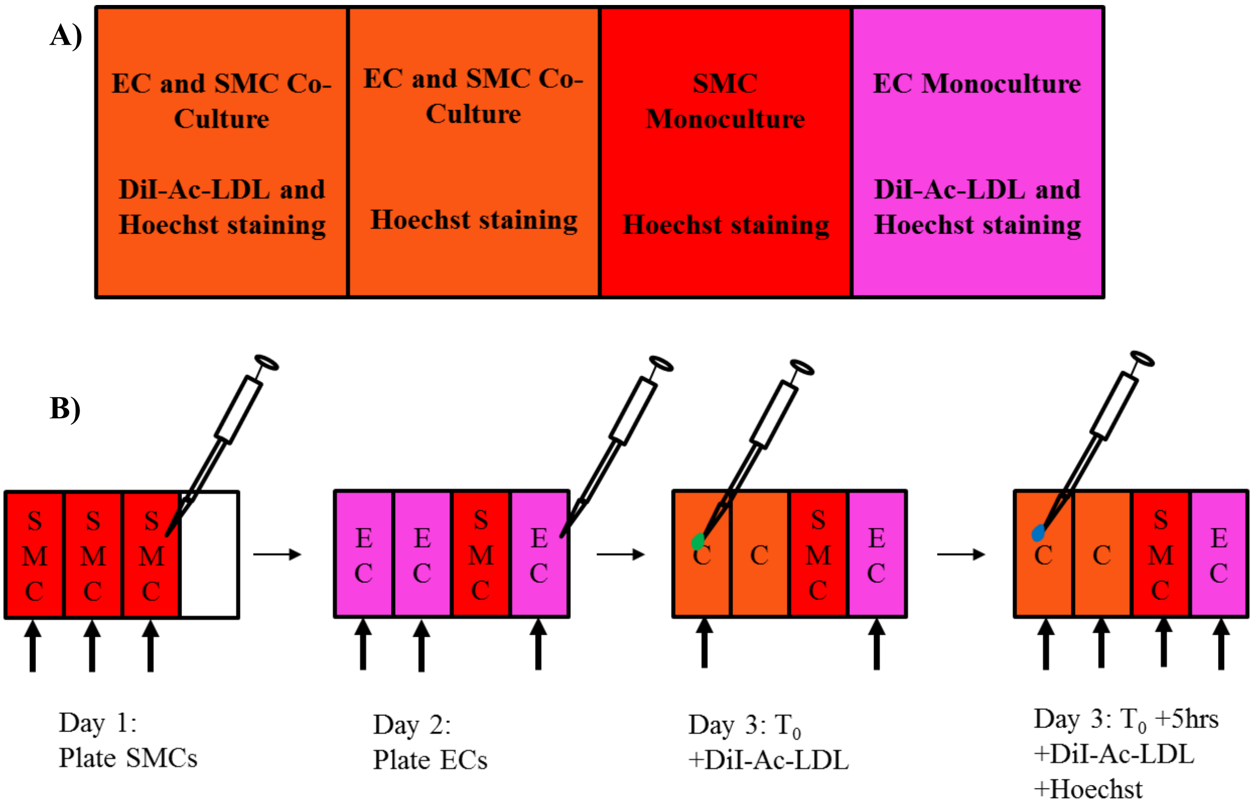

A) Cells were plated in one of four experimental conditions for time-lapse microscopy: 1) EC and SMC co-culture with DiI-Ac-LDL and Hoechst staining, 2) EC and SMC co-culture with Hoechst staining, 3) SMC monocultures with Hoechst staining, or 4) EC monocultures with DiI-Ac-LDL and Hoechst staining. B) To simulate native vasculature, SMCs were plated on day 1, followed by EC plating on day 2, followed by DiI-Ac-LDL staining (where relevant) and subsequent Hoechst staining on day 3 for time-lapse image capture.

Figure 6-1: Example staining and trajectory results for co-culture and monoculture microenvironments.

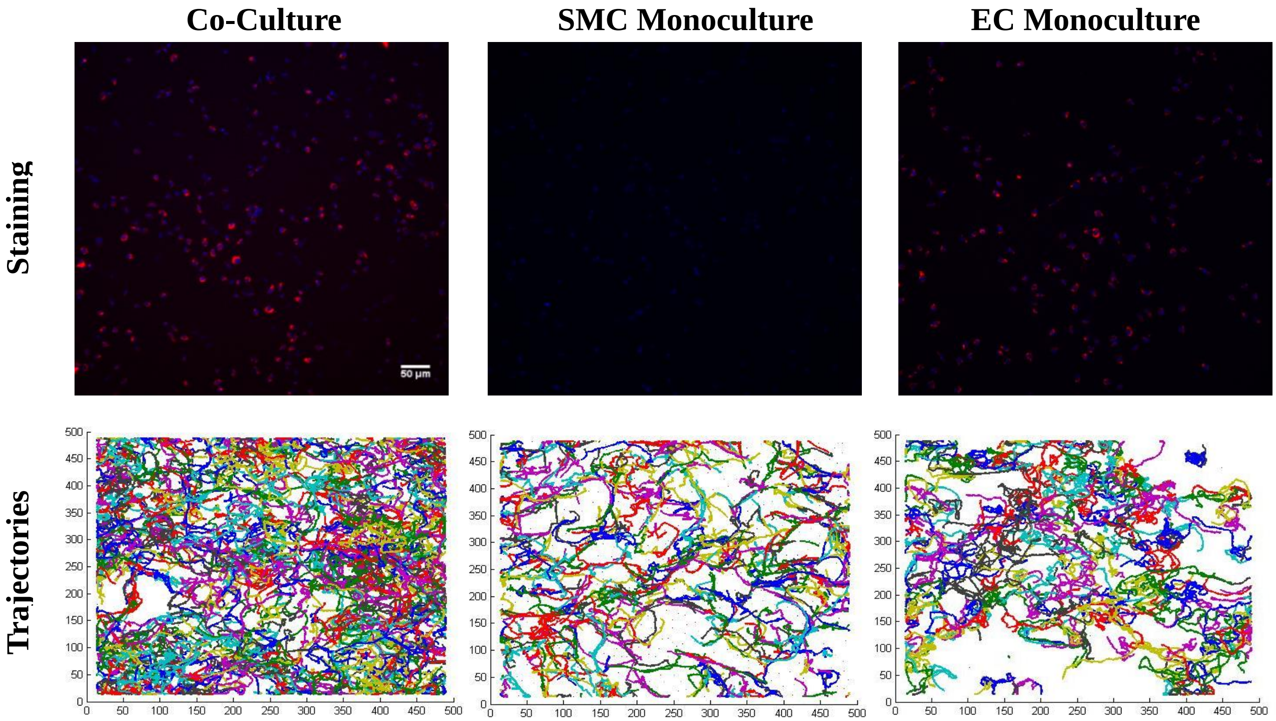

Representative example staining (top row) and trajectory results (bottom row) for EC and SMC co-culture (left), SMC monoculture (middle) and EC monoculture (right) environments. Top row: Cells were stained with Hoechst (blue) and DiI-Ac-LDL (red). DiI-Ac-LDL was used as an endothelial specific marker to differentiate SMC and EC cells in co-culture. Scale bar = 50µm for all images shown. Bottom row: Cell trajectories in all three environments demonstrated random motility, regardless of co-culture or monoculture condition.

Figure 6-2: PAM clustering and silhouette plots for the Iris data set

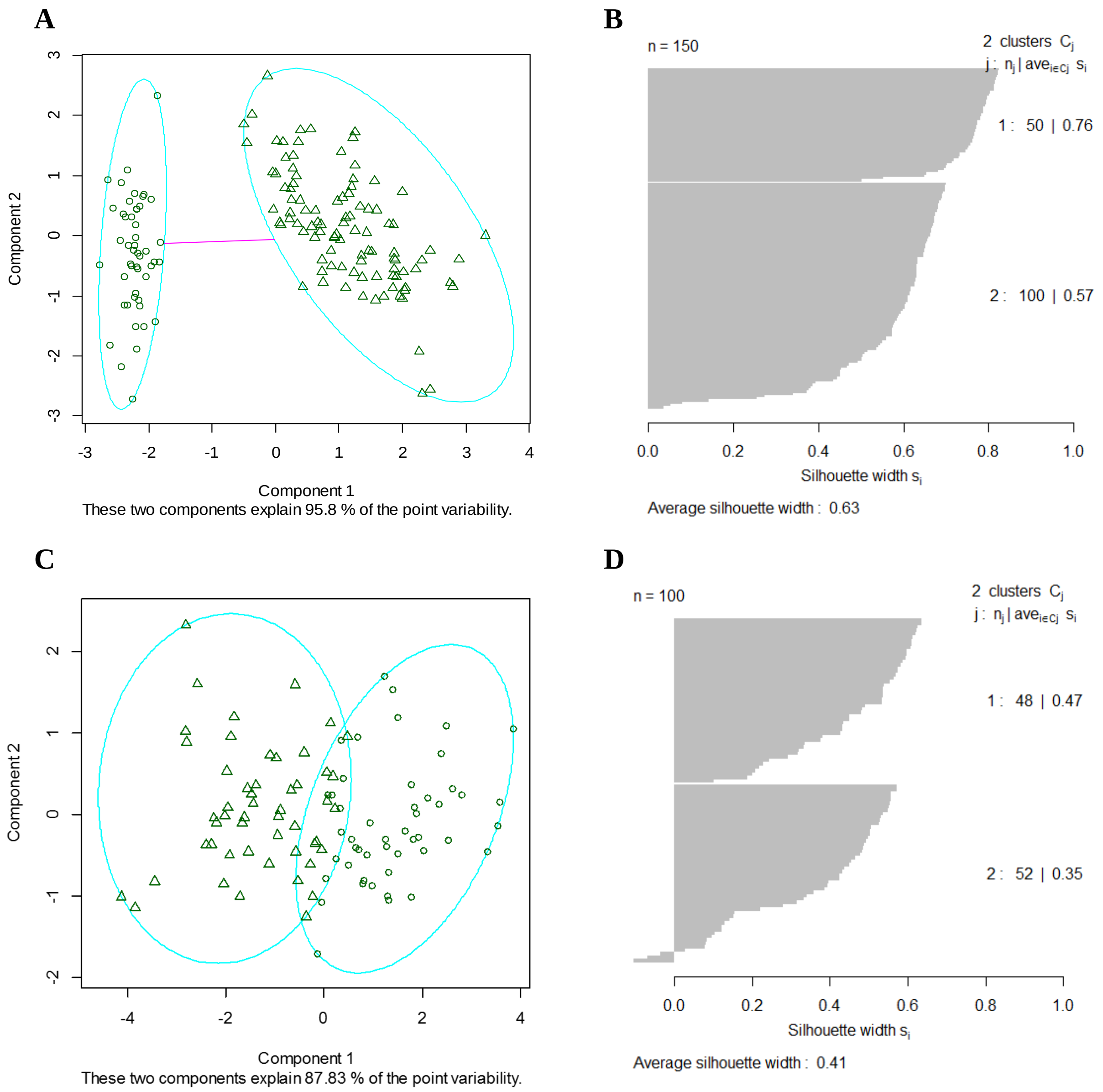

PAM clustering results for the Iris data set revealed A) two distinct clusters with B) “strong” and “reasonable” silhouette widths. After removing the Iris-Setosa data and clustering the remaining populations, C) two subpopulations were again identified, D) however, with weaker silhouette values.

Figure 6-3: PAM clustering of co-culture and monoculture morphometric features

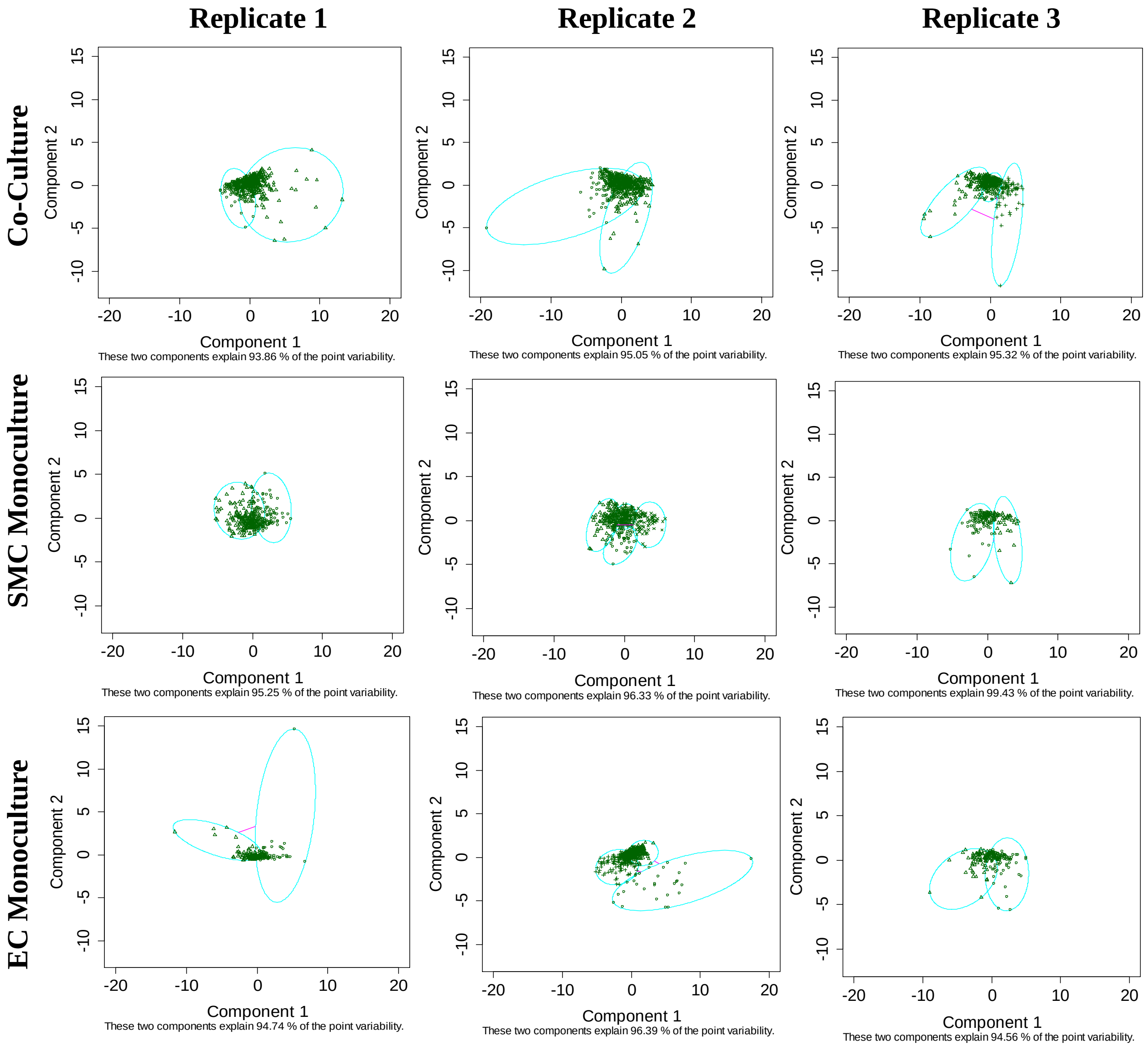

Two dimensional plots of PAM clustering of EC and SMC co-culture (top row), SMC monoculture (middle row), and EC monoculture (bottom row) morphometric data for replicates 1 (left), 2 (middle), and 3 (right). In general, two subpopulations were observed irrespective of culture condition, with some overlap between clusters identified.

Figure 6-4: Silhouette plots for morphometric co-culture and monoculture data

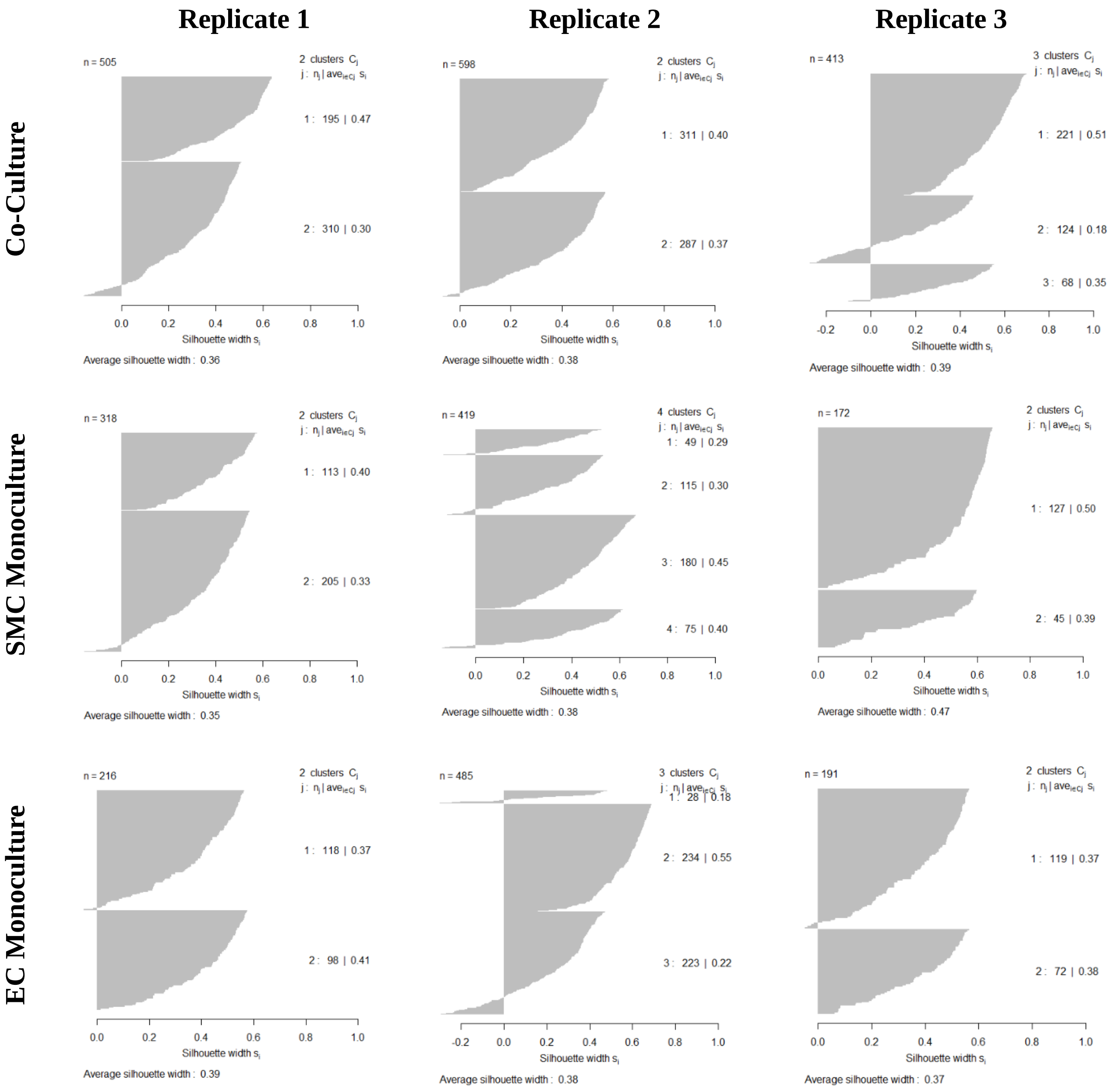

Silhouette plots for the EC and SMC co-culture (top), SMC monoculture (middle), and EC monoculture (bottom) revealed "weak" clustering effectiveness for the majority of the subpopulation groups identified.

Figure 6-5: SMC monoculture morphometric average feature breakdown by clustering subpopulation

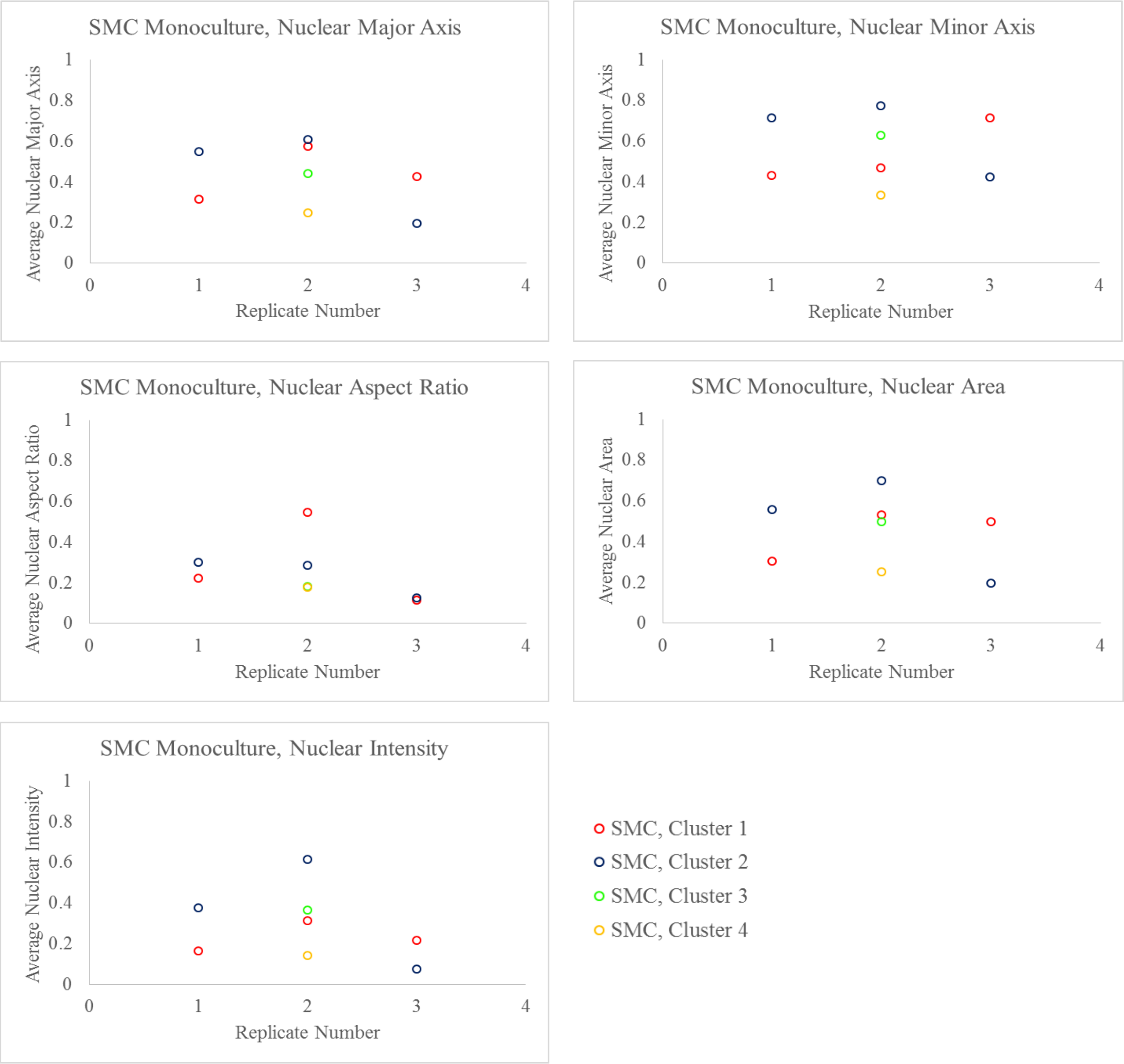

Cell feature averages were plotted for each subpopulation in the SMC monoculture to reveal overarching trends in the morphometric data. Overall, the nuclear major axis, nuclear minor axis, nuclear area, and nuclear intensity showed noticeable differences between cluster averages, indicating that these features were important for cluster classification.

Figure 6-6: EC monoculture morphometric average feature breakdown by clustering subpopulation

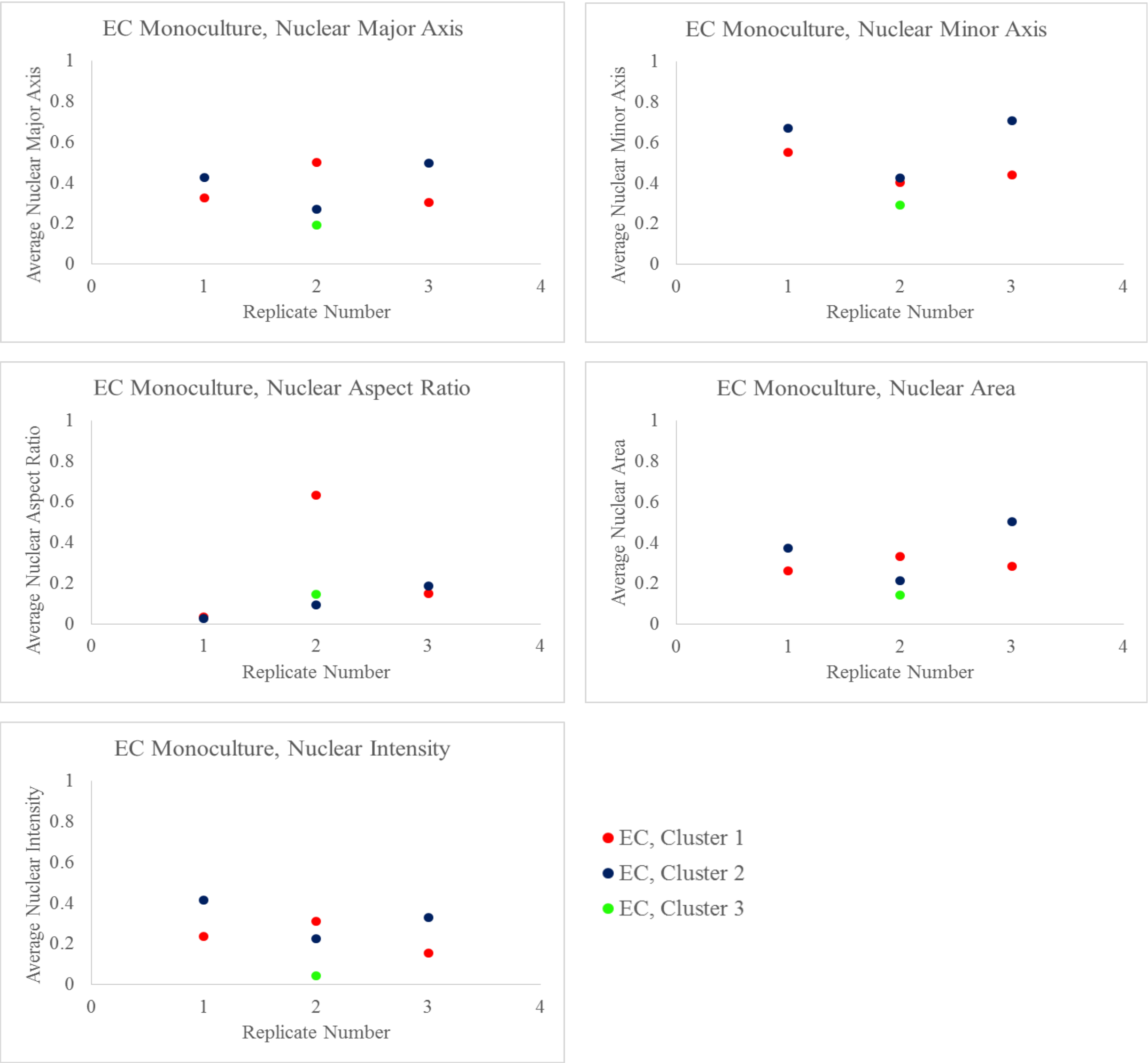

Cell feature averages were plotted for each subpopulation in the EC monoculture to reveal overarching trends in the morphometric data. Similar to the SMC monoculture data, the nuclear major axis, nuclear minor axis, nuclear area, and nuclear intensity showed noticeable differences between cluster averages, indicating that these features were important for cluster classification.

Figure 6-7: Co-culture morphometric average feature breakdown by clustering subpopulation

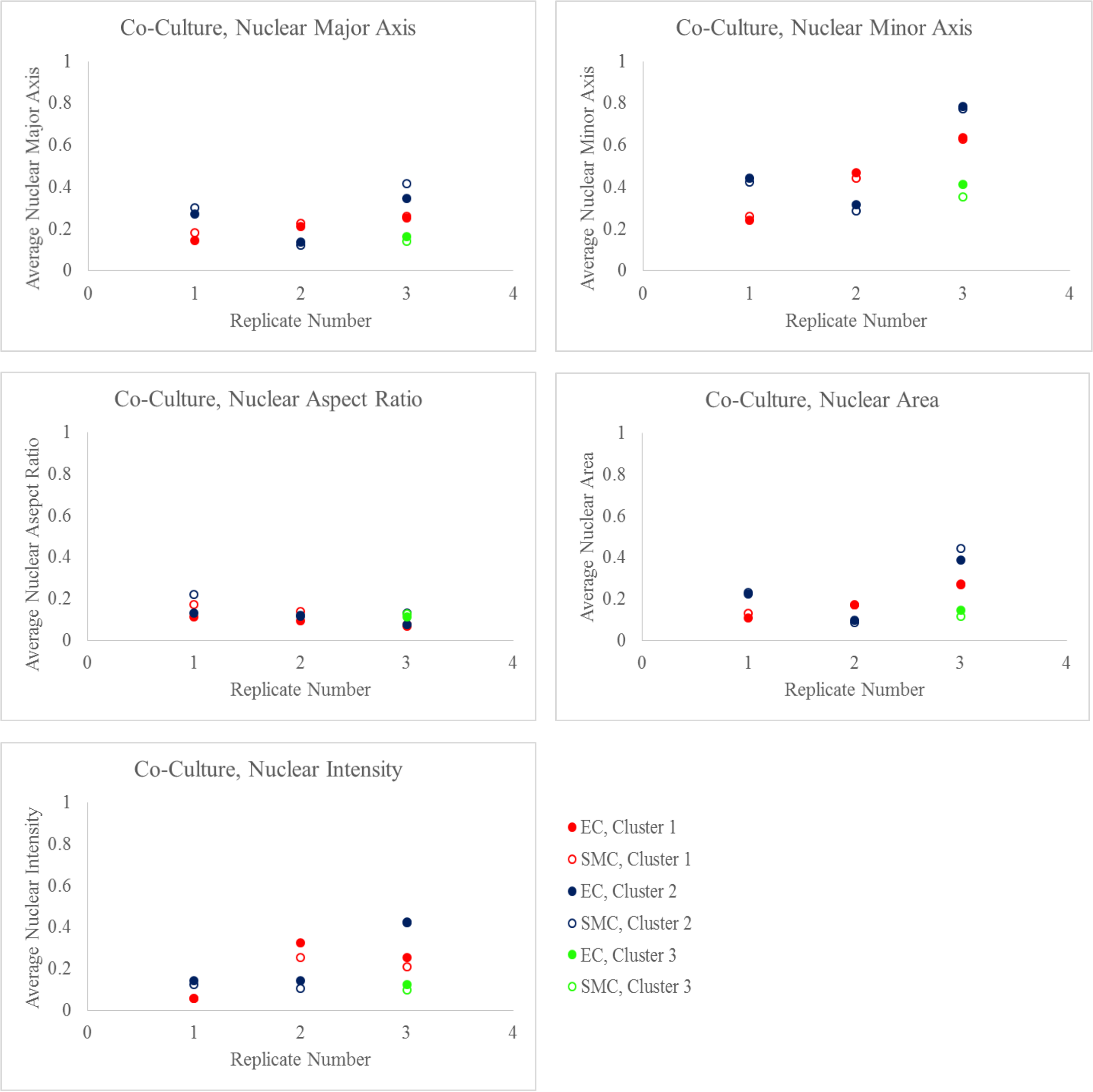

Cell feature averages were plotted for each subpopulation in the SMC and EC co-culture to reveal overarching trends in the morphometric data. No major differences were observed when compared to the EC or SMC monoculture clustering.

Figure 6-8: PAM clustering of co-culture and monoculture motility features

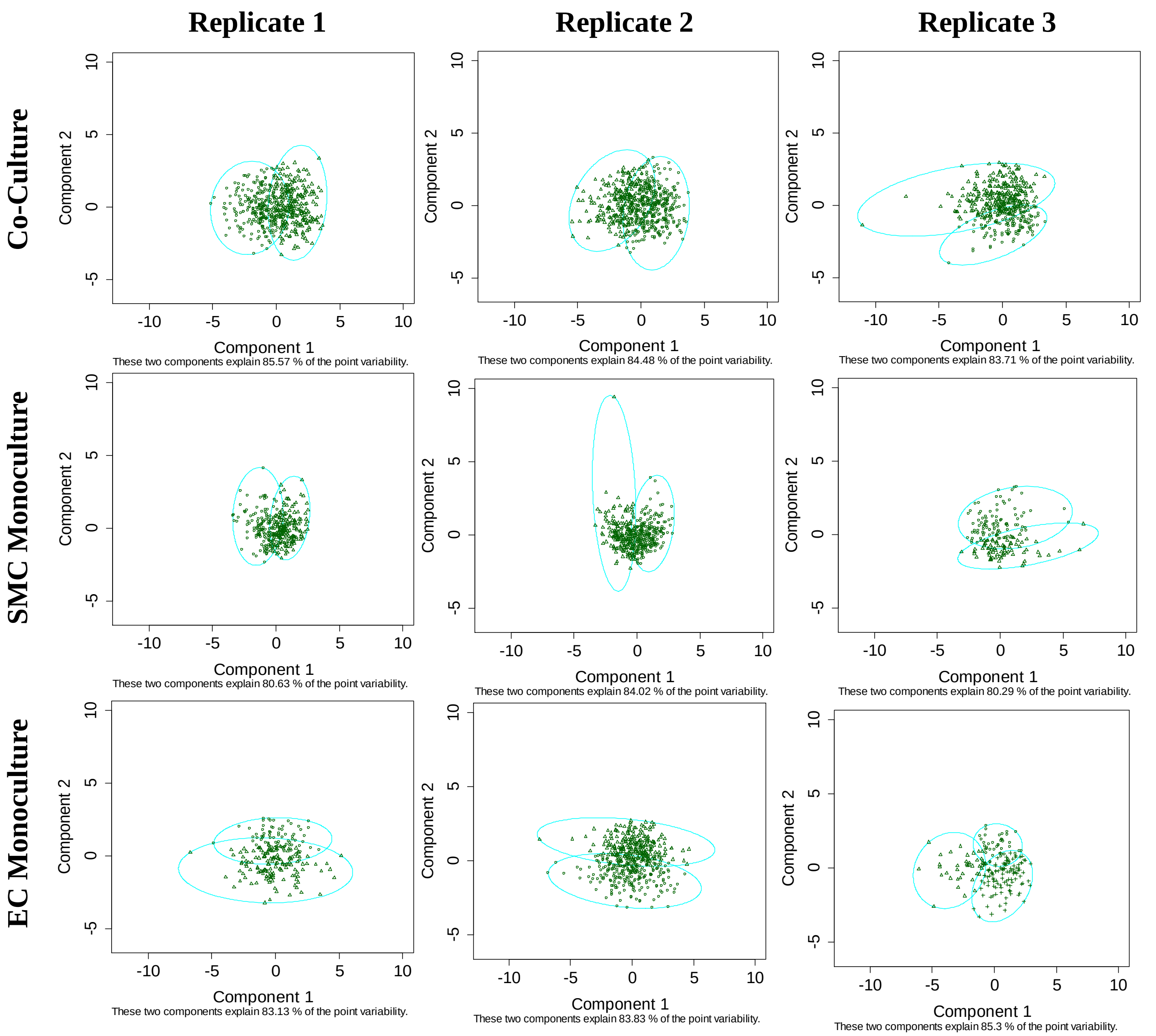

Two dimensional plots of PAM clustering of EC and SMC co-culture (top row), SMC monoculture (middle row), and EC monoculture (bottom row) motility data for replicates 1 (left), 2 (middle), and 3 (right). In general, two subpopulations were observed irrespective of culture condition, with some overlap between clusters identified.

Figure 6-9: Silhouette plots for motility co-culture and monoculture data

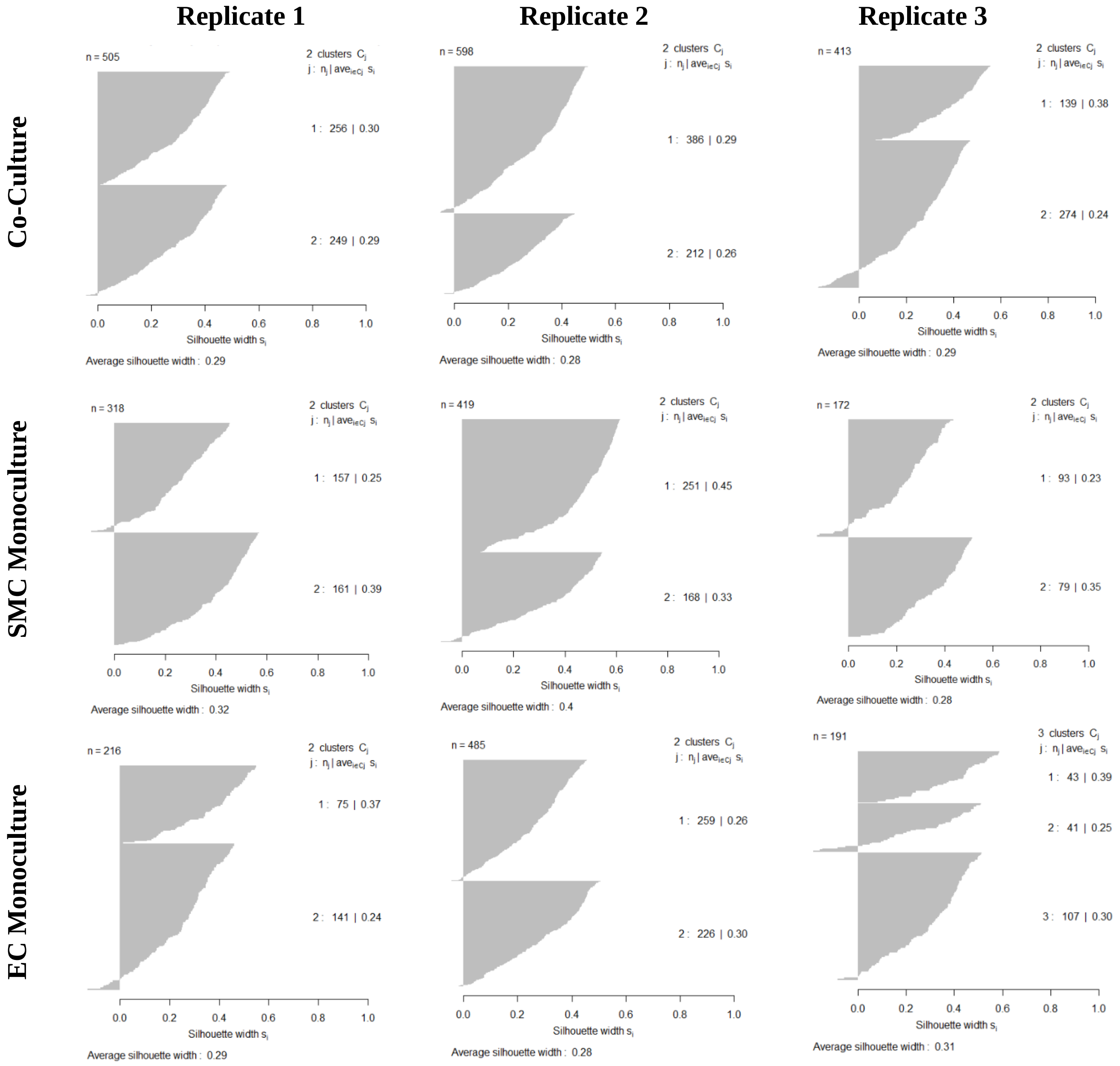

Similar to the morphometric data, silhouette plots for the EC and SMC co-culture (top), SMC monoculture (middle), and EC monoculture (bottom) motility data revealed “weak” clustering effectiveness for the majority of the subpopulation groups identified.

Figure 6-10: SMC monoculture motility average feature breakdown by clustering subpopulation

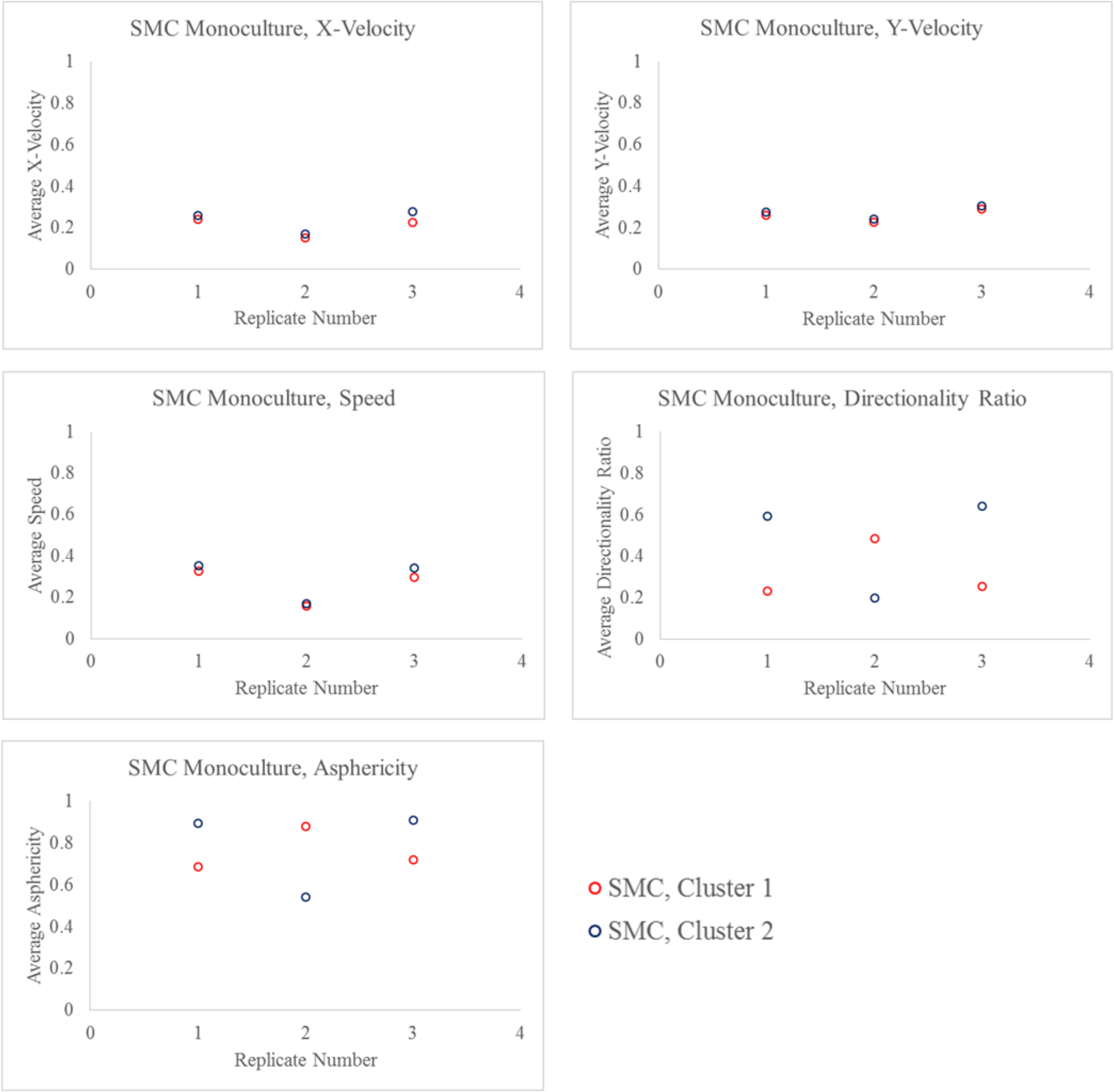

Cell feature averages were plotted for each subpopulation in the SMC monoculture to reveal overarching trends in the motility data. Overall, the track shape features (directionality ratio and asphericity) showed noticeable differences between cluster averages, indicating that these features were important for cluster classification.

Figure 6-11: EC monoculture motility average feature breakdown by clustering subpopulation

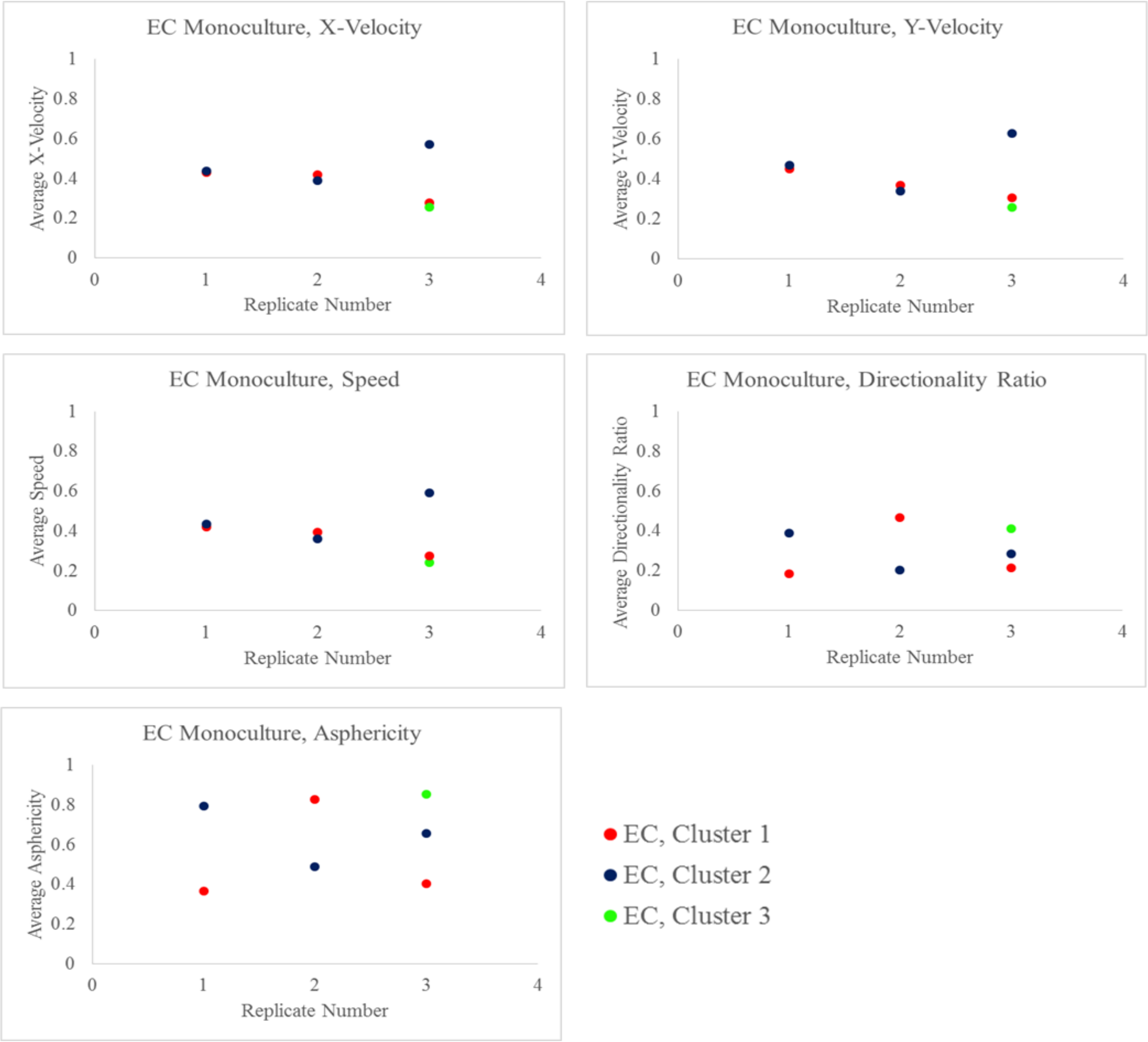

Cell feature averages were plotted for each subpopulation in the EC monoculture to reveal overarching trends in the motility data. Similar to the SMC monoculture data, the track shape parameters showed noticeable differences between cluster averages, indicating that these features were important for cluster classification.

Figure 6-12: Co-culture motility average feature breakdown by clustering subpopulation

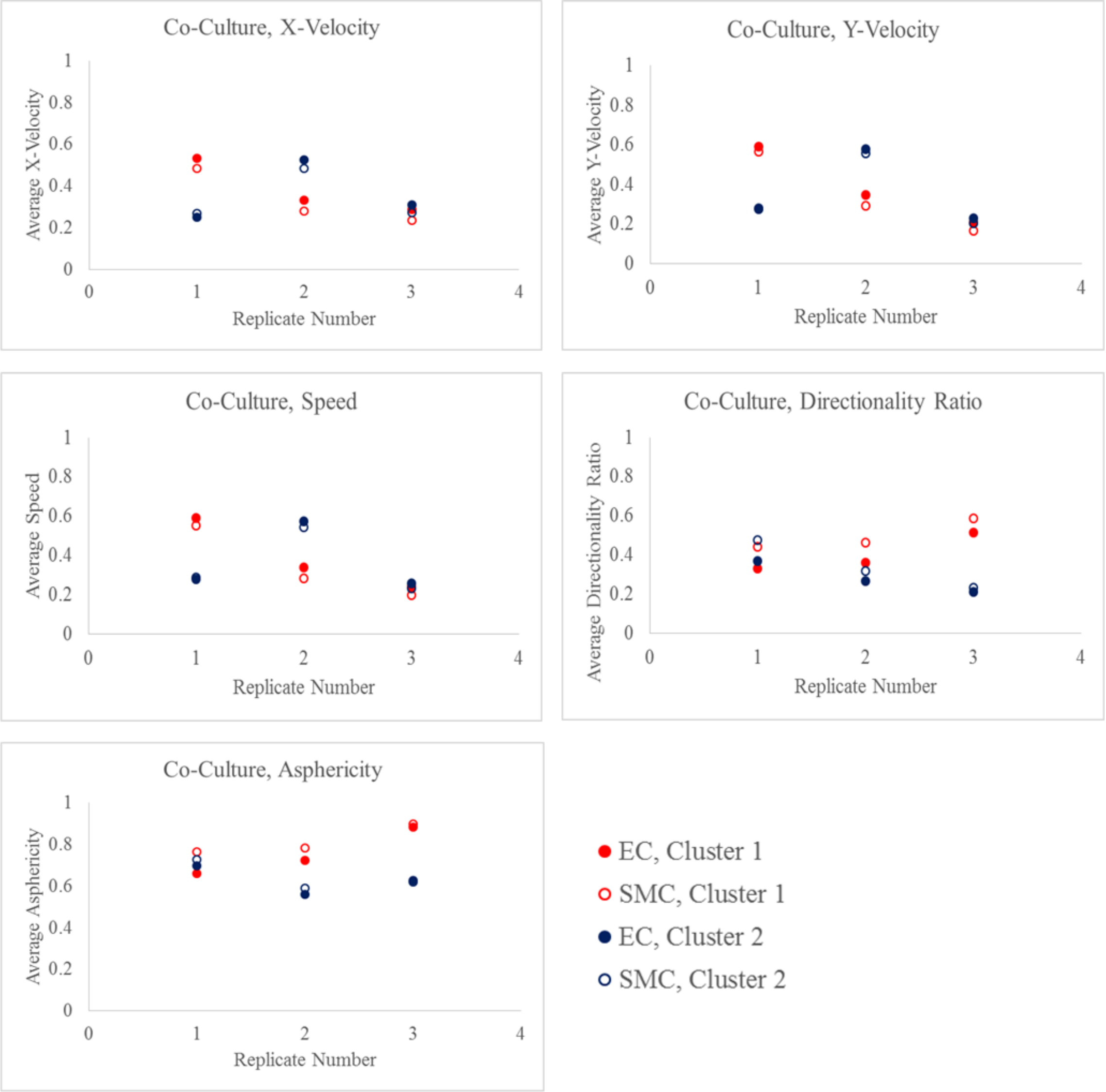

Cell feature averages were plotted for each subpopulation in the SMC and EC co-culture to reveal overarching trends in the motility data. Interestingly, difference in movement rate (x-velocity, y-velocity, and speed) were observed in the co-culture clusters, in addition to differences in the track shape parameters

Chapter 7: Adapting ACT*IV*E for 2D Bacterial Tracking[†,‡]

7.1 Synopsis

Automated contour-based tracking for *in vitro* environments (ACT*IV*E) was designed to track long-timescale motility behaviors of adherent cell populations subject to nuclear staining or transfection. While this was ACT*IV*E's original intended use, we sought to adapt and apply the technique to other experimental systems. Here, we demonstrate how ACT*IV*E was modified and utilized for 2D bacterial tracking in two very different applications. First we describe a method in which ACT*IV*E was adapted to help elucidate mechanisms guiding *Escherichia coli* (*E. coli*) attachment and rotational patterns atop poly(dimethylsiloxane) (PDMS) materials with micron-scale topographies. This work was performed to improve understanding of how topographic features can contribute to antifouling material properties. We then modified ACT*IV*E further to determine whether *E. coli* can sense variations in PDMS material stiffness and characterized their ability to attach and move atop these surfaces for subsequent biofilm formation. This diverse body of work demonstrates that ACT*IV*E is flexible and robust, capable of being applied to a variety of experimental systems to elucidate critical mechanisms guiding cell motility responses for various biomedical applications

---

[†] Adapted (in part) with permission from Gu H, Chen A, Song X, Brasch M, Henderson J, Ren D (2016). How bacteria land and form cell clusters on a surface: a new role of surface topography. *Scientific Reports, 6:29516*.

[‡] Adapted (in part) from Song F, Brasch M, Henderson JH, Sauer K, Ren D. *motB* is involved in mechanosensing of material stiffness during early stage *Escherichia coli* biofilm formation on poly(dimethylsiloxane) surfaces. *Submitted*

7.2 Rotational Analysis of *Escherichia coli* atop Poly(dimethylsiloxane) Line Patterns[1]

7.2.1 Patterned Features Dictate E. coli Attachment

Biofilm formation is an important factor dictating bacterial growth, persistence, and, ultimately, potentially fatal patient infections [1]. Therefore, the creation of novel antifouling surfaces that limit biofilm development and progression are currently an attractive area in biomaterials development. Antifouling techniques include various modifications to surface chemistry, bulk rigidity, and surface patterning as tools to regulate bacterial adhesion, proliferation, and motility responses [2]. With respect to surface patterning, it is generally understood that topographical features on the micron or sub-micron scale influence surface wettability and, therefore, bacterial appendage attachment [3]. The physiological mechanisms regulating these responses, however, remain poorly understood. Hou and colleagues previously reported that 20 μm x 20 μm or 40 μm x 40 μm square lattice poly(dimethylsiloxane) (PDMS) patterns (10 μm tall) encouraged *E. coli* attachment and growth either in planktonic or biofilm formations respectively [4]. In this study, we sought to expand upon these principles, focusing on the mechanism promoting cell attachment, orientation, and subsequent biofilm formation on PDMS surfaces with micron scale topographies [5].

Line patterns with varying widths (5 μm, 10 μm, or 20 μm) and inter-pattern spacing (3 μm, 5 μm, 10 μm, or 20 μm) were fabricated using soft lithography (Scheme 7-1A). Pattern height

---

[1] Dr. Dacheng Ren conceived the concept and Dr. Huan Gu, Aaron Chen, and Xinran Song executed all of the *E. coli* experiments. Megan Brasch modified ACT*IV*E for rotational tracking analysis.

(5 µm) and length (4 mm) were kept consistent throughout. PDMS substrates were sterilized by soaking samples in 190 proof ethanol for 30 minutes, followed by transfer to a clean petri dish for drying (40 mins at 50°C). Biofilm cultures (20mL of LB medium supplemented with 30ug/mL tetracycline) were then added to the PDMS substrates and incubated at 37°C for 2hrs or 24hrs without shaking.

Initial *E. coli* orientation analysis was limited to cells attached to the top of line patterns. Cell orientation was classified into one of three categories: 1) perpendicular (0°-30°), 2) diagonal (30°-60°) or 3) parallel (60°-90°) to the line pattern (Scheme 7-1B). After 24 hrs of inoculation, pattern width had a significant effect on cell orientation, whereas inter-pattern spacing showed no effect (Figure 7-1). More specifically, *E. coli* on narrow patterns (5 µm) exhibited a significant ($p<0.0001$) preferential orientation perpendicular to the line direction. Cells atop medium (10µm) patterns demonstrated a slight skew towards perpendicular orientation ($p<0.0001$), whereas cells atop wide (20 µm) patterns demonstrated a uniform angular distribution of attachment. As previously noted in the literature [6], this effect was most likely due to the need to maximize surface area contact for biofilm attachment and growth. Further investigation of cell orientation atop 5 µm line patterns after 2 hrs of inoculation demonstrated an even larger number of cells oriented perpendicular to the line direction, compared to the 24 hr case (Figure 7-2).

To fully explore the biological mechanisms associated with *E. coli* orientation preferences on 5µm line patterns, four isogenic mutants of the wild type *E. coli* were employed: *fliC, motB, fimA,* and *luxS*. These genes are important for production of flagellin (the major component in flagella) [7], flagellar rotation and mechanical signaling [8], fimbriae production (which in turn is important for bacterial adhesion and movement once attached to a substrate) [9], and quorum sensing [10] respectively. As shown in Figure 7-3, *fliC*, *motB,* and *fimA* mutants no longer demonstrated perpendicular orientation preferences atop 5um line patterns. This indicated that flagella and fimbriae were important regulators of *E. coli* attachment orientation. *luxS* mutants demonstrated a reduction in perpendicular preferential attachment, but did not completely abolish this trend (Figure 7-3D). As such, it was concluded that quorum sensing was not an important regulator of *E. coli* attachment orientation. When *fliC*, *motB,* and *fimA* mutants were complemented with plasmids carrying their respective genes, orientation preference was restored (data not shown).

7.2.2. ACTIVE Modification for E. Coli Rotational Processing

After identifying that flagella and fimbriae were potentially important in regulating *E. coli* orientation, further investigation of the attachment mechanism was explored using fluorescence time-lapse microscopy immediately after inoculation. As shown in Figure 7-4A, example micrographs of a time-lapse series of *E. coli* cells atop 5 µm wide line patterns demonstrated a significant amount of cell body rotation prior to settling in a specific surface orientation. With the addition of time-lapse microscopy experiments, we sought to modify ACT*IV*E as a means to analyze these single cell rotational patterns. Static fluorescent and SEM images further showed the presence of flagellum-like protrusions, which appeared to dictate this rotational response (Figure 7-4B). These protrusions were assumed to be flagella due to their structure and size-scale (consistent with literature reports of *E. coli* flagellar size and length [11]). Flagella attachment was oriented towards one pole of the cell body, which contributed to the rotational motions observed in time-lapse series. Furthermore, when comparing the mutant *E. coli* strains, only *fimA* mutants demonstrated the same structural protrusion, corroborating that polar flagella were responsible for the orientation manipulation after initial attachment (Figure 7-4C-E).

ACT*IV*E analysis was modified to elucidate trends in *E. coli* rotation atop 5 µm, 10 µm, and 20 µm wide line patterns. Time-lapse videos were first cropped to highlight a single cell of interest for rotational analysis (Figure 7-5, top row). Video frames were then segmented using the contour based intensity profiling technique (Figure 7-5, middle row). Individual cells were identified utilizing each cell's unique contour profile and fit with an ellipse to determine the cell's center of mass (Figure 7-5, bottom row). Frame to frame behaviors were tracked by locating the center of mass closest to the midpoint of the image. All other cell information was discarded to limit issues associated with bacteria floating through the field of view, disrupting rotational analyses. Center of mass behavior was overlaid onto original cell images and manually verified for appropriate fit. Once confirmed, frame by frame center of mass information was plotted on the same set of axes to visualize overall rotational motion. A "tether point" was included in the ACT*IV*E analysis to highlight variations in rotational direction as a function of flagellar appendage location.

Rotational behaviors of cells atop narrow, medium, and wide line patterns were then characterized using ACT*IV*E. As shown in Figure 7-6, cells atop medium and wide line patterns demonstrated a circular rotational pattern. This corresponded with a cell body angle between 0°

and 30°, indicating that *E. coli* align parallel to the surface of these patterns. These results are similar to rotational patterns previously observed for *E. coli* cells atop flat surfaces [12]. Rotational patterns of cells on narrow patterns were more irregular, although cell body orientation remained relatively parallel to the substrate surface. Cells tethered to the edge of narrow line patterns were also characterized. Interestingly, these cells demonstrated random and erratic orientation motions, frequently reorienting their cell body in relation to the substrate surface. This behavior is more closely related to rotational patterns of *Pseudomonas aeruginosa* PA01 cells tethered to a flat surface via a single flagellum [12]. We speculate that this response allows cells to rotate off-axis, reducing surface adhesion and potentially stress (discussed below).

7.2.3 The Role of Feature Size on E. Coli Biofilm Formation

ACT*IV*E analysis enabled the identification that *E. coli* cells atop medium and wide line patterns rotated in a circular orientation prior to attachment, allowing for the cells to arrange parallel to the surface (cell body angle between 0° and 30°). ACT*IV*E analysis of cells atop narrow line patterns indicated that cells attaching to the top of the pattern demonstrated similar orientation effects, however, cells tethered to the vertical walls of narrow patterns altered their attachment orientation perpendicular to the line direction. These differences, highlighted by ACT*IV*E analysis, enabled further investigation of cell morphology and metabolic activities. Cell morphology after 24 hrs of inoculation was investigated to identify underlying trends in biofilm formation. Cells atop narrow line patterns were, on average, 4.0 ± 1.1 µm long, compared to 1.9 ± 0.5 µm and 2.2

± 0.7 µm long atop medium and wide patterns respectively (Figure 7-7A). Statistical analysis revealed no significant difference in cell length atop medium or wide patterns. This was also comparable (no significant difference) to cell lengths observed on flat gold surfaces [13]. Cell adhesion after 2 hrs of inoculation was then investigated to determine whether this effect was related to preferential cell attachment or bacterial activity during biofilm growth. Cells atop narrow line patterns were 5.3 ± 1.4 µm long. This was statistically similar ($p > 0.05$) to cells attached to the surface of flat PDMS (4.9 ± 1.49 µm) and planktonic cells (5.1 ± 2.5 µm) collected from the same culture at the same time-point. This indicated that differences in *E. coli* length were linked directly to biofilm growth, instead of selective adhesion.

Metabolic activities directly influence bacterial size [14]. Again, enabled by the orientation results identified by ACT*IV*E, transcriptional activities of *E. coli* cells were qualitatively assessed using acridine orange staining, which expresses green or red fluorescence when binding to DNA or RNA respectively. As shown in Figure 7-7B, cells atop narrow line patterns expressed much more red fluorescence, compared to high levels of green fluorescence expressed for cells atop medium or wide patterns. This suggests that cells atop narrow line patterns have higher transcriptional activities and, potentially, a higher level of gene expression.

To confirm the effect of varying line pattern size on cell adhesion and biofilm growth, cell cluster formation was quantified. Cell clusters were defined as a group of six or more cells, where each cell fell within 1 µm of a neighboring cell. The overall percentage of cells in clusters was defined as:

$$Cluster\ \% = \frac{Number\ of\ Cells\ in\ Clusters}{Total\ Number\ of\ Cells\ on\ Surface} * 100 \qquad \text{(Eq. 7-1)}$$

As shown in Figure 7-8A, pattern width was positively correlated with cell cluster formation (r > 0.75, Pearson correlation). *E. coli* atop 5 µm, 10 µm, and 20 µm line widths formed clusters 2.0 ± 3.2%, 11.0 ± 1.6%, and 22.3 ± 1.8% of the time respectively, with an inter-pattern distance of 3 µm. Inter-pattern spacing demonstrated some effect, resulting in less cluster formation atop patterns with smaller inter-pattern spacing. Biomass aggregation was additionally quantified. Similar to cell cluster formation, the total biomass increased with increasing line size (Figure 7-8B). In this case, inter-pattern spacing was only significant for the narrow line patterns (r > 0.85, Pearson correlation). When comparing biofilm formation on patterned and flat PDMS surfaces, there was a reduction in biofilm formation as the line pattern width decreased (Figure 7-8C). This indicates that, even though a greater overall surface area exists with the line-patterned surfaces (compared to flat PDMS), introduction of micron-sized topography can inhibit biofilm formation. Collectively, the observations presented in this section indicate that the introduction of surface patterns with smaller feature widths and inter-pattern distances improve the antifouling properties of PDMS materials. Furthermore, we were able to demonstrate that minor modification of the ACT*IV*E system could enable powerful orientation analyses of *E. coli* cells, resulting in the discovery of mechanisms guiding cell attachment and biofilm development for antifouling applications.

7.3 Analysis of *Escherichia coli* Motility on Poly(dimethylsiloxane) Surfaces with Varying Stiffness[2]

7.3.1 The Role of Material Stiffness on E. coli Adhesion, Growth, and Motility

More than 90% of bacteria live in biofilms, a collection of attached cells encased in a self-produced polysaccharide matrix comprised of DNA, RNA, and various proteins [1]. These structures contribute to bacterial growth, persistence, and ultimately, development of antibiotic resistance. Nearly 100,000 deaths a year in the U.S. are attributed to biofilm growth, costing billions of dollars in losses annually [15, 16]. As such, understanding the mechanisms driving biofilm formation are critically important for resolving biofilm attributed deaths. The shift from planktonic to biofilm growth occurs when cells attach to a surface, begin forming clusters, and then mature to the point where bacteria can disperse independently [1, 17, 18]. As previously mentioned, initial bacterial attachment can be dictated by a variety of material properties, including surface chemistry, bulk rigidity, and surface patterning [2]. Recently, Song and Ren demonstrated that decreasing the stiffness of PDMS materials promotes the adhesion and growth of *E. coli* and *Pseudomonas aeruginosa* cells. Furthermore, Song and Ren demonstrated that cells on soft surfaces are more elongated and more susceptible to antibiotic treatments, compared to bacteria on stiffer versions of the same material [19]. While this work characterized growth and antibiotic resistance on materials with varying rigidity, no investigation into bacterial responses after initial attachment was performed. Here, we expand upon this analysis using ACT*IV*E to determine

---

[2] Dr. Fangchao Song executed all of the *E. coli* experiments. Megan Brasch modified ACT*IV*E for cell velocity profiling and speed analyses.

whether bacteria can sense variations in material stiffness and characterize their decision to attach to a surface for subsequent biofilm formation.

E. coli RP437 was used as a model strain for this study. Three isogenic mutants, *motB, fliC,* and *fimA* were additionally used to investigate the role of motility, flagella, and type I fimbriae, respectively during biofilm formation. Cells were grown at 37^{o}C with shaking at 200 rpm in Lysogeny Broth (LB) containing 10 g/L tryptone, 5 g/L yeast extract, and 10 g/L NaCl in deionized water [4]. Plasmid pRSH103 was cloned into *E. coli* strains to label the cells with red fluorescent protein. Fluorescent strains were cultured at 37^{o}C with shaking at 200 rpm in LB medium supplemented with 30 µg/mL tetracycline to retain the plasmid. Cells were harvested by centrifugation (8000 rpm for 3 mins at 4^{o}C), followed by a PBS wash three times (pH 7.3) prior to inoculation. PDMS substrates were fabricated using a SYLGARD184 Silicone Elastomer Kit (Dow Corning). Variations in the ratio of base to curing agent allowed for changes in bulk material stiffness. Here, ratios of 5:1 and 40:1 were used to obtain stiff (2.6 MPa) and soft (0.1 MPa) substrates respectively. Substrates were cured for 24 hrs at 60°C, followed by incubation at room temperature for another 24 hrs to ensure full polymerization. Substrates were then cut into 1 cm x 0.6 cm rectangles (~1.5 mm thick) and sterilized by soaking in 200 proof ethanol for 20 mins. Substrates were dried using sterile air and stored at room temperature until use.

7.3.2 Velocity Profiling of "Still", "Rotating", and "Moving" E. coli Using ACTIVE Analysis

ACT*IV*E analysis was modified to evaluate trends in *E. coli* motility dynamics. Adaptation of ACT*IV*E's contour based segmentation yielded successful detection and accurate tracking of *E. coli* behaviors (Figure 7-9). Time-lapse images of RP437/pRSH103 *E. coli* cells were captured every 5 sec for 20 mins on an Axio Observer Z1 fluorescence microscope (Carl Zeiss Inc., Berlin, Germany). Frame to frame cell motility was then categorized into one of three groups: 1) "moving", 2) "rotating", or 3) "still" cells (see Appendix 3 for corresponding code). These groups were determined based on the frame to frame displacement of the cell: 1) if a cell moved more than one average cell body length, the cell was classified as "moving"; 2) if a cell moved between ¼ and 1 average cell body length, the cell was classified as "rotating"; 3) if a cell moved less than ¼ of the average cell body length, the cell was classified as "still" (Figure 7-10). These distance calculations were performed using the center of mass information for each cell frame to frame.

When comparing videos of cells atop the soft and stiff PDMS surfaces, striking differences in cell motility were observed. The majority of *E. coli* cells were "still" on soft PDMS surfaces. The fraction of "rotating" and "moving" cells significantly increased as the substrate stiffness increased. As shown in Figure 7-11A, 62 ± 0.4%, 27 ± 0.4%, and 11 ± 0.3% of the attached cells were classified as "still", "rotating" and "moving", respectively, on soft substrates. On stiff surfaces, the fraction of "still" cells was reduced to 40 ± 0.5%, while the number of "rotating" and "moving" cells increased to 39 ± 0.5% and 21 ± 0.4%, respectively. This was coupled with a lower speed on soft surfaces. On average, *E. coli* moved at a speed of 3.4 ± 0.2 µm/min and 6.2 ± 0.3

μm/min on soft and stiff surfaces, respectively (Figure 7-11B). These results indicate that *E. coli* are mechanosensitive, responding to the stiffness of their extracellular microenvironment.

7.3.3 motB is Influential for Differentiating Soft and Stiff Surfaces in E. coli cells

After identifying that *E. coli* motility was sensitive to the mechanical stiffness of the microenvironment, we sought to determine the underlying mechanism driving this phenomenon. Three isogenic mutants of wild type *E. coli* were employed to analyze the motility mechanism: 1) *fliC,* 2) *motB,* and 3) *fimA*. As previously mentioned, these genes are important for production of flagellin (the major component in flagella) [7], flagellar rotation and mechanical signaling [8], and fimbriae production (which in turn is important for bacterial adhesion and movement once attached to a substrate) [9], respectively. Cell adhesion studies were performed in PBS without any carbon source to assess adhesion in the absence of cell growth. Cell density at inoculation was controlled between 3 x 10^7 cells/mL and 7 x 10^7 cells/mL. After 2 hrs of attachment, (1.1 ± 0.4) x 10^6 cells/cm^2 and (5.3 ± 2.4) x 10^3 cells/cm^2 were observed for the wild-type *E. coli* strain on soft and stiff surfaces, respectively (Figure 7-12A). Overall, *fliC* ([1.6 ± 0.2] x 10^5 cells/cm^2 and [2.3 ± 0.7] x 10^3 cells/cm^2 on soft and stiff surfaces respectively) and *fimA* ([2.0 ± 0.3] x 10^5 cells/cm^2 and [4.4 ± 0.5] x 10^2 cells/cm^2 on soft and stiff surfaces respectively) mutants showed lower cell attachment numbers compared to the wild-type strain, but still demonstrated, at least, a two order of magnitude decrease between soft and stiff PDMS attachment. This decrease in *fimA* and *fliC* mutant attachment compared to the wild type strain was unsurprising, as flagella and type I fimbriae have previously been implicated as important regulators of initial cell attachment [20, 21]. Further, the decrease in attachment for *fimA* and *fliC* mutants between soft and stiff surfaces was comparable to what was observed in the wild-type strain, indicating that these genes were nonessential for *E. coli* mechanosensing. Comparatively, *motB* mutants demonstrated cell attachment on soft PDMS surfaces similar to the wild-type *E. coli* strain. However, *motB* mutants atop the stiff PDMS surfaces showed an increase in cell attachment compared to the wild type (approximately one order of magnitude more for *motB* mutants). When *motB* mutants were complemented with plasmid pRGH103 to recover the gene under a constitutive promoter, cell attachment on soft and stiff surfaces were not statistically different ($p = 0.42$ for soft surfaces; $p = 0.61$ for stiff surfaces; *t* test) from the wild-type *E. coli* strain (Figure 7-12A). Similar results were observed for face-down culture experiments, indicating that this process is not a gravity-driven response (Figure 7-12B). This confirms that *motB* is an important regulator for mechanosensing in *E. coli* cells.

After identifying that *motB* was important in mechanosensing during initial *E. coli* attachment, further investigation into the motility dynamics of *motB* mutants were explored. As seen in Figure 7-13A, ACT*IV*E analysis revealed that the majority of *motB* mutant cells were “still” on both soft and stiff surfaces (83 ± 0.4% and 70 ± 0.5% respectively). The fraction of “rotating” *motB* mutant cells were 11 ± 0.3% and 23 ± 0.5% for soft and stiff PDMS surfaces respectively, while the number of “moving” *motB* mutant cells were 6 ± 0.3% and 7 ± 0.2% on soft and stiff PDMS surfaces respectively. This is markedly different from the behaviors exhibited by the wild-type strain (62 ± 0.4%, 27 ± 0.4%, 11 ± 0.3% for “still”, “rotating” and “moving” cells on soft surfaces respectively, and 40 ± 0.5%, 39 ± 0.5%, 21 ± 0.4% for “still”, “rotating” and “moving” cells on stiff surfaces respectively). We therefore hypothesized that differences in *motB* mutant movement are most likely linked to other modes of cell motility, such as pili driven responses. Surprisingly, *motB* mutant cells were slightly more motile on stiff versus soft surfaces. The difference in "still" and "moving" cells were 13% and 1% respectively, compared to 22% and 10% respectively for the wild-type *E. coli* strain. This suggests that, while *motB* is important in the mechanosensing response of *E. coli* cells, absence of *motB* does not fully abolish mechanical sensitivity of the cells, indicating that other genes may be involved in probing the mechanical microenvironment.

Investigations of movement speed of *motB* mutants further corroborated the displacement results. As shown in Figure 7-13B, *motB* mutants moved at a rate of 2.0 ± 0.3 µm/min and 3.2 ± 0.3 µm/min on soft and stiff PDMS surfaces respectively. This was much smaller than the speed of the wild-type *E. coli* cells, which moved at a rate of 3.4 ± 0.2 µm/min and 6.2 ± 0.3 µm/min on soft and stiff surfaces respectively. When comparing the difference in speeds (stiff speed minus the soft speed) for the *motB* mutant and the wild-type strains, a smaller difference was noted on the soft surfaces (1.4 µm/min versus 2.8 µm/min respectively). This further suggested that *motB* is important for mechanosensing, but is not the only factor dictating the motility response of *E. coli* cells. When *motB* mutants were complemented with the *motB* gene and assessed again, cell motility responses were comparable to the wild-type cells (Figure 7-14). For example, the fraction of "still", "rotating", and "moving" cells was 64 ± 0.3%, 24 ± 0.2%, and 12 ± 0.2% on soft surfaces, and 37 ± 0.4%, 36 ± 0.4%, and 27 ± 0.4% on stiff surfaces, respectively for the complemented *motB* mutant strain. This was coupled with movement speeds of 3.1 ± 0.4 µm/min and 5.8 ± 0.8

µm/min on soft and stiff PDMS surfaces, respectively. These results were similar to the wild-type, indicating that complementation of the *motB* gene restored mechanosensing in the mutant cells.

Movement percentage and speed results of wild-type, *motB* mutant, and *motB* complemented mutant strains were averaged across at least 3 videos with at least 320 frames per video and more than 200 cells per video. As shown in Figure 7-15A, the fraction of “still”, “rotating” and “moving” wild-type cells was 69 ± 5%, 21 ± 4%, and 9 ± 3% on soft surfaces, and 48 ± 4%, 34 ± 3%, and 18 ± 3% on stiff surfaces, respectively. Comparatively, *motB* mutants had 84 ± 3%, 11 ± 2%, and 5 ± 1%, “still”, “rotating” and “moving” cells, respectively, on soft surfaces, whereas 71 ± 2%, 23 ± 2%, and 6 ± 1% were “still”, “rotating” and “moving”, respectively, on stiff surfaces. Complementing the *motB* gene in mutant cells restored results similar to those of the wild-type strain ($p > 0.1$ for all cases, t test). This further corroborated our hypothesis that absence of a functional *motB* gene causes abnormalities in mechanosensing of surface stiffness resulting in differences in cell attachment.

Average cell velocities were additionally assessed to determine differences in cell motility atop soft and stiff PDMS surfaces. As shown in Figure 7-15B, the wild-type *E. coli* cells had a speed of 2.7 ± 0.3 µm/min and 6.1 ± 0.4 µm/min on soft and stiff surfaces respectively. Comparatively, *motB* mutants had a speed of 2.0 ± 0.4 µm/min and 3.5 ± 0.3 µm/min on soft and stiff surfaces respectively. This confirmed that *E. coli* cells were, in general, more motile on stiff versus soft PDMS surfaces. When comparing differences in movement speeds between soft and stiff surfaces, the difference was larger for the wild-type (3.4 µm/min), compared to the *motB* mutants (1.5 µm/min). Distributions of cell velocity speeds were consistent with these results

(Figure 7-15C). Lastly, when complemented with the *motB* gene, *motB* complemented mutants were not statistically different from the wild-type *E. coli* strain (p = 0.64 for soft surfaces, p = 0.36 for stiff surfaces, *t* test).

7.4 Discussion: Controlling Biofilm Growth through Surface Patterning and Stiffness Variation

Research into antifouling surfaces has gained traction in recent years, as biofilm formation promotes bacterial growth, persistence, and infection [1] leading to patient fatalities and severe economic costs [15, 16]. Here, we explored two antifouling techniques (variations in surface patterning and surface stiffness), as a means to control *E. coli* attachment, growth, and motility. As presented in the first study, *E. coli* cells preferentially aligned perpendicular atop PDMS narrow (5 μm) line patterns. Through exploration of various isogenic mutants, we determined that flagella are important constructs dictating this response. This is consistent with previous literature findings [22, 23] that state that bacterial flagella are used to make initial contact with a surface due to their ability to counteract repulsive forces [9]. As we have demonstrated, pattern size is crucial in determining cell attachment behaviors and ultimately biofilm growth potential. On top of wide (20 μm) and medium (10 μm) line patterns, cells made initial contact using flagella as a tether point, rotating in a circular pattern leading to a relatively uniform distribution of cell orientations atop the surface. On narrow patterns, this surface area was limited. As a result, it was much more difficult for the cells to attach directly to the top surface of the line compared to the vertical sides.

Altering the tether point to the vertical side changed the mechanical forces that the cells experienced, leading to a change in orientation predominantly perpendicular to the line direction. This claim was corroborated by the *motB* mutant strain and complementation data. Furthermore, higher levels of stress (based on acridine orange staining) and reduced cluster formation suggested that narrow, 5 µm line patterns inhibit biofilm formation. Recently, it has been shown that bacteria can utilize flagella as a means to overcome submicron scale surface topographies [3, 24, 25]. The flagellar length of planktonic *E. coli* cells can range from 6 µm to 10 µm [26]. Thus, it is important that surface patterns are both narrow (5 µm or smaller in our case) and at least 10 µm tall to prevent bacterial fouling.

We additionally explored the effects of altering PDMS surface stiffness as a means to reduce biofilm formation. Our results showed that *motB* was important for mechanosensing in *E. coli* cells. *motB* is an important part of the flagellar motor that generates rotational motion [27]. In our study, *motB* mutation led to 10 times more attached cells on stiff surfaces compared to the wild-type. This was coupled with more "still" classified cells during the displacement analysis. *motB* mutation also reduced *E. coli* movement speeds, as well as the difference between the soft and stiff surface speeds when compared to the wild-type. These results suggest that material stiffness directly influences bacterial attachment. Similar to the line pattern study above, *E. coli* most likely utilize appendages, such as flagella, to determine whether surface stiffness is favorable for cell attachment. Assuming favorable conditions, cells may reduce their motility (e.g., increase the number of "still" cells) to initiate biofilm formation. As seen on the stiff surfaces, cells may remain motile and potentially detach from the surface and return to the planktonic phase if the material stiffness is unfavorable for biofilm growth. These results are consistent with Song and Ren's previous findings [19]. Evidence of persistent underlying motility of a small population of mutant *motB* cells further suggests that there are additional genes responsible for mechanosensing in *E. coli* cells. To expand upon these ideas, new mutants would have to be isolated to explore any additional mechanisms driving mechanical sensitivity in *E. coli* cells.

The major conclusions obtained in this chapter were enabled by ACT*IV*E analysis. We have demonstrated that, with minimal modification, ACT*IV*E could accurately and effectively be used as a tool to study *E. coli* rotational patterns, cell attachment, and velocity profiling of fluorescently labeled wild type and mutant *E. coli* strains. The videos in this chapter demonstrate the versatility of the ACT*IV*E tracking technique, due to their diverse nature with respect to cell type, size-scale, and density analyzed. As demonstrated in the first study, ACT*IV*E analysis was used to identify rotational patterns of *E. coli* cells. This analysis helped explain the reasoning behind preferential perpendicular attachment orientation of cells atop narrow line patterns. It further encouraged investigation into the metabolic activities of the cells, leading to better understanding of how narrow line patterns contribute to inhibiting biofilm formation. ACT*IV*E analysis played an even more central role in the second study, where attachment and velocity profiling enabled the discovery of *motB* as one of the primary genes dictating mechanotransduction in *E. coli* cells. Furthermore, ACT*IV*E analysis contributed to evidence that cells atop soft PDMS surfaces are more "still" compared to stiff PDMS surfaces, allowing for biofilm initiation and growth. As demonstrated in this chapter, ACT*IV*E is clearly a powerful tool that can be used for a variety of time-lapse enabled applications.

7.5 Conclusions

Biofilm formation is an important factor dictating bacterial growth, persistence, and potentially fatal patient infections. In this chapter, we adapted ACT*IV*E for two very different two-dimensional bacterial tracking applications to determine how surface topographies and surface stiffness could be used to limit biofilm formation. As shown, narrow PDMS line patterns altered *E. coli* attachment orientation, preferentially aligning cells perpendicular to the pattern direction due to rotational tethering via flagellar attachments along vertical walls. This was coupled with higher levels of stress and reduced cluster formation suggesting that 5 μm sized, 10 μm tall features could be utilized to promote antifouling. Similarly, we demonstrated that stiffness influences *E. coli* attachment and motility dynamics. In this case, more cells attached to soft versus stiff surfaces, coupled with an increase in motile cells (as well as cell speed) on stiffer surfaces. We further showed that *motB* was one of the primary genes responsible for mechanosensing in *E. coli* cells. Collectively, we have shown that stiffer surfaces patterned with narrow (~5 μm sized) features promote antifouling. This work, driven by ACT*IV*E analysis, has provided a better understanding of bacterial mechanosensing and attachment dynamics to help guide new designs of biomaterials to promote or deter biofilm formation.

7.6 References

1. Hall-Stoodley, L., J.W. Costerton, and P. Stoodley, *Bacterial biofilms: from the Natural environment to infectious diseases.* 2004. **2**(2): p. 95-108.
2. Campoccia, D., L. Montanaro, and C.R. Arciola, *A review of the biomaterials technologies for infection-resistant surfaces.* Biomaterials, 2013. **34**(34): p. 8533-8554.
3. Hsu, L.C., et al., *Effect of micro- and nanoscale topography on the adhesion of bacterial cells to solid surfaces.* Applied and Environmental Microbiology, 2013. **79**(8): p. 2703-2712.
4. Hou, S., et al., *Microtopographic Patterns Affect Escherichia coli Biofilm Formation on Poly(dimethylsiloxane) Surfaces.* Langmuir, 2011. **27**(6): p. 2686-2691.
5. Gu, H., et al., *How Escherichia coli lands and forms cell clusters on a surface: A new role of surface topography.* Scientific Reports, 2016. **6**.
6. Díaz, C., et al., *Organization of Pseudomonas fluorescens on Chemically Different Nano/Microstructured Surfaces.* ACS Applied Materials & Interfaces, 2010. **2**(9): p. 2530-2539.
7. Haiko, J. and B. Westerlund-Wikström, *The role of the bacterial flagellum in adhesion and virulence.* Biology, 2013. **2**(4): p. 1242-1267.
8. Lele, P.P., B.G. Hosu, and H.C. Berg, *Dynamics of mechanosensing in the bacterial flagellar motor.* Proceedings of the National Academy of Sciences of the United States of America, 2013. **110**(29): p. 11839-11844.
9. Van Houdt, R. and C.W. Michiels, *Role of bacterial cell surface structures in Escherichia coli biofilm formation.* Research in Microbiology, 2005. **156**(5-6): p. 626-633.

10. Hardie, K.R. and K. Heurlier, *Establishing bacterial communities by 'word of mouth': LuxS and autoinducer 2 in biofilm development.* Nature Reviews Microbiology, 2008. **6**(8): p. 635-643.
11. Chattopadhyay, S., et al., *Swimming efficiency of bacterium Escherichia coli.* Proceedings of the National Academy of Sciences of the United States of America, 2006. **103**(37): p. 13712-13717.
12. Qian, C., et al., *Bacterial tethering analysis reveals a "run-reverse-turn" mechanism for pseudomonas species motility.* Applied and Environmental Microbiology, 2013. **79**(15): p. 4734-4743.
13. Gu, H., et al., *Patterned biofilm formation reveals a mechanism for structural heterogeneity in bacterial biofilms.* Langmuir, 2013. **29**(35): p. 11145-11153.
14. Weart, R.B., et al., *A Metabolic Sensor Governing Cell Size in Bacteria.* Cell, 2007. **130**(2): p. 335-347.
15. Klevens, R.M., et al., *Estimating health care-associated infections and deaths in U.S. Hospitals, 2002.* Public Health Reports, 2007. **122**(2): p. 160-166.
16. Klevens, R.M., et al., *Invasive methicillin-resistant Staphylococcus aureus infections in the United States.* Journal of the American Medical Association, 2007. **298**(15): p. 1763-1771.
17. Sauer, K., et al., *Pseudomonas aeruginosa displays multiple phenotypes during development as a biofilm.* Journal of Bacteriology, 2002. **184**(4): p. 1140-1154.
18. Stoodley, P., et al., *Biofilms as complex differentiated communities*, in *Annual Review of Microbiology*. 2002. p. 187-209.

19. Song, F. and D. Ren, *Stiffness of cross-linked poly(dimethylsiloxane) affects bacterial adhesion and antibiotic susceptibility of attached cells.* Langmuir, 2014. **30**(34): p. 10354-10362.
20. Busscher, H.J. and H.C. van der Mei, *How do bacteria know they are on a surface and regulate their response to an adhering state?* PLoS Pathogens, 2012. **8**(1).
21. Petrova, O.E. and K. Sauer, *Sticky situations: Key components that control bacterial surface attachment.* Journal of Bacteriology, 2012. **194**(10): p. 2413-2425.
22. Callow, M.E., et al., *Microtopographic cues for settlement of zoospores of the green fouling alga Enteromorpha.* Biofouling, 2002. **18**(3): p. 237-245.
23. Renner, L.D. and D.B. Weibel, *Physicochemical regulation of biofilm formation.* MRS Bulletin, 2011. **36**(5): p. 347-355.
24. Friedlander, R.S., et al., *Bacterial flagella explore microscale hummocks and hollows to increase adhesion.* Proceedings of the National Academy of Sciences of the United States of America, 2013. **110**(14): p. 5624-5629.
25. Díaz, C., et al., *Have flagella a preferred orientation during early stages of biofilm formation?: AFM study using patterned substrates.* Colloids and Surfaces B: Biointerfaces, 2011. **82**(2): p. 536-542.
26. Eisenbach, M., *Chemotaxis*, I.C. Press, Editor. 2004. p. 8-60.
27. Chun, S.Y. and J.S. Parkinson, *Bacterial motility: Membrane topology of the Escherichia coli MotB protein.* Science, 1988. **239**(4837): p. 276-278.

Scheme 7-1: Depiction of topographic line patterns and *E. coli* attachment classifications.

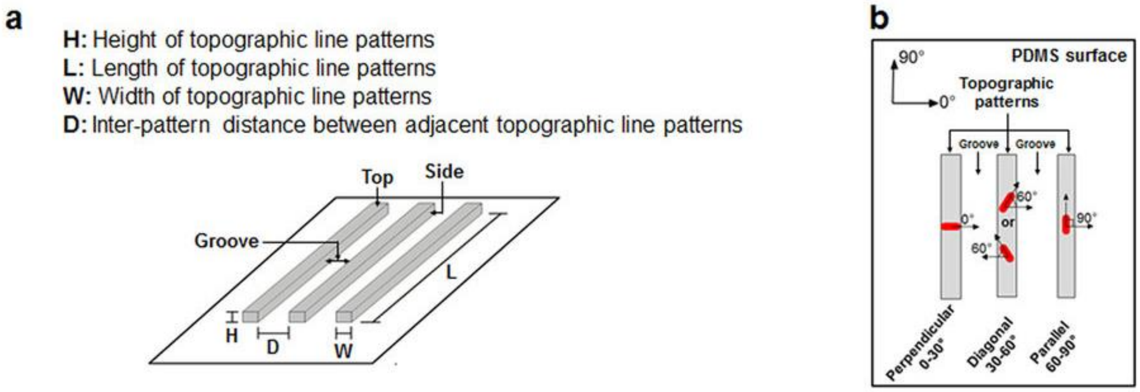

Line patterns were fabricated on PDMS surfaces using soft lithography. A) The pattern height (H) and length (L) were fixed at 5μm and 4mm respectively. Pattern width (W) and inter-pattern distance (D) were varied from 5μm, 10μm, or 20μm and 3μm, 5μm, 10μm, or 20μm respectively. Only *E. coli* present on the top surface of the line patterns were analyzed. B) *E. coli* adhesion was classified as perpendicular (0°-30°), diagonal (30°-60°) or parallel (60-90°) to the pattern direction to collectively visualize trends in the data. Figure courtesy of Dr. Huan Gu.

Figure 7-1: Orientation analysis of *E. coli* cells atop PDMS line patterns 24hrs after inoculation

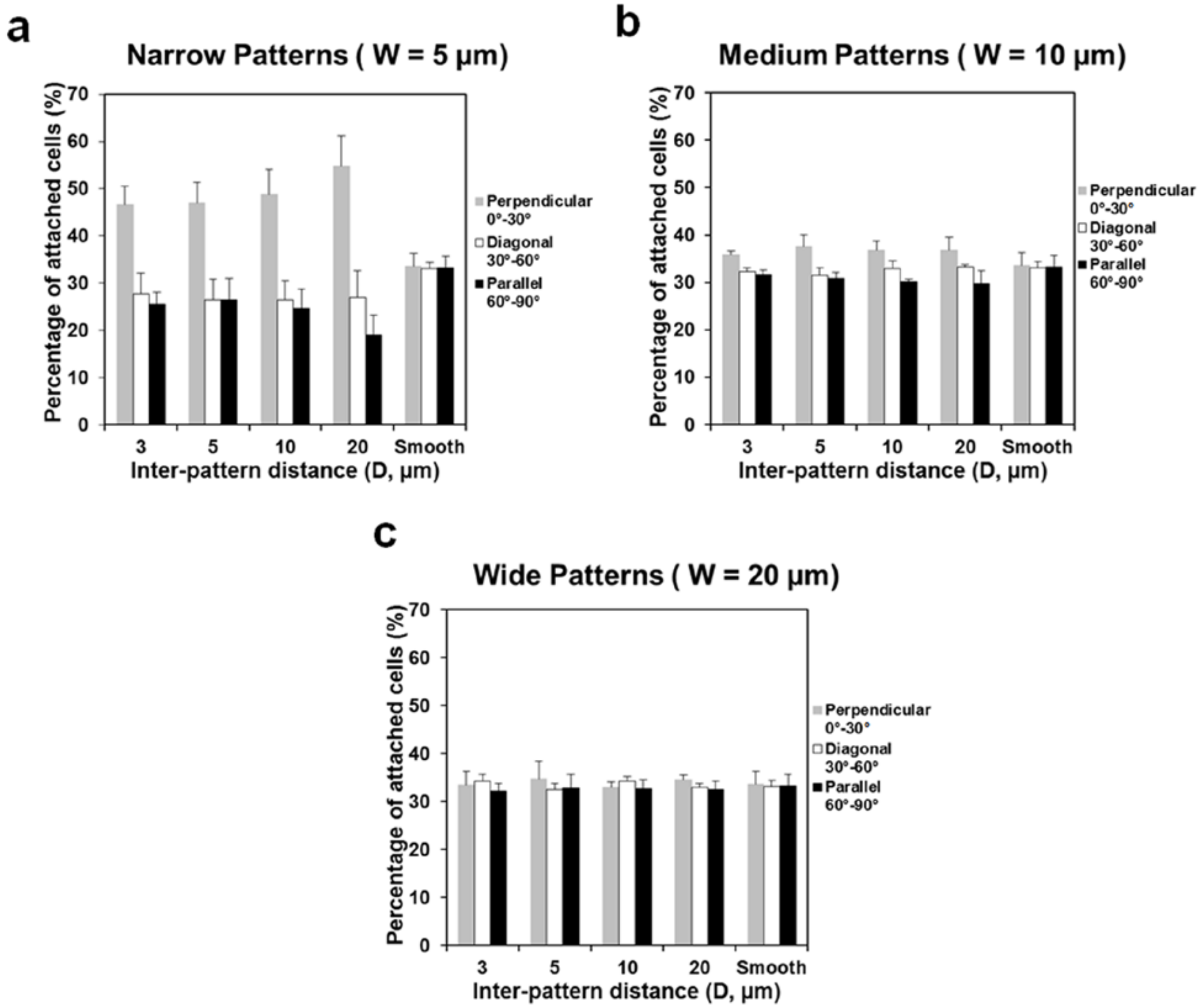

Cell orientation was analyzed on PDMS surfaces with A) narrow (5μm), B) medium (10μm) and C) wide (20μm) lines patterns. Inter-pattern spacing had no effect on cell orientation. However, pattern width was an important factor dictating cell orientation. *E. coli* on narrow surface patterns (A) demonstrated preferential orientation perpendicular to the line direction. Medium patterns (B) demonstrated a mild skew towards perpendicularly oriented cells, whereas wide patterns (C) yielded a uniform angle distribution. Figure courtesy of Dr. Huan Gu.

Figure 7-2: Orientation of *E. coli* cells atop PDMS line patterns 2hrs or 24hrs post inoculation.

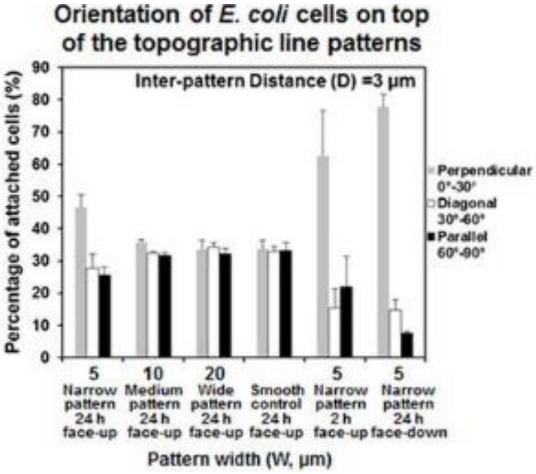

When considering a single inter-pattern spacing (D = 3μm shown), preferences in cell attachment orientation were revealed. *E. coli* atop narrow patterns (W = 5μm) demonstrated a significant preferential orientation perpendicular to the line direction. It is important to note that this effect was observed in both face-up and face-down designs after 24hrs of inoculation, indicating that gravity was not a contributing factor to cell orientation. When considering initial attachment 2hrs after inoculation on narrow patterns, cells showed even greater preference for perpendicular orientation. Cells atop medium patterns (W = 10μm), demonstrated a similar pattern after 24hrs, though to less effect. Cells atop wide patterns (W = 20μm) demonstrated a near-uniform distribution of cell orientation indicating that a size threshold had been achieved with respect to guiding cell orientation behavior. Figure courtesy of Dr. Huan Gu.

Figure 7-3: Orientation preferences of *fliC, motB, fimA,* and *luxS E. coli* mutants atop 5μm wide PDMS line patterns.

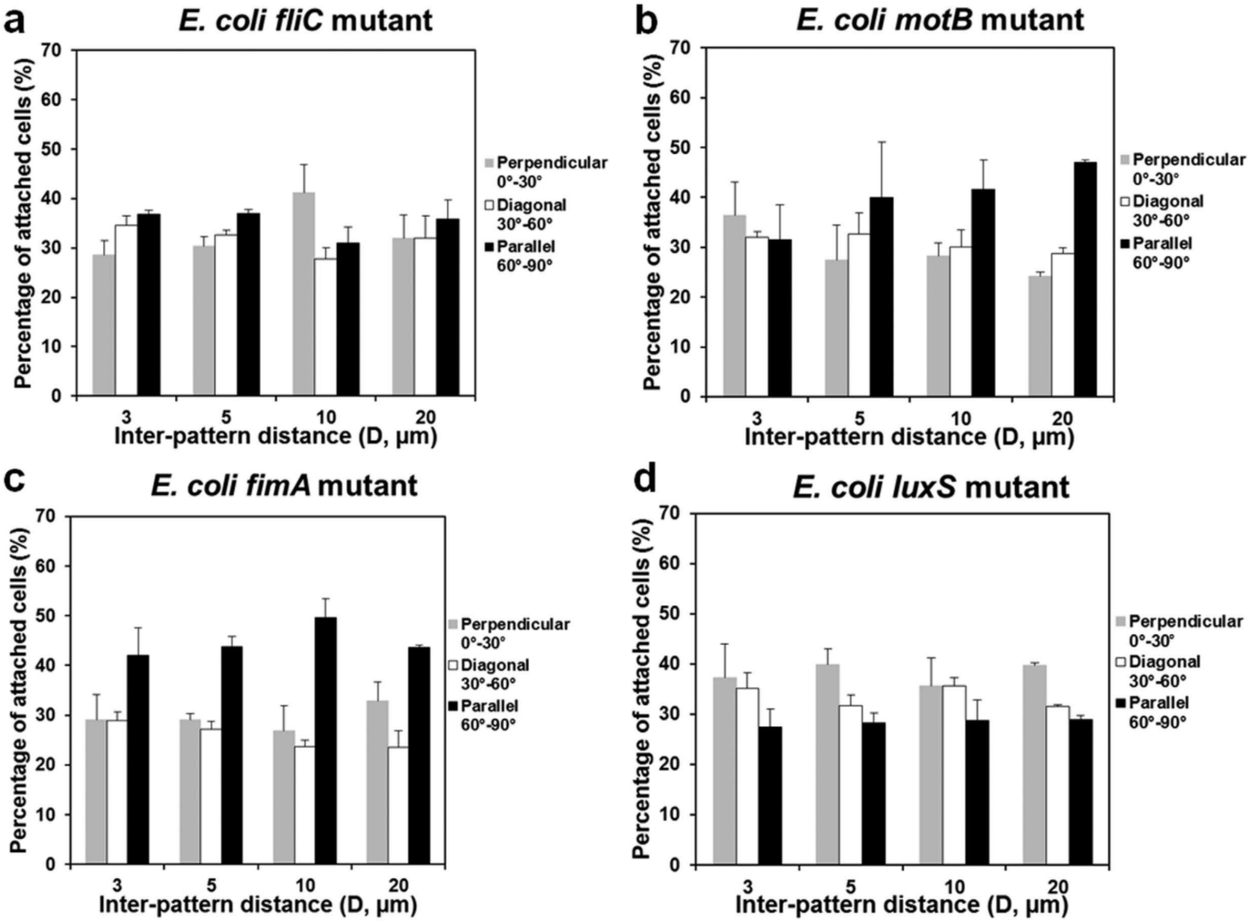

Mutations of A) *fliC,* B) *motB,* C) *fimA,* and D) *luxS* were used to investigate biological activities guiding *E. coli* attachment orientation on 5μm wide line patterns. Preferential perpendicular orientation was abolished for *fliC, motB* and *fimA* mutants, indicating that flagella and fimbriae were most likely important in establishing preferential orientation. Mutation of *luxS* showed a reduction in cell orientation, but did not fully abolish the trend observed. Therefore, *luxS* was not deemed essential for *E. coli* orientation preferences. Figure courtesy of Dr. Huan Gu.

Figure 7-4: Example fluorescent and SEM micrographs from time-lapse and static image capture of single wild-type and mutant *E. coli* cell attachment atop 5μm line patterns.

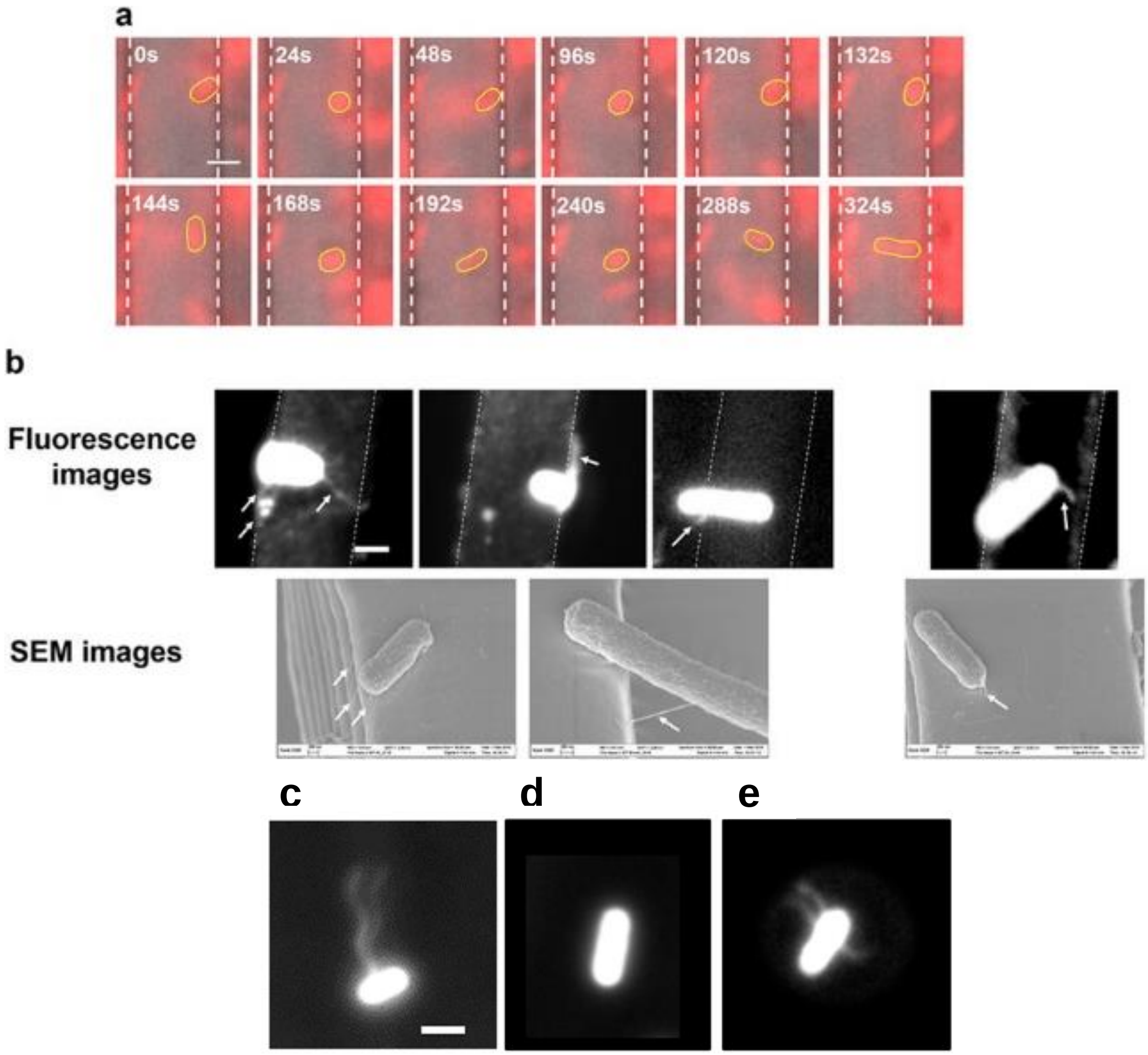

Representative micrographs of *E. coli* cells attached to 5μm line patterns. A) A series of time-lapse images demonstrate that the cell body rotates after initial attachment, prior to settling into a final orientation. The cell body is highlighted in yellow, while white dotted lines indicate pattern boundaries. B) Fluorescent and SEM images of cells show that attachment is due to flagellum-like structures (denoted by white arrows). Fluorescent image comparisons of C) wild-type, D) *fliC* and E) *fimA* mutants confirm the presence of flagella structures. Scale bars = 2 μm. Figure courtesy of Dr. Huan Gu.

Figure 7-5: Time-lapse image stills demonstrating *E. coli* rotation and corresponding ACTIVE analysis

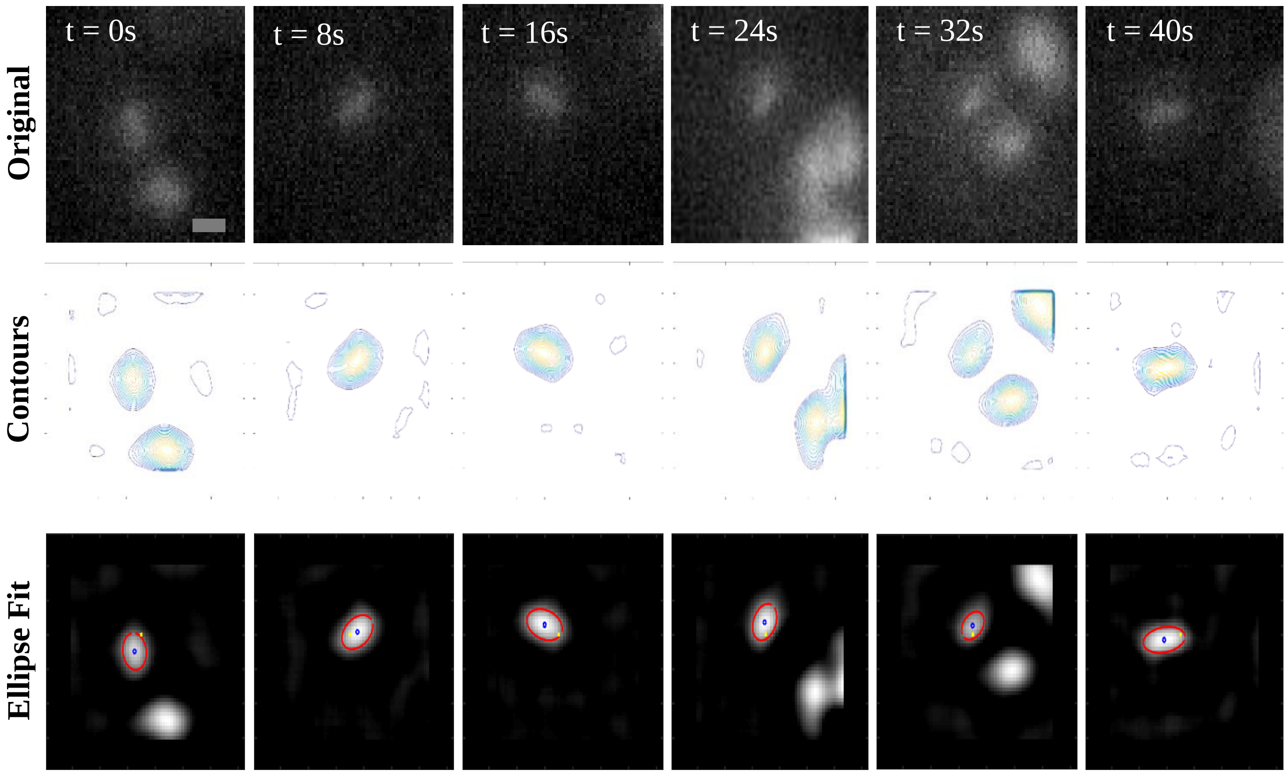

Example micrographs of cell data processed by ACT*IV*E. Top row: A single cell was manually identified and time-lapse videos were cropped to highlight bacterium of interest for rotational analysis. Middle row: ACT*IV*E utilized contour-based intensity segmentation to remove background noise and isolate cell body information. Bottom row: For each frame, a single ellipse (red) was fit and the center of mass (blue) was recorded for orientation analyses. Scale bar = 2μm.

Figure 7-6: Rotation of *E. coli* cells attached to the top and side of PDMS line patterns

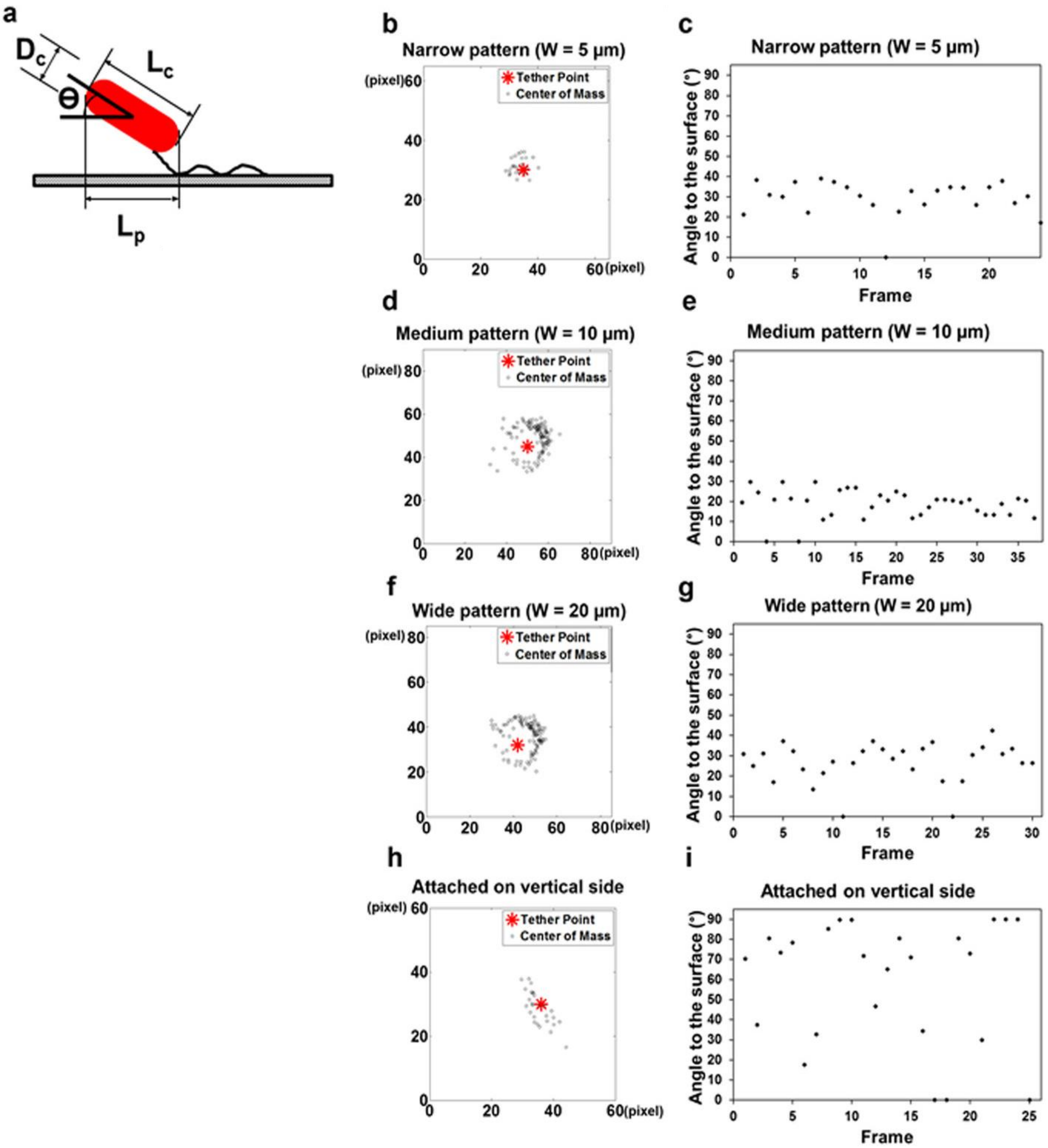

Rotation of *E. coli* cells atop narrow, medium, and wide line patterns. A) After determining that *E. coli* attached to surfaces using polar flagella, cell orientation parameters were defined. Rotational behaviors of cells atop narrow (B,C), medium (D,E), and wide (F,G) line patterns were then characterized using ACT*IV*E. As shown, cells atop medium and wide line patterns demonstrated a circular rotational pattern with a corresponding cell body angle between 0° and 30° (essentially parallel to the surface). Rotational patterns of cells on narrow patterns was more irregular, although cell body orientation remained relatively parallel to the substrate surface. Cells tethered to the edge of narrow line patterns (H, I) were also characterized. These cells demonstrated random and erratic orientation motions and frequently reoriented their cell body in relation to the substrate surface. Figure courtesy of Dr. Huan Gu.

Figure 7-7: *E. coli* morphology and metabolic activity atop narrow, medium, and wide PDMS line patterns

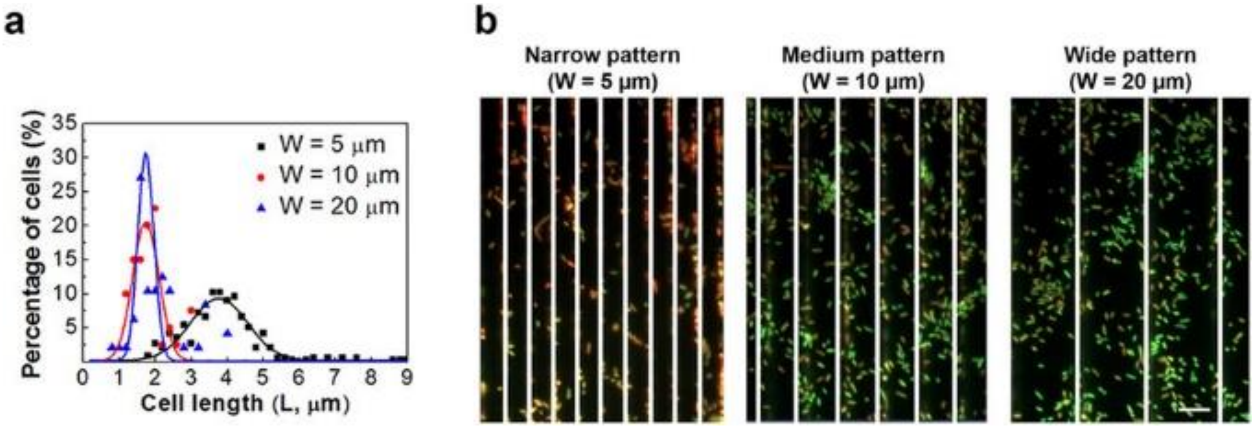

E. coli length is directly related to metabolic activity. A) Cells atop narrow line patterns were approximately twice as long as cells atop medium or wide patterns. B) When acridine orange staining for transcriptional activity was applied, cells atop narrow patterns demonstrated more red fluorescence compared to more green fluorescence atop medium and wide patterns. This indicated that cells atop narrow patterns had more RNA, while cells atop medium and wide patterns had more DNA. Scale bar = 10µm. Figure courtesy of Dr. Huan Gu.

Figure 7-8: Cell cluster and biofilm formation of *E. coli* atop narrow, medium, and wide PDMS line patterns.

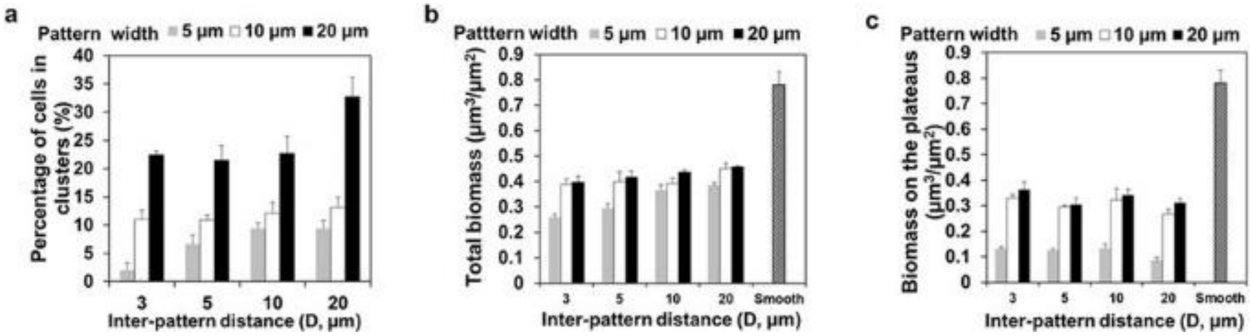

Cell cluster and biomass aggregation varied based on surface topography. A) The number of cell clusters present on the surface was positively correlated with line size. Inter-pattern spacing also demonstrated a minor positive trend, increasing the number of cell clusters as the distance (D) increased. B) Total biomass demonstrated a similar trend: total biomass increased with increased pattern width. C) When compared to flat PDMS surfaces, narrow line patterns with the smallest inter-pattern spacing demonstrated the greatest reduction in biomass formation. Figure courtesy of Dr. Huan Gu.

Figure 7-9: Example ACT*IV*E segmentation and tracking of *E. coli* cells

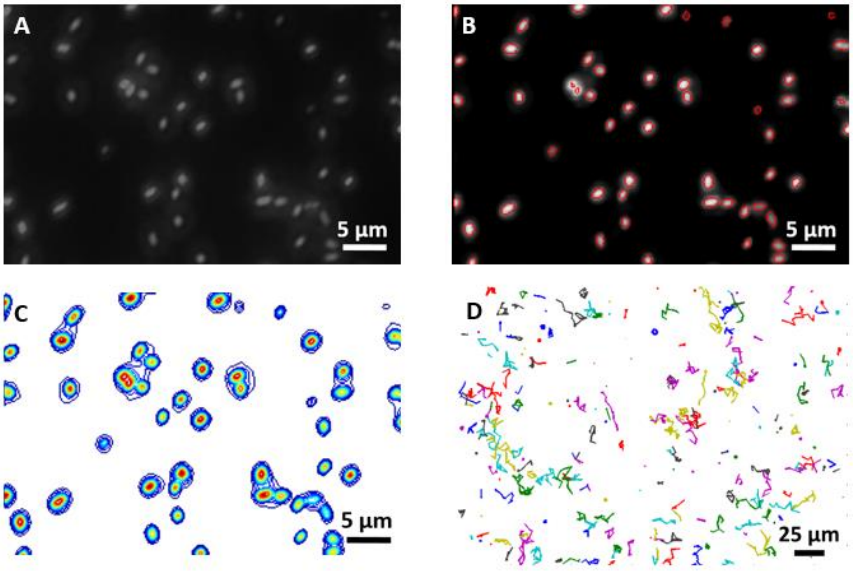

E. coli cells were complemented with pRSH103 vectors for fluorescent time-lapse image capture. A) An example image showing *E. coli* fluorescent expression. B) Cells were fit with ellipses for tracking based on C) the intensity profile of the fluorescent signal analyzed. D) Cells were then tracked over 12 minute intervals to determine collective characteristics (each cell was assigned a separate colored track for visualization). Figure courtesy of Dr. Fangchao Song.

Figure 7-10: Classification of "moving", "rotating" and "still" cells

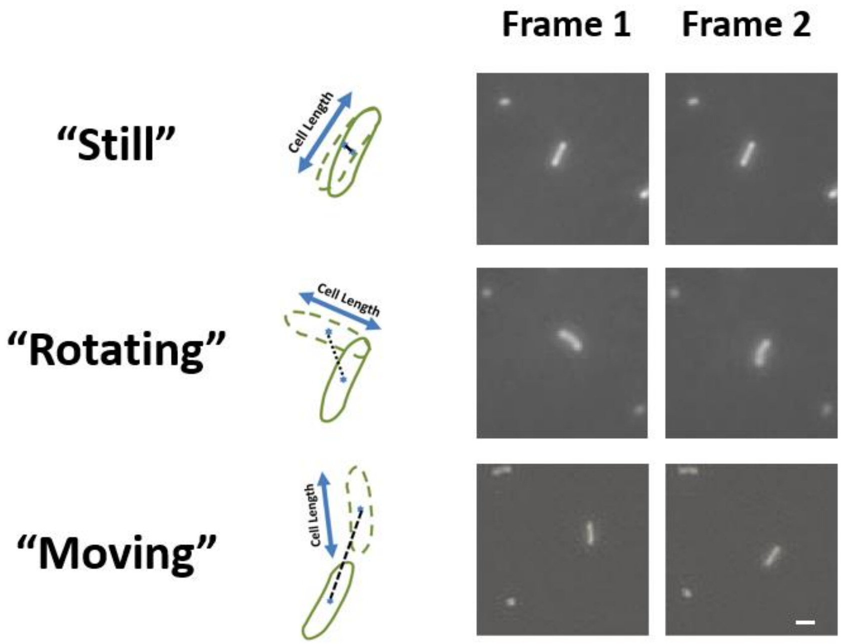

E. coli cells were classified into three categories based on their frame to frame displacement: 1) "still" (top row), 2) "rotating" (middle row), and 3) "moving" (bottom row). These classifications were based on frame to frame cell displacements. "Still" cells displaced less than one quarter of an average cell body length frame to frame. "Rotating" cells typically moved in a circular motion, displacing their center of mass between one quarter and one average cell body length frame to frame. "Moving" cells displaced more than one average cell body frame to frame. Scale bar = 2μm; 5s between frames. Figure courtesy of Dr. Fangchao Song.

Figure 7-11: *E. coli* motility analysis on soft and stiff PDMS surfaces

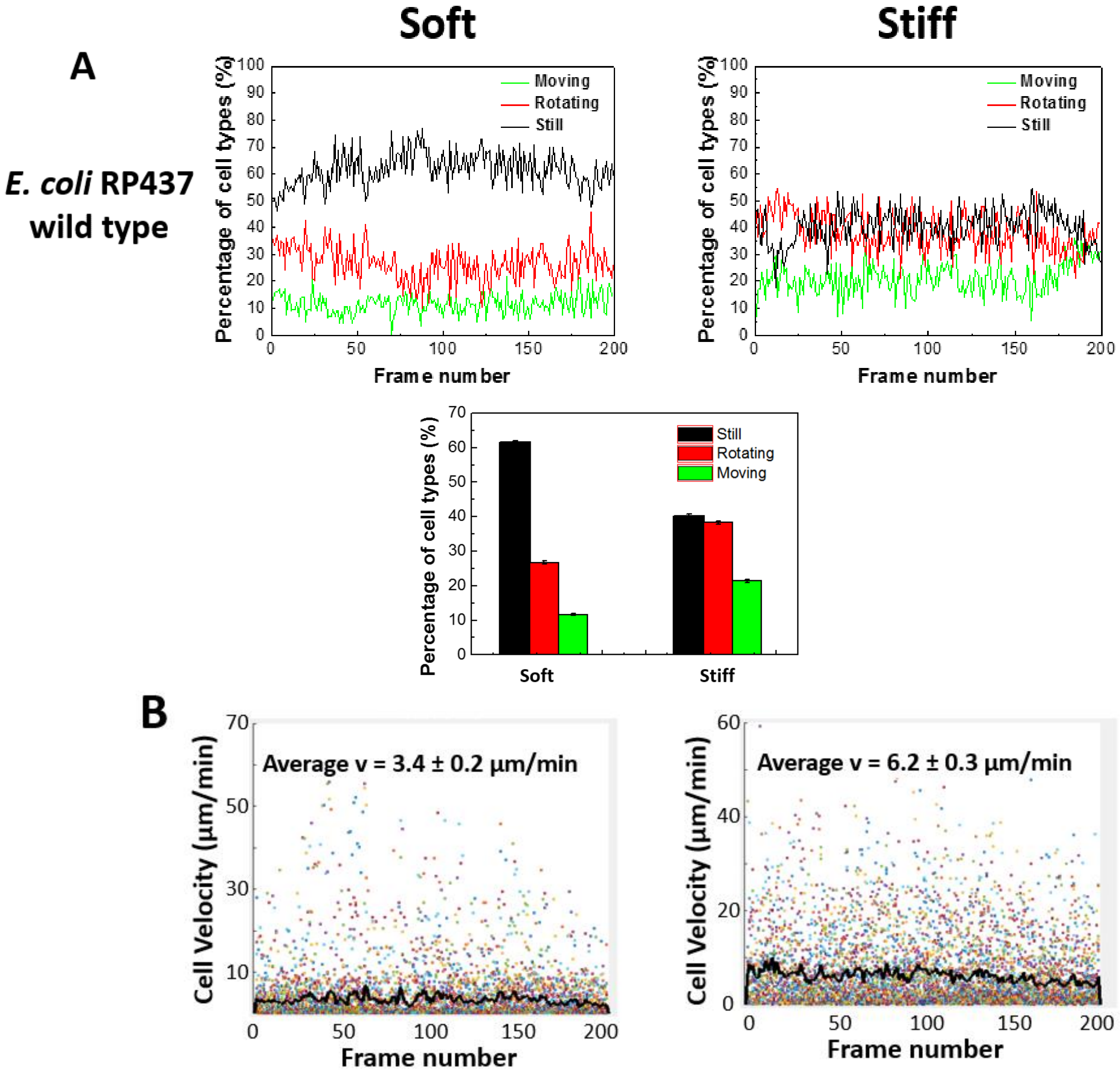

Representative cell motility data of wild-type *E. coli* cells atop soft and stiff PDMS surfaces. A) Cell motility data was classified into “still” (black), “rotating” (red), and “moving” (green) cells. Overall, the percentage of “moving” cells was much higher on stiff compared to soft surfaces. B) When plotting velocity distributions and quantifying average velocity over time, cells on stiff surfaces exhibited approximately double the speed of cells on soft surfaces. Figure courtesy of Dr. Fangchao Song.

Figure 7-12: *E. coli* wild-type, *motB*, *fimA*, and *fliC* attachment on face-up and face-down stiff and soft PDMS surfaces

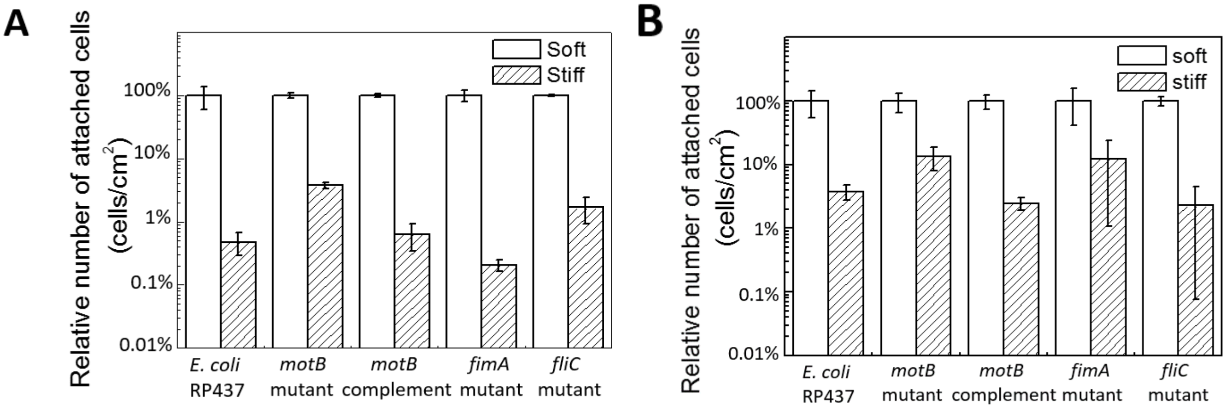

Cell attachment of wild-type *E. coli*, *motB* mutants, *motB* complemented mutants, *fimA* mutants, and *fliC* mutants on A) face-up and B) face-down soft and stiff PDMS patterns after 2 hrs of attachment in PBS. Cell growth was inhibited to assess the mechanism of cell attachment. As shown, *motB* is important in initial mechanosensing for *E. coli* attachment irrespective of gravitational effects. Figure courtesy of Dr. Fangchao Song.

Figure 7-13: *MotB* mutant motility atop soft and stiff PDMS surfaces

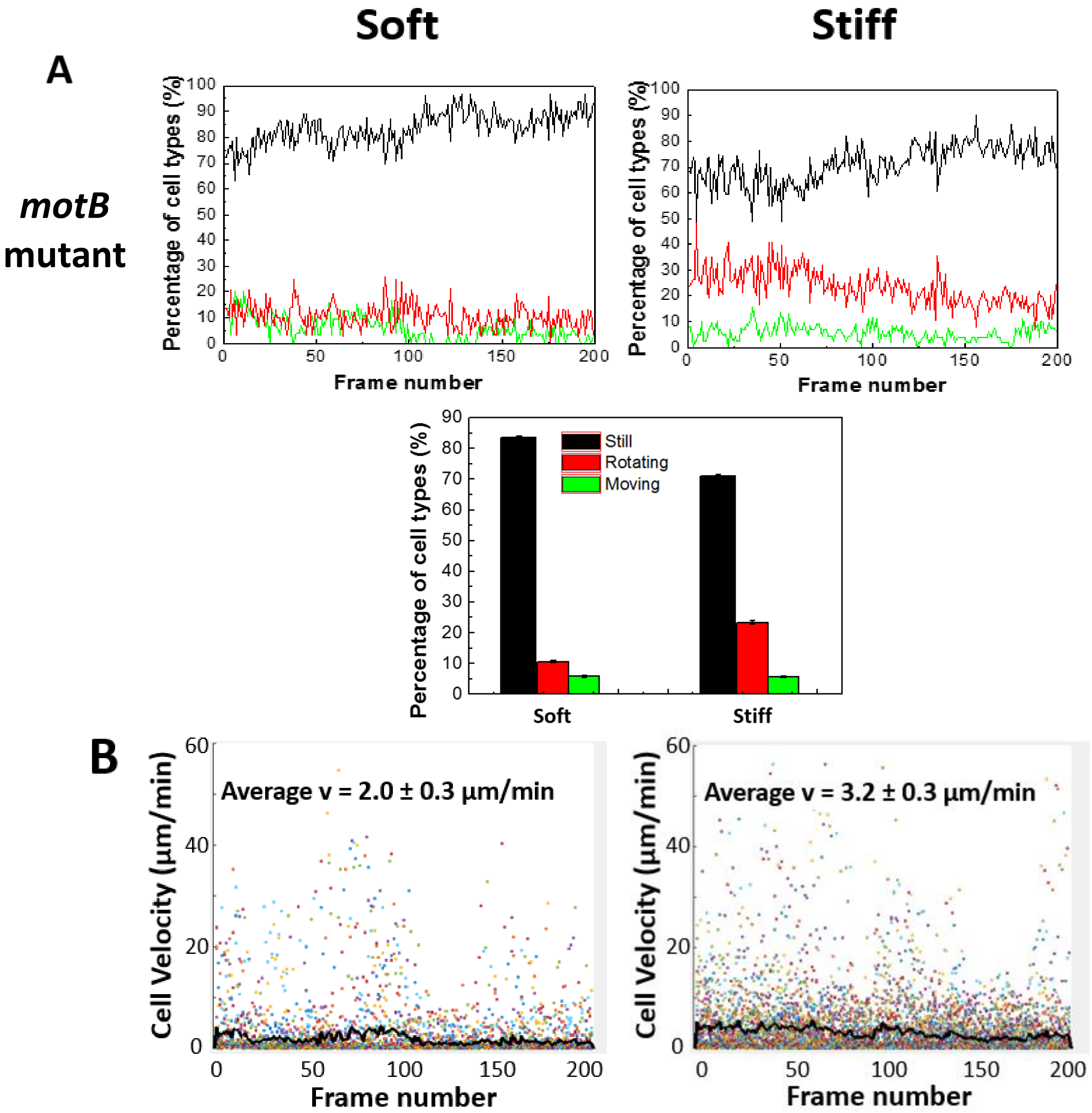

Representative cell motility data of *motB E. coli* mutants atop soft and stiff PDMS surfaces. A) Cell motility data was classified into “still” (black), “rotating” (red), and “moving” (green) cells. Overall, the percentage of “still” cells remained similar on soft and stiff surfaces, whereas there was a slight increase in “moving” and “rotating” cells between soft and stiff surfaces. B) When plotting velocity distributions and quantifying average velocity over time, cells on stiff surfaces had increased speeds compared to soft PDMS surfaces, however, this difference in speed was approximately half the difference observed in the wild-type strain. Figure courtesy of Dr. Fangchao Song.

Figure 7-14: *motB* complement restores wild-type *E. coli* motility atop soft and stiff PDMS surfaces

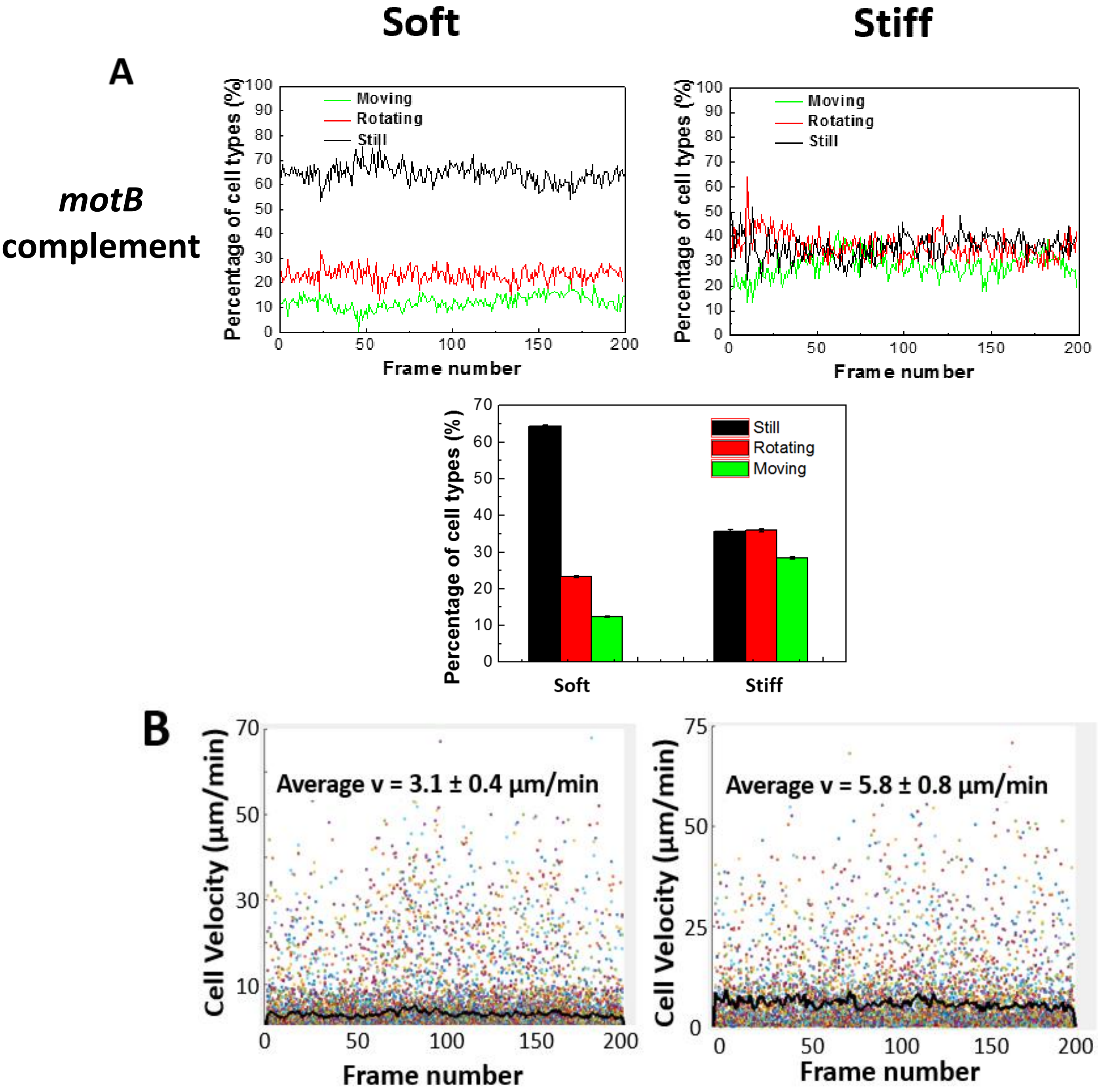

Representative cell motility data of *motB* complemented *E. coli* mutants atop soft and stiff PDMS surfaces. A) Cell motility data was classified into “still” (black), “rotating” (red), and “moving” (green) cells. Overall, the complemented *motB* cells moved with similar behaviors to the wild-type strain on both soft and stiff surfaces. B) When plotting velocity distributions and quantifying average velocity over time, complemented *motB* mutants again demonstrated similar speed characteristics to the wild-type *E. coli* strain. Figure courtesy of Dr. Fangchao Song.

Figure 7-15: Aggregate percentages, average speeds, and speed distributions of wild-type and *motB* mutant *E. coli* cells.

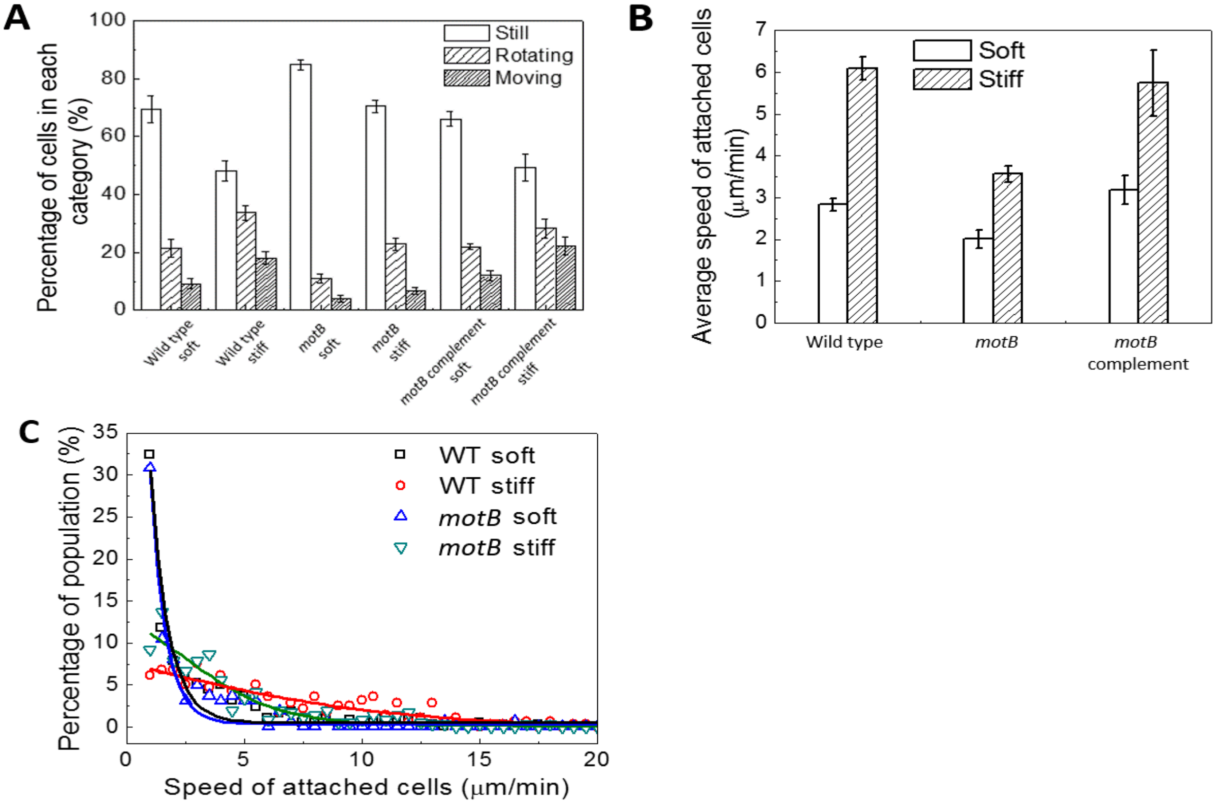

Cell motility data was averaged over 3 videos per cell type with at least 320 frames per video. A) Percentages of "still", "rotating", and "moving" cells for the wild type, *motB* mutant, and *motB* complemented mutant *E. coli* cells. In general, the wild type and *motB* complemented strains demonstrated similar displacement characteristics. Comparatively, *motB* mutants had more "still" cells than the wild-type strain, even though *motB* mutants demonstrated a slight increase in the number of "moving" and "rotating" cells between soft and stiff substrates. B) The average speed of wild type, *motB* mutant, and *motB* complemented mutant *E. coli* cells. On average, *motB* mutants had lower speeds and a smaller difference in speeds between the soft and stiff substrates when compared to the wild type and *motB* complemented cells. C) By plotting distributions of movement speeds compared to population percentages, similar motility patterns were observed for the wild type and *motB* mutant cells on stiff or on soft PDMS surfaces. Figure courtesy of Dr. Fangchao Song.

Chapter 8: Summary and Future Work

8.1 Summary of Presented Work

Cell-extracellular matrix (ECM) interactions are critical in regulating important biological processes, including tissue development, wound healing, and disease progression. Currently, there is a knowledge gap regarding how mechanical changes in the ECM regulate cell motility and polarization responses. Therefore, this dissertation had two fundamental goals: 1) to develop a modular image processing tool that could be applied for *in vitro* motility analysis of cells in complex microenvironments, and 2) to utilize that tool to advance knowledge of mechanobiology and mechanotransduction processes important to morphogenesis, tissue repair, and disease states.

The first portion of this thesis (**Chapters 2 and 3**) dealt with proof of concept for a newly developed automated cell tracking tool termed ACT*IV*E (automated contour-based tracking for *in vitro* environments). In **Chapter 2** we assessed the accuracy of this system, demonstrating that the technique could achieve greater than 95% segmentation accuracy at multiple cell densities (low density, medium density, and near confluence). We additionally improved upon a common source of inaccuracy in cell tracking, reducing error associated with two-body cell-cell interactions by up to 43%. Furthermore, we incorporated a new method for identifying and tracking cell division behaviors with up to 80% accuracy, a feature often missing in automated cell tracking programs. In **Chapter 3**, we successfully utilized ACT*IV*E to analyze differences in cell motility responses of fibroblast cells migrating atop anisotropic or isotropic surfaces at multiple cell densities. We demonstrated that cells atop wrinkled substrates preferentially migrate along the direction of anisotropy, whereas cells atop non-wrinkled or tissue culture polystyrene surfaces showed similar motility dynamics in both x- and y-directions. This was consistent with current literature understanding. Surprisingly, mean squared displacement results showed that cell behavior follows the same functional form, regardless of surface topography or cell density, and that this behavior remained superdiffusive over long timescales. Interestingly, we also observed significant differences in track shape on all surfaces tested, indicating that cell motility relies on both surface topography and cell-ECM interactions. Lastly, we demonstrated, through the use of ACT*IV*E's novel division tracking capabilities, that cells preferentially divide along the wrinkle direction in the presence of surface topography.

After demonstrating proof of concept, we applied ACT*IV*E in multiple experimental designs. This included analysis of fibroblast motility and intracellular reorganization atop a dynamic shape memory polymer microenvironment (**Chapters 4 and 5**), subpopulation identification in a co-culture of endothelial and smooth muscle cells (**Chapter 6**), and investigation of *E. coli* biofilm formation atop poly(dimethylsiloxane) (PDMS) surfaces with varying line patterns or substrate stiffness (**Chapter 7**). These broad applications demonstrated that ACT*IV*E is a versatile and robust system, capable of being applied to clinically relevant systems to elucidate critical mechanisms guiding motility based mechanobiology and mechanotransduction processes.

The first cell system that we analyzed was a shape memory polymer substrate that had the capability to dynamically wrinkle (based on a thermal trigger) with attached and viable cells. In **Chapter 4** we presented the first analysis of cell motility and nuclear alignment responses *during* this active topographic change in the cellular microenvironment. More specifically, we wanted to investigate the mechanobiology response of fibroblasts to the developing topography. Trajectory, diffusion, and mean squared displacement analyses revealed that cells transitioned from random to oriented motion with the introduction of a wrinkled pattern. Mouse fibroblasts additionally reoriented their nuclei to the pattern direction, while adapting an intermediate velocity response when compared to the static microenvironments. In **Chapter 5**, we took this analysis a step further, by examining the mechanism associated with this response. Dual Golgi and nuclear tracking enabled additional analyses of intracellular reorganization phenomenon in response to the topographical change in the microenvironment. In the uninhibited case, we observed that cells atop active wrinkling surfaces demonstrated a decrease in their truncated standard deviation with the introduction of topographical features, akin to behaviors observed in **Chapter 4**. This demonstrated that the Golgi infections had no significant impact on nuclear responses. This was coupled with an increase in the alignment parameter and a minor decrease in the truncated standard deviation associated with the Golgi-nuclear polarization vector once the topography was introduced. With ROCK inhibition, we demonstrated that cells atop the active wrinkling surfaces more closely resembled behaviors observed in the uninhibited non-wrinkled system. Introduction of ROCK abolished the cell's ability to recognize the topographical transition, subsequently resulting in no alignment of the cells after the topography fully developed. In the static wrinkled ROCK inhibited case, we observed a decrease in the nuclear and nuclear-Golgi alignment over time, further demonstrating that the ROCK pathway is important for surface feature recognition.

In **Chapter 6**, we were interested in non-invasive and non-destructive analysis of cell subpopulation dynamics in mono and co-culture. By adapting a combination approach of ACT*IV*E morphometric and motility analysis, principle component feature reduction, and partitioning around medoids clustering, we demonstrated that this technique could be used to identify trends in endothelial and smooth muscle live-cell data. We first showed that the technique could be applied to a known test set, the Iris data, to achieve results consistent with literature understanding. We then applied the technique to morphometric cell data, demonstrating that two primary clusters could be identified, one with large nuclei and one with small nuclei, irrespective of culture condition. Interestingly, application of the technique to motility features showed that endothelial (ECs) and smooth muscle cells (SMCs) adapted different movement rates in co-culture versus monoculture. More specifically, a mixed subpopulation of the EC and SMC data adapted a heightened x-velocity, y-velocity, and speed compared to their monoculture counterparts. A combinatory approach that pooled morphometric and motility data revealed that more sensitive guidelines were required for a mixed approach, as poor clustering was noted for all cases. In general, we demonstrated that this technique could be utilized for heterogeneous microenvironments, satisfying our goal of creating a non-destructive and non-invasive method for subpopulation identification.

Finally, in **Chapter 7**, we adapted ACT*IV*E for two very different two-dimensional bacterial tracking applications. First, we demonstrated that PDMS line patterns altered *E. coli* attachment orientation preferentially aligning cells perpendicular to the pattern direction due to rotational tethering via flagellar attachments along vertical walls. We additionally showed that these behaviors were coupled with increased stress and reduced biofilm formation, suggesting that a 5 μm wide, 10 μm tall line pattern could be used for antifouling applications. In the second study, we showed that stiffness influences both *E. coli* attachment behaviors and motility dynamics. More cells attached to the soft compared to the stiff PDMS surfaces. An increase in motility, as well as cell speed, was additionally observed on stiff surfaces. We further demonstrated that the *motB* gene was one of the primary genes responsible for mechanosensing in *E. coli* cells. Collectively, we showed that stiffer surfaces, patterned with narrow line features promote antifouling phenomena. This work could not have been achieved without the insights provided by the ACT*IV*E tracking system.

8.2 Future Directions

8.2.1 Role of Contact Inhibition on Cell Migratory Responses

In **Chapter 2**, we assessed ACT*IV*E's ability to identify cell-cell merging events. However, a detailed analysis of these contact events and their ultimate impact on cell motility behaviors was never investigated. Cell-cell contact can result in density-dependent inhibition of proliferation [1] or locomotion [2]. Contact inhibition of proliferation exists in tissue level confluent monolayers, where area and mechanical constraints limit local expansion [1]. Similarly, contact inhibition of locomotion (CIL) is common in dense microenvironments, where direct contact of migrating cells results in cytoskeletal reorganization and redirection of migratory behavior. Clinically, malignant cells have exhibited reduced CIL capacity, enabling the ability to invade healthy tissue [2]. CIL has also been implicated as a mechanism controlling neural crest migration *in vivo*, stimulating

RhoA activation and alterations in cell polarity during development [3]. Understanding the dynamics dictating CIL reveals mechanisms controlling cell migration behavior. Improved knowledge of CIL would also contribute to understanding of epithelial to mesenchymal transitions [4] and the relationship between healthy and cancerous cell behavior [5].

Here, we would seek to further understanding of density dependent CIL behavior using ACT*IV*E’s unique merging event identification system. Thus far, cell interaction points have been isolated using ACT*IV*E's shared contour data (**Chapter 2**). Code to generate videos of two-body migratory events from ACT*IV*E data has additionally been achieved. As shown in **Chapter 3**, mean squared displacement (MSD) trends have been assessed on preliminary data with C3H10T1/2 mouse fibroblasts at multiple densities. Interestingly, long-term cell behavior did not yield purely diffusive dynamics, as is commonly hypothesized in the literature, regardless of density. Instead, long term MSD values remained slightly ballistic, indicating that cell-cell interactions do not significantly impact trajectory behavior for this cell type [6]. This indicates that CIL may either: 1) not be an important trend for this particular cell type, or that, 2) on a bulk level, CIL behavior is masked by the general system behavior quantitatively measured by MSD. As this behavior has not been confirmed in other cell types, further analysis both at the individual and bulk scale is required to confirm or deny this trend. In the future, cell density in healthy and cancerous cultures could systematically be varied to identify whether a critical threshold exists enabling or hindering CIL behavior. Similar to **Chapter 5**, dynamics could be investigated at the cytoskeletal, individual, and collective cell levels, enabling new insights into the role of CIL in developmental processes and cancerous cell migratory responses.

8.2.2 In Vitro Substrates as Platforms for Mechanobiology

In **Chapters 4 and 5**, we used a two-dimensional shape memory polymer platform to investigate intracellular, individual, and collective cell dynamics *before, during, and after* a topographical transition in the cellular microenvironment. **Chapter 7** additionally explored the effects of material stiffness and patterned features on *E. coli* attachment, proliferation, and motility. While new insights into mechanistic behaviors were observed with respect to fibroblast motility and *E. coli* dynamics, exploration into other cell systems remains to be investigated. For example, comparison of healthy motility dynamics to a comparable cancerous cell line (e.g., a fibrosarcoma line such as HT1080 [7] or an epithelial adenocarcinoma such as HeLa cells [8]), could further work presented in **Chapters 4 and 5** and provide direct insights into mechanisms enabling cancer cell motility *in vivo*. Similarly, comparing bacterial responses of other motile strains (e.g., pseudomonas aeruginosa [9]) could build upon the new knowledge presented in **Chapter 7**, providing further insight into design parameters for developing antifouling surfaces and preventing antibiotic resistance.

We explored the role of Golgi-nuclear orientation for directed cell migration in **Chapter 5**. In the study presented, we limited our analysis to nuclei (Hoechst dye) and Golgi bodies (viral infection). In the future, this process could be extended to tracking other important organelles and cytoskeletal components, including the centrosome [10], lamellipodia [11], or filopodia [12], which have all been identified as important regulators for cell polarization and leading edge protrusions in mammalian cell motility [13]. Similarly, quantifying the number of focal adhesion sites per cell could provide direct insight into cell-ECM binding affinity [14]. In the study presented in **Chapter 5**, we demonstrated that treating cells with a Rho-associated protein kinase inhibitor (ROCK) abolished C3H10T1/2 fibroblast cells' ability to recognize and alter motility responses in accordance to topographical cues. Additional inhibitors (e.g., Rac or Cdc42 [15]) could be applied to further understanding of mechanisms guiding cell polarization, motility, and ECM binding in the presented dynamic microenvironment.

Finally, variations in the material type or surface chemistry could be used to compare cell-ECM binding affinities and cell homing responses. Incorporation of various surface ligands, such as RGD peptide sequences [16], fibronectin, hylauronan, or gelatin [17], to the poly(tert-butyl acrylate-co-butyl acrylate) shape memory polymer (SMP) substrate's surface (**Chapters 2-5**) could provide new understanding about the relationship between mechanical and surface chemistry effects on cell motility. Similarly, programming and releasing multiple levels of strain in a non-gold coated version of the SMP system at multiple cell densities would provide insight into individual cell versus tissue level responses to mechanical stress in the microenvironment.

The material system could additionally be altered to explore the local effects of chemical, mechanical, or topographic transitions in the microenvironment. In the presented system, the wrinkling effect is induced through surface buckling of the gold layer triggered by compression of the underlying SMP [18]. Local triggering of an SMP surface (e.g., through light induced mechanisms [19]) could provide spatial control of chemical, mechanical or topographic features to carefully manipulate the cell surface and potentially guide cell responses. Similar principles could also be applied to three dimensional shape memory polymer systems. As we have previously demonstrated, 3D foams [20] and fibrous scaffolds [21, 22] alter cell behavioral responses.

Expansion of this work to live-cell motility capture, in cooperation with the completion of section *8.2.4* below, would provide novel understanding about the relationship between mechanical manipulation and cell motility dynamics in three dimensional systems.

8.2.3 Characterizing Cell Subpopulations in Stem Cell Cultures

We presented a combination approach of ACT*IV*E morphometric and motility characterization, principle component analysis, and partitioning around medoids clustering for cell subpopulation identification in **Chapter 6**. In the presented study, we utilized a simple co-culture of endothelial and smooth muscle cells to evaluate cell morphology and motility differences in co-culture versus monoculture. This technique could easily be applied to other heterogeneous cell populations. For example, expanding the analysis to a healthy and cancerous cell model (e.g., human foreskin fibroblasts and HT1080 fibrosarcomas) would improve understanding of subpopulation dynamics that emerge from healthy and diseased cell-cell interactions. These experiments could help further understanding of mechanisms triggering epithelial to mesenchymal transitions [23, 24], as well as provide insight into modifications to healthy cell dynamics that aid cancer metastasis. Similarly, this approach could be applied to stem cell populations to characterize the natural heterogeneity that arises from the differentiation process [25].

8.2.4 Expansion of ACTIVE to Three Dimensional Tracking

ACT*IV*E was designed to analyze adherent cell populations subject to nuclear staining, infection, or transfection. While this dissertation demonstrated the versatility of the ACT*IV*E system, ACT*IV*E is limited to tracking cells in two-dimensional microenvironments. Microscopic grooves, ridges, wells, and channels have been used for decades to study cell-ECM interactions in two dimensions. However, recent attention has been directed towards developing three dimensional synthetic designs [16]. Therefore, expansion of ACT*IV*E to three-dimensional tracking would enable new investigations of spatial and temporal dynamics of cells in 3D systems that better mimic the extracellular environment observed *in vivo*.

8.3 Final Remarks

In summary, in this thesis we were able to present a novel image processing tool for automated cell tracking, ACT*IV*E, and quantify that is was accurate, efficient, and effective, in the context of analyzing time-lapse microscopy data. We then utilized the system to investigate important mechanobiology phenomena, including the role of intracellular reorganization in response to a dynamic change in the extracellular matrix environment, the influence of co-culture versus monoculture in regards to cell subpopulation presence, and detailed investigation of antifouling properties of PDMS materials. We are confident that this approach will continue to be used to identify critical mechanisms regulating important biological processes, including tissue development, wound healing, and disease progression.

8.4 References

1. Puliafito, A., et al., *Collective and single cell behavior in epithelial contact inhibition.* Proceedings of the National Academy of Sciences of the United States of America, 2012. **109**(3): p. 739-744.
2. Mayor, R. and C. Carmona-Fontaine, *Keeping in touch with contact inhibition of locomotion.* Trends in Cell Biology, 2010. **20**(6): p. 319-328.
3. Carmona-Fontaine, C., et al., *Contact inhibition of locomotion in vivo controls neural crest directional migration.* Nature, 2008. **456**(7224): p. 957-961.
4. Revenu, C. and D. Gilmour, *EMT 2.0: shaping epithelia through collective migration.* Current Opinion in Genetics & Development, 2009. **19**(4): p. 338-342.
5. Astin, J.W., et al., *Competition amongst Eph receptors regulates contact inhibition of locomotion and invasiveness in prostate cancer cells.* Nature Cell Biology, 2010. **12**(12): p. 1194-U175.
6. Baker, R.M., et al., *Automated, contour-based tracking and analysis of cell behaviour over long time scales in environments of varying complexity and cell density.* Journal of The Royal Society Interface, 2014. **11**(97).
7. Fourre, N., et al., *Extracellular matrix proteins protect human HT1080 cells against the antimigratory effect of doxorubicin.* Cancer Science, 2008. **99**(8): p. 1699-1705.
8. Cuvelier, D., et al., *The Universal Dynamics of Cell Spreading.* Current Biology, 2007. **17**(8): p. 694-699.

9. O'Toole, G.A. and R. Kolter, *Flagellar and twitching motility are necessary for Pseudomonas aeruginosa biofilm development.* Molecular Microbiology, 1998. **30**(2): p. 295-304.
10. Godinho, S.A. and D. Pellman, *Causes and consequences of centrosome abnormalities in cancer.* Philosophical Transactions of the Royal Society B: Biological Sciences, 2014. **369**(1650).
11. Gupton, S.L., et al., *Cell migration without a lamellipodium: Translation of actin dynamics into cell movement mediated by tropomyosin.* Journal of Cell Biology, 2005. **168**(4): p. 619-631.
12. Yang, C., et al., *Novel Roles of Formin mDia2 in Lamellipodia and Filopodia Formation in Motile Cells.* PLoS Biology, 2007. **5**(11): p. e317.
13. Kurosaka, S. and A. Kashina, *Cell Biology of Embryonic Migration. Birth defects research.* Part C, Embryo today : reviews, 2008. **84**(2): p. 102-122.
14. Deakin, N.O. and C.E. Turner, *Paxillin inhibits HDAC6 to regulate microtubule acetylation, Golgi structure, and polarized migration.* Journal of Cell Biology, 2014. **206**(3): p. 395-413.
15. Parri, M. and P. Chiarugi, *Rac and Rho GTPases in cancer cell motility control.* Cell Communication and Signaling, 2010. **8**.
16. Stevens, M.M. and J.H. George, *Exploring and Engineering the Cell Surface Interface.* Science, 2005. **310**(5751): p. 1135-1138.
17. Lutolf, M.P. and J.A. Hubbell, *Synthetic biomaterials as instructive extracellular microenvironments for morphogenesis in tissue engineering.* Nature Biotechnology, 2005. **23**(1): p. 47-55.

18. Yang, P., et al., *In vitro wrinkle formation via shape memory dynamically aligns adherent cells.* Soft Matter, 2013. **9**(18): p. 4705-4714.

19. Lendlein, A., et al., *Light-induced shape-memory polymers.* Nature, 2005. **434**(7035): p. 879-882.

20. Baker, R.M., J.H. Henderson, and P.T. Mather, *Shape memory poly(ε-caprolactone)-co-poly(ethylene glycol) foams with body temperature triggering and two-way actuation.* Journal of Materials Chemistry B, 2013. **1**(38): p. 4916-4920.

21. Tseng, L.F., P.T. Mather, and J.H. Henderson, *Shape-memory-actuated change in scaffold fiber alignment directs stem cell morphology.* Acta Biomaterialia, 2013. **9**(11): p. 8790-8801.

22. Tseng, L.F., et al., *Osteogenic Capacity of Human Adipose-Derived Stem Cells is Preserved Following Triggering of Shape Memory Scaffolds.* Tissue Engineering - Part A, 2016. **22**(15-16): p. 1026-1035.

23. Yang, J. and R.A. Weinberg, *Epithelial-Mesenchymal Transition: At the Crossroads of Development and Tumor Metastasis.* Developmental Cell, 2008. **14**(6): p. 818-829.

24. Thiery, J.P., et al., *Epithelial-Mesenchymal Transitions in Development and Disease.* Cell, 2009. **139**(5): p. 871-890.

25.Baer, P.C. and H. Geiger, *Adipose-Derived Mesenchymal Stromal/Stem Cells: Tissue Localization, Characterization, and Heterogeneity.* Stem Cells International, 2012: p. 11.

Appendix 1: Protocol for ACTIVE Initiation and Analysis

A1.1 Detailed ACT*IV*E User Manual

A1.1.1 Overview

The Automated Contour-based Tracking for *In Vitro* Environments (ACT*IV*E) approach was designed for automated nuclear cell tracking and was created using MATLAB version 2011a. It requires a valid MATLAB license to run. This user's manual details the main parameters used and the general operation of the tracking code as it was implemented in "Automated, contour-based tracking and analysis of cell behavior over long timescales in environments of varying complexity and cell density". While the suggested parameters are specifically tailored to the aforementioned study, the system was developed to work well for tracking in images that display fluctuations in intensity within a single image or for a series of images that display significant variations in contrast over time.

A1.1.2 Image Preparation

The code is equipped to read 16-bit grayscale image stacks. The stacks must be .tiff, and can be converted to the proper format with ImageJ:

Open stack in Image J --> Image --> Type --> 16-bit --> File --> Save as --> Tiff

There are currently no requirements for the tiff stack name, apart from standard naming conventions relevant to MATLAB (e.g., no symbols, spaces, etc.). Once initialized, the program will direct the user to select the tiff stack for analysis:

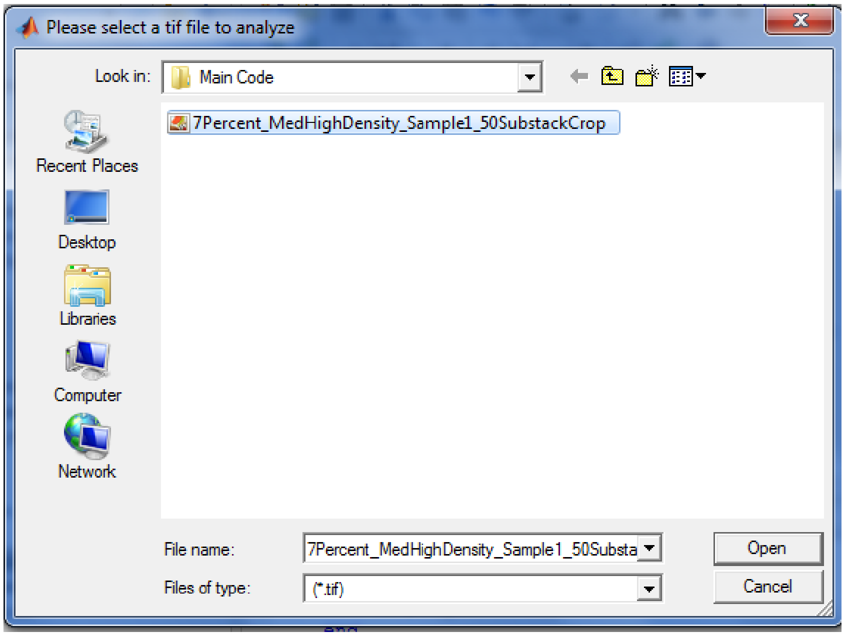
Please select a tif file to analyze

Look in: Main Code

7Percent_MedHighDensity_Sample1_50SubstackCrop

File name: 7Percent_MedHighDensity_Sample1_50Substa

Files of type: (*.tif)

Though it is not required, it is suggested that the tiff stack be placed in the same directory as the unzipped tracking code for convenience.

A1.1.3 Operation

The ACT*IV*E approach operates entirely from the wrapper function, run_tracking_contour2.m. Briefly, contour segmentation of images is first achieved through implementation of the makecontourparentarray.m function and ellipse fitting is accomplished through find_particles_fixed.m. Once segmented, cells are tracked using the modified Kilfoil function trackmem_new.m. Post tracking correction is then completed using the sib_matrix_creation, collision_corrector_rtc2, collision_tags_rtc2_3, mult_sib_creation, mult_event_array, mult_division_adjuster, division_corrector, and relabel functions. Analysis of outputs from the run_tracking_contour2.m function can then be assessed using the supplemental analysis code to generate mean squared displacement, velocity autocorrelation, and asphericity plots, similar to those displayed in the aforementioned manuscript.

A1.1.4 Detailed Tracking Instructions

1. Download the full tracking code from http://henderson.syr.edu/downloads/

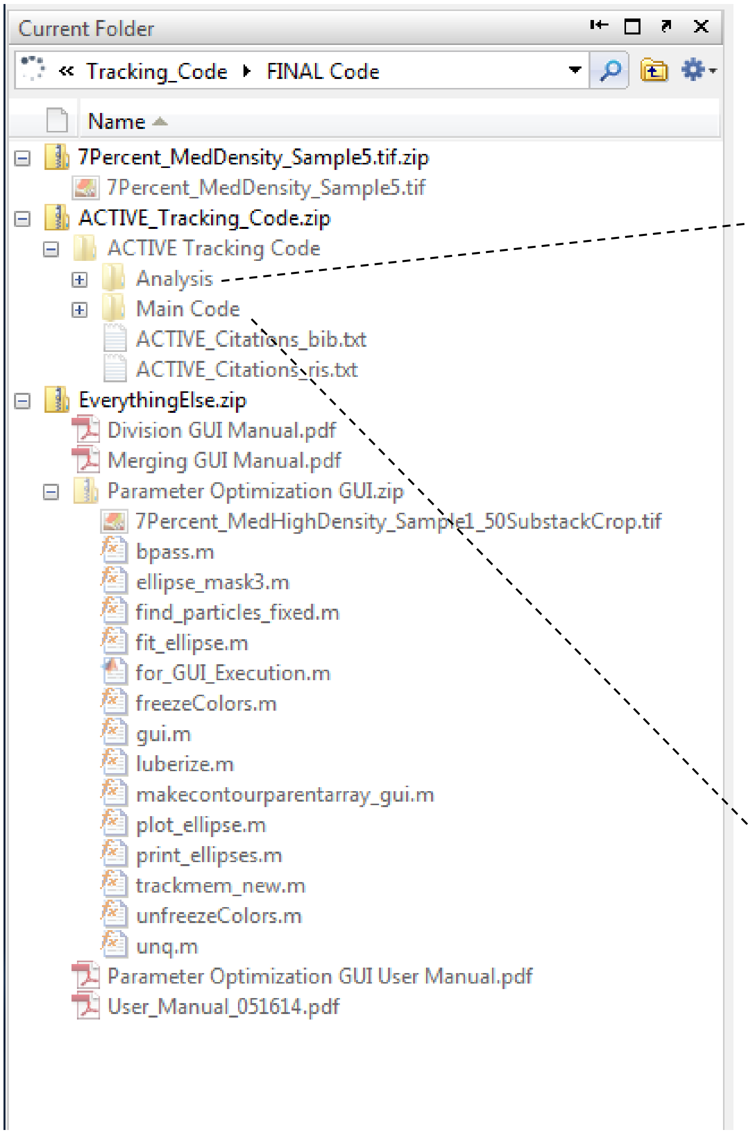

7Percent_MedDensity_Sample5.tif.zip
- 7Percent_MedDensity_Sample5.tif

ACTIVE_Tracking_Code.zip
- ACTIVE Tracking Code
  - Analysis
  - Main Code
  - ACTIVE_Citations_bib.txt
  - ACTIVE_Citations_ris.txt

EverythingElse.zip
- Division GUI Manual.pdf
- Merging GUI Manual.pdf
- Parameter Optimization GUI.zip
  - 7Percent_MedHighDensity_Sample1_50SubstackCrop.tif
  - bpass.m
  - ellipse_mask3.m
  - find_particles_fixed.m
  - fit_ellipse.m
  - for_GUI_Execution.m
  - freezeColors.m
  - gui.m
  - luberize.m
  - makecontourparentarray_gui.m
  - plot_ellipse.m
  - print_ellipses.m
  - trackmem_new.m
  - unfreezeColors.m
  - unq.m
- Parameter Optimization GUI User Manual.pdf
- User_Manual_051614.pdf

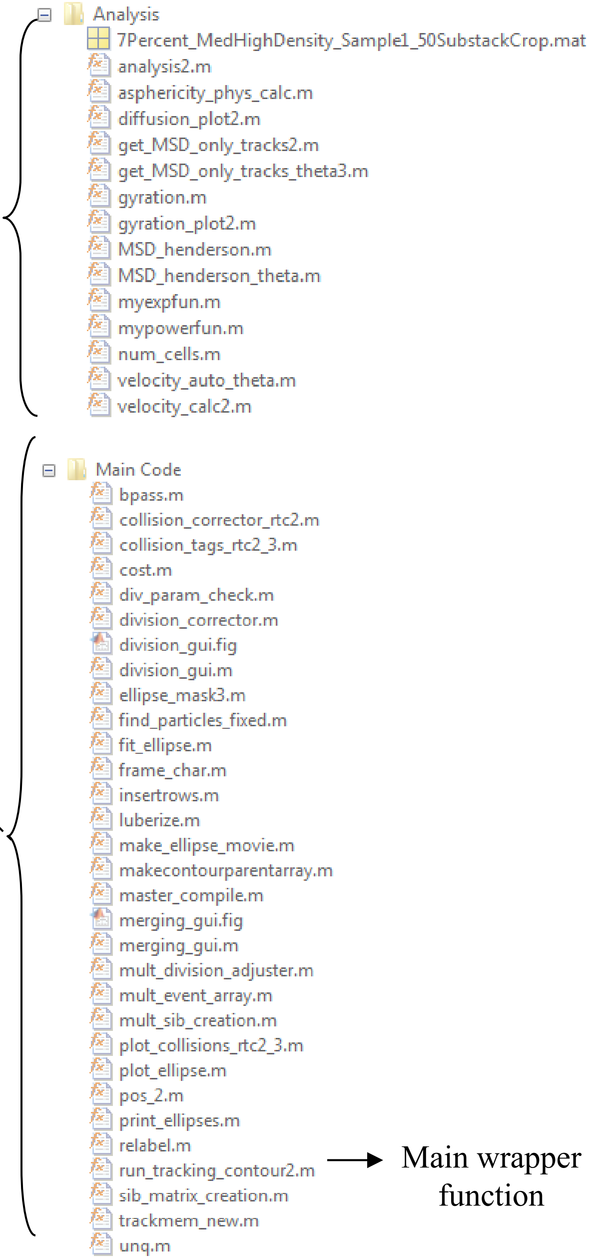

Analysis
- 7Percent_MedHighDensity_Sample1_50SubstackCrop.mat
- analysis2.m
- asphericity_phys_calc.m
- diffusion_plot2.m
- get_MSD_only_tracks2.m
- get_MSD_only_tracks_theta3.m
- gyration.m
- gyration_plot2.m
- MSD_henderson.m
- MSD_henderson_theta.m
- myexpfun.m
- mypowerfun.m
- num_cells.m
- velocity_auto_theta.m
- velocity_calc2.m

Main Code
- bpass.m
- collision_corrector_rtc2.m
- collision_tags_rtc2_3.m
- cost.m
- div_param_check.m
- division_corrector.m
- division_gui.fig
- division_gui.m
- ellipse_mask3.m
- find_particles_fixed.m
- fit_ellipse.m
- frame_char.m
- insertrows.m
- luberize.m
- make_ellipse_movie.m
- makecontourparentarray.m
- master_compile.m
- merging_gui.fig
- merging_gui.m
- mult_division_adjuster.m
- mult_event_array.m
- mult_sib_creation.m
- plot_collisions_rtc2_3.m
- plot_ellipse.m
- pos_2.m
- print_ellipses.m
- relabel.m
- run_tracking_contour2.m → Main wrapper function
- sib_matrix_creation.m
- trackmem_new.m
- unq.m

2. Unzip the file and place all of the functions into a new folder within a stable directory. Navigate to this directory within MATLAB and open the function file labeled run_tracking_contour_rtc2.m.

3. Right click (control click for Mac) on the "Main Code" folder and select "Add to Path" --> "Selected Folders" to add the main code to the current function path.
4. Initialize the run_tracking_contour_rtc2 function within MATLAB. This can be achieved by copying the following code into the command window and pressing enter (return on Macs):

   ```
   [ xyzs_id, xyzs_id_columns, filename, framerate, new_dir] =
   run_tracking_contour2(image_mat_in, inputfilename);
   ```

   *Note that both of the above lines contribute to the single function call.

   - Input variable image_mat_in: A [2,1] matrix used to specify contrast limits for the MATLAB imadjust function. An input of [0;1] will result in no contrast adjustment.
   - Input variable inputfilename: Text file name and location for executing batch processing mode (see section A1.2 below for more details). If this parameter is not included, the GUI will execute as detailed in #5 below.
5. A basic GUI window will pop up with a series of parameters that the user can manipulate. At the current time, these parameters must be manually adjusted. The default setting for these parameters is optimized for a C3H10T1/2 mouse fibroblast dataset with a cell density of 87,500 cells mL^{-1} stained at a Hoechst 33342 dye concentration of 0.01 μg mL^{-1}. Parameter details are described below:
   a. Plot Toggle: Determines whether individual frame images (contour and ellipse plots) are displayed. It is of note that turning on this functionality will produce two plots for each image assessed. For example, in a standard 480 frame tiff stack used in the tracking manuscript, this would result in 960 images produced. For most computers, this will result

in an error in MATLAB, due to insufficient memory. Thus, it is recommended that plot toggle is turned off, unless using a relatively small substack. Plotting individual images significantly increases run time (value of 1 = on, value of 0 = off). Plot Toggle can be used to look at segmentation results (both contour fitting and ellipse fitting), allowing a user to view how changing parameters affects segmentation.

b. Number of Contours: Maximum number of total contour levels into which a single cell's intensity profile can be sectioned. Note that the current tracking version uses a built-in MATLAB histogram stretching function (imadjust) to improve contour fitting. Increasing the number of contours in most cases improves segmentation at the cost of significantly increasing run time.

c. Half Particle Diameter: A half size measurement of a typical cell/object in pixels (must be an odd integer for image filtering purposes). Changing this parameter can be used to optimize segmentation. We found that a value slightly larger than the particle radius worked best for our experimental data.

d. Noise Wavelength: Characteristic noise value for each image (in pixels). This value can be changed to affect the bandpass filtering of the image and consequently the segmentation. Values of 1-3 typically work best.

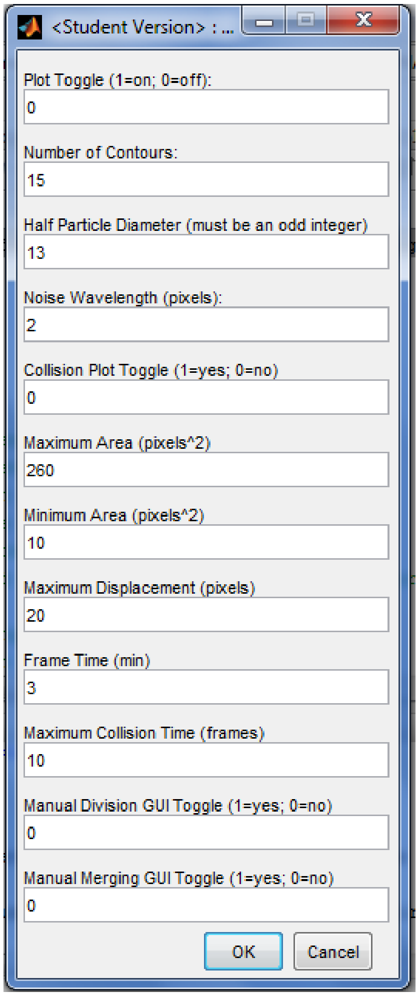

Plot Toggle (1=on; 0=off):
0

Number of Contours:
15

Half Particle Diameter (must be an odd integer)
13

Noise Wavelength (pixels):
2

Collision Plot Toggle (1=yes; 0=no)
0

Maximum Area (pixels^2)
260

Minimum Area (pixels^2)
10

Maximum Displacement (pixels)
20

Frame Time (min)
3

Maximum Collision Time (frames)
10

Manual Division GUI Toggle (1=yes; 0=no)
0

Manual Merging GUI Toggle (1=yes; 0=no)
0

e. Collision Plot Toggle: Determines whether collision event plots/videos are produced. Tracks for a subset of division/collision are produced (~10-15) depending on the total number of collisions identified by the code. These videos can be used to look at cell interactions before and after post-processing to evaluate if post-processing is correctly switching mislabeled cell IDs

f. Maximum Area: Maximum area threshold for a single cell. Particles with an area greater than this parameter are deleted.

g. Minimum Area: Minimum area threshold for a single cell. Particles with an area smaller than this parameter are deleted.

h. Maximum Displacement: Maximum distance a single particle moves, frame to frame (in pixels). This parameter is used for linking and larger values may lead to combinatorics issues. If the parameter leads to combinatorics issues, a warning message is displayed. A typical value is the diameter of an average cell.

i. Frame Time: Time step between two consecutive images (minutes), as defined during experimental capture of the image stack

j. Maximum Collision Time: Maximum time cells can be completely occluded during a merging event. This parameter is used to construct complete merging events during post-processing.

k. Division Toggle: Determines whether the user calls the manual division GUI. A value of 1 will call the GUI, a value of 0 will ignore the manual GUI processing (please see separate Division GUI user manual).

l. Merging Toggle: Determines whether the user calls the manual merging GUI. A value of 1 will call the GUI, a value of 0 will ignore the manual GUI processing (please see separate Merging GUI user manual).

The above parameters were set to the following values for all samples run in Chapter 2 and 3:

Parameter	**Value**
Plot Toggle	0
Number of Contours	15
Half Particle Diameter	13
Noise Wavelength	2
Collision Plot Toggle	0
Maximum Area	260
Minimum Area	10
Maximum Displacement	20 or 17*
Frame Time	3
Maximum Collision Time	10
Division Toggle	0
Merging Toggle	0

*All high density samples for the presented tracking paper were run with a maximum displacement of 17 pixels due to complex combinatorics issues preventing tracking completion or resulting in significantly increased run time. All low and medium density samples were run with a max displacement of 20 pixels.

As data is processed, the following should appear in the command window, indicating progression through the code:

1. A starting statement will appear, indicating that the code has initiated:

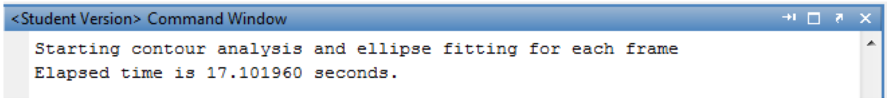

```
Starting contour analysis and ellipse fitting for each frame
Elapsed time is 17.101960 seconds.
```

2. Segmentation will then proceed, with each frame being processed individually. When contour profiling and ellipse fitting are complete, the total number of recognized cells will be recorded in the command window. A timer will additionally record the elapsed time for segmentation:

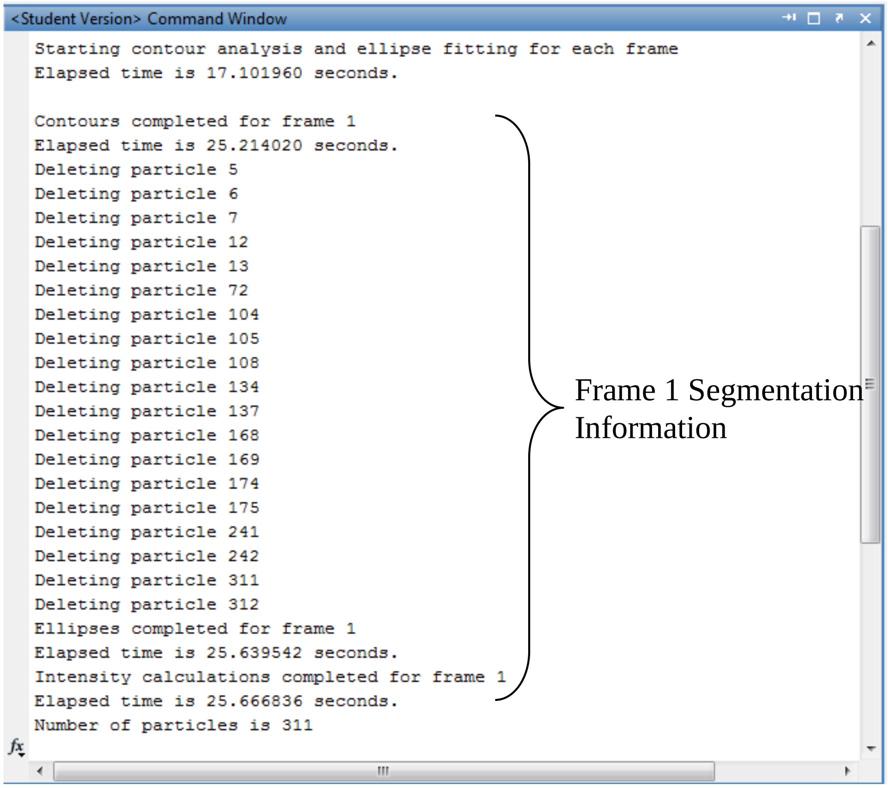

```
Starting contour analysis and ellipse fitting for each frame
Elapsed time is 17.101960 seconds.

Contours completed for frame 1
Elapsed time is 25.214020 seconds.
Deleting particle 5
Deleting particle 6
Deleting particle 7
Deleting particle 12
Deleting particle 13
Deleting particle 72
Deleting particle 104
Deleting particle 105
Deleting particle 108
Deleting particle 134
Deleting particle 137
Deleting particle 168
Deleting particle 169
Deleting particle 174
Deleting particle 175
Deleting particle 241
Deleting particle 242
Deleting particle 311
Deleting particle 312
Ellipses completed for frame 1
Elapsed time is 25.639542 seconds.
Intensity calculations completed for frame 1
Elapsed time is 25.666836 seconds.
Number of particles is 311
```

*Note: Segmentation is the most time-consuming portion of the code. A frame-by-frame breakdown is included to allow the user to estimate total run time

3. Once segmentation is complete, interacting and dividing cells will be identified and positional tracking will proceed:

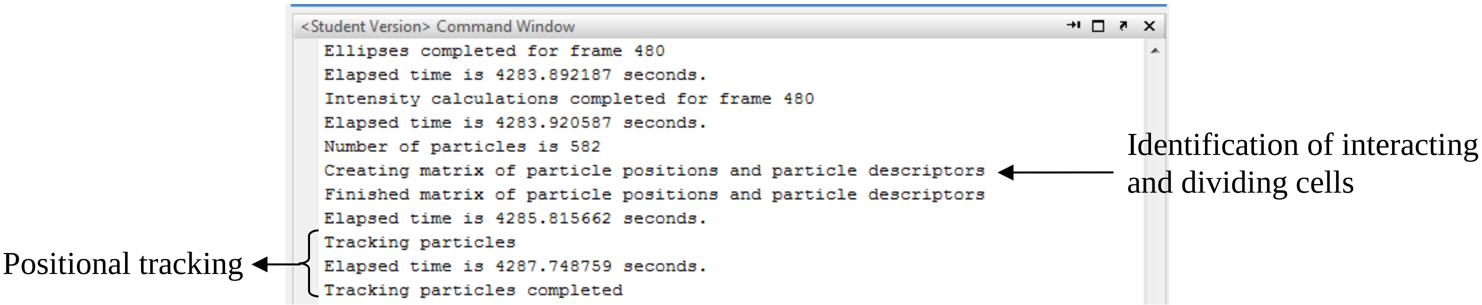

```
Ellipses completed for frame 480
Elapsed time is 4283.892187 seconds.
Intensity calculations completed for frame 480
Elapsed time is 4283.920587 seconds.
Number of particles is 582
Creating matrix of particle positions and particle descriptors
Finished matrix of particle positions and particle descriptors
Elapsed time is 4285.815662 seconds.
Tracking particles
Elapsed time is 4287.748759 seconds.
Tracking particles completed
```

4. The system will then proceed with merging event processing. This step will always include two-body interaction analysis. However, multi-cell interactions (complex merging events) will only be assessed if the manual merging GUI toggle was initialized by the user (see above).

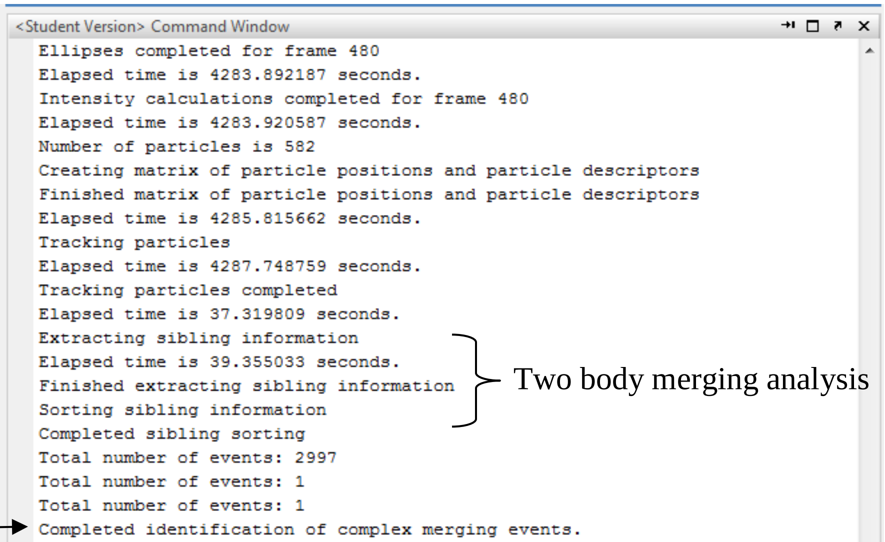

```
Ellipses completed for frame 480
Elapsed time is 4283.892187 seconds.
Intensity calculations completed for frame 480
Elapsed time is 4283.920587 seconds.
Number of particles is 582
Creating matrix of particle positions and particle descriptors
Finished matrix of particle positions and particle descriptors
Elapsed time is 4285.815662 seconds.
Tracking particles
Elapsed time is 4287.748759 seconds.
Tracking particles completed
Elapsed time is 37.319809 seconds.
Extracting sibling information
Elapsed time is 39.355033 seconds.
Finished extracting sibling information
Sorting sibling information
Completed sibling sorting
Total number of events: 2997
Total number of events: 1
Total number of events: 1
Completed identification of complex merging events.
```

Two body merging analysis

Complex merging analysis

5. Division processing is the final component of the system. In addition to a statement in the command window indicating completion of the division processing, a contour plot of cells identified in the final image frame will appear in a separate window:

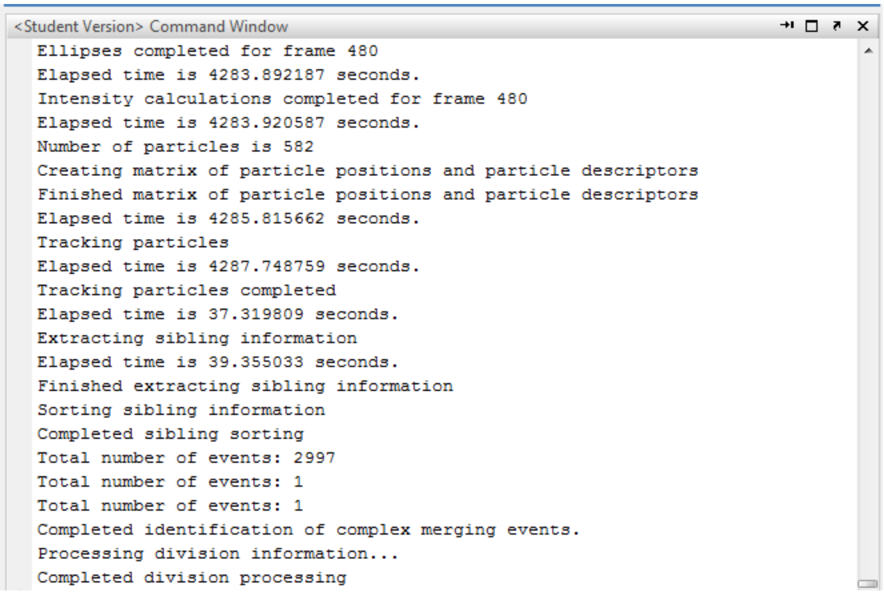

```
Ellipses completed for frame 480
Elapsed time is 4283.892187 seconds.
Intensity calculations completed for frame 480
Elapsed time is 4283.920587 seconds.
Number of particles is 582
Creating matrix of particle positions and particle descriptors
Finished matrix of particle positions and particle descriptors
Elapsed time is 4285.815662 seconds.
Tracking particles
Elapsed time is 4287.748759 seconds.
Tracking particles completed
Elapsed time is 37.319809 seconds.
Extracting sibling information
Elapsed time is 39.355033 seconds.
Finished extracting sibling information
Sorting sibling information
Completed sibling sorting
Total number of events: 2997
Total number of events: 1
Total number of events: 1
Completed identification of complex merging events.
Processing division information...
Completed division processing
```

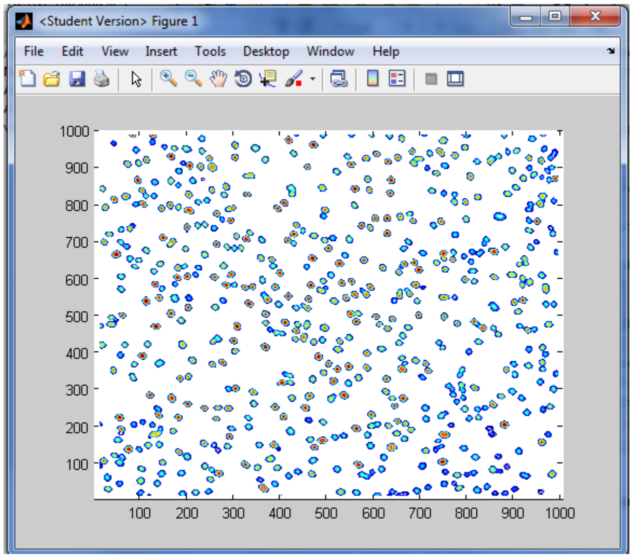

Once processing is complete, a .mat file will appear, saved as the same filename of the tiff stack used. This .mat file includes the following information:

A. ***xyzs_id***: the main output matrix containing all cell information stored for all frames. For the current version of ACT*IV*E, xyzs_id contains the following column outputs:

    1. x-position: the x-position for the center of mass of a cell in a specific frame
    2. y-position: the y-position for the center of mass of a cell in a specific frame
    3. major axis: long-axis length of the fitted cell ellipse
    4. minor axis: short-axis length of the fitted cell ellipse
    5. theta/angle information: positional orientation of the fitted cell ellipse (-3/4*pi to 3/4*pi)
    6. area: calculated area of the fitted ellipse
    7. intensity: calculated intensity for the fitted ellipse
    8. multi-body interaction flag: flag to determine if a cell participates in a 3+ cell merging event
    9. a sibling cell tag for within a specific frame (used for sibling identification)
    10. a sibling cell tag for overall particles (used for matching cell sibling IDs)
    11. an individual reference number for each cell in all frames (used for matching cell sibling IDs)
    12. frame number
    13. cell identification tag

14. overall color number reference for colored ellipse plotting
15. color number reference tailored to Matlab's pre-set color system
16. original cell ID before relabeling

B. ***xyzs_id_columns*****:** the column number in xyzs_id containing cell IDs after linking

C. t_matrix: Same outputs as xyzs_id (columns 1-12), prior to linking; full cell information matrix resulting from segmentation portion only. This matrix can be used to adjust linking parameters (e.g., Max Displacement).

D. frame_avg:

1. Average major axis value per frame
2. Average minor axis value per frame
3. Average aspect ratio pre frame
4. Average angle of orientation of cells per frame
5. Average area of cells per frame
6. Average integrated intensity of cells per frame
7. Average intensity of cells per frame

E. event_array:

1. Cell 1 index into xyzs_id
2. Cell 1 ID

3. Cell 2 ID
4. Frame
5. Color number reference (relates to columns 13/14 in xyzs_id)
6. Type of collision (division, collision, or continuing collision only)
7. Index used to build the event array
8. Event number
9. Cell 2 index into xyzs_id

F. ***event_array2:*** An updated event_array (same information as above), with cell IDs in the events updated post division-correction

A1.1.5 Code to Plot Tracks (Separate Analysis)

Users may plot track information separately without additional analysis by executing the following code after loading a .mat file processed by ACT*IV*E:

```
% Local parameters
frameindx = 12;
cellindx = 13;
plot_toggle = 1;

nframes = max(xyzs_id(:,frameindx));
ncells = max(xyzs_id(:,cellindx));
```

```
% initialization
if plot_toggle ==1
    figure(1);
    cmap = colormap(lines(ncells));
end
ltracks = zeros(ncells,1);
xpos = zeros(ncells,nframes);
ypos = zeros(ncells,nframes);
zpos = zeros(ncells,nframes);


% Plot tracks
for i=1:ncells
    %boolean matrix identifying all cells with id i
    boolcell = (xyzs_id(:,cellindx) == (i));
    ltracks(i) = nnz(boolcell); % length of that track
    if plot_toggle ==1
        hold on;
        plot(xyzs_id(boolcell,1),xyzs_id(boolcell,2), '-
','Linewidth',2,'Color',cmap(i,:));
    end


    xpos(i,xyzs_id(boolcell,frameindx)) = xyzs_id(boolcell,1);
    ypos(i,xyzs_id(boolcell,frameindx)) = xyzs_id(boolcell,2);
    %zpos(i,xyzs_id(boolcell,9)) = xyzs_id(boolcell,3);
end
```

Cell tracks will be displayed as individual lines, where each color represents a single track. An example output is shown below:

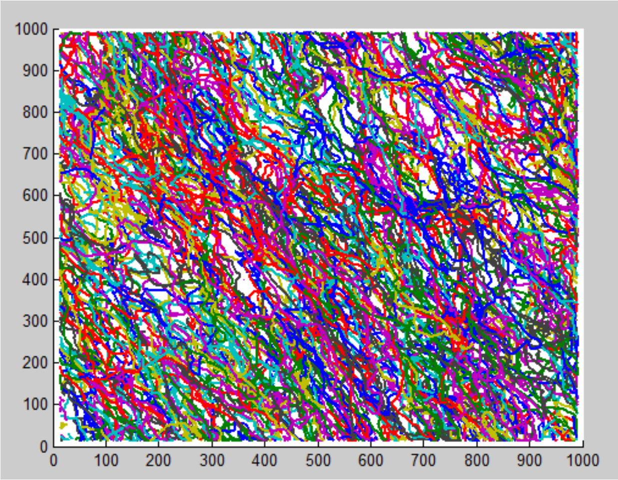

A1.1.6 Detailed Analysis Instructions

1. Additional analyses can be directly processed after running run_tracking_contour2.m and storing the output, or from loading the .mat file saved after running run_tracking_contour2.m
2. Right click (control click for Mac) on the "Analysis" folder and select "Add to Path" --> "Selected Folders" to add the analysis code to the current function path.
3. Within the "Analysis" folder, place all of the .mat files that the user wishes to assess.

   ***Please note that the analysis function requires the .mat files from ACT*IV*E to be contained within the same folder as the analysis function. Any additional .mat files existing in this folder will result in an error in the system. ***

File directory breakdown for Analysis code:

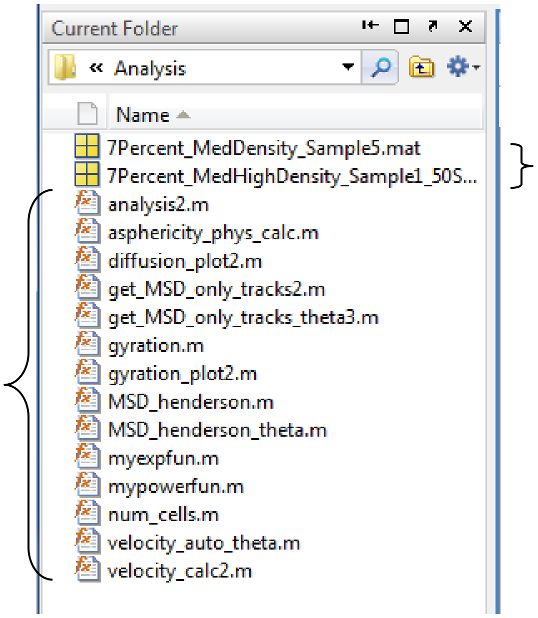

7Percent_MedDensity_Sample5.mat
7Percent_MedHighDensity_Sample1_50S...
analysis2.m
asphericity_phys_calc.m
diffusion_plot2.m
get_MSD_only_tracks2.m
get_MSD_only_tracks_theta3.m
gyration.m
gyration_plot2.m
MSD_henderson.m
MSD_henderson_theta.m
myexpfun.m
mypowerfun.m
num_cells.m
velocity_auto_theta.m
velocity_calc2.m

Samples to be processed

Code required to run analysis

4. Input parameters should then be initialized:
   a. angle_vec: a vector of angle values (in radians), specifying sample anisotropy for each of the .mat files. Angle values should be entered into the angle_vec in the same order they appear in the directory window (alphabetically by .mat file name). Note: a value of 0 should be input if a substrate is isotropic.
   b. plot_toggle: a toggle indicating whether the user would like to save/display plots generated during the analysis. A value of 1 will display plots; a value of 0 will not display plots.

5. The main code for the correlation analyses is analysis2.m This function runs the MSD, velocity auto-correlation, diffusion plot generation, and cell track asphericity calculations. The call to the function is:

```
analysis2(angle_vec, plot_toggle)
```

6. Call the function with the appropriate parameters specified.

Once processing is complete, a .mat file will appear, saved as the name 'Final_Analysis.mat' located in a new folder in the directory with the original .mat file from run_tracking_contour2. This .mat file includes the following information:

A. ***MSD_mat:*** cell array with the first row of cells containing parameter labels and the second row containing the parameter values for the MSD analysis. The columns of the cell array are:
    1. Short timescale slope
    2. Long timescale slop
    3. Mobility parameter (Intercept of line fit to long timescale data)

B. ***Angle_vec*****:** angle vector used by the analysis code to process the .mat files.

C. ***Decomp_MSD_mat:*** cell array with the first row of cells containing parameter labels and the second row containing the parameter values for the decomposed MSD analysis. The columns of the cell array are:
    1. X-Short timescale slope
    2. X-Long timescale slope

3. X-Mobility parameter
4. Y-Short timescale slope
5. Y-Long timescale slope
6. Y-Mobility parameter

D. ***output_list:*** matrix displaying final MSD, velocity autocorrelation, and asphericity parameters (with labels) for all samples analyzed. A comparable Excel file will also be generated in the analysis directory.

E. ***vel_MAT:*** cell array with the first row of cells containing parameter labels and the second row containing the coefficients of the exponential decay fit for the velocity auto-correlation analysis. The columns of the cell array are:

1. X-Amplitude
2. X-Decay constant
3. X-Offset
4. Y-Amplitude
5. Y-Decay constant
6. Y-Offset
7. X- and Y-Decay constant difference

Along with saving a .mat file containing the parameter values, the following plots will be generated and saved if plot_toggle is turned on: (Note all plots will be saved to a new folder that is created in the new_dir path)

8. filename_full_tracks: This is a plot of all cell tracks
9. filename_full_alpha: This is a semilog plot of the Gaussian parameter alpha v time for the complete MSD analysis.
10. filename_full_MSD: This is a log10 MSD v. log10 Δt plot containing lines fit to the short timescale and long timescale data of the MSD profiles.
11. filename_MSD_decomp: This is a log10 MSD v. log10 Δt plot containing lines fit to the short timescale and long timescale data for both the x and y direction MSD profiles.
12. filename_alpha_power_fit: This is a semilog plot of the Gaussian parameter alpha v time, for both the x and y directions, for the decomposed MSD analysis. This plot also contains power law fits to the alpha traces.
13. filename_alpha_no_fit: This is a semilog plot of the Gaussian parameter alpha v time, for both the x and y directions, for the decomposed MSD analysis. This plot also does not contain power law fits to the alpha traces.
14. filename_velocity: This is a plot of the velocity auto-correlation v. Δt in both the x and y directions. An exponential decay is fit to each trace and the fit coefficients displayed.
15. filename_gyration_plot: This is a plot of the terminal cell positions, with respect to a common origin, rotated by the principle eigenvecter direction for each cell track. The anisotropy of the terminal positions is directly proportional to track asphericity.

16. filename_diffusion_plot: This is a plot of the terminal cell positions for all cells with respect to a common origin. The anisotropy of the terminal positions qualitatively shows the degree of collective anisotropic cell motility.
17. Diffusion and gyration tiff plots: In a new folder in this same directory, a series of tiff images containing the cell positions from (8) and (9) above for each frame, rather than terminal position, is saved. From these images videos can be generated to show how the cells diffuse and track asphericity develops as a function of time.

A test stack, 7Percent_MedHighDensity_Sample1_50SubstackCrop.mat, has been included to test the code.

A1.1.7 Acknowledgements

The ACT*IV*E approach builds upon IDL code written by Timon Idema and colleagues for segmentation [1] and code initially written by John Crocker in IDL [2] and updated for execution in MATLAB by Maria Kilfoil for linking [3]. Cell division and merging event identification, as well as the post-processing and analysis code, are original to the ACT*IV*E system.

A1.2 Example Text File for Batch Processing

To operate ACT*IV*E in batch processing mode, the user must create a new text (.txt extension) file specifying the input parameters required to operate ACT*IV*E. The body of an example text file is shown below:

```
15          Contour Levels
13          Half Particle Diameter
2           Noise Wavelength
0           Collision Plot Toggle
260         Particle Area Thresh
10          Min Area
20          Max Displacement
3           Time Btwn Frames
1           Sibling Toggle
E:\BMMB\Active_SMP_24hr_30_to_37C_95_5_tBA_BA_111215\Tiff_Stacks\A_S1_Pos1.ti
f    Filename
```

The numerical values shown above are identical to the operating parameters described in Table 2.1. Of note, all of the graphical user interface (GUI) related features, such as the plot or GUI toggles, are not specified in batch processing mode, as no output display will be generated by the system. One additional input is required for batch processing: the file location for the Tiff stack to be processed. In all of the specified parameters above, the text following the numerical or file name is interchangeable; the system will process all of the text following the input identically. Each new numerical entry must be entered on a new line within the text body in order for the system to read the file appropriately.

A1.3 References

1. Idema, T., et al., *Wavefronts and Mechanical Signaling in Early Drosophila Embryos.* Biophysical Journal, 2013. **104**(2): p. 329A-329A.
2. Crocker, J.C. and D.G. Grier, *Methods of digital video microscopy for colloidal studies.* Journal of Colloid and Interface Science, 1996. **179**(1): p. 298-310.
3. Gao, Y. and M.L. Kilfoil, *Accurate detection and complete tracking of large populations of features in three dimensions.* Optics Express, 2009. **17**(6): p. 4685-4704.

Appendix 2: Expanded Analysis of Combined Morphometric and Motility Data for Cell Subpopulation Identification

A2.1 Expanded Analysis: Clustering Combined Morphometric and Motility Features

Results from the combined morphometric and motility clustering analysis were briefly detailed in **Chapter 6**. Here, the analysis was expanded to demonstrate the subpar classification identified in **Chapter 6**, Section 6.4.4. As with the individual morphometric and motility data, PCA analysis was first used to determine features for PAM clustering. As shown in Table A2-1, three principle components were selected to achieve the 75% variance cut-off established for the co-culture and EC monocultures; in the case of the SMC monocultures, four components were instead required. When further analyzing the features by dimension, all of the parameters, except for the aspect ratio, were included for the co-culture and EC monocultures (Table A2-2). The fourth dimension for the SMC monoculture expanded the PAM clustering to include all of the original features. For all experimental conditions analyzed, the nuclear major axis, nuclear minor axis, nuclear area, and nuclear intensity contributed to the majority of the variance in the first dimension, the x-velocity, y-velocity, and speed contributed to the majority of the variance in the second dimension, and the directionality ratio and the asphericity contributed to the majority of the variance in the third dimension. In the case of the SMC monoculture, the aspect ratio was the primary contributor to the variance for the fourth dimension.

PAM clustering revealed that co-culture, SMC monoculture, and EC monoculture replicates should be clustered into 2, 2, and 2 subpopulations (medians presented, Table A2-3). This corresponded to average silhouette widths of 0.24 ± 0.013, 0.21 ± 0.04, and 0.23± 0.0047 respectively for the EC and SMC co-culture, SMC monoculture, and EC monoculture groups. All of the average silhouette width values fell below the “weak” structure range for the combined morphometric and motility features. This indicated that expanding the clustering analysis to include mixed features convoluted clustering capabilities. This is particularly apparent in the point by point two dimensional cluster plots, where multiple subpopulations overlapped and sometimes fully encased one another. (Figure A2-1). Silhouette plots by subpopulation further confirmed this trend, as most of the values for clustering effectiveness fell below 0.25 (Figure A2-2).

Smooth muscle cell monocultures demonstrated the most variability in subpopulation number, with 2, 2, and 6 clusters identified for replicates one, two, and three respectively. Silhouette width values were extremely poor for the SMC monoculture data: replicate one consisted of 209 (silhouette = 0.13) and 109 cells (silhouette = 0.0.23) in subpopulations 1 and 2 respectively, replicate two consisted of 300 (silhouette = 0.25) and 119 cells (silhouette = 0.27) in subpopulations 1 and 2 respectively, and replicate three consisted of 20 (silhouette = 0.20), 47 (silhouette = 0.16), 18 (silhouette = 0.0.26), 39 (silhouette = 0.28), 18 (silhouette = 0.13), and 30 cells (silhouette = 0.01) in subpopulations 1, 2, 3, 4, 5, and 6 respectively. Feature plots revealed similar trends to the individual morphometric and motility data sets (Figure A2-3). In general, the nuclear morphology features (nuclear major axis, nuclear minor axis, nuclear area, and nuclear intensity) and the track shape features (directionality ratio and asphericity) were most important in categorizing the identified cell subpopulations.

In regards to the EC monoculture data, all technical replicates showed significant overlap in cluster identification (Figure A2-1). In particular, replicates one and two showed one fully encased cluster in the two dimensional plots, signifying that the combined morphometric and motility data complicated cluster identification. Even though two subpopulations were identified for each replicate in the EC monoculture groups, silhouette width values were in the artificial range for at least one of the two subpopulations in each group. Replicate one had 47 (silhouette = 0.41) and 169 (silhouette = 0.19) cells in clusters 1 and 2 respectively, replicate two had 260 (silhouette = 0.22) and 225 cells (silhouette = 0.25) in clusters 1 and 2 respectively, while replicate three had 84 (silhouette = 0.14) and 107 cells (silhouette = 0.30) in clusters 1 and 2 respectively. Feature plots of the combined morphometric and motility averages by cluster further showed that the cell track features (directionality ratio and asphericity) were the only characteristics that consistently demonstrated differences that would lead to cluster differentiation (Figure A2-4). Replicate 3 showed some additional differences in the nuclear morphometric parameters (nuclear major axis, nuclear minor axis, nuclear area, and nuclear intensity), as well as the movement rate parameters (x-velocity, y-velocity, and speed).

Co-culture PAM analysis of the combined morphometric and motility parameters revealed that all three replicates were clustered into two groups. Just as with the monoculture data, two dimensional plots of the point by point combined co-culture clustering revealed substantial overlap between the subpopulations identified (Figure A2-1). In regards to the individual replicates, replicate one was split into subpopulation 1 (249 cells, silhouette = 0.30), which contained 89.86% ECs and 10.14% SMCs, and subpopulation 2 (256 cells, silhouette = 0.20), which contained 89.33% ECs and 10.67% SMCs. Replicate two consisted of subpopulation 1 (255 cells, silhouette = 0.21) with 69.33% ECs and 30.67% SMCs and subpopulation 2 (343 cells, silhouette = 0.27) with 41.67% ECs and 58.33% SMCs. Replicate three was very similar to replicate two, with one subpopulation (216 cells, silhouette = 0.27) of 47.15% ECs and 52.85% SMCs, compared to subpopulation 2 (197 cells, silhouette = 0.18) with 72.78% ECs and 27.22% SMCs. Similar to the motility only data, feature plots for the combined analysis revealed that clustering was based predominantly on cell movement rate and track shape features (Figure A2-5). However, poor overall clustering limits conclusions drawn from the combined data. Overall, performance of PAM clustering on the dual morphometric and motility parameters complicated clustering effectiveness, leading to poor subpopulation identification in the mono and co-culture data. We conclude that, in order to more effectively determine trends, feature types should either be considered separately or more stringent feature inclusion parameters should be predetermined to minimize the number of features utilized for more accurate and effective clustering.

Table A2-1: Average eigenvalue and variance PCA for the combined morphometric and motility co-culture and monoculture SMC and EC data

		Eigenvalue	**Percentage of Variance (%)**	**Cumulative Percentage of Variance (%)**
Co-Culture	*Component 1*	3.77 ± 0.14	37.70 ± 1.42	37.70 ± 1.42
	Component 2	2.57 ± 0.09	25.65 ± 0.93	63.36 ± 1.19
	Component 3	1.46 ± 0.01	14.59 ± 0.14	77.95 ± 1.32
SMC Monoculture	*Component 1*	3.46 ± 0.15	34.62 ± 1.53	34.62 ± 1.53
	Component 2	2.52 ± 0.05	25.19 ± 0.54	59.81 ± 1.49
	Component 3	1.42 ± 0.04	14.20 ± 0.42	74.01 ± 1.33
	Component 4	1.26 ± 0.05	12.56 ± 0.52	86.57 ± 1.05
EC Monoculture	*Component 1*	3.63 ± 0.04	36.30 ± 0.41	36.30 ± 0.41
	Component 2	2.76 ± 0.01	27.62 ± 0.07	63.92 ± 0.45
	Component 3	1.45 ± 0.04	14.53 ± 0.44	78.45 ± 0.08

Table A2-2: Combined morphometric and motility co-culture and monoculture feature contributions by PCA dimension (averaged across all replicates)

	Co-culture			**SMC Monoculture**				**EC Monoculture**		
	Dim 1 (%)	**Dim 2 (%)**	**Dim 3 (%)**	**Dim 1 (%)**	**Dim 2 (%)**	**Dim 3 (%)**	**Dim 4 (%)**	**Dim 1 (%)**	**Dim 2 (%)**	**Dim 3 (%)**
Major	21.48 ± 2.14	3.73 ± 1.95	1.24 ± 0.75	23.99 ± 0.96	0.78 ± 1.07	3.11 ± 1.90	6.83 ± 0.23	23.37 ± 1.07	1.01 ± 0.62	0.67 ± 0.47
Minor	18.53 ± 0.84	2.78 ± 2.04	0.02 ± 0.01	20.85 ± 1.97	1.59 ± 0.06	6.14 ± 5.31	9.61 ± 5.19	19.73 ± 1.36	3.99 ± 2.63	1.44 ± 1.60
AR	2.69 ± 1.96	0.82 ± 0.82	2.35 ± 1.59	2.42 ± 1.71	1.17 ± 0.96	21.20 ± 13.7	45.17 ± 12.6	1.15 ± 1.29	2.45 ± 3.27	5.64 ± 6.10
Area	22.31 ± 2.59	4.65 ± 2.51	0.72 ± 0.32	27.11 ± 0.20	1.07 ± 1.15	0.34 ± 0.25	0.17 ± 0.17	25.06 ± 0.61	2.18 ± 0.89	0.18 ± 0.13
Intensity	19.46 ± 2.66	1.98 ± 1.09	0.05 ± 0.06	20.65 ± 1.95	0.95 ± 0.77	1.54 ± 2.05	1.78 ± 1.96	22.20 ± 0.49	1.35 ± 0.61	0.01 ± 0.01
X-Vel	3.91 ± 2.13	26.95 ± 2.05	0.84 ± 0.05	1.20 ± 1.25	27.71 ± 0.36	0.49 ± 0.28	0.66 ± 0.24	2.15 ± 1.04	28.40 ± 1.95	0.54 ± 0.63
Y-Vel	4.10 ± 2.29	26.58 ± 2.34	0.38 ± 0.23	0.83 ± 0.86	27.31 ± 0.19	0.21 ± 0.13	1.38 ± 0.73	2.59 ± 1.09	27.58 ± 2.83	0.07 ± 0.06
Speed	4.58 ± 2.58	31.48 ± 2.82	0.88 ± 0.21	1.30 ± 1.40	37.36 ± 1.99	0.15 ± 0.11	0.55 ± 0.47	2.74 ± 1.34	31.95 ± 2.23	0.29 ± 0.19
DR	2.09 ± 0.56	0.08 ± 0.02	44.72 ± 1.88	0.86 ± 0.5	1.54 ± 0.44	37.59 ± 6.78	10.51 ± 4.50	0.22 ± 0.09	0.74 ± 0.46	46.22 ± 5.00
Aspher.	0.85 ± 0.47	0.96 ± 0.40	48.80 ± 1.22	0.79 ± 0.57	0.53 ± 0.48	29.23 ± 14.1	23.33 ± 16.4	0.78 ± 0.53	0.35 ± 0.35	44.93 ± 3.22

Highlighting indicates features with a majority percentage selected from each dimension for clustering analysis. Columns from top to bottom: 1) Nuclear Major Axis, 2) Nuclear Minor Axis, 3) Nuclear Aspect Ratio, 4) Nuclear Area, 5) Nuclear Intensity, 6) X-Velocity, 7) Y-Velocity, 8) Speed, 9) Directionality Ratio, and 10) Asphericity

Table A2-3: Silhouette width analysis for combined morphometric and motility co-culture and monoculture cell data (averaged across all replicates)

	Median Number of Clusters Identified	**Average Silhouette Width**	**Average Number of Cells Analyzed**
Co-Culture	2	0.24 ± 0.013	505 ± 75
SMC Monoculture	2	0.21 ± 0.04	303 ± 101
EC Monoculture	2	0.23± 0.0047	297 ± 133

Figure A2-1: PAM clustering of co-culture and monoculture combined morphometric and motility features

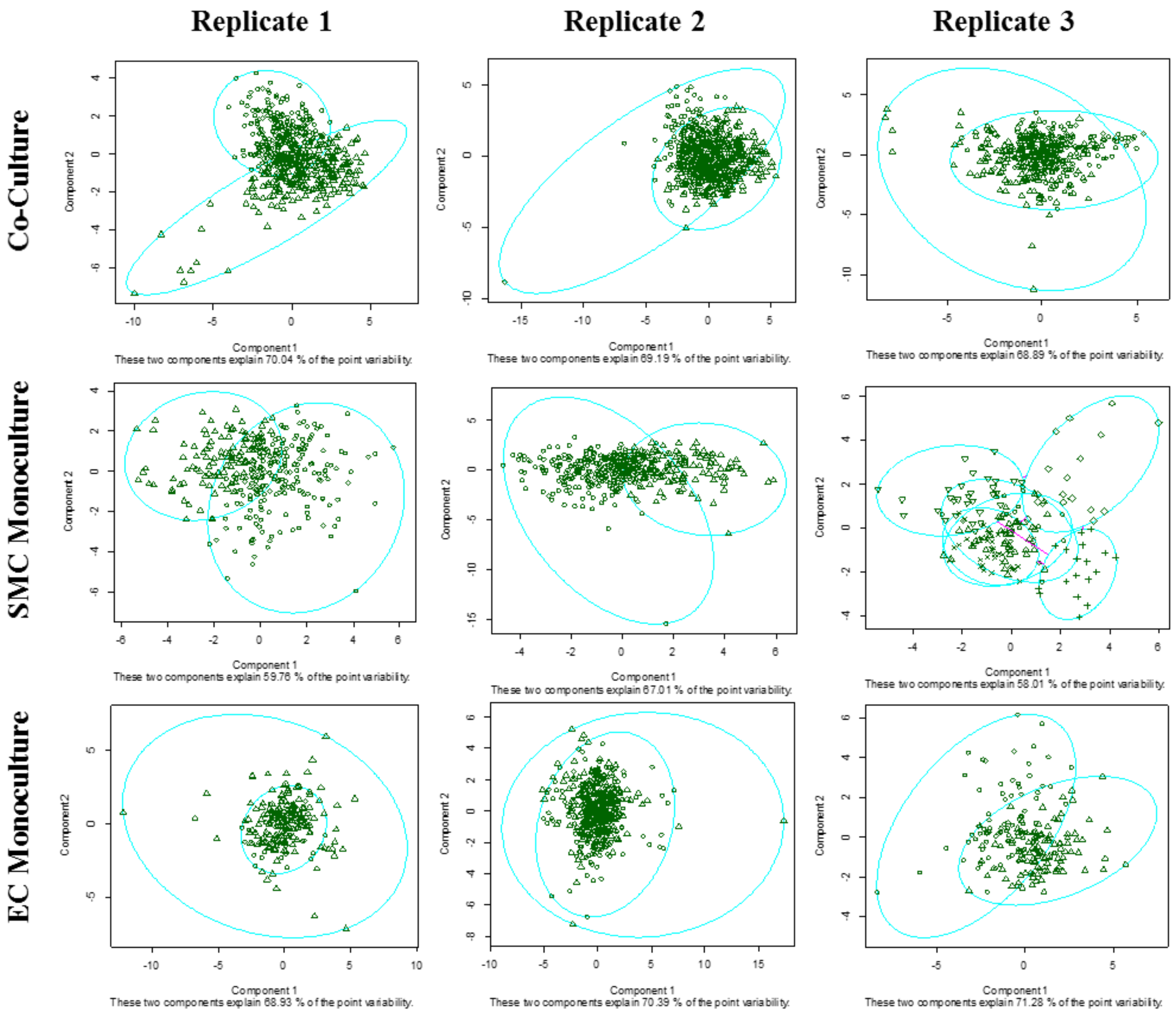

Two dimensional plots of PAM clustering of EC and SMC co-culture (top row), SMC monoculture (middle row), and EC monoculture (bottom row) combined morphometric and motility data for replicates 1 (left), 2 (middle), and 3 (right). In general, two subpopulations were observed irrespective of culture condition, with significant overlap between clusters observed.

Figure A2-2: Silhouette plots for combined morphometric and motility co-culture and monoculture data

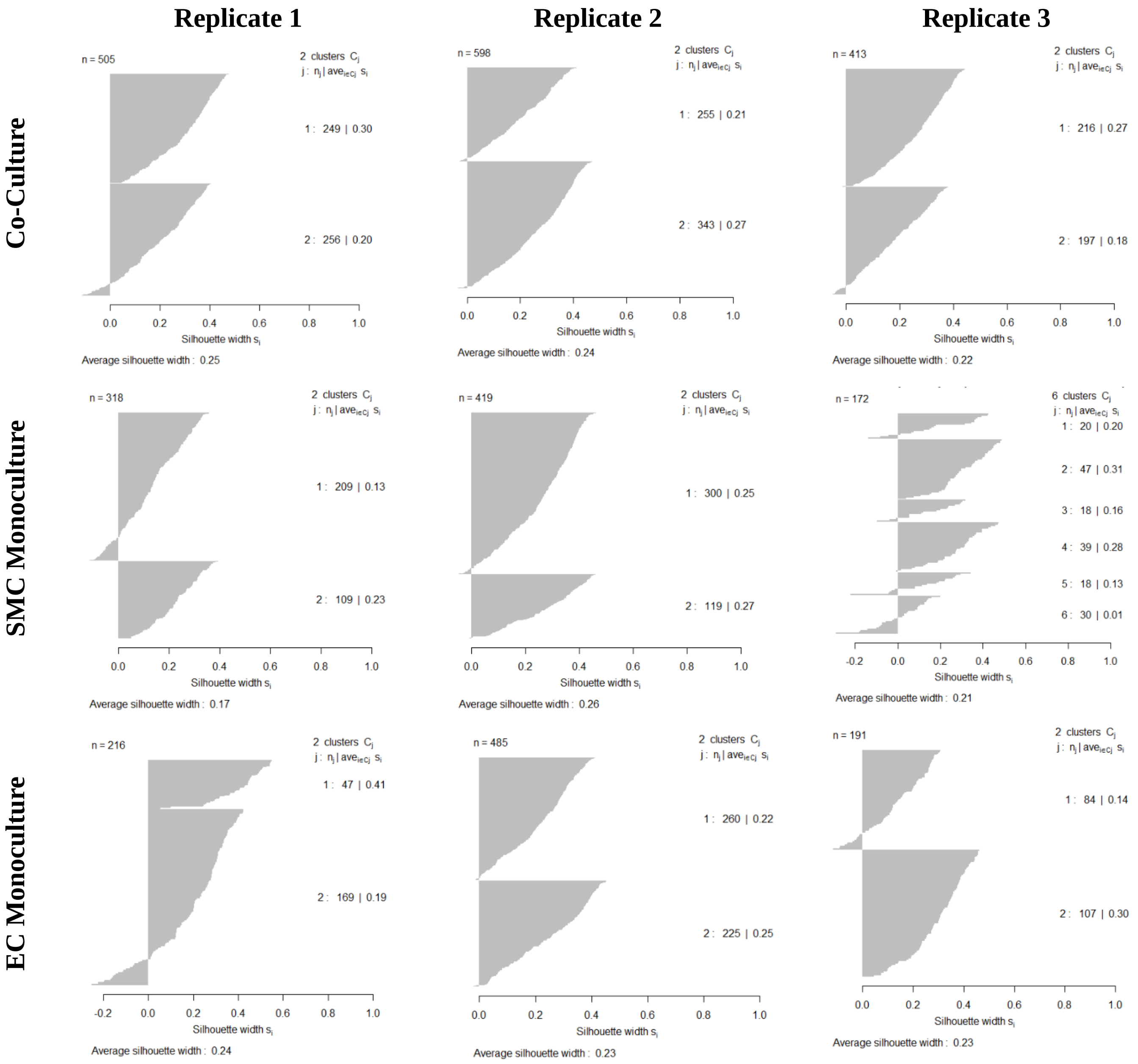

Silhouette plots for the EC and SMC co-culture (top), SMC monoculture (middle), and EC monoculture (bottom) revealed subpar or artificial clustering for the majority of the subpopulation groups identified in the combined morphometric and motility clustering.

Figure A2-3: SMC monoculture combined morphometric and motility average feature breakdown by clustering subpopulation

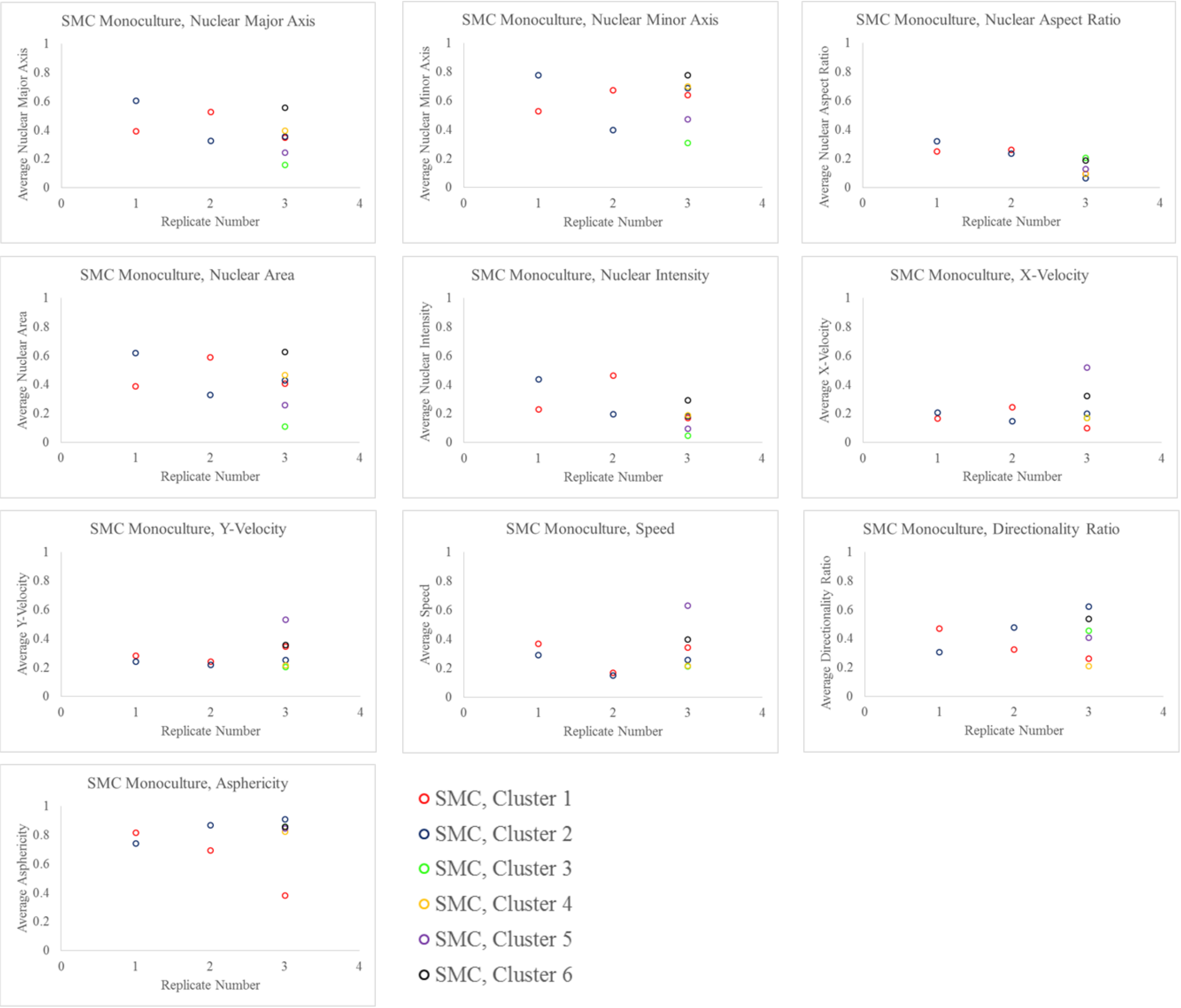

Cell feature averages were plotted for each subpopulation in the SMC monoculture to reveal overarching trends in the combined morphometric and motility data. Overall, the nuclear major axis, nuclear minor axis, nuclear area, nuclear intensity and track shape parameters showed noticeable differences between cluster averages, indicating that these features were important for cluster classification

Figure A2-4: EC monoculture combined morphometric and motility average feature breakdown by clustering subpopulation

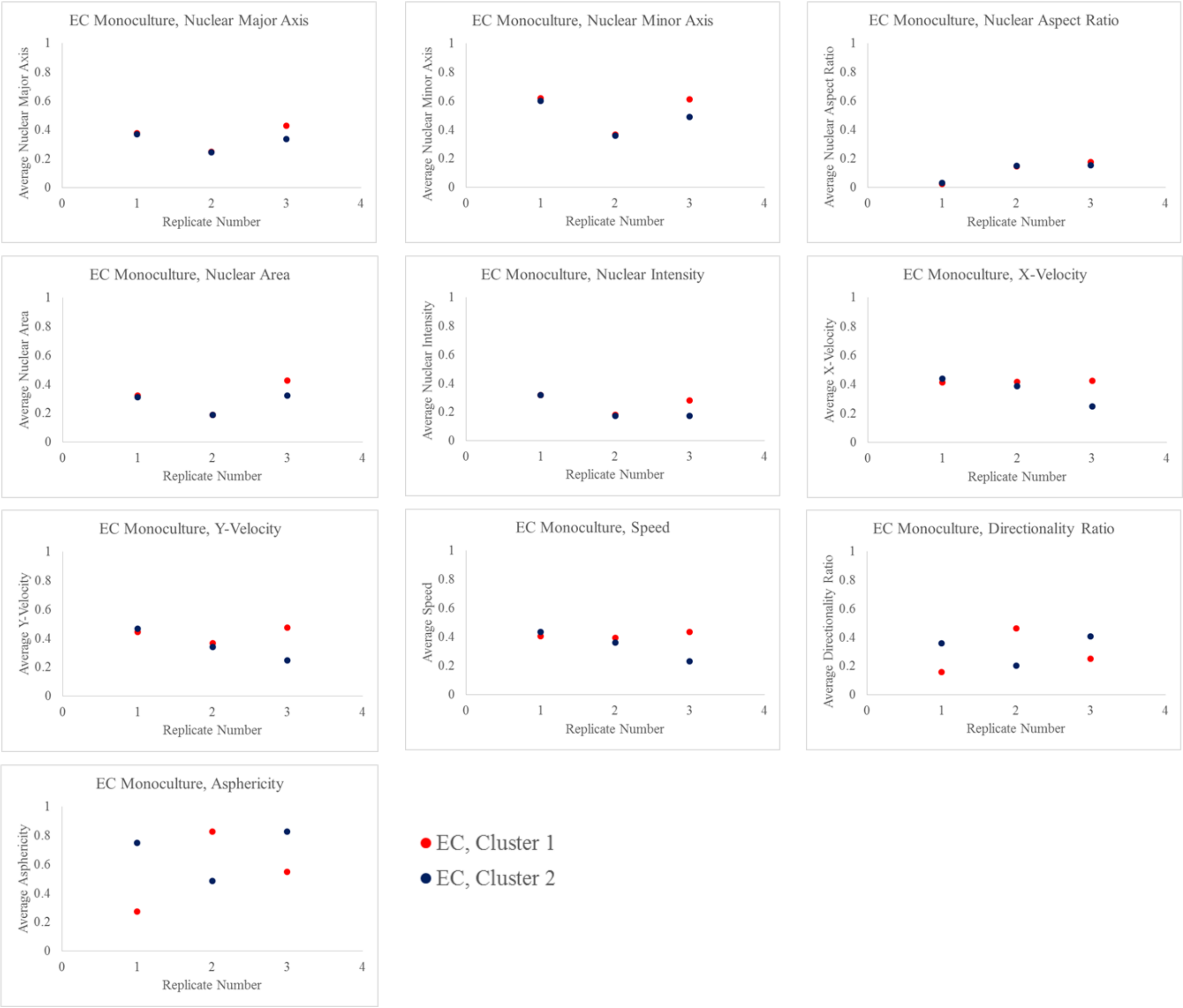
EC Monoculture, Nuclear Major Axis

EC Monoculture, Nuclear Minor Axis

EC Monoculture, Nuclear Aspect Ratio

EC Monoculture, Nuclear Area

EC Monoculture, Nuclear Intensity

EC Monoculture, X-Velocity

EC Monoculture, Y-Velocity

EC Monoculture, Speed

EC Monoculture, Directionality Ratio

EC Monoculture, Asphericity

Cell feature averages were plotted for each subpopulation in the EC monoculture to reveal overarching trends in the morphometric data. Unlike the SMC monoculture data, the track shape parameters were the only features that showed noticeable differences between cluster averages, indicating that these two features were important for cluster classification.

Figure A2-5: Co-culture combined morphometric and motility average feature breakdown by clustering subpopulation

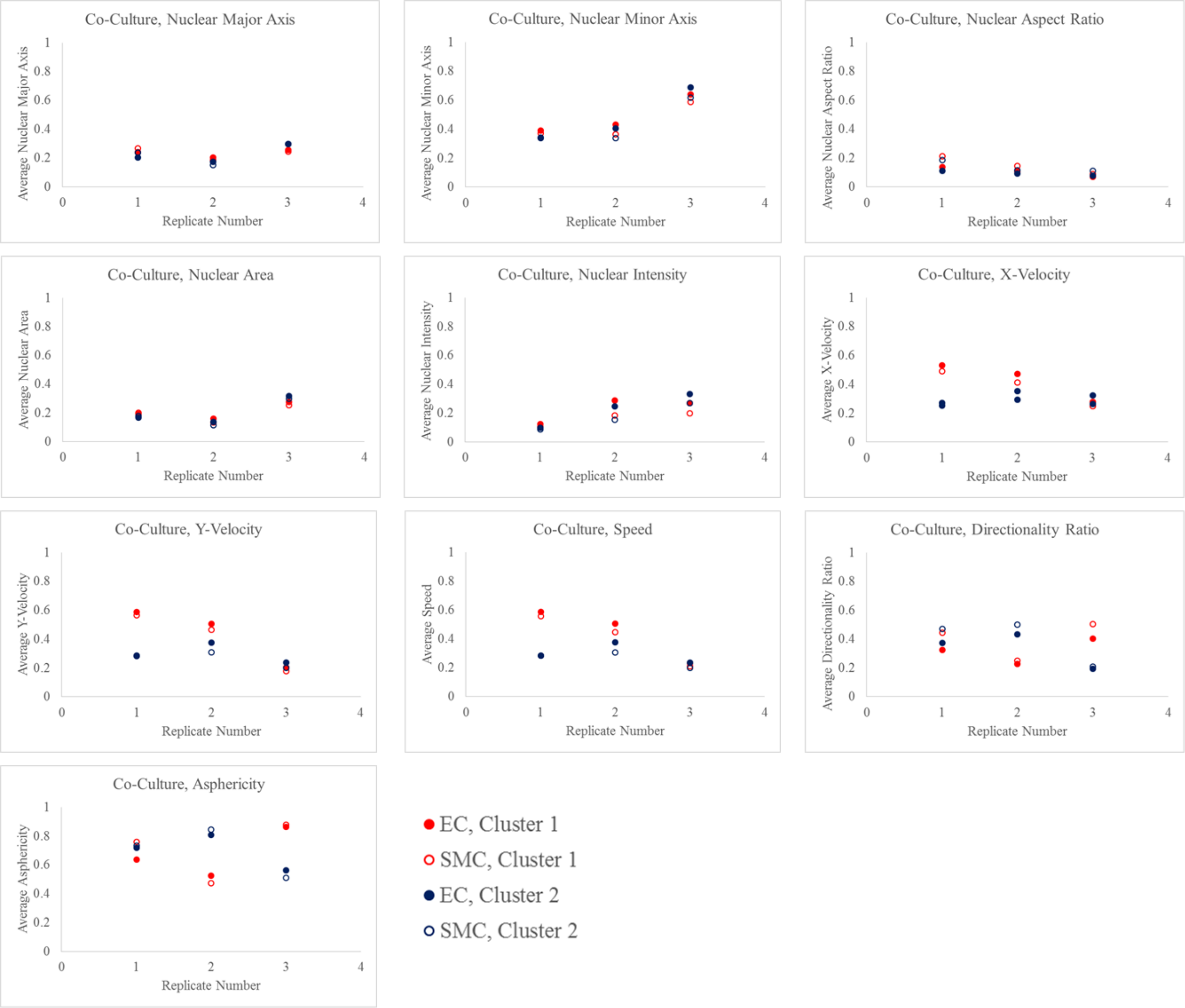

Cell feature averages were plotted for each subpopulation in the SMC and EC co-culture to reveal overarching trends in the combined morphometric and motility data. Unlike the monocultures, cell movement rate was an influential factor in cluster identification. This was in addition to the cell track features, which also demonstrated substantial differences in population averages.

Appendix 3: ACT*IV*E Supplementary Analysis for Bacterial Tracking

A3.1 Removing Noise Particles from *E. coli* Data

Due to the nature of bacterial biofilm formation and growth, *E. coli* cells may attach and detach from a material surface at any time. This means that cells flowing through the field of view need to be differentiated from attached cells moving atop a material surface. The easiest way to differentiate these behaviors (and eliminate noise in the system in the process) was to put a frame number requirement on the cell motility data. An attached cell will remain on the surface for at least a set number of frames in the video, whereas a flowing cell will move extremely quickly and disappear from the field of view in a time interval below this frame limit. The code to truncate ACT*IV*E data based on this parameter is reproduced below:

```
%Frame requirement for cells to be processed
percent = 0.025;

%Read in cell data
[filename, pathname] = uigetfile({'*.mat'}, 'Select a txt data file');
load([pathname,filename]);

%Find cells that are present in >x% of frames
max_frames = max(xyzs_id(:,12));
if percent ~= 0
    min_frames = max_frames*percent;
else
    min_frames = 1;
end
unq_cells = unique(xyzs_id(:,13));
num_cells = size(unq_cells,1);
min_frame_cells = zeros(ceil(num_cells/2),1);
cell_count = 1; xyzs_count = 1;
xyzs_id_min_cells = zeros(ceil(size(xyzs_id,1)/2),ceil(size(xyzs_id,2)));
```

```
num_frames_cell = zeros(ceil(num_cells/2),1);

for r = 1:num_cells
    bool_cell = unq_cells(r) == xyzs_id(:,13);
    if sum(bool_cell) >= min_frames
        min_frame_cells(cell_count,1) = unq_cells(r);
        xyzs_id_min_cells(xyzs_count:(xyzs_count+sum(bool_cell)-1),:) = 
xyzs_id(bool_cell,:);
        num_frames_cell(cell_count,1) = sum(bool_cell);
        cell_count = cell_count+1;
        xyzs_count = xyzs_count+sum(bool_cell);
    end
end

%Get rid of extra zeros:
min_frame_cells(min_frame_cells == 0) = [];
num_frames_cell(num_frames_cell == 0) = [];
xyzs_id_min_cells(all(xyzs_id_min_cells == 0,2),:) = [];

%Print metrics of interest:
fprintf('There are %d cells present in more that %d %% frames \n',
size(min_frame_cells,1), (percent*100))
```

A3.2 Classifying “Moving”, “Rotating”, and “Still” Cells

In **Chapter 7.3**, *E. coli* behavioral dynamics were classified into one of three categories: 1) “moving”, 2) “rotating”, and 3) “still” cells. These cells were grouped based on their frame-to-frame displacement characteristics. The code, reproduced below, executes the following:

1. The average length of each cell is calculated to define the mean cell length used in movement definitions.
2. Each cell is classified into one of three categories based on the following definitions:
    a. “Moving”: A cell displaces greater than 1 average cell body length frame to frame.
    b. “Rotating”: A cell displaces between ¼ and 1 average cell body length frame to frame.

    c. “Still”: A cell displaces less than 1 average cell body length frame to frame.

3. The number of cells falling into each movement category is tallied and information is plotted frame by frame to visualize collective trends in movement behavior.

```
%% Process Cell Data
%Classify bacteria into "moving" and "rotating" cells

%Calculate the boundary to classify "moving" versus "rotating" cells (one
%average cell length)
major_axis = xyzs_id_min_cells(:,[3,xyzs_id_columns]);
unique_cell_ids = unique(major_axis(:,2));
num_cells = size(unique_cell_ids,1);
cell_length = zeros(1,num_cells);

%Calculate average individual cell lengths
for i = 1:num_cells
   bool_cell = major_axis(:,2) == unique_cell_ids(i);
   cell_data = major_axis(bool_cell,:);
   cell_length(i) = mean(cell_data(:,1));
end

%Calculate overall average cell length
average_cell_length = mean(cell_length);

%Each cell must be classified as either a moving, rotating, or still cell
%(per frame to frame iteration). For frame 1, all cells are classified as
%moving (no way to differentiate). From frame 2 on, this flag will be based
%on whether the change in displacement is larger than the
%average_cell_length calculated above. Moving cells are defined as cells
%moving more than 1 cell length per frame, rotating cells are defined as
%cells moving between 1/4 and 1 cell length, and still cells are defined as
%cells moving less than 1/4 cell length

%Pull out data of interest: 1) x position, 2) y position, 3) major axis, 4)
%minor axis, 5) angle (theta), 6) area, 7) intensity, 8) frame number, 9)
%cell ID, 10) flag: 2="moving", 1="rotating", 0="still,
%11) displacement (frame_x - frame_x-1)
all_cell_data = zeros(size(xyzs_id_min_cells,1),11);
all_cell_data(:,1:9) = xyzs_id_min_cells(:,[1:7, xyzs_id_columns-1,
xyzs_id_columns]);
frame_idx = 8;
cell_idx = 9;
flag_idx = 10;
dist_idx = 11;
```

```
%Classify all cells present in frame 1 as "moving" cells
bool_frame1 = all_cell_data(:,frame_idx) == 1;
all_cell_data(bool_frame1, flag_idx) = 1;
all_cell_data(bool_frame1, dist_idx) = NaN;
overall_idx = 1;

%Calculate cell displacements
for j = 1:num_cells
    bool_single_cell = all_cell_data(:,cell_idx) == unique_cell_ids(j);
    single_cell_data = all_cell_data(bool_single_cell,:);
    datapoints = size(single_cell_data, 1);

    %Frame by frame analysis: frame_x - (frame_x-1); note: gaps in data are
    %ignored (e.g. if a cell is present in frames 10 and 15 only, the
    %change in displacement would be calculated between frames 15 and 10.
    %This can be changed in the future
    for k = 2:datapoints
        dist = sqrt((single_cell_data(k,1)-single_cell_data(k-
1,1))^2+(single_cell_data(k,2)-single_cell_data(k-1,2))^2);
        single_cell_data(k,dist_idx) = dist;

        %flag if cell is considered "moving" or "rotating"; default value
        %will otherwise be 0 ("still" cell classification).
        if dist > average_cell_length
            single_cell_data(k,flag_idx) = 2;
        elseif (average_cell_length/4) < dist && dist < (average_cell_length)
            single_cell_data(k,flag_idx) = 1;
        end
    end

    %Transfer individual cell data into large matrix and advance processing
    all_cell_data(bool_single_cell, flag_idx:dist_idx) =
single_cell_data(:,flag_idx:dist_idx);
    overall_idx = overall_idx + datapoints;
end

%% Analyze Data
%Generate plots of interest

%Plot cell number over time
num_frames = max(all_cell_data(:,frame_idx));
cell_count = zeros(num_frames, 4);

%Count total number of cells, total number of moving cells, and total
%number of rotating cells by frame.
for m = 1:num_frames
    bool_frame = all_cell_data(:,frame_idx) == m;
    cell_count(m,1) = sum(bool_frame);
```

```
    bool_move = all_cell_data(:,frame_idx) == m & all_cell_data(:, flag_idx)
== 2;
    cell_count(m,2) = sum(bool_move);

    bool_rotate = all_cell_data(:,frame_idx) == m & all_cell_data(:,
flag_idx) == 1;
    cell_count(m,3) = sum(bool_rotate);

    bool_still = all_cell_data(:,frame_idx) == m & all_cell_data(:, flag_idx)
== 0;
    cell_count(m,4) = sum(bool_still);
end

%Plot cell totals of interest
figure;
hold on
%1) Plot total cell numbers over time
plot(1:num_frames, cell_count(:,1),'or')
axis([0, num_frames, 0, max(cell_count(:,1))+10])
xlabel('Time (Frame Number)')
ylabel('Number of Cells')

%2) Plot "moving" cells over time
plot(2:num_frames, cell_count(2:end,2),'ob')

%3) Plot "rotating" cells over time
plot(2:num_frames, cell_count(2:end,3),'og')

%4) Plot "still" cells over time
plot(2:num_frames, cell_count(2:end,4),'om')

legend('Total Cell Count', 'Total Moving Cells', 'Total Rotating Cells',
'Total Still Cells');
hold off
```

A3.3 Velocity Analysis of *E. coli*

The original ACT*IV*E analysis package contains code to calculate x and y cell velocity behaviors using the finite differences approximation. It does not, however, visualize or package the information outside of the standard *xyzs_id* matrix. Therefore, a supplementary function, velocity_profile, was written to generate the cell velocity distribution plots shown in Chapter 7.3, and package the cell velocity information for aggregate calculations. The code to analyze velocity data is reproduced below.

```
function [x_mat, y_mat, mag_mat] = velocity_profile(mat_loc, accuracy,
framerate, frame_pct, mtp_ratio)
%Computes and plots the velocity distribution for cells processed by ACTIVE
%   Inputs:
%   1) mat_loc: directory location for processed ACTIVE .mat file
%   2) accuracy: accuracy value for finite differences theorem velocity
%   calculations (accepted values = 2, 4, 6, or 8
%   3) framerate: number of minutes between time-lapse frames (e.g. 3
%   minute intervals)
%   4) frame_pct: cut-off for processing cell velocity values. Cells must
%   be present in x/total frame number. For example, if you have
%   200 images and want to evaluate all of the cells present for at least
%   20 frames or more, 20/200 = 0.1; frame_pct = 0.1.
%   5) mtp_ratio: micron to pixel ratio. Conversion value for velocity
%   display in microns/min


accuracy=2;
framerate=0.1;
frame_pct=0.3;
mtp_ratio=0.5;
%Load ACTIVE processed data
mat_loc='\\stu03-fsrv.ad.syr.edu\fasong$\Desktop\Cell tracking (Henderson
Lab)\ACTIVE Code\ALL\motB stiff1.mat';


load(mat_loc);

%Calculate velocity based on finite differences theorem:
[xyzs_id] = velocity_calc2(xyzs_id, xyzs_id_columns, accuracy);

%Find relevant cell information
max_frames = max(xyzs_id(:,xyzs_id_columns-1));
unq_cells = unique(xyzs_id(:,xyzs_id_columns));
num_cells = size(unq_cells,1);

%Remove "cells" that are not present in x% of frames (most likely due to
%noise being picked up as a cell or from a cell being present in FOV for
%small window of time)

pct_frames = floor(max_frames*frame_pct);
```

```
pct_frame_cells = zeros(num_cells,2);
cell_count = 1; xyzs_count = 1;
xyzs_id_pct_cells = zeros(size(xyzs_id,1),size(xyzs_id,2));

%Identify total number of frames each cell is present for
for r = 1:num_cells
    bool_cell = unq_cells(r) == xyzs_id(:,xyzs_id_columns);
    if sum(bool_cell) > pct_frames
        xyzs_id_pct_cells(xyzs_count:(xyzs_count+sum(bool_cell)-1),:) =
xyzs_id(bool_cell,:);
        pct_frame_cells(r,1) = sum(bool_cell);
        cell_count = cell_count+1;
        xyzs_count = xyzs_count+sum(bool_cell);

        cell_id = unq_cells(r);
        pct_frame_cells(r,2) = cell_id;
    else
        pct_frame_cells(r,1) = sum(bool_cell);
    end
end

%Get rid of extra zeros:
xyzs_id_pct_cells(all(xyzs_id_pct_cells == 0,2),:) = [];

%Find all unique cells that are present in greater than x% frames
bool = pct_frame_cells(:,2) ~= 0;
final_cells = pct_frame_cells(bool,2);
final_frames = pct_frame_cells(bool,1);

%Create cell vectors to hold information: 1) average vx, 2) average vy
%3) cell ID number, 4) total number of frames cell is present for, 5)
%average magnitude, 6) total number of frames used to calculate vx, 7)
%total number of frames used to calculate vy
cell_vec = zeros(size(final_cells,1),7);
cell_vec(:,3) = final_cells;
cell_vec(:,4) = final_frames;

% %Select a few cells for velocity profiling:
% cell_prof_interval = floor(size(final_cells,1)/10);
% cell_prof_list =
[cell_prof_interval:cell_prof_interval:size(final_cells,1)];
% cell_prof_array = cell(size(cell_prof_list,2),1);
% cell_prof_counter = 1;

%Obtain relevant cell information
for i = 1:size(final_cells,1)
    bool_cell_data = xyzs_id_pct_cells(:,xyzs_id_columns) == final_cells(i);
    cell_data = xyzs_id_pct_cells(bool_cell_data,:);
```

```
    %X velocity component, vx
    vx = cell_data(:,(size(xyzs_id,2)-1));
    vx(vx == 0) = []; %Remove zeros
    vx = vx.*(mtp_ratio/framerate); %Convert to um/min
    avg_vx = sum(abs(vx))/(size(vx,1));       %Note: divide by size of vx
instead of total number of frames (missing some velocity data in some frames)
    cell_vec(i,1) = avg_vx;
    cell_vec(i,6) = size(vx,1);             %Total number of frames used to
calculate vx

    %Y velocity component, vy
    vy = cell_data(:,(size(xyzs_id,2)));
    vy(vy == 0) = []; %Remove zeros
    vy = vy.*(mstp_ratio/framerate); %Convert to um/min
    avg_vy = sum(abs(vy))/(size(vy,1));       %Note: divide by size of vy
instead of total number of frames (missing some velocity data in some frames)
    cell_vec(i,2) = avg_vy;
    cell_vec(i,7) = size(vy,1);             %Total number of frames used to
calculate vy

    %Magnitude:
    cell_vec(i,5) = sqrt(avg_vx^2+avg_vy^2);

end

% Note: vx/vy/mag size may be different then total number of frames where
% cell is present because not every frame where a cell is present will
% have a velocity value present (e.g. cell disappears for a frame)

%% Cell Velocity Profile Plotting

mkdir([pwd, '\Velocity_Plots'])
addpath([pwd, '\Velocity_Plots'])
xref = size(xyzs_id,2)-1;
yref = size(xyzs_id,2);

%Start by looking at the x-velocity distribution (for aligned/wrinkled
%systems, this may be intersting to compare to perpendicular y-direction)
mean_values_x = zeros(max(xyzs_id_pct_cells(:,xyzs_id_columns-1)),1);

%Store x velocity frame information
x_vel_cell = cell(max(xyzs_id_pct_cells(:,xyzs_id_columns-1)),1);

figure;
hold on
for p=1:max(xyzs_id_pct_cells(:,xyzs_id_columns-1))

    bool_xvel = xyzs_id_pct_cells(:,xyzs_id_columns-1) == p;
```

```
    x_vel_values = xyzs_id_pct_cells(bool_xvel,xref);
    x_vel_cell{p} = x_vel_values;
    bool_xvel_nozeroes = x_vel_values ~= 0;  %Remove zero values from
distribution (non-existent)

    if sum(bool_xvel_nozeroes) > 1
        mean_values_x(p) = mean(abs(x_vel_values(bool_xvel_nozeroes)));
        plot(p,x_vel_values(bool_xvel_nozeroes), 'o','MarkerSize',2);
    else
        mean_values_x(p)=0;   %No average velocity for first and last frames
depending on accuracy selected
    end
end

[~, name, ~] = fileparts(mat_loc);
title(name)
xlabel('Frame Num')
ylabel('X Cell Velocity (um/min)')

saveas(gcf, [pwd, '\Velocity_Plots\', name,
'_X_Velocity_Distribution_Accuracy_', num2str(accuracy)],'fig')

%plot average velocity values over the distribution
%Note: average velocity values will always be computed based on the abs
%velocity of the cells (to prevent zero-ing effects from pos/neg values)
plot(1:max(xyzs_id_pct_cells(:,xyzs_id_columns-1)),mean_values_x, '-
k','LineWidth',3);

%Configure text box with overall mean velocity value
x_pos = floor(max_frames/20);
y_bounds = ylim;
range = abs(y_bounds(1))+abs(y_bounds(2));
y_pos = floor(y_bounds(1)+floor(range/5));
%Note: overall_mean will disregard any "zero" values that stem from the
%finite differences processing method (e.g. first and last frame for
%accuracy = 2, first two and last two frames for accuracy = 4, etc.)
overall_mean_x = mean(mean_values_x((accuracy/2+1):size(mean_values_x-1,1)-
(accuracy/2)));
text(x_pos, y_pos, ['Average Velocity: ', num2str(overall_mean_x)])

saveas(gcf, [pwd, '\Velocity_Plots\', name,
'_X_Velocity_Distribution_with_Mean_Accuracy_', num2str(accuracy)'],'fig')

%Now do the same plotting for the y-velocity
mean_values_y = zeros(max(xyzs_id_pct_cells(:,xyzs_id_columns-1)),1);

%Store y velocity frame information
y_vel_cell = cell(max(xyzs_id_pct_cells(:,xyzs_id_columns-1)),1);
```

```
figure;
hold on
for p=1:max(xyzs_id_pct_cells(:,xyzs_id_columns-1))

    bool_yvel = xyzs_id_pct_cells(:,xyzs_id_columns-1) == p;
    y_vel_values = xyzs_id_pct_cells(bool_yvel,yref);
    y_vel_cell{p} = y_vel_values;
    bool_yvel_nozeroes = y_vel_values ~= 0;  %Remove zero values from
distribution (non-existent)

    if sum(bool_yvel_nozeroes) > 1
        mean_values_y(p) = mean(abs(y_vel_values(bool_yvel_nozeroes)));
        plot(p,y_vel_values(bool_yvel_nozeroes), 'o','MarkerSize',2);
    else
        mean_values_y(p)=0;   %No average velocity for first and last frames
depending on accuracy selected
    end
end

[~, name, ~] = fileparts(mat_loc);
title(name)
xlabel('Frame Num')
ylabel('Y Cell Velocity (um/min)')

saveas(gcf, [pwd, '\Velocity_Plots\', name,
'_Y_Velocity_Distribution_Accuracy_', num2str(accuracy)],'fig')

%plot average velocity values over the distribution
%Note: average velocity values will always be computed based on the abs
%velocity of the cells (to prevent zero-ing effects from pos/neg values)
plot(1:max(xyzs_id_pct_cells(:,xyzs_id_columns-1)),mean_values_y, '-
k','LineWidth',3);

%Configure text box with overall mean velocity value
x_pos = floor(max_frames/20);
y_bounds = ylim;
range = abs(y_bounds(1))+abs(y_bounds(2));
y_pos = floor(y_bounds(1)+floor(range/5));
%Note: overall_mean will disregard any "zero" values that stem from the
%finite differences processing method (e.g. first and last frame for
%accuracy = 2, first two and last two frames for accuracy = 4, etc.)
overall_mean_y = mean(mean_values_y((accuracy/2+1):size(mean_values_y-1,1)-
(accuracy/2)));
text(x_pos, y_pos, ['Average Velocity: ', num2str(overall_mean_y)])

saveas(gcf, [pwd, '\Velocity_Plots\', name,
'_Y_Velocity_Distribution_with_Mean_Accuracy_', num2str(accuracy)'],'fig')
```

```
%Lastly, look at the overall magnitude distribution
% Note: magnitude will always be positive, because of need squaring values
% for magnitude calculation will always result in a positive value.
mean_magnitude = zeros(max(xyzs_id_pct_cells(:,xyzs_id_columns-1)),1);

mag_vel_cell = cell(max(xyzs_id_pct_cells(:,xyzs_id_columns-1)),1);

figure;
hold on
for p=1:max(xyzs_id_pct_cells(:,xyzs_id_columns-1))

    bool_yvel = xyzs_id_pct_cells(:,xyzs_id_columns-1) == p;
    x_vel_values = xyzs_id_pct_cells(bool_yvel,xref); %note: bool_yvel is
just a boolean to find all of the velocity values for a single frame (not
specific to y)
    y_vel_values = xyzs_id_pct_cells(bool_yvel,yref);
    bool_yvel_nozeroes = y_vel_values ~= 0;  %Remove zero values from
distribution (non-existent)
    bool_xvel_nozeroes = x_vel_values ~= 0;

    if sum(bool_yvel_nozeroes) > 1
        frame_mag =
sqrt(x_vel_values(bool_xvel_nozeroes).^2+y_vel_values(bool_yvel_nozeroes).^2)
;
        mag_vel_cell{p} = frame_mag;
        mean_magnitude(p) = mean(frame_mag);
        plot(p,frame_mag, 'o','MarkerSize',2);
    else
        mean_magnitude(p)=0;   %No average velocity for first and last frames
depending on accuracy selected
        mag_vel_cell{p} = 0;   %No magnitude values to report.
    end
end

[~, name, ~] = fileparts(mat_loc);
title(name)
xlabel('Frame Num')
ylabel('Cell Velocity (um/min)')

saveas(gcf, [pwd, '\Velocity_Plots\', name,
'_Mag_Velocity_Distribution_Accuracy_', num2str(accuracy)],'fig')

%plot average velocity values over the distribution
%Note: average velocity values will always be computed based on the abs
%velocity of the cells (to prevent zero-ing effects from pos/neg values)
plot(1:max(xyzs_id_pct_cells(:,xyzs_id_columns-1)),mean_magnitude, '-
k','LineWidth',3);
```

```
%Configure text box with overall mean velocity value
x_pos = floor(max_frames/20);
y_bounds = ylim;
range = abs(y_bounds(1))+abs(y_bounds(2));
y_pos = floor(y_bounds(2)-floor(range/5));
%Note: overall_mean will disregard any "zero" values that stem from the
%finite differences processing method (e.g. first and last frame for
%accuracy = 2, first two and last two frames for accuracy = 4, etc.)
overall_mean_magnitude =
mean(mean_magnitude((accuracy/2+1):size(mean_magnitude-1,1)-(accuracy/2)));
text(x_pos, y_pos, ['Average Velocity: ', num2str(overall_mean_magnitude)])

saveas(gcf, [pwd, '\Velocity_Plots\', name,
'_Mag_Velocity_Distribution_with_Mean_Accuracy_', num2str(accuracy)'],'fig')

close all

%% Package matrix output (revised 3/8/16)

%Matlab does not support matrices with rows/columns of differing sizes. To
%accommodate, excess entries will be filled with NaN (which is not
%processed as a number by Matlab)

num_frames = max(xyzs_id(:,xyzs_id_columns-1));
cell_list = unique(xyzs_id_pct_cells(:,xyzs_id_columns));
num_cells_pct = size(cell_list,1);
x_ref = size(xyzs_id_pct_cells,2)-1;
y_ref = size(xyzs_id_pct_cells,2);

%Start with x velocity output:
x_mat = NaN(num_cells_pct, num_frames);

for r = 1:num_cells_pct
    %Pull out info for each cell
    current_cell = cell_list(r);
    bool_cell = xyzs_id_pct_cells(:,xyzs_id_columns) == current_cell;   %cell
reference info in main matrix
    frame_list = xyzs_id_pct_cells(bool_cell,xyzs_id_columns-1);
%frame information for cell of interest
    x_vec = xyzs_id_pct_cells(bool_cell,x_ref);
%velocity info

    %Transfer info of interest into main x velocity matrix for output
    x_mat(r,frame_list) = x_vec;
end

%Now do the same with the y velocity output:
```

```
y_mat = NaN(num_cells_pct, num_frames);

for q = 1:num_cells_pct
    %Pull out info for each cell
    current_cell = cell_list(q);
    bool_cell = xyzs_id_pct_cells(:,xyzs_id_columns) == current_cell;   %cell
reference info in main matrix
    frame_list = xyzs_id_pct_cells(bool_cell,xyzs_id_columns-1);
%frame information for cell of interest
    y_vec = xyzs_id_pct_cells(bool_cell,y_ref);
%velocity info

    %Transfer info of interest into main x velocity matrix for output
    y_mat(q,frame_list) = y_vec;
end

%And finally the magnitude
mag_mat = NaN(num_cells_pct, num_frames);
mag_mat = sqrt(x_mat.^2+y_mat.^2);

end
```

VITA

NAME OF AUTHOR: Megan E. Brasch

PLACE OF BIRTH: Rochester, NY, USA

DATE OF BIRTH: May 5, 1989

EDUCATION:

B.S. Bioengineering, SUNY Binghamton University (2011)

Ph.D. in Bioengineering, Syracuse University (2017)

PUBLICATIONS:

* = Co-first authors

1. Gu H, Chen A, Song X, **Brasch M**, Henderson J, Ren D (2016). How bacteria land and form cell clusters on a surface: a new role of surface topography. *Scientific Reports* 6, 29516
2. **Brasch ME***, Baker RM*, Manning ML, Henderson JH (2014). Automated, contour-based tracking and analysis of cell behavior over long timescales in environments of varying complexity and cell density, *Journal of the Royal Society Interface* 11, 1742-5662
3. Song F, **Brasch M**, Henderson JH, Sauer K, Ren D. *motB* is involved in mechanosensing of material stiffness during early stage *Escherichia coli* biofilm formation on poly(dimethylsiloxane) surfaces. *Submitted*
4. **Brasch ME**, Passucci G, Gulvady A, Manning ML, Turner CE, Henderson JH. The Role of Intracellular Reorganization and ROCK Inhibition in Fibroblast Cell Motility Responses to a Developing Shape Memory Polymer Based Wrinkle Pattern. *In Preparation*
5. **Brasch ME**, Pena AN, Henderson JH. Image-Based Cell Subpopulation Identification through ACT*IV*E Automated Cell Tracking, Principle Component Analysis, and Partitioning Around Medoids Clustering. *In Preparation*
6. Passucci G, **Brasch ME**, Deakin NO, Turner CE, Henderson JH, Manning ML. Heterogeneous rotational diffusion generates super-diffusive dynamics consistent with mouse fibroblast trajectories. *In Preparation*
7. Wang J, Quach A, **Brasch ME**, Turner CE, Henderson JH. On-Command On/Off Switching of Progenitor Cell and Cancer Cell Polarized Motility and Aligned Morphology Via a Cytocompatible Shape Memory Polymer Scaffold. *In Preparation*